

# *Non-Invasive Electrical Imaging of the Heart*

Leo Cheng

[l.cheng@auckland.ac.nz](mailto:l.cheng@auckland.ac.nz)

Supervised by

Associate Professor Andrew Pullan

[a.pullan@auckland.ac.nz](mailto:a.pullan@auckland.ac.nz)

A thesis submitted in partial fulfilment of the  
requirements for the degree of Doctor of Philosophy



**THE UNIVERSITY OF AUCKLAND**  
**NEW ZEALAND**

Department of Engineering Science  
School of Engineering  
The University of Auckland  
New Zealand

December 2001



# *Abstract*

Non-invasive electrical imaging of the heart aims to quantitatively reconstruct information about the electrical activity of the heart from multiple thoracic ECG signals. The computational framework required to produce such electrical images of the heart from non-invasive torso surface signals is presented. It is shown reliable electrical images of the heart can be obtained under a controlled environment. This has been demonstrated using an anatomically realistic boundary element porcine torso model.

The procedures required to create a subject specific model using a small number of control points and to create a specific heart model from three-dimensional ultrasound images using a linear fitting procedure are presented. From discrete ECG electrodes a continuous representation of the potential field over the entire torso surface can also be produced using this linear fitting procedure.

The construction of the transfer matrices for the two predominant electrocardiographic sources (epicardial potentials and myocardial activation times) are described in detail. The transfer matrices are used to compute activation times within the heart and epicardial potentials on the heart surface. Myocardial activation times are computed using an algorithm based on the Critical Point Theorem while epicardial potentials are computed using standard Tikhonov and Truncated SVD spatially regularised methods as well as Greensite's spatial and temporal regularisation method. The regularisation parameters for the epicardial potentials are determined using a variety of methods (*e.g.*, CRESO criterion, L-curve, zero-crossing).

The potential and activation based formulations are compared in a comprehensive inverse simulation study. To try and capture the dynamic and variable nature of cardiac electrical activity, the study is performed with three different types of cardiac sources with a realistic porcine model. These simulations investigate the effect on the computed solutions of individual and combinations of modelling errors. These errors include corruption in the torso surface signals, changes in material properties and geometric distortion.

In general, the activation based formulation is preferred over the epicardial potential formulations, with Greensite's method found to be the best method for reconstructing epicardial potentials. Under optimal conditions, the activation approach could reconstruct the activation times to within 4 ms RMS. Both potential and activation based formulations were found to be relatively insensitive to changes in material properties such as lung conductivities and activation function shapes. When

examining individual errors, the geometry and positions of the torso and heart had the greatest effects on the inverse solutions. The relative heart position needed to be determined to within 5 mm to obtain results within 2 ms of the solutions obtained under control conditions. When the modelling errors are combined to produce errors which can be expected in a clinical or experimental situation the activation based solutions were consistently more accurate than potential based solutions.

The next necessary step in this project is the detailed validation of the results against *in-vivo* data. This step is necessary before such algorithms can be reliably used to aid in the assessment of heart function in a clinical environment.

# *Acknowledgements*

There are large number of people to thank for the work presented throughout this thesis. A large portion has been based upon the foundations provided by CMISS – of which a large number of people (past and present) have contributed. For that reason I would like to deeply thank Professor Peter Hunter for having the vision, so long ago, to establish this framework which we have all learnt to love (and hate). Without this unique environment, the goals of this thesis would not have been able to be met.

Also, thanks to my supervisor, Associate Professor Andrew Pullan. His guidance and support leading up to and throughout the duration of this thesis have been indispensable while his enthusiasm has been an outstanding source of encouragement. I would also like to acknowledge Dr David Budgett for his stellar supervision during the first year of my studies while Andrew was on sabbatical.

Special mention should go to close colleagues who have directly aided in this project. In Auckland, John Bodley and Dr Greg Sands. Your contributions and friendship has been invaluable throughout the last year. In Oxford, Drs Martyn Nash, Chris Bradley and David Patterson for supplying the experimental data without which a large portion of this thesis would not exist.

Shane Blackett, Dr Richard Christie and Dr David Bullivant for developing such a wonderful canvas for us all to analyse and visualise our results. It has been invaluable for many of the figures included in this thesis. Also, many thanks to Dr Karl Tomlinson for sharing with me his vast knowledge of CMISS (and everything else for that matter).

I am grateful to Auckland UniServices Ltd., the Graduate Research Fund and the Bioengineering Research Group for their financial support. Without their assistance I would not have been able to attend valuable conferences in Auckland, Atlanta, Pakatoa Island, Waitangi, Waiheke, Hutchinson Island, Boston, Queenstown and Christchurch. Its tough but somebody had to do it!

My fellow students (and the best of friends) who have endured and shared the ups and downs for the past four years. The few that managed to leave, those that left but came back, and the majority that could not quite bring themselves to leave this wonderful family. Special mention to Richard ‘Munce’ Boyes, David ‘Andre’ Nickerson, Warren ‘Java Boy’ Hedley, Carey ‘Bad Place’ Stevens and Martin Buist for their valued friendship for the better part of a decade.

I also would like to thank Mum and Dad for their love and support throughout my life. Finally, to Phong, the dearest of friends. Your distractions from work have been a refreshing delight.



*Good, Better, Best ...*

*Don't Ever Stop Until,*

*Good is Better, and Better is Best.*





# Contents

<b>Abstract</b>	<b>iii</b>
<b>Acknowledgements</b>	<b>v</b>
<b>List of Figures</b>	<b>xv</b>
<b>List of Tables</b>	<b>xv</b>
<b>Notation</b>	<b>xxiii</b>
<b>Glossary of Symbols &amp; Abbreviations</b>	<b>xxv</b>
<b>1 Introduction &amp; Historical Overview</b>	<b>1</b>
1.1 Cardiac Anatomy & Function . . . . .	3
1.2 Electrocardiology . . . . .	7
1.2.1 The Problems of Electrocardiology . . . . .	8
1.2.2 Electrocardiograms . . . . .	8
1.2.3 The Standard 12-lead ECG . . . . .	11
1.2.4 Invasive Mapping Techniques . . . . .	14
1.2.5 Body Surface Potential Mapping . . . . .	15
1.2.6 Technical Requirements . . . . .	16
1.3 Data Visualisation . . . . .	17
1.4 Thesis Overview . . . . .	19
<b>2 The Finite Element &amp; Boundary Element Methods</b>	<b>21</b>
2.1 Mesh Division . . . . .	22
2.2 One-Dimensional Basis Functions . . . . .	22
2.2.1 Lagrange Basis Functions . . . . .	24
2.2.2 Hermite Basis Functions . . . . .	26
2.3 Two and Three Dimensional Basis Functions . . . . .	28

2.3.1	Bilinear Lagrange . . . . .	28
2.3.2	Bicubic Hermite . . . . .	28
2.4	Sector Elements . . . . .	30
2.5	Mesh Refinement . . . . .	32
<b>3</b>	<b>Geometric &amp; Field Fitting with the Finite Element Method</b>	<b>33</b>
3.1	Interpolation and Fitting . . . . .	34
3.2	Field Fitting . . . . .	35
3.2.1	Data Projection . . . . .	35
3.2.2	Linear Field Fitting . . . . .	36
3.2.3	Error Metrics . . . . .	37
3.2.4	Sobolev Smoothing . . . . .	38
3.3	Applications of Geometric and Field Fitting . . . . .	42
3.3.1	Activation Time Fitting . . . . .	42
3.3.2	Signal Fitting . . . . .	43
3.3.3	Geometric Fitting . . . . .	45
3.4	Model Customisation . . . . .	48
3.4.1	Host Mesh Customisation . . . . .	50
3.4.2	Heart Customisation . . . . .	52
<b>4</b>	<b>Geometric Torso &amp; Cardiac Source Models</b>	<b>57</b>
4.1	Previous Geometric Models for Electrophysiology . . . . .	58
4.2	Model Generation . . . . .	59
4.3	Generic Male Torso Model . . . . .	61
4.4	Generic Porcine Model . . . . .	64
4.4.1	Fitting Results . . . . .	67
4.5	Material Properties . . . . .	68
4.5.1	Passive Electrical Conductivities . . . . .	68
4.5.2	Bidomain Conductivities . . . . .	70
4.6	Cardiac Sources . . . . .	70
4.6.1	Normal Ventricular Activation Sequence . . . . .	72
4.6.2	Single Dipole Source . . . . .	73
4.6.3	Eikonal Activation Profile . . . . .	74
4.6.4	Point Stimulus Activation Profile . . . . .	75
4.6.5	Experimentally Derived Activation Profile . . . . .	76

<b>5</b>	<b>The Forward Problem of Electrocardiology</b>	<b>81</b>
5.1	Governing Equations . . . . .	82
5.1.1	Generalised Laplace's Equation . . . . .	83
5.1.2	Poisson Equation . . . . .	84
5.1.3	Boundary Conditions . . . . .	85
5.2	Coupling Regions . . . . .	85
5.3	Transfer Matrices From a Boundary Element Point of View . . . . .	88
5.4	Activation Function . . . . .	95
5.5	Analytic Test Cases . . . . .	97
5.5.1	Laplace's Equation Analytic Test Problem . . . . .	98
5.5.2	Poisson Equation Analytic Test Problem . . . . .	104
5.6	Convergence Analysis of Generic Model . . . . .	118
5.6.1	Mesh Resolution . . . . .	119
5.6.2	Potential Based Convergence . . . . .	119
5.6.3	Activation Based Convergence . . . . .	123
5.6.4	Convergence Summary . . . . .	125
<b>6</b>	<b>The Inverse Problem of Electrocardiology</b>	<b>127</b>
6.1	Singular Value Decomposition . . . . .	129
6.2	Epicardial Potential Formulation . . . . .	131
6.2.1	Tikhonov Regularisation . . . . .	131
6.2.2	Truncated SVD Regularisation . . . . .	133
6.2.3	Greensite Temporal & Spatial Regularisation . . . . .	134
6.2.4	Determining the Regularisation Parameter . . . . .	135
6.3	Myocardial Activation Time Formulation . . . . .	138
6.3.1	Determining & Refining the Activation Sequence . . . . .	139
6.3.2	Estimation of the Activation Sequence . . . . .	140
6.3.3	Critical Points & Times . . . . .	141
6.3.4	Critical Point Function . . . . .	142
6.3.5	Myocardial Activation Regularisation Constraints . . . . .	145
6.3.6	Critical Point & Times Constraints . . . . .	148
6.4	Control Inverse Simulations . . . . .	149
6.4.1	Double Point Stimulus Activation Profile . . . . .	150
6.4.2	Eikonal Activation Profile . . . . .	151
6.4.3	Experimentally Derived Activation Profile . . . . .	152
6.4.4	Summary for Control Inverse Simulations . . . . .	153

6.4.5	Effect of Refinement Level . . . . .	154
<b>7</b>	<b>The Sensitivity of Inverse Solutions to Modelling Errors</b>	<b>155</b>
7.1	Previous Investigations . . . . .	156
7.2	Simulation Study Overview . . . . .	157
7.3	Effect of Signal Errors . . . . .	160
7.3.1	Effect of Uncorrelated Electrical Noise . . . . .	161
7.3.2	Effect of Uncorrelated Electrode Displacement . . . . .	166
7.3.3	Effect of Correlated Electrode Displacement . . . . .	168
7.4	Effect of Material Property Errors . . . . .	170
7.4.1	Effect of the Transmembrane Jump Magnitudes . . . . .	170
7.4.2	Effect of the Width of the Activation Upstroke . . . . .	171
7.4.3	Effect of Lung Masses & Conductivities . . . . .	172
7.5	Effect of Geometric Errors . . . . .	174
7.5.1	Effect of Heart Translation in the Lateral Directions . . . . .	174
7.5.2	Effect of Heart Translation in the Posterior-Anterior Directions . . . . .	176
7.5.3	Effect of Heart Translation in the Superior-Inferior Directions . . . . .	178
7.5.4	Effect of Heart Rotation About the Coronal Plane . . . . .	180
7.5.5	Effect of Heart Rotation About the Sagittal Plane . . . . .	182
7.5.6	Effect of Heart Size . . . . .	184
7.5.7	Effect of Torso Size . . . . .	186
7.6	Effect of Realistic Experimental Errors . . . . .	188
7.7	Comparisons Between Activation & Potential Formulations . . . . .	196
7.7.1	Effect of Individual Errors . . . . .	197
7.7.2	Effect of Combined Errors . . . . .	199
7.7.3	General Comparisons . . . . .	199
<b>8</b>	<b>Conclusions, Validation &amp; Future Developments</b>	<b>201</b>
8.1	Validation of Numerical Methods . . . . .	202
8.2	Future Developments . . . . .	204
<b>A</b>	<b>Laplace's &amp; Poisson Equation Analytic Test Solutions</b>	<b>207</b>
A.1	Convergence of Analytic Laplace's Equation Problem . . . . .	207
A.2	Convergence of Analytic Poisson Equation Problem . . . . .	209
A.2.1	Convergence Analysis of Potential and Normal Current . . . . .	209
A.2.2	Comparison of Potential and Normal Current with Analytic Solution . . . . .	210

---

<b>B</b>	<b>Convergence Analysis of Generic Porcine Model</b>	<b>211</b>
B.1	Porcine Model Surface Information . . . . .	212
B.2	Forward Simulation with Dipole Source . . . . .	213
B.3	Forward Simulation with an Activation Source . . . . .	220
<b>C</b>	<b>Inverse Simulation Results</b>	<b>227</b>
C.1	Effect of Signal Errors . . . . .	228
C.2	Effect of Material Properties . . . . .	231
C.3	Effect of Geometric Errors . . . . .	233
C.4	Typical Experimental Error . . . . .	242
<b>D</b>	<b>CMISS Routines &amp; Command Files</b>	<b>245</b>
D.1	Computer Systems . . . . .	246
D.2	Commonly Used Routines in CMISS . . . . .	247
D.2.1	General Routines . . . . .	247
D.2.2	Fitting Routines . . . . .	248
D.2.3	Forward Problem Routines . . . . .	248
D.2.4	Inverse Problem Routines . . . . .	249
D.3	Signal Fitting Comfile . . . . .	250
D.4	Host Mesh Customisation Comfile . . . . .	252
D.5	Geometric Fitting Comfile . . . . .	254
D.6	Forward Problem With Dipole Source Comfile . . . . .	256
D.7	Activation Inverse Problem Comfile . . . . .	258
D.8	Activation and Potential Simulation Comfile . . . . .	264
	<b>References</b>	<b>273</b>



# *List of Figures*

<b>1</b>	<b>Introduction &amp; Historical Overview</b>	<b>1</b>
1.1	Cross-section of a human heart . . . . .	3
1.2	Fibre distribution on the Auckland canine heart model . . . . .	4
1.3	Electrical activity, pressure and ventricular volume through the cardiac cycle . . . . .	5
1.4	Relationship between the action potential, intracellular calcium and force in a ventricular cell . . . . .	6
1.5	Waller’s first demonstration of non-invasive electrical recordings from a human . . . . .	7
1.6	Einthoven’s triangle formed from three bipolar leads . . . . .	9
1.7	Temporal relationships between a body surface ECG and a cardiac action potential . . . . .	10
1.8	Traces from a standard 12-lead ECG . . . . .	12
1.9	Electrode placements for a standard 12-lead ECG and the Auckland BSPM setup . . . . .	13
1.10	Two-dimensional and three-dimensional potential maps . . . . .	18
<b>2</b>	<b>The Finite Element &amp; Boundary Element Methods</b>	<b>21</b>
2.1	Mapping between global space and local $\xi$ space . . . . .	23
2.2	Linear and quadratic Lagrange basis functions . . . . .	25
2.3	Cubic Hermite basis functions . . . . .	27
2.4	Schematic of a bicubic Hermite element . . . . .	30
2.5	Formation of a sector elements from a collapsed quadrilateral element . . . . .	31
2.6	Refinement of a bicubic Hermite element . . . . .	32
<b>3</b>	<b>Geometric &amp; Field Fitting with the Finite Element Method</b>	<b>33</b>
3.1	Adjusting the nodal parameters of a mesh to match data points . . . . .	34
3.2	Orthogonal projection of data points onto a finite element surface . . . . .	35
3.3	Effect of Sobolev smoothing on a fitted surface . . . . .	41
3.4	Fitted epicardial activation field from epicardial electrodes . . . . .	43
3.5	Schematic torso showing a subset of the full recording electrodes . . . . .	44

3.6	Traces comparing recorded and fitted signals . . . . .	46
3.7	Body surface potential map created by fitting data from 240 electrodes . . . . .	47
3.8	MRI and ultrasound images with the traced heart surfaces . . . . .	48
3.9	Geometric fitting of an epicardial surface to ultrasound data . . . . .	49
3.10	Host mesh customisation example . . . . .	51
3.11	Host mesh fitting of the generic porcine model to a specific subject . . . . .	52
3.12	Ultrasound transducer with magnetic receiver . . . . .	53
3.13	Three-dimensional ultrasound calibration process . . . . .	55
3.14	Two-dimensional ultrasound image from the calibration process . . . . .	55
3.15	Constructing a three-dimensional model from two-dimensional ultrasound images .	56
<b>4</b>	<b>Geometric Torso &amp; Cardiac Source Models</b>	<b>57</b>
4.1	Generic human and canine heart models . . . . .	62
4.2	Generic human male torso model . . . . .	63
4.3	Digitised CT slices used to create the generic porcine model . . . . .	65
4.4	Generic porcine torso model . . . . .	66
4.5	Cardiac source derived from an eikonal equation model of ventricular activation . .	75
4.6	Cardiac source generated from two activation seed points . . . . .	76
4.7	Experimentally recorded and fitted epicardial signals . . . . .	78
4.8	Experimentally derived cardiac source . . . . .	79
<b>5</b>	<b>The Forward Problem of Electrocardiology</b>	<b>81</b>
5.1	A transverse slice through the torso at heart level . . . . .	82
5.2	Coupling regions to provide conservation of potential and current . . . . .	87
5.3	Transmembrane action potential compared with the Heaviside step approximation .	95
5.4	Approximation of the transmembrane potential jump with a sigmoidal function . .	96
5.5	Schematic of Laplace's equation analytic solution . . . . .	99
5.6	Convergence of potential for Laplace's equation problem . . . . .	104
5.7	Convergence of normal current for Laplace's equation problem . . . . .	104
5.8	Analytic potential solutions for Laplace's equation problem . . . . .	105
5.9	Schematic of Poisson equation analytic solution . . . . .	106
5.10	Extracellular potential convergence analysis for Poisson equation problem . . . . .	115
5.11	Normal current convergence analysis for Poisson equation problem . . . . .	115
5.12	Convergence of potential and normal currents for Poisson equation problem . . . .	116
5.13	Analytic extracellular potential solutions for the Poisson equation problem . . . . .	117



5.14	Refinement of the endocardial surfaces . . . . .	118
5.15	Schematic of electrode locations of the signals used for convergence analysis . . .	120
5.16	Torso surface signals using the dipole source . . . . .	121
5.17	Potential maps of reference simulation with dipole cardiac source . . . . .	122
5.18	Convergence comparison between bicubic Hermite and linear Lagrange basis functions with the dipole source . . . . .	123
5.19	Torso surface signals using the eikonal source . . . . .	124
5.20	Potential maps of reference simulation with eikonal cardiac source . . . . .	125
<b>6</b>	<b>The Inverse Problem of Electrocardiology</b>	<b>127</b>
6.1	Singular value spectra from an SVD decomposition of a signal matrix . . . . .	130
6.2	Generic L-curve for determining a regularisation parameter . . . . .	137
6.3	Critical points and times of an activation wavefront . . . . .	142
6.4	Comparison of critical point functions between critical and non-critical points . . .	144
6.5	Comparison of critical point algorithm estimates between clean and noisy signals .	145
6.6	Central difference approximation to the second derivative . . . . .	147
6.7	Surface Laplacian for a two-dimensional grid . . . . .	148
6.8	Activation maps of double point source inverse simulation with control conditions .	150
6.9	Activation maps of eikonal source inverse simulation with control conditions . . .	152
6.10	Activation maps of experimentally derived source inverse simulation with control conditions . . . . .	153
<b>7</b>	<b>The Sensitivity of Inverse Solutions to Modelling Errors</b>	<b>155</b>
7.1	Schematic of the positions of the electrodes illustrated in Figure 7.2 . . . . .	162
7.2	Simulated signal traces with Gaussian noise . . . . .	163
7.3	Effect of Gaussian electrical noise on inverse solutions . . . . .	165
7.4	Effect of uncorrelated electrode displacement on inverse solutions . . . . .	167
7.5	Effect of correlated electrode displacement on inverse solutions . . . . .	169
7.6	Effect of the transmembrane jump magnitude on the activation based formulation .	170
7.7	Effect of the width of the activation upstroke on the activation based formulation .	171
7.8	Effect of lung conductivities on inverse solutions . . . . .	173
7.9	Effect of lateral heart translations on inverse solutions . . . . .	175
7.10	Effect of posterior-anterior heart translations on inverse solutions . . . . .	177
7.11	Effect of superior-inferior heart translations on inverse solutions . . . . .	179
7.12	Effect of heart rotations about the coronal plane on inverse solutions . . . . .	181

---

7.13	Effect of heart rotations about the sagittal plane on inverse solutions . . . . .	183
7.14	Effect of heart size on inverse solutions . . . . .	185
7.15	Effect of torso size on inverse solutions . . . . .	187
7.16	Activation maps of inverse simulation with a double point source and realistic errors	190
7.17	Effect of realistic errors with double point source . . . . .	191
7.18	Activation maps of inverse simulation with eikonal source and realistic errors . . .	192
7.19	Effect of realistic errors with eikonal source . . . . .	193
7.20	Activation maps of inverse simulation with experimentally derived source and realistic errors . . . . .	194
7.21	Effect of realistic errors with experimentally derived source . . . . .	195
7.22	Comparison between activation times and those derived from potentials . . . . .	197

# *List of Tables*

<b>1</b>	<b>Introduction &amp; Historical Overview</b>	<b>1</b>
1.1	Electrode placements for a standard 12-lead ECG . . . . .	12
1.2	Mapping system setups from different research groups . . . . .	17
<b>2</b>	<b>The Finite Element &amp; Boundary Element Methods</b>	<b>21</b>
<b>3</b>	<b>Geometric &amp; Field Fitting with the Finite Element Method</b>	<b>33</b>
3.1	Effects of Sobolev smoothing on a fitted surface . . . . .	42
3.2	Comparison measures between recorded and fitted signals . . . . .	45
<b>4</b>	<b>Geometric Torso &amp; Cardiac Source Models</b>	<b>57</b>
4.1	Fitting results for generic male torso model . . . . .	62
4.2	Fitting results for generic porcine model . . . . .	67
4.3	Summary of passive material conductivity values . . . . .	69
4.4	Summary of bidomain conductivity values . . . . .	70
<b>5</b>	<b>The Forward Problem of Electrocardiology</b>	<b>81</b>
<b>6</b>	<b>The Inverse Problem of Electrocardiology</b>	<b>127</b>
6.1	Double point source inverse simulation with control conditions . . . . .	151
6.2	Eikonal source inverse simulation with control conditions . . . . .	151
6.3	Experimental source inverse simulation with control conditions . . . . .	153
<b>7</b>	<b>The Sensitivity of Inverse Solutions to Modelling Errors</b>	<b>155</b>
7.1	Noise levels applied to four simulated electrodes . . . . .	161
7.2	Heart scaling parameters . . . . .	184
7.3	Torso scaling parameters . . . . .	186

7.4	Comparison between activation times and those derived from corresponding potentials . . . . .	196
7.5	Summary of preferred inverse algorithms for typical levels of modelling error . . .	198
<b>A</b>	<b>Analytic Test Solutions</b>	<b>207</b>
A.1	Convergence analysis of potential for Laplace's equation problem . . . . .	208
A.2	Convergence analysis of current for Laplace's equation problem . . . . .	208
A.3	Convergence analysis of the extracellular potential for Poisson equation problem .	209
A.4	Convergence analysis of the normal current distributions for Poisson equation problem . . . . .	209
A.5	Convergence of extracellular potential distributions to the Poisson equation problem	210
A.6	Convergence of current distributions to the Poisson equation problem . . . . .	210
<b>B</b>	<b>Convergence Analysis of Generic Porcine Model</b>	<b>211</b>
B.1	Mesh statistics for porcine model with different refinement levels . . . . .	212
B.2	Convergence of epicardial surface by examining the epicardial potentials . . . . .	214
B.3	Convergence of epicardial surface by examining the torso potentials . . . . .	215
B.4	Convergence of the lung surfaces by examining the epicardial potentials . . . . .	216
B.5	Convergence of the lung surfaces by examining the torso potentials . . . . .	216
B.6	Convergence of torso surface by examining the epicardial potentials . . . . .	217
B.7	Convergence of torso surface by examining the torso potentials . . . . .	217
B.8	Convergence of epicardial surface by examining the epicardial potentials with linear interpolation . . . . .	218
B.9	Convergence of epicardial surface by examining the torso potentials with linear interpolation . . . . .	219
B.10	Convergence of the epicardial surface by examining the epicardial potentials . . . .	221
B.11	Convergence of the epicardial surface by examining the torso potentials . . . . .	221
B.12	Convergence of the left ventricular surface by examining the epicardial potentials .	222
B.13	Convergence of the left ventricular surface by examining the torso potentials . . . .	222
B.14	Convergence of the right ventricular surface by examining the epicardial potentials	223
B.15	Convergence of the right ventricular surface by examining the torso potentials . . .	223
B.16	Convergence of the lung surfaces by examining the epicardial potentials . . . . .	224
B.17	Convergence of the lung surfaces by examining the torso potentials . . . . .	224
B.18	Convergence of the torso surface by examining the epicardial potentials . . . . .	225
B.19	Convergence of the torso surface by examining the torso potentials . . . . .	225

<b>C</b>	<b>Inverse Simulation Results</b>	<b>227</b>
C.1	Effect of Gaussian electrical noise on RMS error metric . . . . .	228
C.2	Effect of Gaussian electrical noise on the SI error metric . . . . .	228
C.3	Effect of Gaussian electrode displacement on the RMS error metric . . . . .	229
C.4	Effect of Gaussian electrode displacement on the SI error metric . . . . .	229
C.5	Effect of correlated electrode displacement on the RMS error metric . . . . .	230
C.6	Effect of correlated electrode displacement on the SI error metric . . . . .	230
C.7	Effect of transmembrane jump on the RMS error metric . . . . .	231
C.8	Effect of transmembrane jump on the SI error metric . . . . .	231
C.9	Effect of the width of the activation upstroke on the RMS error metric . . . . .	231
C.10	Effect of the width of the activation upstroke on the SI error metric . . . . .	231
C.11	Effect of lung conductivities on the RMS error metric . . . . .	232
C.12	Effect of lung conductivities on the SI error metric . . . . .	232
C.13	Effect of heart translation in the lateral directions on the RMS error metric . . . . .	233
C.14	Effect of heart translation in the lateral directions on the SI error metric . . . . .	233
C.15	Effect of heart translation in the posterior-anterior directions on the RMS error metric	234
C.16	Effect of heart translation in the posterior-anterior directions on SI error metric . . . . .	234
C.17	Effect of heart translation in the superior-inferior directions on the RMS error metric	235
C.18	Effect of heart translation in the superior-inferior directions on the SI error metric . . . . .	236
C.19	Effect of heart rotation in the sagittal plane on the RMS error metric . . . . .	237
C.20	Effect of heart rotation in the sagittal plane on the SI error metric . . . . .	238
C.21	Effect of heart rotation in the coronal plane on the RMS error metric . . . . .	239
C.22	Effect of heart rotation in the coronal plane on the SI error metric . . . . .	239
C.23	Effect of heart size on the RMS error metric . . . . .	240
C.24	Effect of heart size on the SI error metric . . . . .	240
C.25	Effect of torso size on the RMS error metric . . . . .	241
C.26	Effect of torso size on the SI error metric . . . . .	241
C.27	Typical experimental errors with double point source on the RMS error metric . . . . .	242
C.28	Typical experimental errors with double point source on the SI error metric . . . . .	242
C.29	Typical experimental errors with eikonal source on the RMS error metric . . . . .	243
C.30	Typical experimental errors with eikonal source on the SI error metric . . . . .	243
C.31	Typical experimental errors with experimentally derived source on the RMS error metric . . . . .	244
C.32	Typical experimental errors with experimentally derived source on the SI error metric	244



# *Notation*

- Mathematical variables represented by bold lower case symbols are vector quantities (*e.g.*,  $\mathbf{x}$ ) and bold upper case symbols refer to tensor quantities (*e.g.*,  $\mathbf{X}$ ).
- Einstein summation is used, where repeated indices imply summation over the individual components. For example a vector dot product may be written as

$$a_i b_i = \mathbf{a} \cdot \mathbf{b} = \sum_{i=1}^N a_i b_i$$

where  $N$  is the length of the vector.

- An inner product of two column vectors is denoted by  $\langle \ , \ \rangle$ .





# *Glossary of Symbols & Abbreviations*

## **Scalar Symbols**

<b>Symbol</b>	<b>Description</b>
$a$	resting potential
$b$	transmembrane potential jump
$d$	data point number
$D$	total number of data points
$e$	element number
$h$	characteristic element size
$n$	local node number
$N$	global node number or full rank of matrix
$s_e$	element based scale factors
$S_n$	nodal based scale factors
$t$	time
$T$	total number of time steps
$u_n$	dependant variable at local node $n$
$\alpha$	Sobolev weighting on the first derivative terms
$\beta$	Sobolev weighting on the second derivative terms
$\phi_e$	extracellular potential
$\phi_i$	intracellular potential
$\phi_m$	transmembrane potential
$\xi$	local element coordinates
$\lambda$	regularisation parameter
$\lambda_t$	regularisation parameter at time $t$
$\omega$	activation window
$\varepsilon$	an unspecified basis function
$\varphi_n$	Lagrange basis function
$\Psi_n^d$	Hermite basis function
$\zeta_n$	Hermite sector basis function collapsed at local node 1
$\eta_n$	Hermite sector basis function collapsed at local node 3
$\mathcal{L}_n$	surface Laplacian at node $n$

## Vector & Matrix Symbols

Symbol	Description
$a$	column of transfer matrix
$A$	transfer matrix
$A_{\lambda_i}^\dagger$	pseudo inverse of transfer matrix regularised at $i$
$B$	magnetic induction
$d$	dipole source vector
$D$	electric displacement
$E$	electric field intensity
$E_1$	Gaussian noise
$E_2$	correlated noise
$G$	first-order Tikhonov regularisation matrix (surface gradient)
$H$	magnetic field intensity
$I$	zero-order Tikhonov regularisation matrix (identity matrix)
$J$	current density
$J_i$	impressed source current density
$L$	second-order Tikhonov regularisation matrix (surface Laplacian)
$n$	unit outward normal
$P$	boundary element global potential matrix
$q$	flux vector
$Q$	boundary element global flux matrix
$R$	reduced global matrix or Tikhonov regularisation matrix
$s$	solution vector
$U$	spatial SVD decomposition of a matrix
$V$	temporal SVD decomposition of a matrix
$x$	node on heart surface
$y$	node on torso surface
$z_d$	global position of data point $d$
$\sigma_e$	extracellular conductivity tensor
$\sigma_i$	intracellular conductivity tensor
$\hat{\phi}_B$	calculated torso potentials from a cardiac source
$\phi_B$	measured torso potentials
$\tau$	activation field on the heart
$\Gamma$	surface mesh domain
$\Omega$	mesh domain
$\Phi$	signal data matrix
$\Sigma$	singular values from an SVD

## Abbreviations

Abbreviation	Description
AHA	American Heart Association
ARI	Activation Recovery Interval
AT	Activation Time
AV node	Atrioventricular node
BEM	Boundary Element Method
BSM	Body Surface Map
BSPM	Body Surface Potential Mapping
CMISS	Continuum Mechanics, Image analysis, Signal processing and System identification
CPA	Critical Point Algorithm
CT	Computed Tomography
ECG	ElectroCardioGram
FEM	Finite Element Method
LA	Left Atria
LV	Left Ventricle
MRI	Magnetic Resonance Imaging
RA	Right Atria
RV	Right Ventricle
SA node	Sinoatrial node
UnEmap	Universal Electrophysiological Mapping System
WCT	Wilson Central Terminal



# ***1 Introduction & Historical Overview***

Since the first electrocardiogram was recorded by Waller (1887), clinicians have been trying to deduce the electrical activity within the heart by examining recorded potentials on the body surface. Cardiovascular diseases accounted for 30% of all deaths in 1999 (World Health Organisation 2000), therefore, the ability to accurately diagnose abnormal cardiac conditions using non-invasive measurements would be highly beneficial both as a clinical aid and as a mass screening tool. This effectively involves obtaining an accurate electrical image of the heart from electrical information obtained from electrodes located on the torso surface.

By placing two electrodes anywhere on the torso surface, the potential difference between them provides an indication of the electrical activity of the heart and can be displayed as an electrocardiogram (ECG). The electrical currents within the heart, which control its mechanical motion, are reflected on the body surface and produce electrical potentials which vary continuously throughout the cardiac cycle. By placing more electrodes on the torso, different ‘views’ of the electrical activity of the heart can be obtained and by examining this information, cardiac function can be inferred.

The standard 12-lead ECG is now an essential tool for the clinical diagnosis and monitoring of irregular heart conditions. It is estimated that 100 million standard 12-lead ECGs are recorded annually in the United States (Geselowitz 1989). By examining the amplitudes and timings of the ECG waveforms and the relative positions between each electrode, clinicians are able to deduce information about the electrical activity which is occurring within the heart. The analysis of this information is an inverse problem (*i.e.*, determining heart function from the corresponding torso surface potentials) and is largely accomplished by experience based on pattern matching to signals from known disorders. However, it is only able to provide a weak qualitative assessment of heart function since it only obtains subsampled information from nine recording electrodes (of which

only six are located near the heart).

The cause of some cardiac arrhythmias can be cured through the elimination of an arrhythmogenic substrate by applying high levels of electrical energy to generate heat at key sites within the heart. This technique is called radio frequency ablation and involves placing a catheter directly onto the target tissue and the burning of the surrounding area. The quick and accurate localisation of the site is crucial to the successful clinical outcome of these ablative procedures. Practically, the catheter ablation of conditions such as ventricular tachycardia is limited, in part, by the difficulty in identifying suitable sites for ablation (Schilling, Peters & Davies 1998). In such procedures, in addition to the recordings from 12-lead ECGs, invasive measurements from within the heart are usually also required so that a clearer electrical image of the heart can be built up. This process can still be extremely time consuming and the heart must be in a state which permits prolonged monitoring.

An alternative approach for obtaining detailed non-invasive electrical images of the heart involves the use of mathematical modelling and multiple ECG signals. These electrical images potentially provide a clearer picture of the electrical activity than a standard 12-lead ECG. Methods to create such images have been investigated for the past 30 years but, to date, no clinically accepted system has been developed to augment the information provided by the 12-lead ECG (Brooks & MacLeod 1997).

A number of persistent barriers prevent the widespread use of electrical imaging methods in clinical cardiology. In comparison to the standard 12-lead ECG, a far greater amount of data must be gathered (*e.g.*, heart position and orientation, torso geometry, a large number of electrode locations and signals). Even if this data can be obtained, it still remains questionable whether the additional information produced by the electrical image will be sufficient to justify collecting the additional information. The fact that dense torso ECG sampling can provide more information than the standard 12-lead ECG is of little doubt (SippensGroenewegen, Spekhorst, van Hemel, Kingma, Hauer, de Bakker, Grimbergen, Janse & Dunning 1993). However, significant challenges remain in data processing, extraction and presentation of results in an appropriate form.

## 1.1 Cardiac Anatomy & Function

The heart is an organ whose primary task is to pump blood around the body. It is situated near the centre of the thoracic cavity between the two lungs. Figure 1.1 shows the anatomy of the four heart chambers of a human heart. The lower, larger, thick walled chambers are the left ventricle (LV) and right ventricle (RV), while the smaller upper chambers are the left atrium (LA) and right atrium (RA). The heart muscle is called the myocardium and it encompasses the muscle between the inner endocardial surfaces and the outer epicardial surface. The myocardium is composed of a complex sheet and fibre structure that greatly varies throughout the heart (Le Grice, Smaill, Chai, Edgar, Gavin & Hunter 1995). Figure 1.2 shows the heart fibres displayed on the endocardial and epicardial surfaces on a canine heart model. The directions at which the fibres and sheets are oriented affect the flow of the electrical activity and the mechanical motion of the heart.

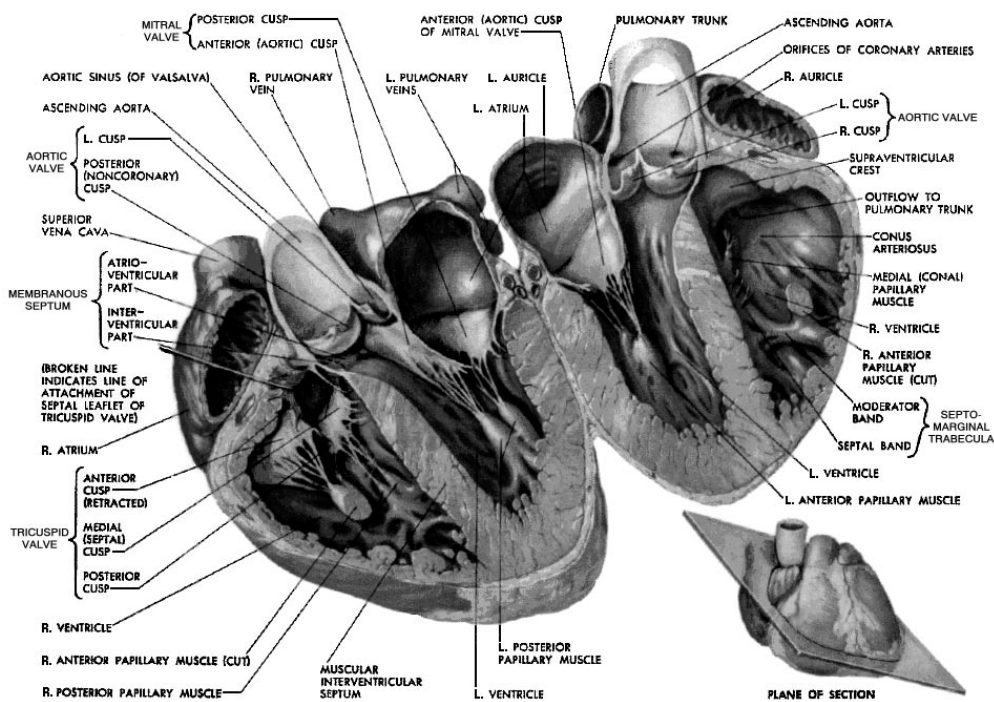


**Figure 1.1:** A cross-section of a human heart taken through the four major chambers showing that the wall of the left ventricle is substantially thicker than the right ventricular free wall. Reproduced from Netter (1997).

The atria are relatively thin walled chambers which collect blood before feeding it into the ventricles upon contraction. In contrast, the ventricles are larger chambers that forcefully contract, pumping the blood out through arteries to the lungs and the body. Each respective atrium and ventricle pair are separated by valves which help to regulate the blood flow; the tricuspid valve on the right and

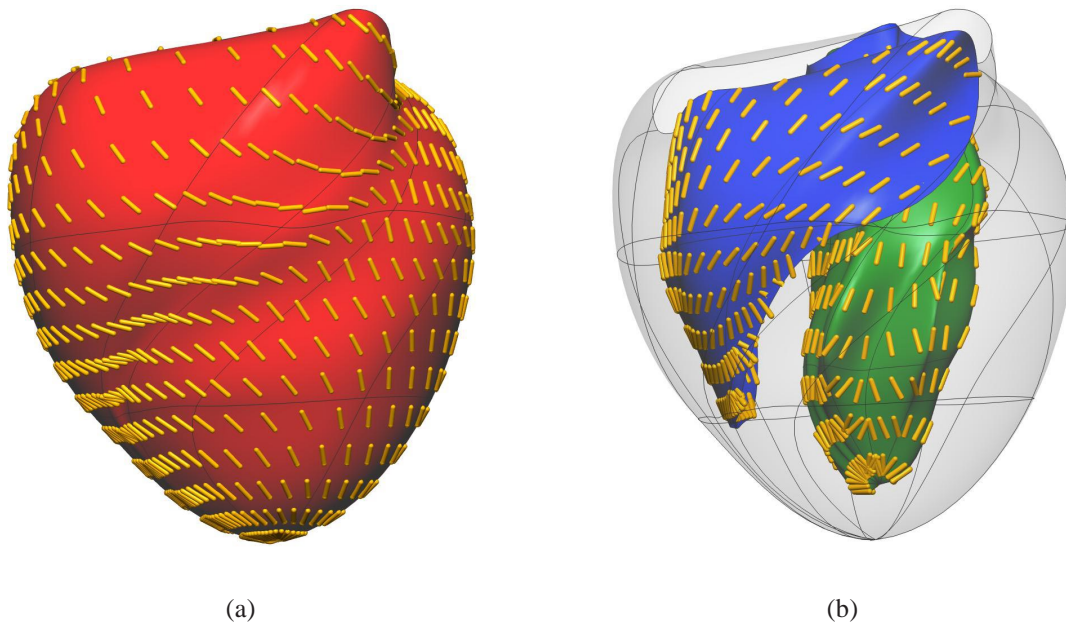


**Figure 1.2:** The Auckland canine rectangular Cartesian heart model created from the data of Le Grice et al. (1997) showing the varying fibre distribution within the myocardium. The gold cylinders represent the complex fibre distribution on the epicardial and endocardial surfaces. The epicardium is shown as dark red in (a) and a transparent surface in (b). In (b), the left ventricle is shown as a green surface and the right ventricle as a blue surface.

the mitral (bicuspid) valve on the left.

The LV is responsible for pumping oxygenated blood around the body. Blood travels from the LV through the aortic valve into the aorta. The aorta is the largest blood vessel in the body and carries blood up towards the head and the arms, before arching over and travelling down the vertebral column to carry blood towards the internal organs and the legs. The right ventricle pumps blood, as it returns from the body, into the pulmonary artery which leads to the lungs, where the blood is re-oxygenated ready for another cycle.

The heart is a unique organ which possesses an electrical conduction system which is capable of providing coordinated rhythmic contraction to pump blood around the body. The different stages of the cardiac cycle and how they relate to the mechanical motions of the heart and its ability to pump the blood around the body is shown in a Wiggers diagram in Figure 1.3. The changes in ventricular volume and resultant change in pressure are governed by the passage of the electrical wavefront through the myocardium.

Each wave of cardiac activation originates from a group of self regulating pacemaker cells called



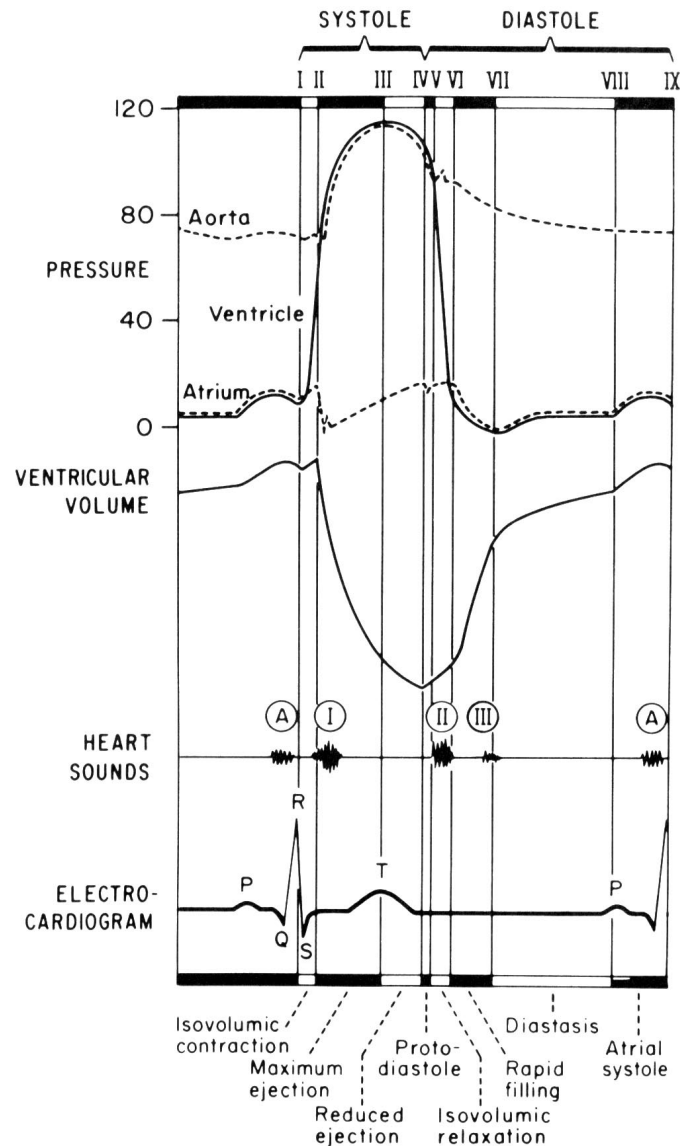


**Figure 1.3:** Wiggers diagram illustrating the eight primary phases of a cardiac cycle. The top three traces show the pressure in the aorta, left ventricle and left atria in millimetres of mercury. The next curve represents the left ventricular volume. Below that are the relative timings of sounds produced by the heart in the cycle as heard using a stethoscope. The bottom trace represents the standard ECG reading with P wave, QRS complex and T waves marked. The Wiggers diagram illustrates the relationship between the electrical wave in the myocardium, shown by the ECG, the resultant mechanical deformation of the heart, shown by the change in volume and the resultant change in pressure within the heart chambers. Reproduced from Katz (1992).

the sinoatrial (SA) node which is located in the RA. From the SA node, the activation wave spreads firstly through the RA, followed by the LA before gathering at the atrioventricular (AV) node. This node is the only electrical pathway between the atria and the ventricles in a healthy human heart. From the AV node the wavefront travels along a fast conducting pathway, known as the *bundle of His*, to the bottom of the septum. From there, it spreads across the endocardial surface of both ventricles via a fast conduction network, known as the *Purkinje fibres* and then through the ventricular myocardium.

An action potential is a measure of the difference between the potential in the intracellular and extracellular space (*i.e.*, the transmembrane potential) of a single cardiac cell (*myocyte*) over time. It provides a representation of the electrical activity within the cell. The activation-contraction cycle within cardiac muscle cells is controlled largely by the concentration of calcium ions in the myocardial cell. The relative timing of the action potential, intracellular calcium ion concentration and the resultant force in a myocyte is shown in Figure 1.4. This shows the electrical-mechanical coupling which occurs at a cellular level. Action potentials typically have a duration of 250–300 ms and there exists a delay of 80–100 ms between the action potential upstroke and the mechanical contraction of the muscle.

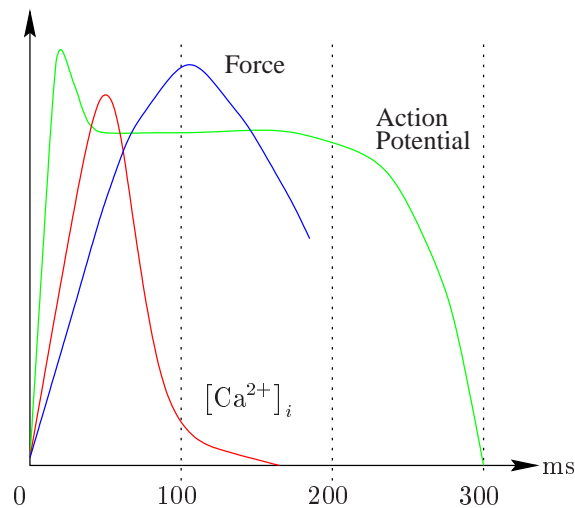


**Figure 1.4:** Schematic of the relationship between the action potential, intracellular calcium ion concentration and the resultant force in a cardiac cell. The rising action potential causes the intracellular calcium ion concentration to rise which in turn causes the cell to contract and develop force. The relative time (ms) is shown on the horizontal axis. The effect of the electrical wave on the ventricular volume and the pressure is further illustrated in the Wiggers diagram in Figure 1.3.

## 1.2 Electrocardiology

The study of the electrical activity of the heart is known as electrocardiology. This can be achieved examining the electrical recordings measured directly within the heart, or interpreting non-invasive recordings on the torso surface.

ECG theory and notation was initially proposed by Einthoven (1903). The first human ECG traces recorded by Waller (1887), as shown in Figure 1.5, contained simultaneous recordings of the electric and the mechanical motion which accompany each heart beat. Since then, non-invasive imaging of mechanical heart motion has advanced from a cardiograph to clinically accepted imaging modalities such as magnetic resonance imaging (MRI), computed tomography (CT) and ultrasound. However, the techniques for electrically imaging the heart non-invasively have not advanced significantly. In the last few decades there has been renewed interest in attempting to extract clearer and more detailed information from the potentials measured on the torso surface. Rapidly increasing computing power and improvements in mathematical modelling have allowed further advancement in this field.

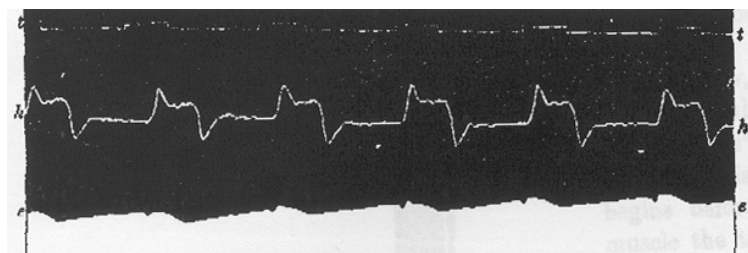


**Figure 1.5:** The first demonstration on a human of electromotive changes and mechanical motions which accompany the heart's beat. The upper trace (t.t.) provides a measure of time, while the middle trace (h.h.) indicates the heart's movement from a cardiograph and the lower trace (e.e.) the level of the mercury in a electrometer capillary measuring the resultant voltage difference between a pair of electrodes. Reproduced from Waller (1887).

As non-invasive electrical imaging of the heart is a passive sensing method, it is theoretically more difficult than other established medical imaging modalities (such as CT, MRI or ultrasound) which actively measure the transmission or scattering of energy injected into the organ. The energy transmitted by these active methods may be altered to provide varying conditions for improved results when imaging different structures. In contrast, the ECG passively measures the energy which has been generated by the heart and cannot be externally altered during a normal ECG recording.

### 1.2.1 The Problems of Electrocardiology

The problem of electrocardiology can be broken into two distinct problems, the *forward problem* and *inverse problem*. Both problems involve determining the relationship between electrical activity at the heart level and on the torso surface.

A forward problem is the name given to the general class of problems which seek to determine the resultant field that is generated from some imposed source. Thus, the forward problem of electrocardiology seeks to determine the potentials and/or currents in the torso that result from a given cardiac source.

The inverse problem of electrocardiology belongs to a class of ill-posed, remote sensing problems. Given the resultant torso surface potential field, it seeks to determine the underlying cardiac source generator. Effectively, all clinicians “solve” an inverse problem every time a diagnosis is made from ECG signals. Torso surface potentials are spatially smoothed projections of the electrical current sources associated with the cardiac activation. The inverse problem involves removing the masking effects of the tissue between the heart and torso surface. The difficulty in the problem arises from its non-unique solutions and ill-posed nature. By posing the problem in terms of reconstructing a single dipole, a unique solution can be obtained. However, this solution provides little insight into the underlying physiological events. If the inverse problem is posed in terms of epicardial potentials or myocardial activation times, a unique solution can be obtained, but the problem becomes ill-posed in nature. This means that any noise entering the process of measurement and modelling will be amplified in the solution in an unknown and uncontrolled fashion (Huiskamp & Greensite 1997).

Practically, the inverse problem is the more useful of the two problems for use in diagnosis of cardiac conditions from non-invasive recordings.

### 1.2.2 Electrocardiograms

When Waller (1887) performed the first human ECG, it was known that electrical activity could be recorded from an exposed heart and that each heart beat was accompanied by changing voltages. He decided to investigate the possibility of recording the resultant potential changes from the limbs of animals and humans. He dipped his right hand and left foot into a two basins of salt solutions which were connected to two poles of an electrometer and “at once had the pleasure of seeing the

mercury column pulsate with each pulsation of the heart” (Besterman & Creese 1979).

Almost from the beginnings of electrocardiography, the concept of a vector force was invoked initially by Waller (1889) who suggested that the electromotive force of the heart could be represented by a single dipole.

In 1901, Einthoven modified a string galvanometer to provide the earliest high-fidelity recording of the ECG. The machine weighed approximately 600 pounds and required 5 operators (Einthoven 1903). Later the I, II and III leads were defined by utilising three electrodes on the left arm, right arm and left leg, which he assumed to be at the corners of an equilateral triangle as shown in Figure 1.6. This was later termed Einthoven’s triangle . A cardiac vector could be used to represent the total electrical activity by combining each of the three limb leads.

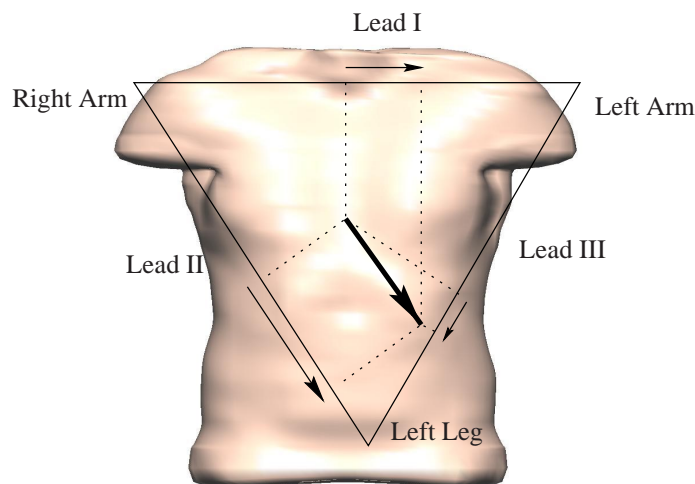


**Figure 1.6:** The orientation of the three bipolar leads I, II and III, forming Einthoven’s Triangle. Einthoven simplified interpretation of the ECG by assuming the heart to lie in the centre of an equilateral triangle, the corners of which are in contact with electrodes placed on the left arm, right arm and the left leg. A normal mean QRS vector is shown at the centre of the triangle and the dipole vector’s contribution to each of the leads is shown by projecting the head of the dipole vector orthogonally onto each side of the triangle (dotted lines).

Each limb used in the recording of the ECG was regarded as an apex of an equilateral triangle, equidistant electrically from the heart. This idea has its limitations in that it assumes the body is an electrically homogeneous sphere. However, Einthoven’s original model has proven extremely useful and still dominates much of current electrocardiology. This is primarily due to its simplicity and ability to extract a large amount of information about the state of the heart using only a small amount of measured data.

A schematic diagram of a normal ECG trace and its temporal relationship with a ventricular action potential is shown in Figure 1.7. The action potential shows the contribution of a single myocyte to the ECG, while the ECG represents a global summation of the electrical activity within the entire heart volume. The characteristic deflections of the ECG, were named at the beginning of the last century by Einthoven after letters (P,Q,R,S and T). Intervals and segments are defined as regions (e.g., the P-R and S-T intervals) and additional complexes were defined as groups of waves (e.g., the QRS complex).

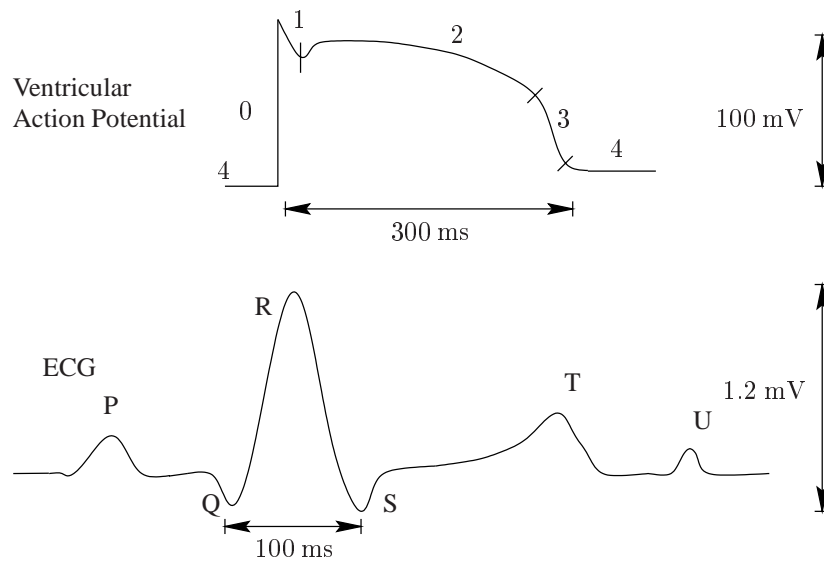


**Figure 1.7:** Temporal relationships between a body surface ECG and a cardiac action potential. The QRS complex is produced by the combination of the upstrokes of all the action potentials throughout the ventricle. The P wave represents the depolarisation phase of the atria while the isoelectric ST segment corresponds to the plateau in the action potential (phase 2) and the T wave represents the repolarisation (phase 3) of the ventricular mass. The isoelectric segment (phase 4) that comes after the T wave corresponds to ventricular diastole. The poorly understood U wave is thought to represent the repolarisation of the Purkinje network.

In a normal heart, the first deflection of an ECG, which represents atrial depolarisation, is the P wave. The duration of the P wave reflects the time taken for the wave of depolarisation to propagate over the atria. After the P wave, the ECG returns to its baseline as the changing potential within the heart cannot be detected on the torso surface. Within the heart, the wave propagates through the AV node and Purkinje network. The QRS complex represents the wave of depolarisation passing through the ventricular myocardium. The amplitude of the QRS complex is greater than that of the P wave because of the larger ventricular mass compared to the atria. As a first approximation, the QRS complex corresponds to the upstroke of the action potential, the ST segment to the plateau and the T wave to repolarisation.

Following the QRS, the ECG normally returns to its baseline, where it remains until the start of the T wave. The isoelectric phase of the ST segment occurs when all regions of the ventricle are in a depolarised state. The duration of the ST segment thus reflects the normally long plateau of the ventricular action potential. Repolarisation of the ventricles generates the T wave, which corresponds to phase 3 of the cardiac action potential as defined in Figure 1.7. The duration of the T wave is considerably longer than that of the QRS complex because unlike ventricular depolarisation, repolarisation does not spread as a rapidly propagated wave. In some normal ECGs a small deflection is seen after the T wave. This is the U wave, whose origin remains uncertain. It has been postulated that the U wave may be related to repolarisation of the Purkinje network, in which the action potential duration is greater than that of the ventricular myocardium (Katz 1992). The atria, like the ventricles, generate a potential difference during their repolarisation. The effect of this is not usually seen on an ECG because its amplitude is small and its effect is masked by the much larger QRS complex. The QT interval is a useful index of the ventricular action potential duration. However, again, there is only a rough correlation as the ECG is a representation of the sum of the potential differences produced by the entire ventricular myocardium.

### 1.2.3 The Standard 12-lead ECG

The most commonly used system of ECG leads is the standard 12-lead system. It uses a combination of 9 electrodes on the torso surface to produce 12 waveforms which provide a representation of the heart's electrical activity. Standard 12-lead traces from a healthy subject are shown in Figure 1.8.

The standard 12-lead uses six precordial electrodes placed on the thorax at the heart level and three extremity electrodes, placed on the left and right arms and the left leg. The exact locations of these electrodes is shown in Table 1.1. Figure 1.9 shows a comparison between the 9 electrodes used with a standard 12-lead ECG and the 256 electrode body surface mapping system currently used at The University of Auckland. Further comparisons between other mapping systems around the world are also shown in Table 1.2.

The extremity limb electrodes are used to derive a reference potential against which the other electrodes are measured relative to. In standard electrocardiography the *erroneous* belief that there exists a point in space at which the potential should be assigned a zero value has led to the search for the position of this 'ideal' reference location. The most commonly used reference point is the



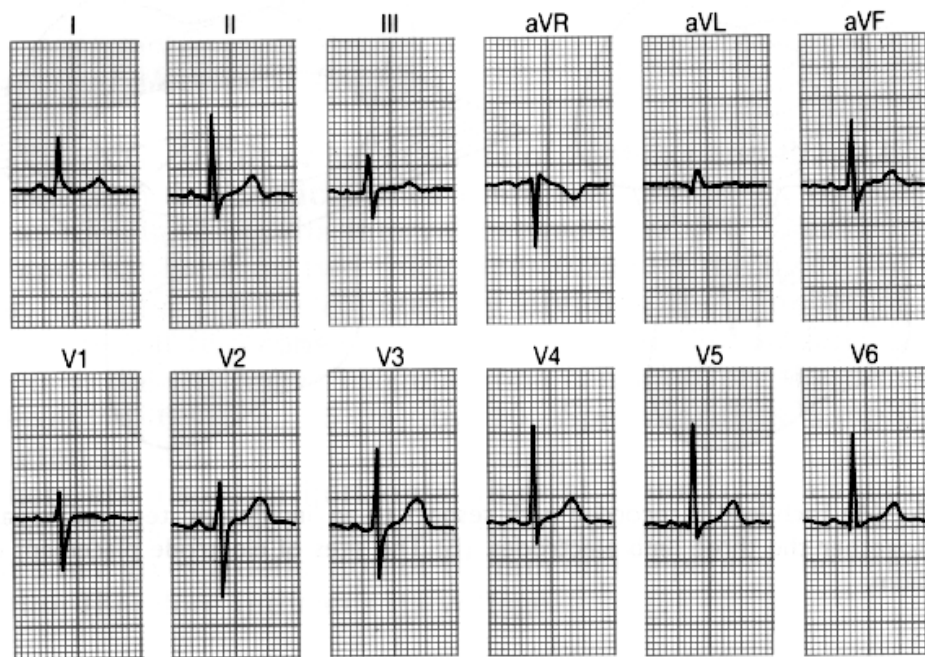


**Figure 1.8:** Traces from a standard 12-lead ECG from a healthy subject. The physical location of the recording electrodes are shown in Figure 1.9.

ELECTRODE	SYMBOL	ATTACHMENT LOCATION
Right arm	R	Right wrist
Left arm	L	Left wrist
Left foot	F	Left ankle
Right foot	G	Right ankle
V <sub>1</sub>		Right sternal margin, fourth intercostal space
V <sub>2</sub>		Left sternal margin, fourth intercostal space
V <sub>3</sub>		Midway between V <sub>2</sub> and V <sub>4</sub>
V <sub>4</sub>		Left mid-clavicular line, fifth intercostal space
V <sub>5</sub>		Left anterior auxiliary line, V <sub>4</sub> space
V <sub>6</sub>		Left mid-auxiliary line, V <sub>4</sub> and V <sub>5</sub> level

**Table 1.1:** Placements of the nine electrodes used for a standard 12-lead ECG. These locations are shown graphically in Figure 1.9.



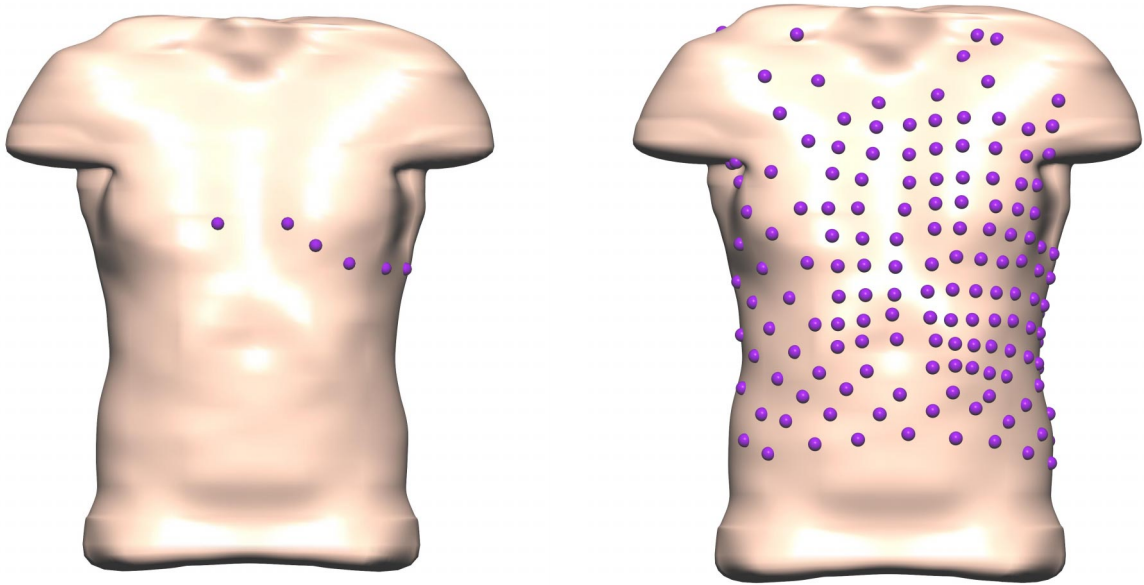


**Figure 1.9:** The electrode placement for the precordial leads of a standard 12-lead ECG (left) compared with the 256 electrode BSPM setup used at The University of Auckland (right). Each sphere represents an electrode on the torso surface. In both cases the electrodes are concentrated over the heart to capture the higher potential gradients in that region. Typical recordings from the 12-lead ECG setup is shown in Figure 1.8.

Wilson's Central Terminal (WCT). This is an artificial reference point formed by averaging the potentials observed at both arms and the left leg proposed by Wilson, MacLoed & Barker (1933). Its major importance lies in the fact that so many electrocardiologists in the past have examined its 'ideal' nature and it has now been accepted as a standard.

The six chest leads proposed by Kossmann & Johnston (1935) are useful in evaluating abnormalities arising in the ventricles. This is because the chest electrodes are placed so that the QRS complexes recorded in leads  $V_1$  and  $V_2$ , over the anterior right chest wall, are influenced by the spread of the wave of depolarisation of the right ventricle, whereas  $V_5$  and  $V_6$ , over the left side of the chest, reflect left ventricular depolarisation. In a normal ECG, however, the potentials generated by the left ventricle are so dominant that they overwhelm, and usually completely obscure, the potential differences caused by right ventricular depolarisation. For this reason, although the normal QRS complexes in  $V_5$  and  $V_6$  are upright because they record the approaching wave of depolarisation over the left ventricle, QRS complexes recorded in leads  $V_1$  and  $V_2$  are normally inverted because they are generated almost entirely by the wave of depolarisation of the left ventricle that moves away from the right side of the chest.

The strengths of a standard 12-lead system are undoubted. With only a small number of electrodes and little time, a clinical diagnosis is possible. The fact that the 12-lead standard has largely remained unchanged since the addition of the augmented limb leads (Goldberger 1942) to Einthoven's original three limb leads and the additional six chest leads, indicates its success. However, its limitations are also evident. Anterior regions can be easily detected due to the proximity of electrodes but there exist significant errors in other regions. Standard electrocardiology has limited sensitivity to regional cardiac events and there is an emphasis on the intensity of ECG forces. It is also highly reliant on interpretation via pattern matching. An experienced physician will know the ranges of normal ECG readings given an individual's age, sex, weight and a number of other considerations. These factors however, increase the chance of a misdiagnosis. The rate of false diagnosis in myocardial infarctions is as high as 30% and results in unnecessary health-care costs and in the United States this is estimated at US\$4 billion per year (Selker 1989). A large proportion of these expenses could be conserved if more accurate and advanced assessment tools were available.

#### **1.2.4 Invasive Mapping Techniques**

In a clinical situation, due to the lack of detailed information provided by the standard 12-lead ECG, a clearer electrical image of the heart is often required. One solution to this problem involves obtaining invasive measurements directly at the heart level. These potentials recorded directly on the epicardial and/or endocardial surfaces are situated close to the underlying cardiac electrical sources and therefore provide an opportunity for direct interpretation of electrical events that non-invasive measurements will not permit. Unlike the recordings on the torso surface, these measurements have not been affected by the torso volume.

There currently exist several established techniques for invasively obtaining electrical activity of the heart. These include endocardial point-based contact catheters, non-contact catheter systems, epicardial socks and plunge electrodes. Endocardial point-based catheters record the electrical activity at localised region on the end of catheters (Biosense Webster 2000, Smeets, Ben-Haim, Rodriguez, Timmermans & Wellens 1998). The non-contact methods involve a similar process but mathematically reconstruct the activity of a chamber of the heart from measurements obtained within the heart chamber (Schilling et al. 1998, Gornick, Adler, Pederson, Hauck, Budd & Schweitzer 1999, Strickberger, Knight, Michaud, Pelosi & Morady 2000). More invasive methods involve large numbers of direct measurement on and within the heart itself. These include covering the epicardial surface

with an electrode sock (Nash, Bradley, Cheng, Pullan & Paterson 2000*b*) or by inserting arrays of electrodes directly into the myocardium (Langrill & Roth 2001).

A drawback of these techniques is that they are all invasive and cannot be used for long-term monitoring. Point-based catheter mapping techniques fail to provide a global view of chamber activation and cannot assess information on the epicardial surface. Some ventricular tachycardias utilise the epicardium for part of the reentry circuit and, due to the limited field of view, unstable arrhythmias cannot be easily mapped. Global activation maps are required to obtain a better understanding of the critical elements necessary to initiate and maintain tachycardias.

### 1.2.5 Body Surface Potential Mapping

One of the major deficiencies of the conventional 12-lead ECG is that information is constructed from an inadequately sampled subset of the body surface data. In general, accurate localisation of the abnormal electrical events of the heart cannot be obtained from this subsampled data, especially in the anterior regions. The technique known as Body Surface Potential Mapping (BSPM) involves sampling potentials at a greater number of sites on the torso surface (in the range of 32–256 electrodes). With these additional recording sites, information missed by the standard 12-lead ECG can be obtained.

The wave forms of ECG signals recorded at the body surface depend not only on the heart's electrical activity, but also on the positions of the electrode pairs used. When multiple lead positions are used, each lead provides a different aspect of the heart's electrical activity. The display of a set of instantaneous potential data on a map representing the body surface is called a Body Surface Map (BSM). The increasing experimental and clinical use of BSPM has shown that such maps can be related to certain regional electrical processes in the heart. A body surface map is a low resolution projection of cardiac electrical events filtered by the torso cavity.

With this greater amount of information, it is necessary to display this information in a useful manner and interpret the information in accordance with known electro-physiological principles to provide an accurate assessment of the cardiac state. These data can be interpreted directly in the form of potential maps with pattern matching techniques as is now accepted in Japan for daily clinical diagnosis (Watanabe 1996). However, the ability to determine details of regional electrical activity in the heart from visual inspection of the BSPM is limited. There has been some

directions made towards identifying sites of reentry based on visual examination of QRS integral maps (SippensGroenewegen et al. 1993).

A better prospect would involve processing the large quantity of data through some form of mathematical modelling, to unravel the filtering effects of the torso and recover the electrical information at the heart level (*i.e.*, solving the inverse problem of electrocardiology).

Accurate solutions of the inverse problem from body surface maps will have great benefit for improving diagnosis and hence decisions about the treatment of patients. For the successful non-invasive computational calculation of cardiac sources, high quality body surface potential data must be obtained as the input for an inverse solution. The practical acquisition of high quality data is a non-trivial matter. However, this is becoming easier with the development of disposable electrode strips and portable multichannel recording systems.

### **1.2.6 Technical Requirements**

For ECG measurements to be used as input for a quantitative inverse procedure, a far greater quantity of data, compared to the standard 12-lead ECG, must be gathered. In addition to the potential measured at the electrodes, the electrode locations must be known and the torso volume conductor must be accurately modelled for each subject. The accuracy to which the input components (*e.g.*, signals and torso geometry) must be determined to obtain an accurate inverse solution is still unknown and is investigated in Chapter 7.

As BSPM has been primarily used for research, unlike the standard 12-lead, there is no internationally recognised standard for electrode positioning and recording systems. As shown in Table 1.2 there are many different lead systems in use for the purpose of recording body surface maps (Hoekema, Uijen, Stilli & van Oosterom 1998). These differ in electrode placement as well as in the number of leads in use. In most lead systems, the electrodes are attached to the torso stripwise (*i.e.*, the electrodes are incorporated in vertical strips that are attached to the torso). The number of strips, however, differs between lead systems, as does the number of leads per strips. The variation in recording setups has resulted in difficulties in comparing data between different research groups around the world.

The requirements for potential measurements are different for recording at different locations.

SYSTEM	CHANNELS	DESCRIPTION
AMSTERDAM/NIJMEGEN	64	11 vertical strips
AUCKLAND	256	torso suit
BATH	40 – 82	6 horizontal strips
BRUSSELS	120	15 vertical strips
DALHOUSIE	120	14 vertical strips with 4 – 7 electrodes
GRAZ/MONTREAL	63	10 vertical strips
HELSINKI	123	15 vertical strips
JAPAN	87	11 vertical strips
OXFORD	256	torso suit / epicardial sock
PARMA	219	18 vertical strips
UTAH (LUX-32)	32	5 strips on anterior and individual electrodes on posterior
UTAH (LUX-192)	192	16 vertical strips

**Table 1.2:** Mapping system setups from different research groups around the world. The number of channels indicates the maximum number of electrodes which can be recorded at any one time. Modified from Hoekema et al. (1998).

Generally faster responses and higher frequencies are required to accurately capture information closer to the underlying cardiac sources (Barr & Spach 1977).

Brooks & MacLeod (1997) states that a BSPM system must have a flat response between 0.05 Hz and 250 Hz. These limits are of particular importance to body surface mapping as different sites on the surface have been found to have different high frequency components. Changes to the high frequency cutoff will result in loss of information and changes to both limits will result in changes in isopotentials. Temporal sampling rates are accepted to be between 0.25 kHz and 2 kHz. The mapping of epicardial and endocardial potentials has different requirements. It is believed that information about the wavefront velocity, the thickness of the wavefront and potential gradient are lost if the spatial resolution is greater than 2 mm. Typical recording frequencies are around 1–2 kHz while the frequencies of 5–10 kHz are required for transmural mapping.

### 1.3 Data Visualisation

As with many computational techniques there is the recurring problem of interpretation and analysis of the vast amounts of data which can be produced. The appropriate visualisation of these data is a key component of the analysis of results. It must be presented in an intuitive form which can be easily interpreted by clinicians.

The irregular spatial sampling of potentials over a complex surface is another feature which differentiates it from medical imaging modalities such as MRI and CT where the data is typically provided in the form of uniformly distributed stacks. For both visualisation and modelling requirements, the locations of the electrodes are needed in addition to the potential data itself. The potential information can either be fitted to a regular grid and then standard interpolation techniques used or directly interpolated from the measured data locations themselves.

There are a number of established methods for visualising large volumes of mapping data. They include potential maps, integral maps and activation maps. The advantages and disadvantages of each method are discussed below.

**Potential Maps** represent potentials at a given time instant and display the potentials on a specific geometry. The geometry may either be a realistic model (as shown on the left in Figure 1.10) or a stylised representation such as a two-dimensional projection of a three-dimensional shape (as shown on the right in Figure 1.10). This is a cylindrical projection of the torso surface with the anterior region in the left half of each map and the posterior region on the right. The central shared edges correspond to the left mid-auxiliary line. The fact that this data representation does not display temporal information may lead to misinterpretations. This has been overcome to some degree by displaying sequences of maps or spatial and temporal signals at the same time.

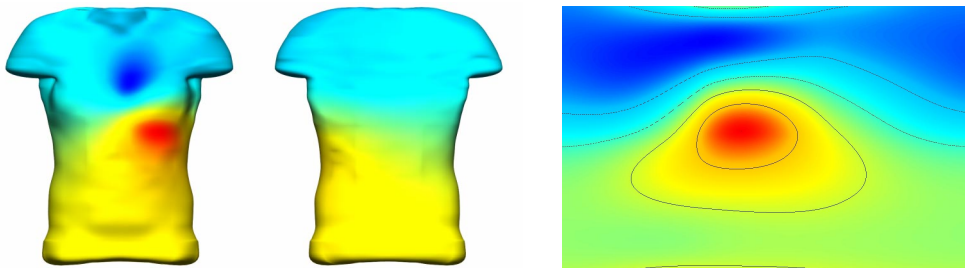


**Figure 1.10:** Potential distribution displayed on a realistic model on the left with views from anterior and posterior perspectives. On the right is a stylised two-dimensional representation of the same data set. The data is displayed on a cylindrical projection which has been unrolled. The anterior of the torso is shown on the left half of the map and the posterior on the right. The marked centre of the map corresponds to the left mid-auxiliary line.

**Integral Maps** dramatically reduce the data by integrating each signal over time to produce an integrated potential. The period over which the signal is integrated is usually over specific intervals in the cardiac cycle (*i.e.*, the QRS, ST and QRST intervals or over the whole heart cycle). This technique also has the problem that temporal information is lost, however, there is some possibility of direct physiological interpretation of the resulting maps. It has been previously shown by



Geselowitz (1985) that time integrals of QRS and QRST are related to the amplitude, area and activation time of the cellular action potentials on the closed surface surrounding the ventricles.

**Activation Maps** are used to display the time, in and on the heart, at which each point is first depolarised. Figure 3.4 shows an example of an experimentally measured activation field. The progression of the depolarisation wave determines the contraction pattern and is essential for determining heart function. A common method of determining the activation time is the maximum negative downstroke of the extracellular potential. A similar method can be used for determining the repolarisation time. The activation recovery interval (ARI) can be calculated by taking the difference between the activation time and the repolarisation time.

## 1.4 Thesis Overview

The aim of this research is the development of a framework from which quantitative electrical images of the heart can be obtained using non-invasive measurements on the torso surface. The thesis will describe the computational and modelling issues associated with generating an electrical image of the heart.

**Chapter 1: Introduction & Historical Overview.** An introduction to cardiac anatomy, standard electrocardiographic techniques and the forward and inverse problems of electrocardiography.

**Chapter 2: The Finite & Boundary Element Methods.** The concepts of the finite element and the boundary element methods are introduced in this chapter. The different basis functions and element types used throughout this thesis are described along with concepts associated with mesh refinement.

**Chapter 3: Geometric & Field Fitting with the Finite Element Method.** The linear field fitting techniques using finite elements are described. The fields include scalar fields such as potentials and activation times and three-dimensional geometric fitting techniques. The Sobolev smoothing used to provide additional constraints on the fit is also introduced. The use of these methods are then described for a number of different applications in Chapter 4. The fitting of potential fields using the finite element method is a new approach to creating a potential field across the entire torso surface. The customisation of generic models using control points is also new approaches for creating a subject specific model given only a few landmark positions.

**Chapter 4: Geometric Torso & Cardiac Source Models.** The construction process of the generic porcine model using the techniques described in Chapter 3 is described along with the fitting results. The ability to easily customise a generic model using the host mesh customisation method is presented. A number of different cardiac sources which attempt to capture various aspects of cardiac activation are also described. These different cardiac sources are later used in Chapters (5)–(7). A porcine model is used as the basis for all the numerical simulations. This model is chosen so that the results derived from the simulation study presented in Chapter 7 can be used to enhance and compliment the methods and results obtained from the validation experiments conducted by Nash et al. (2000*b*).

**Chapter 5: The Forward Problem of Electrocardiology.** Construction of the transfer matrices for the potential and activation based inverse methods are described. The formulation of the governing equations is a generalisation of previous work. Analytic test cases for the potential and activation based transfer matrices using simplified geometries are presented. Finally, a convergence analysis for the forward problem is performed using both potential and activation based cardiac sources on the generic porcine model.

**Chapter 6: The Inverse Problem of Electrocardiology.** The different algorithms for creating non-invasive electrical images of the heart using epicardial potential based and activation time based approaches are introduced. Standard spatially regularised Tikhonov and Truncated Singular Value Decomposition potential based methods as well as the spatially and temporally regularised method of Greensite & Huiskamp (1998) are described. The techniques for obtaining an activation based inverse solution through the use of the Critical Point Theorem are also described.

**Chapter 7: The Sensitivity of Inverse Solutions to Modelling Errors.** Results from a detailed simulation study which analyses and compares the sensitivity and the reliability of the potential and activation based inverse algorithms to a variety of modelling errors is presented. The effect of material conductivities, correlated and uncorrelated signal errors and geometric modelling errors are investigated. Finally, the algorithms are subjected to realistic errors which could be expected in a clinical situation. This simulation study is the first known study which compares a variety of inverse algorithms (potential and activation based) under a large variety of modelling and experimental errors.

**Chapter 8: Conclusions, Validation & Future Development.** The important findings of this thesis, limitations of the models and algorithms which have been developed and suggestions for the orientation of future developments in this field of research are presented.



# 2 *The Finite Element & Boundary Element Methods*

Use of the Finite Element Method (FEM) and the Boundary Element Method (BEM) for analysis of a variety of problems has been widely accepted in many branches of science and engineering. They are computational methods which break down a complex continuous problem into smaller discrete components which are more amenable for analysis. These types of numerical techniques are essential for solving problems which are too difficult to be solved using analytical approaches. FEM is best suited for solving differential equations while BEM is a technique for solving linear equations.

One of the key differences between the two methods is that FEM analyses the entire volume of the area of interest, the solution domain, while BEM analyses problems by solving only over the surface of the domain. They both solve problems by discretising the domain into *elements* to form a piecewise description. For a three-dimensional problem, FEM discretises the domain into three-dimensional volumes, while BEM uses two-dimensional surface elements in a three-dimensional space. By using the BEM approach the problem size is essentially reduced by one dimension. However, since the underlying integral equations couple the dependent variables at one element with every other element, the coefficient matrix characterising the set of equations to be solved is fully populated for any simply connected domain. As FEM is volume-based it is able to explicitly account for anisotropies within the solution domain, with more elements and consequently more solution Degrees of Freedom (DOF). However, as the dependent variables are expressed only in terms their nearest neighbours, the coefficient matrix, while large, is also sparse.

For both methods, the elements are defined by *nodes* throughout the domain. The elements are formed from groups of surrounding nodes. The solution can be found at all points within the domain by interpolating the nodal values through the use of basis functions defined in Section 2.2. Through the use of high order cubic Hermite basis functions (see Section 2.2.2) the geometry of

models and solution fields is well defined with much coarser meshes than finite difference schemes (which use essentially constant basis functions).

## 2.1 Mesh Division

Typically elements are formed from simple structures such as quadrilaterals, cuboids, triangles or tetrahedra. The triangulation approach allows complex domains to be discretised using unstructured meshes, while quadrilaterals and cuboids usually form structured meshes.

The elements of the mesh are defined from key points in the domain known as *nodes*. Each element is defined using a surrounding group of local nodes. Local nodes are a subset of all the global nodes in the mesh. When solving a FEM or BEM problem each element is mapped to a normalised material or local coordinate system, called  $\xi$  space. With this mapping each element, even though they may physically be a different size, can be treated numerically identical in local  $\xi$  space. The  $\xi$  coordinate system always varies between 0 and 1 for each  $\xi$  direction (*i.e.*,  $0 \leq \xi_j \leq 1$ ) within all elements.

The union of the set of smaller sub-domains cover the entire domain of interest without overlapping. Adjacent elements share nodal parameters, which ensures that dependent variables are continuous throughout the entire domain.

This concept can be seen by considering a two-dimensional fluid flow problem with a U shaped domain as shown in Figure 2.1a. The curved domain can be divided into elements, in this case twenty. Computationally, each element in local  $\xi$  space will form a unit square as shown in Figure 2.1c. Each of these elements now has its own coordinate system, with each direction normalised between 0 and 1.

## 2.2 One-Dimensional Basis Functions

Basis functions or interpolation functions are used to approximate quantities of interest between nodal values (*e.g.*, geometric or solution variables) that vary over a particular domain. They consist of sets of polynomials of different degrees, depending on the type of interpolation required and provide the weighting for each local node for evaluating a field within the element.

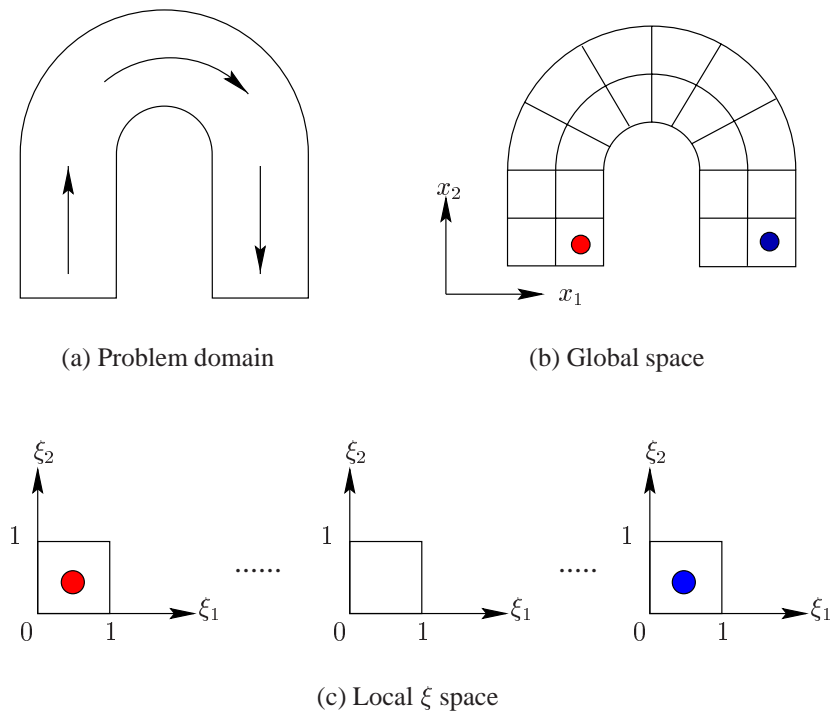


**Figure 2.1:** Schematics illustrating the mapping between global space and local  $\xi$  space. The original problem (a) is defined in terms of a global  $x$  coordinate system. After discretising the problem into elements (b), each element in the mesh can then be mapped to a local  $\xi$  coordinate system as shown in (c). Each element is then of unit size and can be considered numerically equivalent.

Basis functions can be grouped into two main families, *Lagrange* and *Hermite*. These two types of basis function families determine the level of continuity of the interpolation variable across element boundaries. Lagrange basis functions preserve continuity of the values of the dependent variables across element boundaries ( $C^0$  continuity) and are explained further in Section 2.2.1. Hermite basis functions, in addition to the values, also preserve continuity of the first derivative ( $C^1$  continuity) and are described in further detail in Section 2.2.2.

Different interpolation schemes can also be used to alter the type of variation of the field within an element. The three main interpolation methods for the Lagrange family are *linear*, *quadratic* and *cubic*. This determines the variation of a field within an element. Typically, low order polynomials are chosen as the elements are of such a size that there is a relatively low variation within an element and they can be easily numerically integrated using Gaussian quadrature schemes. Higher than third order polynomials have the ability to represent a field more accurately at key points but highly oscillatory and unphysiological fields may result between these points.

The interpolation scheme and the continuity family are then paired to provide a description of the field throughout the mesh (*e.g.*, a quadratic Lagrange basis function will have quadratic variation within an element and no derivative continuity across element boundaries, whilst a cubic Hermite basis function will have cubic variation within an element and also preserve variable and derivative continuity across element boundaries).

The standard interpolation formula for interpolating within an element is given by

$$u(\boldsymbol{\xi}) = \varepsilon_n(\boldsymbol{\xi}) u_n \quad (2.1)$$

where  $u_n$  are the local nodes defining the element and  $\varepsilon_n(\boldsymbol{\xi})$  represents an unspecified basis function evaluated at the location  $\boldsymbol{\xi}$  within the element and Einstein's summation is implied.

### 2.2.1 Lagrange Basis Functions

The Lagrange basis functions are functions which are chosen such that at each local node only one basis function has a value of 1 and all the other basis functions are equal to 0 (*i.e.*, the nodal value is exactly preserved at the node). At all points within an element, the sum of the basis functions is equal to 1. Linear and quadratic Lagrange basis functions are plotted in Figure 2.2, showing the weighting contribution from each basis function as the position varies throughout an element.

The  $n^{\text{th}}$  Lagrange basis function evaluated at the position defined by  $\boldsymbol{\xi}$  is denoted by  $\varphi_n(\boldsymbol{\xi})$ .

#### Linear Lagrange

A linear Lagrange basis function is the simplest of the basis functions. For a one-dimensional case, two nodes are required to define an element.

By considering an arbitrary scalar function,  $u(x)$ , which varies over a one-dimensional element, a linear approximation of  $u$  can then be used to represent the variation of the  $u$  within the element. Through the introduction of a normalising distance measure,  $\xi$ , Equation (2.2) can be used to

interpolate nodal values in an arbitrary element.

$$\begin{aligned}
 u(\xi) &= \varphi_1(\xi) u_1 + \varphi_2(\xi) u_2 \\
 \text{where } \varphi_1(\xi) &= 1 - \xi \\
 \varphi_2(\xi) &= \xi
 \end{aligned} \tag{2.2}$$

where  $u_1$  and  $u_2$  are the values of dependent variable at each end of the element, and variation within the element is provided by  $u(\xi)$ .

### Quadratic Lagrange

A quadratic Lagrange element is constructed from three nodes and provides a quadratic variation within an element. To interpolate within a quadratic Lagrange element Equation (2.3) can be used.

$$\begin{aligned}
 u(\xi) &= \varphi_1(\xi) u_1 + \varphi_2(\xi) u_2 + \varphi_3(\xi) u_3 \\
 \text{where } \varphi_1(\xi) &= 2(\xi - 0.5)(\xi - 1) \\
 \varphi_2(\xi) &= -4(\xi)(\xi - 1) \\
 \varphi_3(\xi) &= 2\xi(\xi - 0.5)
 \end{aligned} \tag{2.3}$$

where  $u_1, u_2$  and  $u_3$  are the values of a dependent variable at each of the local nodes within the element.

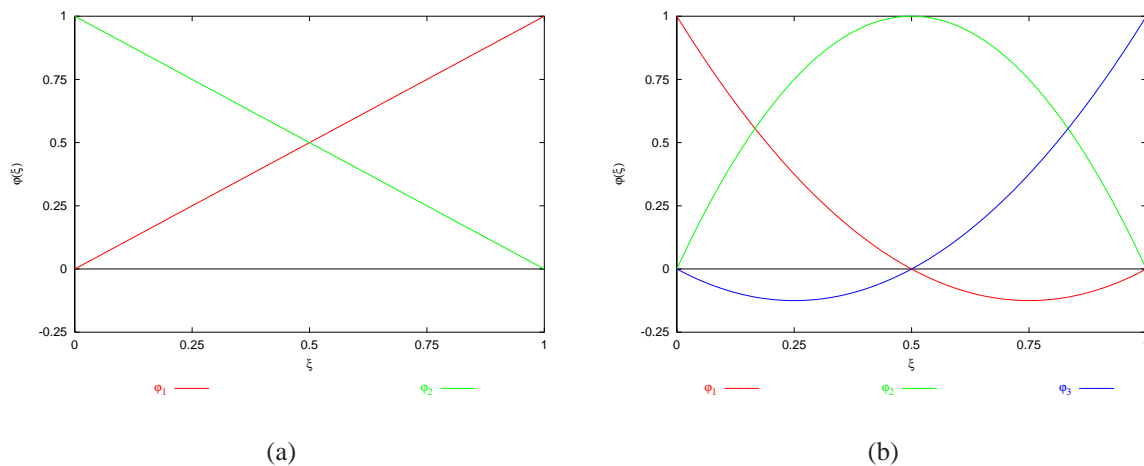


**Figure 2.2:** Lagrange basis functions. Illustrated are the linear (a) and quadratic (b) basis functions and how the weight of each basis function varies through  $\xi$  space within an element. All Lagrange basis functions have  $C^0$  continuity across elements. Linear basis functions allow linear variation within an element while the quadratic basis functions allow quadratic variation.

## 2.2.2 Hermite Basis Functions

Like the Lagrange basis functions, Hermite basis functions provide continuity of the dependent variable across element boundaries. In addition, they also provide continuity in the first derivative with respect to arc length. For this reason, Hermite bases are ideal for representing a smoothly varying curve or surface over the domain of interest.

With a Hermite basis function, interpolation of the dependent variable is determined from both the values and the derivatives at each local node. A Hermite basis function at node  $n$ , derivative  $d$  and evaluated at the position defined by  $\xi$  is denoted by  $\Psi_n^d(\xi)$ . Note that the 0<sup>th</sup> order derivative refers to the value of  $u$ .

### Cubic Hermite Basis Functions

Cubic Hermite elements require two nodes to define a one-dimensional element. The interpolation formula within an element can be given by the four cubic polynomials in Equation (2.4) and is illustrated in Figure 2.3. The basis functions have values of 0 and 1 at each local node while the derivative basis functions have derivatives of 0 and 1 at each local node.

The value of the field at a node  $n$  is given by  $u_n$  while two additional nodal parameters,  $\left. \frac{\partial u}{\partial \xi} \right|_n$ , are introduced to ensure that there is continuity of the first derivative between neighbouring elements. The value  $\left. \frac{\partial u}{\partial \xi} \right|_n$  is defined as the derivative of the field at node  $n$  with respect to the local  $\xi$ -coordinate.

$$\begin{aligned}
 u(\xi) &= \Psi_1^0(\xi) u_1 + \Psi_2^0(\xi) u_2 + \Psi_1^1(\xi) \left. \frac{du}{d\xi} \right|_1 + \Psi_2^1(\xi) \left. \frac{du}{d\xi} \right|_2 \\
 \text{where} \quad \Psi_1^0(\xi) &= 1 - 3\xi^2 + 2\xi^3 \\
 \Psi_2^0(\xi) &= \xi(\xi - 1)^2 \\
 \Psi_1^1(\xi) &= \xi^2(3 - 2\xi) \\
 \Psi_2^1(\xi) &= \xi^2(\xi - 1)
 \end{aligned} \tag{2.4}$$

However, as the derivative parameters are dependent upon the local element  $\xi$ -coordinate, which will vary non-linearly between elements of different sizes, the parameters will usually be different in two adjacent elements. To overcome this problem, a physical derivative  $\left. \frac{\partial u}{\partial s} \right|_N$  at each node is

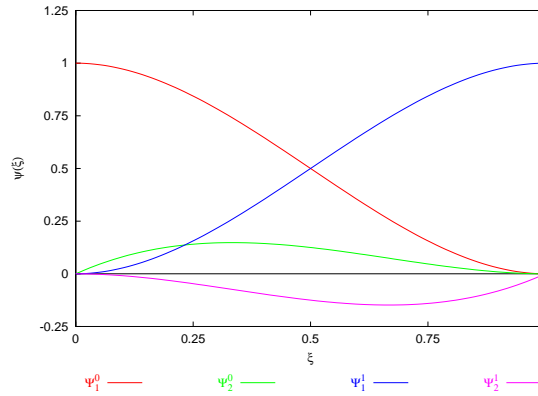


**Figure 2.3:** The four basis functions required for interpolating within cubic Hermite elements (two for values and two for derivatives) are plotted. Hermite elements have nodal value and derivative continuity across element and a cubic variation within the element. The variation of the dependent variable within an element is defined by the value at each of the local nodes and also by the derivative at the nodes. At each local node, one of the value basis functions has a value of 0 and the other 1, while both derivative basis functions have a value of 0.

introduced, where  $s$  is the arc-length and  $N$  is the global node. The derivative at a local node can be calculated from Equation (2.5),

$$\left. \frac{\partial u}{\partial \xi} \right|_n = \left( \frac{du}{ds} \right)_N \left( \frac{ds}{d\xi} \right)_e \quad (2.5)$$

where  $\left( \frac{\partial u}{\partial s} \right)_N$  is the physical arc-length derivative at global node  $N$  and  $\left( \frac{\partial s}{\partial \xi} \right)_e$  represents an element scale factor which scales the arc-length derivative of global node  $N$  to the  $\xi$ -coordinate derivative of element node  $n$ . Thus  $\frac{\partial u}{\partial s}$  is constrained to be continuous across element boundaries rather than  $\frac{du}{d\xi}$ .

By defining  $S_e = \left( \frac{\partial s}{\partial \xi} \right)_e$ , the cubic Hermite interpolation formula now becomes

$$u(\xi) = \Psi_1^0(\xi) u_1 + \Psi_2^0(\xi) u_2 + \Psi_1^1(\xi) \frac{du_1}{ds} S_e + \Psi_2^1(\xi) \frac{du_2}{ds} S_e \quad (2.6)$$

## 2.3 Two and Three Dimensional Basis Functions

Two-dimensional and three-dimensional basis functions are obtained by taking the tensor (or outer product) of multiple one-dimensional basis functions. The two main types of basis function families considered in this thesis are the bilinear Lagrange and bicubic Hermite basis functions.

### 2.3.1 Bilinear Lagrange

The product of two linear Lagrange basis function results in the interpolation formula given in Equation (2.7). The element has four degrees of freedom and, as with the one-dimensional linear Lagrange basis function, preserves continuity of the interpolation variable,  $u$ , across elements.

$$\begin{aligned}
 u(\xi_1, \xi_2) &= \varphi_1(\xi_1, \xi_2) u_1 + \varphi_2(\xi_1, \xi_2) u_2 + \varphi_3(\xi_1, \xi_2) u_3 + \varphi_4(\xi_1, \xi_2) u_4 \\
 \text{where } \varphi_1(\xi_1, \xi_2) &= (1 - \xi_1)(1 - \xi_2) \\
 \varphi_2(\xi_1, \xi_2) &= \xi_1(1 - \xi_2) \\
 \varphi_3(\xi_1, \xi_2) &= (1 - \xi_1)\xi_2 \\
 \varphi_4(\xi_1, \xi_2) &= \xi_1\xi_2
 \end{aligned} \tag{2.7}$$

### 2.3.2 Bicubic Hermite

A bicubic Hermite element is defined from four local nodes. As with the one-dimensional cubic Hermite interpolation, both value and derivative continuity are preserved across elements.

A bicubic Hermite element has 16 degrees of freedom, 4 associated with each node, as shown in Figure 2.4. At each node, there exists the value of the node, two derivatives of the value leaving the node in each  $\xi$  direction and also a cross derivative, which governs the ‘twist’ within an element

$$u, \quad \frac{\partial u}{\partial \xi_1}, \quad \frac{\partial u}{\partial \xi_2} \quad \text{and} \quad \frac{\partial^2 u}{\partial \xi_1 \partial \xi_2}$$

The need for the second-order cross-derivative term arises from the fact that as  $u$  is cubic in both  $\xi_1$  and  $\xi_2$  independently, the derivative  $\frac{\partial u}{\partial \xi_1}$  is quadratic in the  $\xi_1$  direction while cubic in the  $\xi_2$



direction. The cubic variation of  $u$  with  $\xi_2$  is specified by the four nodal parameters:  $u_1, u_3, \left(\frac{\partial u}{\partial \xi_2}\right)_1$  and  $\left(\frac{\partial u}{\partial \xi_2}\right)_3$  defined at local nodes 1 and 3. However, since  $\left(\frac{\partial u}{\partial \xi_1}\right)$  is cubic in  $\xi_2$  and independent of these four parameters, additional parameters must be introduced. For local nodes 1 and 3, these are

$$\left(\frac{\partial u}{\partial \xi_1}\right)_1, \left(\frac{\partial u}{\partial \xi_1}\right)_3, \left(\frac{\partial^2 u}{\partial \xi_1 \partial \xi_2}\right)_1 \quad \text{and} \quad \left(\frac{\partial^2 u}{\partial \xi_1 \partial \xi_2}\right)_3$$

Similarly,  $\frac{\partial^2 u}{\partial \xi_1 \partial \xi_2}$  needs to be defined at local nodes two and four.

The bicubic interpolation of these nodal parameters is given by

$$\begin{aligned} u(\xi_1, \xi_2) = & \Psi_1^0(\xi_1) \Psi_1^0(\xi_2) u_1 + \Psi_2^0(\xi_1) \Psi_1^0(\xi_2) u_2 \\ & + \Psi_1^0(\xi_1) \Psi_2^0(\xi_2) u_3 + \Psi_2^0(\xi_1) \Psi_2^0(\xi_2) u_4 \\ & + \Psi_1^1(\xi_1) \Psi_1^0(\xi_2) \left(\frac{\partial u}{\partial \xi_1}\right)_1 + \Psi_2^1(\xi_1) \Psi_1^0(\xi_2) \left(\frac{\partial u}{\partial \xi_1}\right)_2 \\ & + \Psi_1^1(\xi_1) \Psi_2^0(\xi_2) \left(\frac{\partial u}{\partial \xi_1}\right)_3 + \Psi_2^1(\xi_1) \Psi_2^0(\xi_2) \left(\frac{\partial u}{\partial \xi_1}\right)_4 \\ & + \Psi_1^0(\xi_1) \Psi_1^1(\xi_2) \left(\frac{\partial u}{\partial \xi_2}\right)_1 + \Psi_2^0(\xi_1) \Psi_1^1(\xi_2) \left(\frac{\partial u}{\partial \xi_2}\right)_2 \\ & + \Psi_1^0(\xi_1) \Psi_2^1(\xi_2) \left(\frac{\partial u}{\partial \xi_2}\right)_3 + \Psi_2^0(\xi_1) \Psi_2^1(\xi_2) \left(\frac{\partial u}{\partial \xi_2}\right)_4 \\ & + \Psi_1^1(\xi_1) \Psi_1^1(\xi_2) \left(\frac{\partial^2 u}{\partial \xi_1 \partial \xi_2}\right)_1 + \Psi_2^1(\xi_1) \Psi_1^1(\xi_2) \left(\frac{\partial^2 u}{\partial \xi_1 \partial \xi_2}\right)_2 \\ & + \Psi_1^1(\xi_1) \Psi_2^1(\xi_2) \left(\frac{\partial^2 u}{\partial \xi_1 \partial \xi_2}\right)_3 + \Psi_2^1(\xi_1) \Psi_2^1(\xi_2) \left(\frac{\partial^2 u}{\partial \xi_1 \partial \xi_2}\right)_4 \end{aligned} \quad (2.8)$$

where  $\Psi_1^0(\xi)$ ,  $\Psi_2^0(\xi)$ ,  $\Psi_1^1(\xi)$  and  $\Psi_2^1(\xi)$  are the one-dimensional cubic Hermite basis functions as defined in Equation (2.4).

As with one-dimensional cubic Hermite elements, the derivatives with respect to  $\xi$  in the two-dimensional interpolation formula are expressed as the product of a nodal arc-length derivative and a nodal scale factor. There is now a scale factor in each  $\xi$  direction at each node  $n$ ,

$$\left(\frac{du}{d\xi_i}\right)_n = \left(\frac{du}{ds_i}\right)_N (S_i)_e \quad (2.9)$$

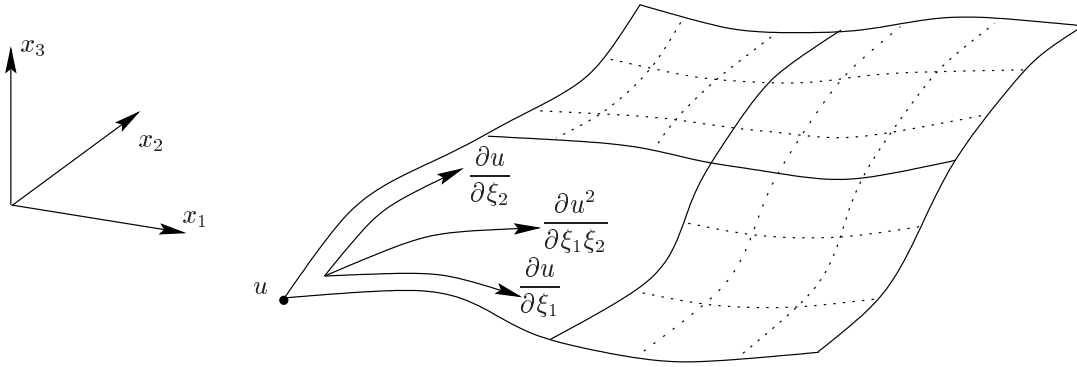


**Figure 2.4:** Bicubic Hermite elements with four degrees of freedom associated with each node, a value, two derivatives and a cross-derivative term. This results in 16 degrees of freedom for each element for each scalar variable.

and for the cross-derivative term

$$\left( \frac{\partial^2 u}{\partial \xi_1 \partial \xi_2} \right)_n = \left( \frac{\partial^2 u}{\partial s_1 \partial s_2} \right)_N (S_1)_e (S_2)_e \quad (2.10)$$

## 2.4 Sector Elements

One problem which arises when using quadrilateral elements (such as bicubic Hermite elements) to describe a surface is that it is impossible to ‘close the surface’ in three-dimensions whilst maintaining consistent  $\xi$  directions at the two ‘ends’ of the mesh.  $C^1$  continuity requires either consistent  $\xi$  directions or a transformation at each node to take into account the inconsistent directions (Peters & Pittman 1994).

One solution is to place one of the local nodes of a quadrilateral element in the same geometric positions as another node, resulting in a triangular element. With effectively a repeated node, one  $\xi$  direction is undefined and there is zero distance between the nodes. Numerical problems can result from this zero distance due to the Gaussian quadrature integration used in BEM. An alternative formulation involves using sector elements with three local nodes. The sector elements maintain consistent  $\xi$  directions and close three-dimensional surfaces while maintaining  $C^0$  continuity at the collapsed end of the element.

Considering the apex node (node 3) shown in Figure 2.5b, interpolation in the  $\xi_1$  direction is a standard interpolation. Interpolation in the  $\xi_2$  direction is different as that the nodal arc-length derivative has been removed because it is no longer defined at node 1. Interpolation for the line

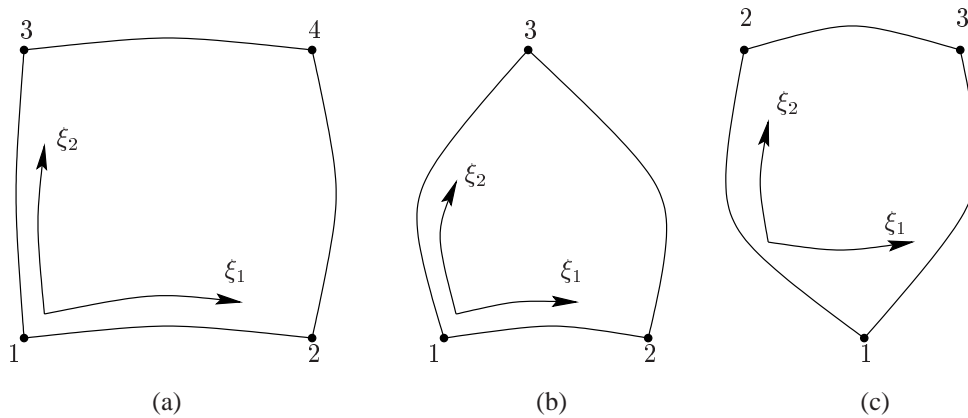


**Figure 2.5:** Three noded sector elements formed by collapsing a four noded quadrilateral element. Here, the  $\xi_1$  direction has been collapsed: at the  $\xi_1=0$  end (b) and at the  $\xi_1=1$  end (c). Alternatively, the elements could be collapsed in the  $\xi_2$  directions.

connecting local node  $n$  with local node 3 is given by Equation (2.11).

$$u(\xi_2) = \eta_1(\xi_2) u_n + \eta_2(\xi_2) u_3 + \eta_3(\xi_2) \left. \frac{\partial u}{\partial \xi_2} \right|_n$$

$$\text{where } \begin{aligned} \eta_1(\xi) &= 1 - \xi^2 \\ \eta_2(\xi) &= \xi^2 \\ \eta_3(\xi) &= \xi - \xi^2 \end{aligned} \quad (2.11)$$

Considering the apex node (node 1) shown in Figure 2.5c, interpolation for the line between local node 1 and local node  $n$  is now quadratic and is given by Equation (2.12). Interpolation in the  $\xi_1$  direction is a standard interpolation.

$$u(\xi_2) = \zeta_1(\xi_2) u_n + \zeta_2(\xi_2) u_1 + \zeta_3(\xi_2) \left. \frac{\partial u}{\partial \xi_2} \right|_n$$

$$\text{where } \begin{aligned} \zeta_1(\xi) &= 1 - \xi^2 \\ \zeta_2(\xi) &= \xi^2 \\ \zeta_3(\xi) &= \xi - \xi^2 \end{aligned} \quad (2.12)$$

The full interpolation formulation can then be found by taking the tensor product of the interpolation in the  $\xi_1$  direction with the interpolation in the  $\xi_2$  direction (Equation (2.11) or Equation (2.12)). The interpolation formula can be converted from nodal  $\xi$  derivatives to nodal arc-length derivatives using the procedure outlined in Section 2.3.2.

## 2.5 Mesh Refinement

When using a numerical solution method, the accuracy and reliability of the method needs to be carefully investigated by performing a *convergence analysis*. This involves monitoring the error in the solution of a particular problem as the problem size (number of DOF used to solve the problem) is systematically increased. By refining the mesh, the number of DOF associated with that mesh increases and it becomes possible to accurately represent more complex fields.

When using a structured mesh, one method of uniformly increasing the resolution of a mesh is to *refine* the elements. To ensure the DOF are uniformly distributed, the mesh is refined in all elements at a certain location in  $\xi$  space. Local refinement is not considered in this thesis to avoid the additional problem of hanging nodes (Stouboulis & Haque 1992).

Consider the case shown in Figure 2.6, where a single bicubic Hermite element is refined three times. It was refined once in the  $\xi_1$  direction and twice in the  $\xi_2$  direction. If the mesh had a field  $u$  associated with each node, then the initial single element would have 16 solution DOF (see Section 2.3.2). By refining the mesh, there are now 192 solution degrees of freedom, four at each nodal position.

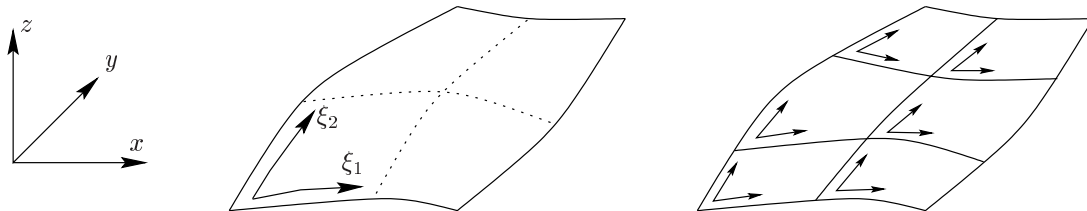


**Figure 2.6:** Refining a single bicubic Hermite element once in the  $\xi_1$  direction and twice in the  $\xi_2$  direction, resulting in six elements. The element has been refined evenly in  $\xi$  space, with element division in the  $\xi_1$  direction at  $\xi_1 = 0.5$  and at  $\xi_2 = \frac{1}{3}$  and  $\frac{2}{3}$  in the  $\xi_2$  direction.

# 3 *Geometric & Field Fitting with the Finite Element Method*

The geometric torso model of the subject and their temporally varying torso potentials are necessary inputs for the inverse problem of electrocardiology. This type of information is usually supplied at discrete locations or *data points*. These data can be in the form of geometric coordinates (*e.g.*, points from a digitised surface) or a combination of geometric location and an associated field at that point (*e.g.*, electrical potentials at a particular location on the torso surface or fibre orientation at a given location within the myocardium).

Densely sampled field measurements typically provide a non-uniform geometrically discrete data set. There are typically different numbers of sample points than computational nodes and their locations do not usually coincide. There are two main reasons for this: (i) the number of computational nodes is controlled by the mesh resolution required for a converged solution, a process independent to the data gathering; and (ii) there are errors in the computational model and the locations where the field measurements were obtained.

Mathematically, it is more useful to have the information as a continuous field, which means being defined at the finite element node points. This way, the field can be evaluated at all points within the domain using the standard interpolation formula given in Equation (2.1). The field fitting procedure described in Section 3.2 can be used to create an accurate piecewise representation of the described data.

When fitting different types of fields, the same least squares minimisation principles are used but the objective function formulations are slightly different. Several different applications of geometric and field fitting are outlined in Section 3.3 and their differences discussed.

### 3.1 Interpolation and Fitting

The term *curve fitting* or *data fitting* is used to describe the general problem of finding a function which best matches a set of observed values at a number of discrete points. In the context of finite elements, it describes the process of altering a set of finite element nodal parameters in such a way that it provides an accurate representation of the data.

Consider the goal of finding a function to relate a set of geometric points,  $x_1, x_2, \dots, x_D$  with their corresponding field values  $u_1, u_2, \dots, u_D$  (*i.e.*,  $u(x)$ ). In a simple case, this could be expressed as an analytic function, but this is usually not the case. The field can also be approximated using piecewise low order polynomials in a finite element representation. The approximated function should provide *reasonable* function values between the data points (*interpolation*) and may be required to provide function values outside of the data range (*extrapolation*).

By using finite element field fitting it is possible to produce an accurate piecewise field representation of an irregularly sampled field. By adjusting the nodal parameters (*i.e.*, values and/or derivatives) the field of the finite element mesh can provide an accurate representation at the data points. One method is to minimise the squared distance between the data point values and the finite element field  $u$  evaluated at the  $\xi_d$  position corresponding to each data point  $d$  (*i.e.*,  $u(\xi_d)$ ).

By considering a one-dimensional mesh, such as that shown in Figure 3.1, the problem of presenting a series of four points using two elements can be illustrated. If  $u_d$  is defined to be the known discrete field values at irregularly spaced data point locations ( $d = 1, \dots, D$ ), by adjusting the value and derivative of the centre node and the derivatives at the end nodes, a good representation of the data can be obtained.



**Figure 3.1:** Adjusting the nodal parameters of the mesh to minimise the least-squares distance between each data point ( $\times$ ) and its orthogonal projection on the surface. Shown is the effect of adjusting the nodal and derivative parameters of the middle node and the derivative values of the end nodes.

## 3.2 Field Fitting

Smooth spatially varying fields can be efficiently defined in terms of nodally based fields on a finite or boundary element mesh. By defining the fields at nodal positions the field can then be interpolated throughout the finite element mesh through the use of the appropriate basis functions. By storing nodally based information it is possible to directly use these data with the algorithms described in Chapter 5 and Chapter 6 for solving in the forward and inverse problems of electrocardiology.

### 3.2.1 Data Projection

In practice, the locations at which field data is acquired will not lie exactly on the computational mesh due to experimental errors and physical limitations of equipment. By orthogonally projecting a data point,  $d_n$ , onto the mesh surface, as shown in Figure 3.2, the local  $\xi$  positions and the element within which it lies can be determined. This provides the closest point on the computational mesh to the data point. The length of the projection vectors between the data point positions in space and their orthogonal projection onto the mesh surface provides a measure of this geometric error.

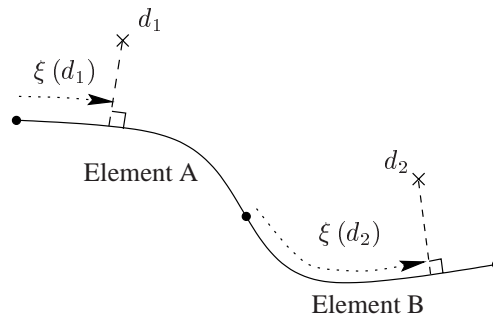


**Figure 3.2:** Projection of data points  $d_n$  ( $\times$ ) onto different elements of a surface. The dashed lines show the orthogonal projections of the data points onto the surface of the mesh and the  $\xi$  positions for each data point within elements A and B.

To calculate  $\xi_d$ , a non-linear iterative procedure is required. Given a starting  $\xi$  position for the data point projection, the geometric position of this projection is given by the standard interpolation formula in Equation (2.1). An error function can then be set up as the Euclidean distance between this point and the actual position of the data point. The local  $\xi$  position that minimises this function can then be found using the Newton-Raphson root finding method on the derivative of this function. This  $\xi$  position is effectively the orthogonal projection of the data point onto the finite element

surface. Convergence of the Newton-Raphson method is highly dependent on the non-linearity of the objective function and the choice of the initial solution. For initial solutions sufficiently close to the true solution, convergence is quadratic. The initial starting location was taken as the closest element centre (*i.e.*, at  $\xi = 0.5$  for each element) for each data point.

### 3.2.2 Linear Field Fitting

The field fitting problem is formulated as a minimisation procedure in which the objective is to minimise the sum of squared differences, over all data points, between the known value at each data point,  $u_d$ , and the finite element field approximation evaluated at the projected  $\xi_d$  position of the data point,  $u(\xi_d)$ , *i.e.*,

$$\min F(u) = \sum_{d=1}^D [u(\xi_d) - u_d]^2 \quad (3.1)$$

The field values of the nodes ( $u_n$ ) of the element containing a data point can be interpolated to give the value at an  $\xi$  location within the element (*i.e.*, through the use of Equation (2.1)) or more specifically

$$u(\xi_d) = \varphi_n(\xi_d) u_n \quad (3.2)$$

where  $\varphi_n(\xi_d)$  represents basis function  $n$  evaluated at location  $\xi_d$ . The sum of squared differences between this value and the measured value  $u_d$  for all the data points ( $d = 1, \dots, D$ ) is

$$\Upsilon = \sum_{d=1}^D (\varphi_n(\xi_d) u_n - u_d)^2 \quad (3.3)$$

Minimising  $\Upsilon$  with respect to the nodal parameters  $u_m$  results in

$$\frac{\partial \Upsilon}{\partial u_m} = 2 \sum_{d=1}^D (\varphi_n(\xi_d) u_n - u_d) \varphi_m(\xi_d) = 0 \quad m, n = 1, \dots, N \quad (3.4)$$

$$\text{or} \quad \left( \sum_{d=1}^D \varphi_m(\xi_d) \varphi_n(\xi_d) \right) u_n = \sum_{d=1}^D \varphi_m(\xi_d) u_d \quad m, n = 1, \dots, N \quad (3.5)$$



This can then be assembled into a global system of equations  $E_{mn}u_n = F_m$  where

$$\begin{aligned} E_{mn} &= \sum_{d=1}^D \varphi_m(\xi_d) \varphi_n(\xi_d) \\ F_m &= \sum_{d=1}^D \varphi_m(\xi_d) u_d \end{aligned} \tag{3.6}$$

and  $u_n$  are the unknown field values at each finite element node  $n$ .

The solution of this system gives the fitted values of the field at nodal positions. This field can then be evaluated using Equation (2.1) at all points within the mesh.

Thus, for a particular choice of interpolation or basis functions,  $\varphi_m$ , and the known field values,  $u_d$ , the right hand side terms,  $F_m$  can be computed. The unknown set of nodal parameters,  $u_n$ , are then determined by solving the resulting system of linear equations. The set of fitted parameters may then be substituted back into Equation (3.2) to compute the finite element field approximation at any given  $\xi$  location in an element.

### 3.2.3 Error Metrics

The finite element fitting method minimises the deviation between the data and the interpolated field (*i.e.*, it minimises the root mean squared (RMS) error as defined in Equation (3.7)). The use of only one error metric can be a misleading measure of the accuracy of a fit. By using a number of different error metrics the quality of the solution can be better assessed.

Defined in Equations (3.7)–(3.9) are the RMS, relative RMS and similarity index (SI) error metrics. They are the three primary error metrics which are used throughout this thesis. The metrics provide a comparison between two scalar fields, a master field  $\phi_m$  and a comparison field  $\phi_c$ , each with  $N$  samples.

The RMS error provides a direct error measure between the two fields, while the relative RMS error provides a normalised error measure. Both are useful for determining the changes in magnitude

between two fields.

$$\text{RMS} = \sqrt{\frac{\sum (\phi_m - \phi_c)^2}{N}} \quad (3.7)$$

$$\text{Relative RMS} = \sqrt{\frac{\sum (\phi_m - \phi_c)^2}{\sum \phi_m^2}} \quad (3.8)$$

The similarity index (SI), is a measure which is independent of the magnitudes of the two fields. It provides a measure for the changes in pattern between two fields.

$$\text{Similarity Index} = \frac{\sum \phi_m \phi_c - \frac{(\sum \phi_m \sum \phi_c)}{N}}{\sqrt{\sum \phi_m^2 - \frac{(\sum \phi_m)^2}{N} \sum \phi_c^2 - \frac{(\sum \phi_c)^2}{N}}} \quad (3.9)$$

### 3.2.4 Sobolev Smoothing

One of the primary aims of fitting discrete data is to provide a uniform distribution of the information supplied by the data. Ultimately, in a well determined problem, there would be a large quantity of evenly distributed data compared to mesh DOF and there would be no error associated with the data. However, in practice, these data will be distributed in a non-uniform manner and will have some degree of error associated with them. In some cases, the amount of data may be sparsely distributed and the number of DOF used to represent this data may greatly outweigh the information supplied (*e.g.*, fitting torso surface potentials to a computational mesh). In other cases the data may be non-uniformly distributed or not obtainable in some locations (*e.g.*, the lack of right ventricular free wall information from ultrasound images as explained in Section 3.4.2).

Errors may be associated with the geometric location of the data point, the value of the field associated with the data point or a combination of the two. Typically, when dealing with experimentally measured data there will be errors associated with both the geometric location and the field val-

ues. The presence of these errors mean that minimising the least squared error between data points and the evaluated field in Equation (3.1) will not necessarily produce an accurate finite element representation of the underlying field being modelled. Even with clean data, free of any error, minimisation of Equation (3.1) may produce a highly oscillatory field which is usually not desired.

With the lack of data in some locations, if the objective function is only measured in terms of deviation from the data points, as in Equation (3.1), the finite element representation of the field may deviate in an unwanted manner without affecting the objective function. This situation was encountered when constructing a right ventricular surface from three-dimensional ultrasound images (see Section 3.3.3). Typically, views of the right ventricular free walls are difficult to obtain, especially when the subject is lying in a supine position, and it was found that lack of data in these locations would cause the surface to collapse if it were not appropriately constrained. This was overcome by constraining the position of a small number of nodes. An alternative approach is to perform the model fitting process using three-dimensional volume elements instead of two-dimensional surface elements (*i.e.*, model the myocardium volume instead of modelling the endocardial and epicardial surfaces). This way wall thickness, ventricular chamber volumes and the volumes of groups elements can be explicitly modelled and constrained. Alternatively the addition of a shape deformation penalty function to the objective function, as used by Cordier & Magnenat-Thalmann (2000), or a host mesh fitting approach such as that described in Section 3.4.1 used.

When modelling realistic biological fields, discontinuities do not generally occur. By providing a penalty on discontinuities and excessively curved surfaces, accurate representations can be achieved. This *smoothness constraint* or Sobolev value provides a penalty against excessive curvature in a surface. The Sobolev value reduces the effect of error in the known data information, both in the geometric locations of the field value and the actual field value and helps to prevent ill-conditioning in the matrix when the information supplied by the data outweighs the DOF of the fitted field.

The  $p^{\text{th}}$  order weighted Sobolev norm is defined as

$$g_{p,w}(x) = \sum_{q=0}^p \sum_{i+j=q} w_{ij} \left\| \frac{\partial^q x}{\partial \xi_1^i \partial \xi_2^j} \right\|_2 \quad (3.10)$$

where  $w_{ij}$  are weighting values applied to the component of  $g(x)$ . If the Sobolev norm is defined

over the entire mesh then the Sobolev value can be calculated over the entire solution domain  $\Omega$  as

$$G(x) = \int_{\Omega} g(x) d\Omega \quad (3.11)$$

The constraint is then introduced by adding an additional term to the objective function in Equation (3.1), *i.e.*,

$$\min F(u) = \sum_{d=1}^D [u(\xi_d) - u_d]^2 + \int_{\Omega} g(u(\xi)) d\xi \quad (3.12)$$

For a two-dimensional surface, the smoothing constraint is given by

$$\int_{\Omega} g(u(\xi)) d\xi = \int_{\Omega} \alpha \left( \left\| \frac{\partial u}{\partial \xi_1} \right\|_2 + \left\| \frac{\partial u}{\partial \xi_2} \right\|_2 \right) + \beta \left( \left\| \frac{\partial^2 u}{\partial \xi_1^2} \right\|_2 + 2 \left\| \frac{\partial^2 u}{\partial \xi_1 \partial \xi_2} \right\|_2 + \left\| \frac{\partial^2 u}{\partial \xi_2^2} \right\|_2 \right) d\xi \quad (3.13)$$

The first term in Equation (3.12), represents the error between the known and constructed field, while the second term in Equation (3.12) measures the deformation of the surface. This smoothness constraint hence provides a penalty against excessive curvature in a surface. The parameter  $\alpha$  is applied to the first-derivative terms (a measure of length) and controls the tension of the surface and the parameter  $\beta$  is applied to the second-derivative terms and controls the degree of surface curvature (Terzopoulos 1986).

As the residual error and the Sobolev values are calculated independently, care must be taken to balance their contributions to the objective function, when choosing the weighting values  $\alpha$  and  $\beta$ . The weights must be chosen such that the Sobolev value does not overwhelm the data residual and the resulting field has little resemblance to the data.

A low Sobolev weighting often results in a mesh that closely matches the data, but has high local curvature while a high Sobolev weighting will result in a mesh with low curvature (taking a form of lowest energy) which does not match the data well. Examples of under, over and typical smoothing values are illustrated in Figure 3.3.

Consider the case of fitting an element to data specified by the analytic function

$$f(z) = \frac{\sqrt{x^2 + y^2}}{2} \quad (3.14)$$

in a rectangular-Cartesian coordinate system. The function was specified at 14 randomly spaced data points in the  $x - y$  plane with the  $z$  elevations analytically specified by Equation (3.14) and are shown as purple spheres in Figure 3.3. A single  $10 \times 10$ mm square bicubic Hermite element is used to represent this surface. The horizontal  $x$  and  $y$  nodal values and derivatives were fixed and the  $z$  elevation values and derivatives allowed to deviate. Different levels of smoothing were applied and the resultant solutions shown in Figure 3.3 and Table 3.1 obtained.

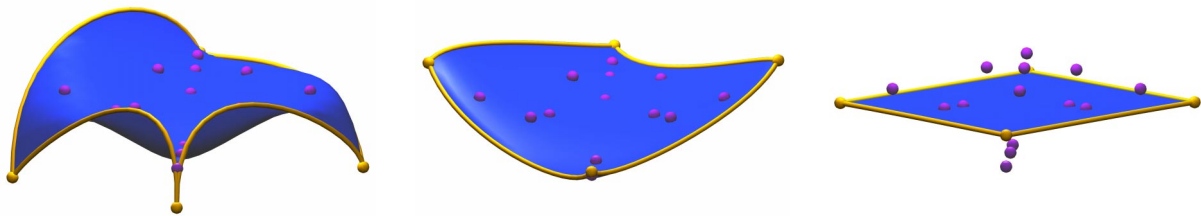


**Figure 3.3:** The effects of Sobolev smoothing values ( $\alpha$  and  $\beta$ ) on a fitted surface. From the left, the effects of under, typical and over smoothing the fitted surface. The smoothing values, the RMS errors measuring the deviation between the data points (purple spheres) and the blue surface as well as the RMS deviation between nodal points (gold spheres) and Equation (3.14) are given in Table 3.1.

The primary measure of the accuracy of a good fit is the deviation between the known field values at data points and the interpolated finite element field value.

As a known field (with the analytic function specified by Equation (3.14)) is being reconstructed, it is possible to evaluate the field at extremities where data points are not influencing the fit (*e.g.*, the nodal positions at the corners on the mesh). By examining the deviation between the field at the nodes and the analytic values in Table 3.1, an improved measure of the accuracy of the fit can be used.

From the RMS errors in Table 3.1, all three surfaces provide RMS errors of less than 1 mm. However, only the fit with typical smoothing values of  $\alpha$  and  $\beta$  equal to  $1 \times 10^{-3}$  provides an accurate representation of the function at the nodal positions. The under-smoothed field matches the data most accurately but suffers from very high local curvatures and the over-smoothed field does not provide a true representation of the curvature present in the data.

	UNDER SMOOTHING	TYPICAL SMOOTHING	OVER SMOOTHING
$\alpha$	$1 \times 10^{-5}$	$1 \times 10^{-3}$	$1 \times 10^0$
$\beta$	$1 \times 10^{-5}$	$1 \times 10^{-3}$	$1 \times 10^0$
RMS AT DATA POINTS	0.05	0.12	0.75
RMS AT NODES	2.29	0.46	2.66

**Table 3.1:** The effects of Sobolev smoothing values ( $\alpha$  and  $\beta$ ) on a fitted surface. RMS errors (mm) measure the deviation between the surface and 11 data points and the deviation between the 4 nodal positions and the analytic expression Equation (3.14). The surfaces are shown in Figure 3.3. All three fields have an RMS error at the data points of less than 1 mm, but only the surface produced with normal-smoothing values provided an accurate representation of the analytic function.

### 3.3 Applications of Geometric and Field Fitting

The theory described in Section 3.2 provides a general procedure for creating a full finite element field from discretely sampled data. Although the same principles are used, slight variations are introduced when different forms of the data are being fitted to. Sections (3.3.1)–(3.3.3) outline a number of different applications of the fitting techniques.

#### 3.3.1 Activation Time Fitting

Potentials on the heart surface may be measured experimentally using an electrode sock. From these signals an activation time can be calculated using a moving finite difference scheme at each electrode. The point of greatest negative slope was considered to be activation of that location. Displaying this information over the entire ventricular heart surface is known as an activation map (see Section 1.3).

As the information is supplied at discrete positions, a full field must be created to display the information over the entire heart surface. The data for the fit is provided by the location of the electrode and an activation time for each electrode. The physical locations of the electrodes are assumed to remain constant. This can be considered an accurate assumption as only the QRS interval is modelled and little cardiac motion occurs during this phase of the cardiac cycle.

Figure 3.4 shows the fitted activation field with data obtained from potential recordings using an epicardial sock with 127 electrodes. The potentials were measured directly on the epicardial surface of an anaesthetised pig using the methods of Nash et al. (2000b). Activation times were

then calculated from each of the potential traces as the point of maximum downstroke, then a full field created using the linear fitting methods described in Section 3.2.

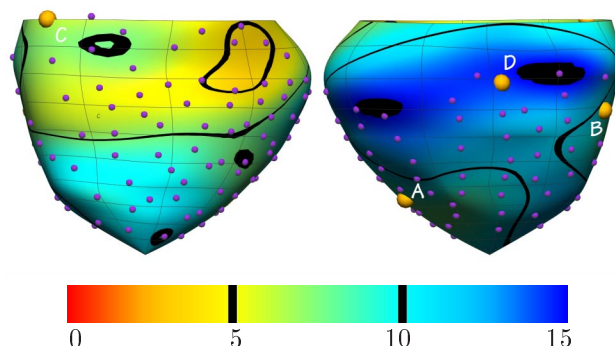


**Figure 3.4:** Fitted activation field (ms) derived from signals obtained from a 127 electrode epicardial sock. The locations of the electrodes are shown as purple spheres and the labelled gold spheres (A–D) represent the four electrode traces shown in Figure 4.7. The activation times were fitted with an RMS difference of 1.5 ms and the duration of the recorded activation times at the electrodes was 16 ms compared with 15 ms for the entire fitted field. The anterior epicardial surface is shown on the left and the posterior on the right.

The final fitted field had an RMS error of 1.5 ms and the duration of the recorded activation field was 16 ms compared with 15 ms for the fitted field. Considering the likely presence of errors in the geometrical location of the electrodes, this fit provides a good representation of the actual activation field.

### 3.3.2 Signal Fitting

For the inverse problem of electrocardiography it is necessary to have information about the temporally varying potentials on the surface of the torso. With the discretisation process of the FEM it is only necessary to provide information at each nodal site to be able to recreate the field at any location within the domain. However, due to experimental limitations it is not possible to directly measure the potentials at each nodal site. To overcome this problem, it is necessary to use the known experimental data to interpolate information at the nodal sites.

The potentials on the heart surfaces and torso surface are both temporally varying. They can however, be treated as being independent at each time step (Plonsey 1969). Fitting of such a temporally varying scalar field uses the same principles as Section 3.3.1, except that the right hand

side of the system in Equation (3.6) is recalculated at each time step. As with Section 3.3.1, each data point is the location of the recording site of an electrode. The positions of the electrodes are assumed to be constant during the recording period. This is a valid assumption since potentials are recorded from the subjects during breath-holds so little respiratory motion occurs.

The potential field on the torso surface of a pig was reconstructed from ECG recordings obtained simultaneously from 256 sites. The potentials were recorded for 8 seconds over 16 heart cycles at a frequency of 1 kHz and then beat-averaged to produce a representative control heart cycle for this animal. Of the 256 recordings, 16 were rejected due to poor or faulty recordings. The locations of the recording sites were measured using a mechanical digitiser and then orthogonally projected onto the model surface.

The model was customised using the generic model using the process outlined in Section 3.4.1. The RMS error between the recorded electrode positions and their projected positions on the customised torso surface was 15.23 mm. This was considered to be a large error but is the only complete data set available.

The signals were fitted to a bicubic Hermite field using Sobolev smoothing factors  $\alpha$  and  $\beta$  (from Equation (3.13)) equal to  $1 \times 10^{-3}$  and the fitted signal subsequently constructed through the use of Equation (2.1). A subset of 8 electrode traces showing both fitted and recorded signals is given in Figure 3.6 and their relative locations on the torso surface are shown in Figure 3.5.

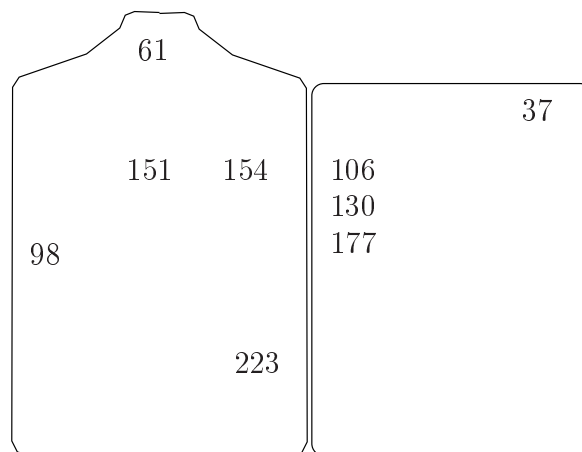


**Figure 3.5:** Location of a subset of electrodes on the torso. The signals recorded from electrodes 37, 61, 98, 106, 130, 154, 177 and 223 are shown in Figure 3.6. The signal recorded from electrode 151 along with an instantaneous potential field on the surface of the pig model is shown in Figure 3.7. The anterior surface is shown on the left and the posterior on the right. The common edge down the centre corresponds to the left mid-auxiliary line.



The numerical errors associated with these signals are given in Table 3.2. The time instances of 20, 30 and 40 ms were chosen as times to compare the recorded and fitted signals as this was the period with the sharpest gradients in the potential fields and were expected to be the hardest to represent. An integral measure was also used over what was considered to be the QRS interval (20–30 ms). From Table 3.2 and Figure 3.6, it can be seen that the fitted signals provide a good representation of the recorded signals. The fitting has also removed some of the effects of experimental error in the electrode location and signal noise. From the traces in Figure 3.6, the fitted signal has less electrical noise artifacts if we assume that the true body surface signal is temporally smooth.

MEASURE	20 ms	30 ms	40 ms	QRS INTERVAL
REL. RMS	0.185	0.127	0.140	0.108
SI	0.970	0.991	0.987	0.994
MAX. $ \Delta\Phi $	$1.024 \times 10^{-02}$	$1.053 \times 10^{-01}$	$2.171 \times 10^{-02}$	$1.524 \times 10^{-01}$
MIN. $ \Delta\Phi $	$3.224 \times 10^{-03}$	$2.851 \times 10^{-02}$	$1.558 \times 10^{-04}$	$5.727 \times 10^{-02}$
MAX. $\Delta\Phi\%$	-2.310	13.530	-4.180	-3.830
MIN. $\Delta\Phi\%$	0.410	1.650	-0.040	0.410

**Table 3.2:** Comparison of the 240 recorded electrodes and the fitted signals with different measures: relative RMS, similarity index (SI), percentage and absolute differences (mV) of the maximum and minimum signals. The error metrics are defined in Section 3.2.3. The signals are compared at specific time instances and by integrating over the QRS interval.

An illustration of the full fitted field displayed on the pig model, at a specific time instant, is given in Figure 3.7. The recorded signal from a single electrode is also displayed to mark the instant at which this electrical state was recorded.

### 3.3.3 Geometric Fitting

With geometric fitting, the information is typically provided in the form of clouds of data which have been extracted from medical images such as MRI, CT or ultrasound. The data points corresponding to surfaces of interest which have been extracted from the images. Figure 3.8 shows traced images of the epicardial and endocardial heart surfaces from MRI and ultrasound data.

By minimising the sum of squares distance between each data point and its nearest point on the surface, a geometric surface representation of the data can be achieved. To this point, it has been assumed that the orthogonal  $\xi$  projections onto the finite element surface remain constant as the

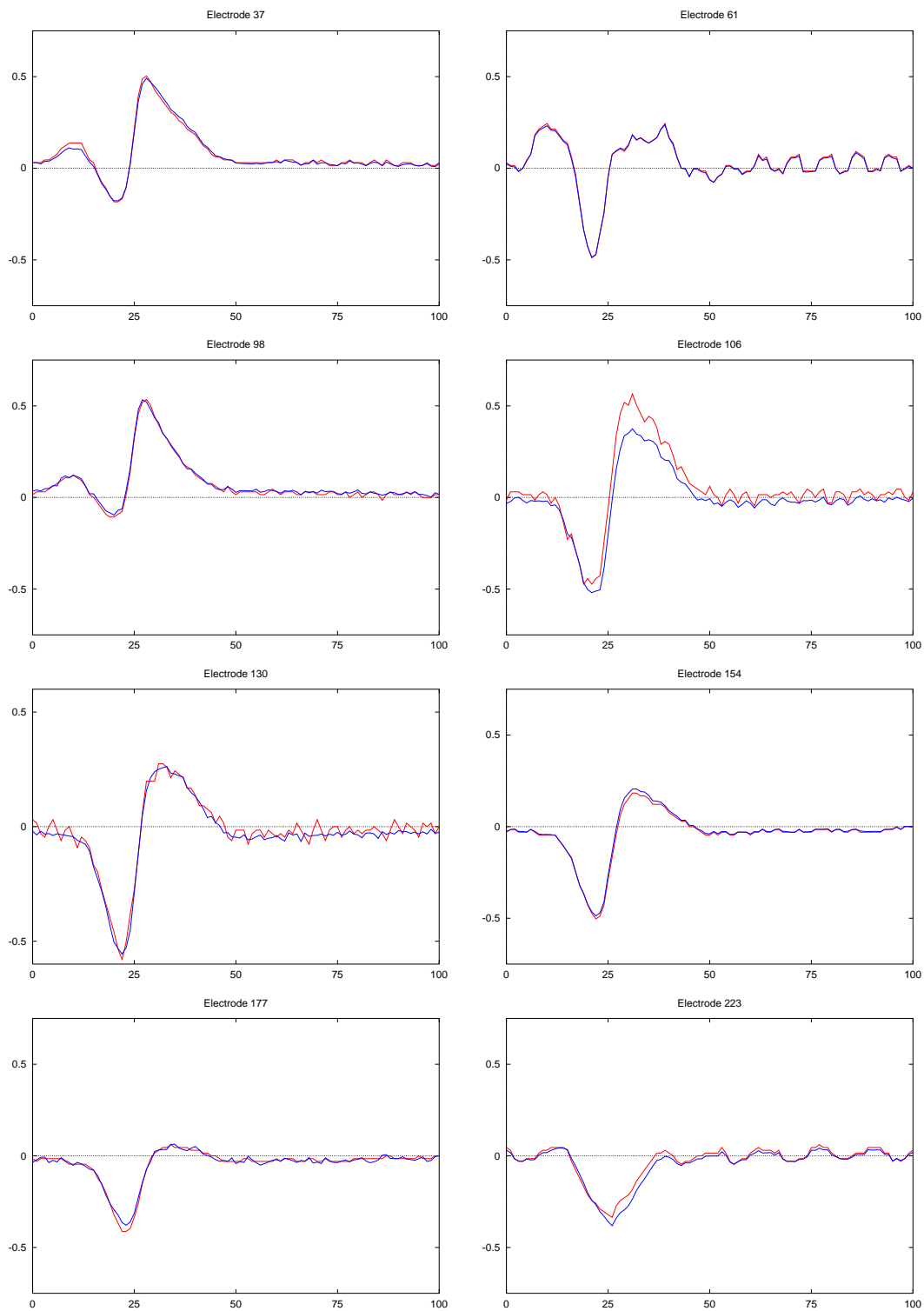


**Figure 3.6:** The recorded signals (red) compared with the fitted signals (blue) of 8 electrode locations. Time (ms) is shown on the horizontal axis and potential (mV) on the vertical axis. The electrode locations are illustrated in Figure 3.5.

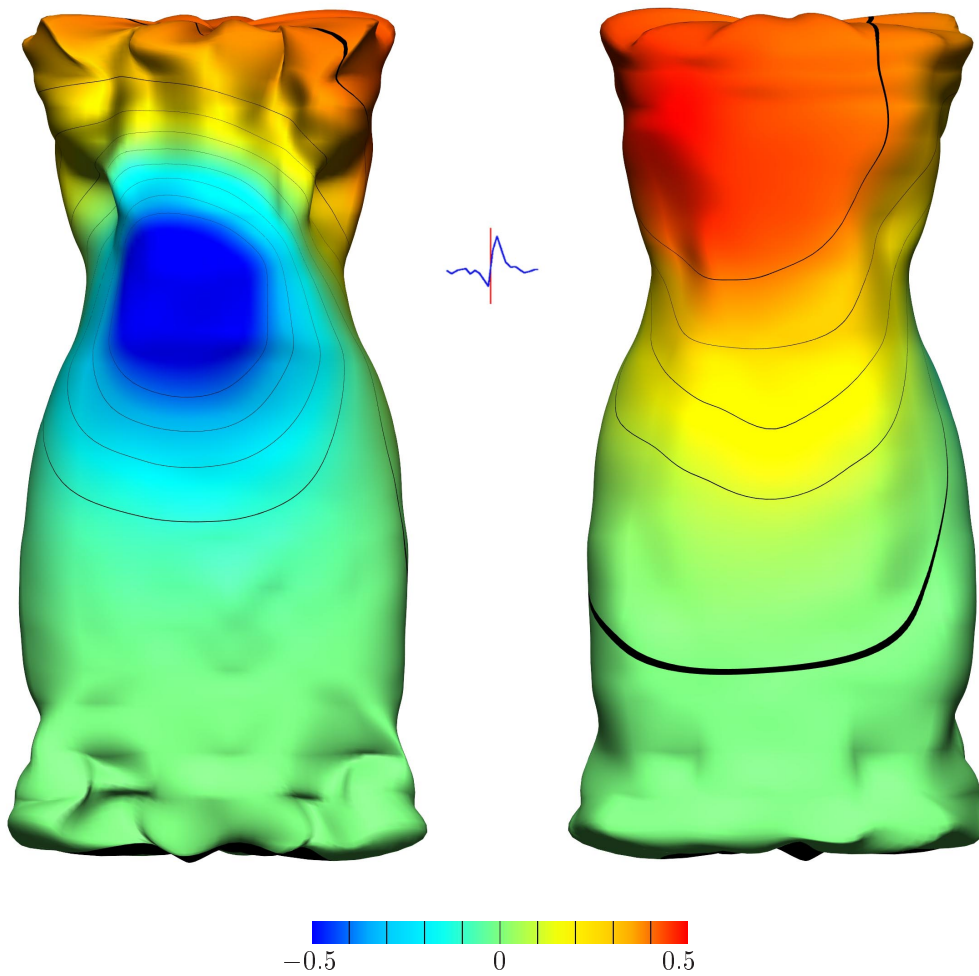


**Figure 3.7:** Body surface potential map (mV) created by fitting data from 240 electrodes to a geometrically customised computational pig torso model. The coloured field shows the spatially varying potential field, from most negative (blue) to most positive (red). A trace from a single electrode to mark the instant (red line) at which this electrical state was recorded is shown in the centre. The location of this electrode (151) on the torso surface is shown in Figure 3.5.

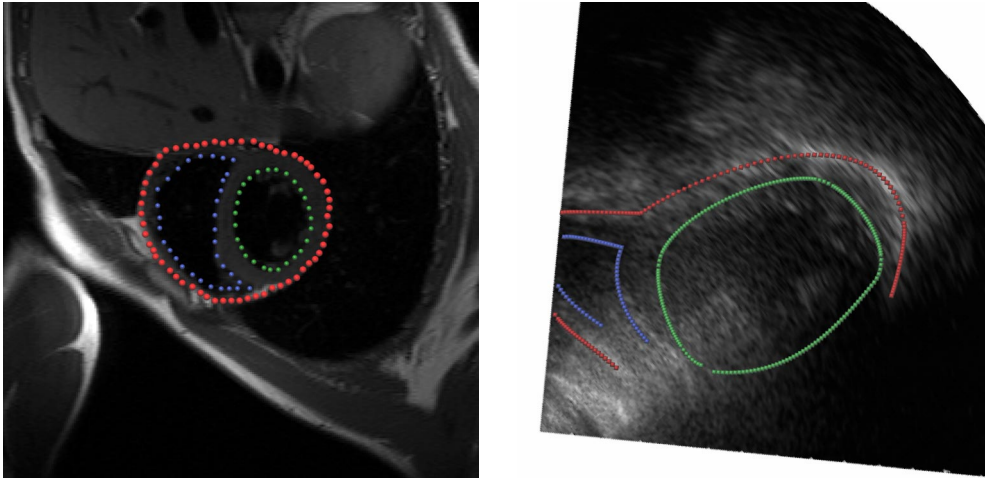


**Figure 3.8:** Epicardial and endocardial surface information is obtained by tracing around the appropriate borders. On the left is a short axis MRI image through the heart and on the right an ultrasound short axis view through the heart. The epicardial surface is traced with red points, left ventricular chamber with green points and right ventricular chamber with blue points.

fitted field changes. This is usually an accurate assumption, except in the case where the geometry of the surface changes after a fit (and thus the orthogonal projections). This can be overcome by using an iterative linear fitting approach. Multiple fits are performed with the  $\xi$  projections (and scale factors, if a Hermite mesh is used) being re-calculated after each linear fit until an adequate solution has been obtained. As the calculation of the  $\xi$  projections change in a non-linear fashion, the more accurate the initial mesh or starting solution, the faster the solution will converge to a global minimum, although in practice only a few iterations are required.

Figure 3.9 illustrates fitting an epicardial surface model to sparse data obtained from three-dimensional ultrasound images. The orthogonal projections at each iteration are shown as green vectors. The crude initial mesh has no derivative information. The general topology of the epicardium has already been reconstructed after one iteration. The RMS errors between the data points and the orthogonal projections reduces from 8.5 mm to 2.7 mm after one iteration. After three iterations the RMS error has been reduced to 2.2 mm.

### 3.4 Model Customisation

To use the information provided by imaging techniques such as MRI and CT it is necessary to extract surface or volume information from the images. Even if the automated segmentation techniques of Lorensen & Cline (1987) were completely reliable, the creation of a model of each surface

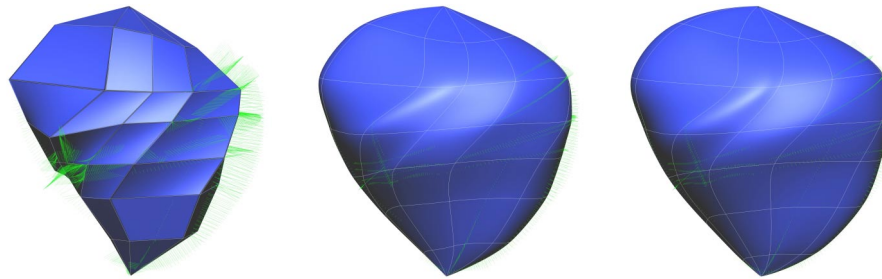


**Figure 3.9:** Fitting an epicardial surface to sparse ultrasound data. Green error vectors indicate the distances between each data point and its orthogonal projection onto the surface. Shown on the left is the crude initial mesh with no derivative information. The subsequent images show the mesh after one and three iterations. The RMS error has reduced from 8.5 mm to 2.7 mm after the first iteration. The final RMS error after three iterations is 2.2 mm.

from the geometric data using triangulation techniques or the methods presented in Section 4.2, is a non-trivial exercise. Such a complicated and time-consuming approach is impractical for routine clinical applications.

The organs and structures being modelled typically have the same topological features for each subject and it would be beneficial that *a priori* information can be used to help create a subject specific model. The main objective of the customisation process is to have the ability to deform a generic mesh to match a specific subject given only a relatively small number of parameters.

Cordier & Magnenat-Thalmann (2000) compared two techniques for organ reconstruction using the Visible Human Dataset. The first technique was a semi-automatic snake technique, which defined organ contours on each slice, then joined up the contours to create surfaces. Another technique involved a Shape Constrained Deformable Model. The idea of this method is that shapes of organs are similar for most patients. The initial shape was approximately placed within the organ and the initial shape then deformed using the image information and the shape memory. The segmentation process was formulated as the minimisation of a cost function which involved a shape memory force that kept the shape of the generic model and an image interest force that moved vertices towards high edge densities. Both of these methods require the full volumetric data in the form of image slices, which is time consuming to obtain, with an MRI study taking the order of several hours.

One method of creating a subject specific model is to use a ‘generic’ model with similar topological features and ‘customise’ it by minimising the differences between the generic model and the subject. Crocombe (1997) investigated such techniques for quickly constructing models of

a specific object with little geometric information given prior knowledge about the structure and form of the data. The method consisted of two main steps: variable length scaling and radial scaling. The variable length scaling attempted to adjust the elevation of each node according to key landmark measurements (*e.g.*, the distance between hips and the Xiphoid process and the distance between the Xiphoid and the supra-sternal notch). To account for radial variations in the models, circumferential measurements at a number of elevations were obtained and polynomial functions as a function of the elevation and cosine functions as a function of the angle around the girth were adjusted. The polynomial functions provided a constant scaling at each elevation while the cosine function allowed for variations at a given height. As the entire mesh is still being adjusted, but being minimised with respect to fewer constraints than a full fitting technique, this procedure was still quite time consuming. One major drawback to the radial scaling technique is that it assumed that the data was located centrally around a given axis. If the subject is not lying on an orthogonal axis then the data will need to be appropriately transformed.

### 3.4.1 Host Mesh Customisation

The method of host mesh customisation provides a novel method of customising a generic model to a specific given only a few key landmark positions. It reduces the number of degrees of freedom which are involved in the customisation process. This is achieved by embedding the object of interest, the *slave* mesh (*e.g.*, a heart or torso model), within a larger *host* mesh. The geometric parameters of the slave mesh (*e.g.*, nodal position and derivatives) are then defined as material coordinates, or  $\xi$  positions within the host mesh. By then deforming the host mesh, the slave mesh is implicitly transported within it. The host mesh is able to transform the slave mesh (which may contain a large number of DOF) by only manipulating a relatively small number of parameters, or DOF.

The local  $\xi$  coordinates of the slave mesh remain constant within the host mesh, yet the global positioning has changed due to the deformation of the host mesh. The global positions of the slave mesh can then be updated to produce the customised model. By using different types of basis functions to interpolate the host mesh, it is possible to represent different variations in the target data (*i.e.*, cubic Hermite basis functions will also allow a cubic variation and enforce continuous derivatives across elements).

The deformation of the slave mesh can be controlled in a number of fashions. It can be moved

by eye, till a suitable customised mesh results or an automated technique which involves control points. Control points are pairs of landmark points which are identifiable on both the generic model and the subject.

The control points typically consist of external landmarks such as the supra-sternal notch, the Xiphoid process, hip and shoulder locations and girths at these locations. As the subject lies supine on a table for the entire experimental procedure, it was assumed that this back plane was concurrent between the generic and specific meshes. This provides the fitting process with an additional constraint. Key features of the heart size and orientation are also used to position the initial heart model inside the torso cavity. Detailed information about heart geometry can be added later in the customisation process and is outlined further in Section 3.4.2

The RMS distances between the control point pairs are then minimised by adjusting the host mesh through the use of the FEM fitting procedure from Section 3.2. The new positions of the embedded slave mesh can then be recomputed from the new host mesh positions.

Figure 3.10 illustrates a simple example of this fitting technique where the slave mesh (shaded circle) has been embedded within the square host mesh. The host mesh has then been deformed to minimise the distances between the landmark points (white circles) and the target points (black circles). The embedded slave mesh is thus deformed along with the host mesh.

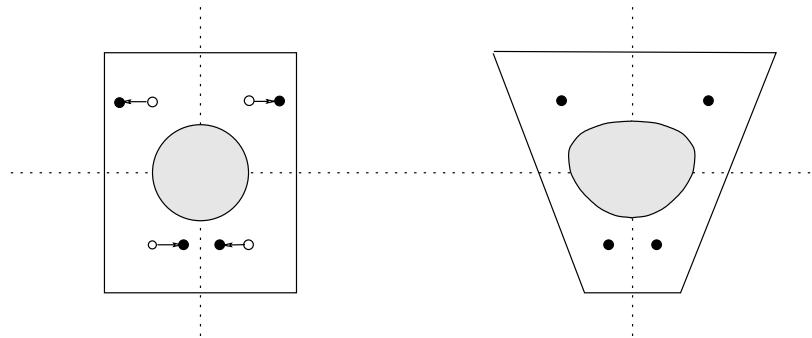


**Figure 3.10:** A simple host mesh customisation example using bilinear basis functions. Four landmark points are located within the left host mesh (white circles) and the corresponding target points on the right (black circles). By deforming the host mesh to minimise the differences, a new host mesh geometry is created on the right. The shaded circular object embedded within the host mesh was then transformed accordingly.

The customisation process for a specific animal is illustrated in Figure 3.11. The smaller generic mesh has been customised to produce a mesh of a larger specific animal. Here, nine common landmark pairs (the landmark points shown as gold spheres and the target points as green spheres)



were used to control the slave mesh. All the landmarks and the generic mesh were placed within an arbitrary host volume mesh and the local  $\xi$  coordinates calculated. This produced the deformed outer green host mesh in Figure 3.11.

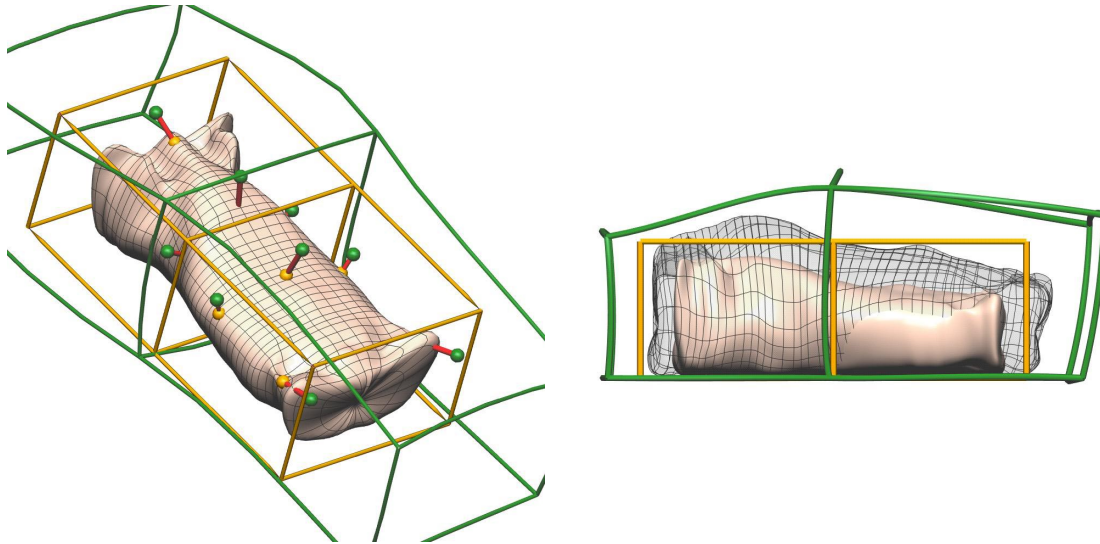


**Figure 3.11:** Host mesh fitting of the generic porcine model. The original host mesh is shown in gold and the resulting deformed host mesh in green. On the left, the generic landmarks are shown as gold spheres and target points as green spheres. The solid generic mesh is enclosed within the original host mesh. Shown on the right is the opaque generic mesh and the transparent customised model. The original host mesh, shown in gold, is deformed to the green mesh to minimise the distance between the target and generic landmark positions.

While the customisation process is not as accurate as what can be achieved by using full CT or MRI information in a fitting procedure, it provides a quick way of tailoring a generic mesh to a given animal. With full CT or MRI data the following process can be used to generate a starting mesh from which to then do further non-linear fitting using the methods outlined in Section 4.2.

### 3.4.2 Heart Customisation

The orientation and size of each subject's heart must be accurately determined for it to be effectively used in the modelling process. The time, cost and availability of full MRI data for each subject has meant that an alternative non-invasive imaging technique was required to obtain quantitative three-dimensional geometry of a given subject's heart. The use of three-dimensional ultrasound has been used to provide an efficient non-invasive means by which to obtain heart geometry from humans and unlike MRI does not exclude subjects with pacemakers.



The three-dimensional ultrasound setup used was similar to the system used at the University of Washington (Legget, Leotta, Bolson, McDonald, Martin, Li, Otto & Sheehan 1998). It was developed for the examination of heart valve geometry and has been adapted to obtain left and right ventricular heart geometry. The setup consists of a standard two-dimensional ultrasound transducer with a magnetic tracker mechanism attached as shown in Figure 3.12. The Flock of Birds magnetic tracker system (Asension Technology Corporation 2000) consists of a magnetic field transmitter and receiver that generates and receives three orthogonal magnetic fields. These are used to compute the receiver's three-dimensional position  $(x, y, z)$  and orientation (azimuth, elevation and roll) in space with respect to the transmitter. The magnetic-field system allows the position and orientation of the trans-thoracic transducer to be tracked during freehand scanning. This allows acquisition of images from randomly oriented image planes from different acoustic windows. The magnetic field system allows images to be acquired from any combination of intersecting, parallel or oblique imaging planes, in order to fully interrogate the heart.

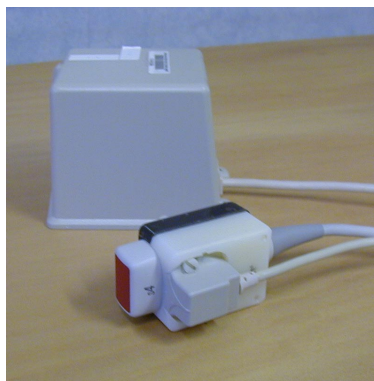


**Figure 3.12:** Hewlett-Packard S4 Ultrasound transducer with magnetic receiver. The ultrasound transducer (red) with holder (black and white) and the attached Flock of Birds magnetic receiver. The larger square box in the background is the magnetic transmitter.

To minimise interference from the ferromagnetic materials, patients are scanned on a wooden bed frame with brass screws. The subject lies supine (in the same position in which electrical recordings will occur) and remain still for the duration of the scanning procedure, approximately 20 minutes. Landmark positions on the torso surface are obtained at the beginning and end of the procedure to ensure the patient has not moved excessively. These are also used to align and combine the different imaging modalities at a later stage. The two-dimensional ultrasound images are obtained at 25 Hz with a concurrent ECG trace so that images can be extracted at end-diastole. This corresponds to the heart geometry during the QRS segment of the cycle as required for activation inverse modelling of the ventricles.

The spatial relationship between the Flock of Birds magnetic receiver and the image plane must

be known in order to achieve accurate image registration in three-dimensional space. The location and orientation of the image plane was offset by the holder and the ultrasound transducer by an unknown amount. To determine this relationship, a similar calibration process as that performed by Legget et al. (1998) was employed. As shown in Figure 3.13, a glass bead was suspended from a thread in a water phantom with a diameter of 125 mm. A Hewlett-Packard Sonos 5550 ultrasound machine with a S4 ultrasound transducer was used with a depth setting of 10 cm.

This bead was then imaged from 32 evenly spaced locations around the phantom. The location of the centre bead in each image was then digitised by hand. As the size of the bead was small (approximately 2 mm in diameter), its acquisition with the ultrasound beam was also difficult. However, the small size of the bead also ensured the centre of the bead was repeatedly imaged and the error in digitisation was reduced. However, digitisation of the bead's location was also difficult due to the poor clarity of the images and the shadow and distortion effects caused by the bead itself. An example of such distortions are shown in Figure 3.14.

Given the relative locations of the transducer and the glass bead, the system was calibrated by minimising the predicted and measured distances in a least squares sense. The calibration process was performed an additional two times with the transmitter in different orientations. The results for the three independent calibration runs generated a transformation matrix which matched the digitised data to within 2 mm RMS. The ability to localise a point in three-dimensional space was of similar accuracy of that reported by Legget et al. (1998) and better than that shown by Moritz, Pearlman, McCabe, Medema, Ainsworth & Boles (1983).

Traditionally, ultrasound views of the heart have concentrated on the left ventricle and the valves. Our procedure requires geometry of the left and right ventricles and the subject to be in a supine position during the scanning process. The ultrasound views which were used included a combination of standard views as well as some views which have been tailored to obtain additional right ventricular information. The views used include: parasternal long and short axis, apical two and four chamber views, posterior apical chamber and subcostal views.

From the two-dimensional images, valve rings, epicardial and both endocardial surfaces were manually traced. An example of tracing a two-dimensional slice is shown in Figure 3.15a. These were then transformed and collated into three-dimensional data surfaces from which geometric models can be created, such as shown in Figure 3.15b.

The large variability in heart shape between subjects and the difficulty in obtaining an even coverage

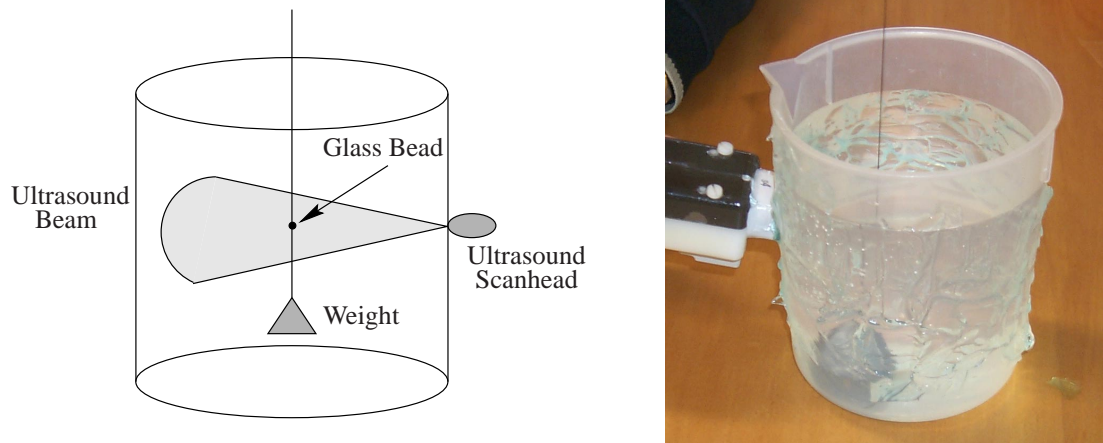


**Figure 3.13:** The calibration process of the ultrasound setup. Shown on the left is a schematic of the calibration setup and on the right the recording process. Ultrasound conductivity gel was coated on the outside of the water phantom to ensure good contact with the transducer. The glass bead was suspended inside the phantom and held still by a weight. The bead was then imaged from 32 locations around the phantom, producing images like that shown in Figure 3.14.

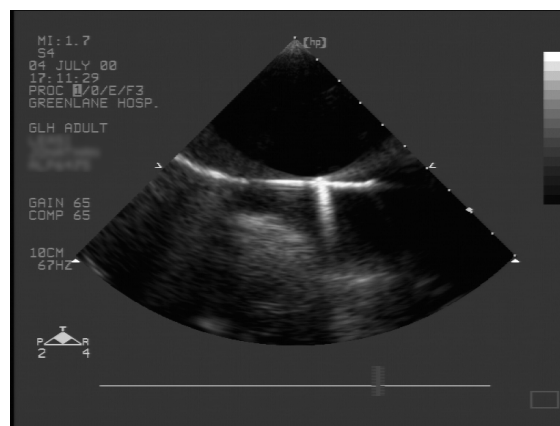


**Figure 3.14:** Two-dimensional ultrasound image of the glass bead obtained from the calibration setup shown in Figure 3.13.

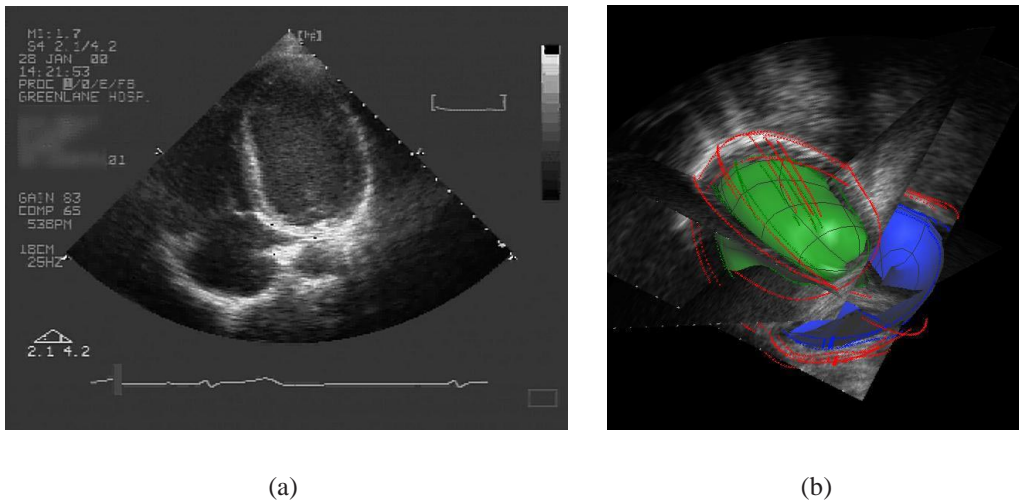


**Figure 3.15:** Constructing a three-dimensional model from two-dimensional ultrasound images. (a) A two-dimensional ultrasound with traced surfaces. The epicardial, left ventricular and right ventricular chamber surfaces were then identified and traced. (b) The three-dimensional model constructed from two-dimensional data assembled into three-dimensional space using the information from the magnetic tracker.

of data has meant the techniques described in Section 3.4.1 for customising the torso surface are not totally suitable for creating a subject specific heart mesh. At this stage, the traditional linear fitting methods described in Section 3.2 are used for creating the heart meshes as shown in Section 3.3.3.

# **4** *Geometric Torso & Cardiac Source Models*

Over the last two decades, increasingly accurate numerical torso models have been used to study a variety of electrical phenomena, including defibrillation, calculation of radiation doses in radiotherapy, and the forward and inverse problems of electrocardiography (Skouibine, Trayanova & Moore 1999, Bradley, Pullan & Hunter 1997). To study these events (using a mathematical modelling approach) it is necessary to describe the electrical activity within the heart and the geometry of the torso mathematically. This chapter describes the geometric and cardiac source models which are used in Chapters (5)–(7) in forward and inverse simulations.

There now exists complete, high resolution, three-dimensional data sets of the male and female human body from the Visible Human Project (National Library of Medicine 1994), to which geometric torso models have been created (Lorensen 1996, Sachse, Werner, Mery-Waarden & Dossel 1998, Magnenat-Thalmann & Cordier 2000). The Visible Human Project is the creation of complete, anatomically detailed three-dimensional representations of normal male and female human bodies. Acquisition of transverse CT, MRI and cyrosection images of a male and female cadaver have been completed and the data is freely available. However, as the subjects are deceased, the heart is not in its natural state when these images were acquired.

With the common availability of non-invasive, medical imaging modalities such as MRI and CT, obtaining further non-invasive data from specific subjects is also now possible. The data from these imaging modalities is typically presented as a series of two-dimensional image planes, which when stacked form a three-dimensional volume of data. From these data, realistic and accurate geometric models can be created.

## 4.1 Previous Geometric Models for Electrocardiology

There are three main model types which are used in modelling the inverse problem of electrocardiology: physical, analytic and numerical. Physical models approximate the solution domain but measure, rather than solve, the governing physical equations. Analytic models grossly approximate the solutions domains (usually in the form of regular, spherical or cylindrical domains) so that the governing equations can be exactly solved everywhere with an analytic expression. Numerical models approximate the solution domain, usually with discrete surfaces or volumes (finite/boundary elements) and solve governing equations at a number of computational points within the solution domain.

Physical models typically consist of an electrolyte filled torso shaped tank. Different materials are used to represent the internal torso homogeneities (*e.g.*, porous sand bags for lungs). Currently, the most advanced physical models are those of Rush (1971) and MacLeod, Taccardi & Lux (1995). These types of models are an essential part of understanding the problem and provide a controlled and idealised environment from which detailed *in-vivo* measurements can be obtained for validation purposes. Physical models provide a near control environment in which it is possible to investigate the effect of different modelling errors, however, they do not provide the complete controlled environment of mathematical simulations or provide the exposure to the variety of errors which are present in *in-vivo* experiments.

The earliest analytic models were based on dipoles within a spherical medium (Wilson & Bayley 1950). These models, despite their simplicity, provide some useful results regarding the effects of geometry and individual inhomogeneities on the torso potentials and currents. The most advanced analytic model to date is the eccentric spheres model of Rudy & Plonsey (1979) and Messinger-Rapport & Rudy (1986) where a system of eccentric spheres approximated ventricular blood masses, the myocardium and the pericardium. Another torso model used surface Harmonic expansions for modelling the human torso Hren & Stroink (1995). This was an efficient method for modelling the human torso surface. However, the complex structures of the internal organs cannot be modelled using these methods and there was no associated analytic solution.

The rapid increase in computing power has seen a shift away from using physical and analytic models towards using numerical models to solve the problems of electrocardiology. There have been a few Finite Difference (FD) models (Budgett 1995), but the majority of numerical models have been Finite Element (Yamashita & Takahashi 1984, Johnson, MacLeod & Ershler 1992) and Boundary Element based (Tilg, Wach, SippensGroenewegen, Fischer, Modre, Roithinger, Mlynash, Reddy,

Roberts, Lesh & Steiner 1999, van Oosterom & Huiskamp 1989). There now exist coupled FEM-BEM models which incorporated the advantages from each of the methods into the appropriate regions (Bradley et al. 1997, Fischer, Tilg, Modre, Huiskamp, Fetzer, Rucker & Wach 2000).

## 4.2 Model Generation

Medical imaging techniques such as MRI and CT are able to produce *in-vivo* volumetric data sets of biological samples by exploiting the varying material properties of the different organs within the torso. The volumetric data sets produced by the medical imaging techniques however, do not directly provide information about the subject's structure. From this volumetric data set, the information must be classified or segmented such that regions of interest can be extracted.

Techniques such as Marching Cubes (Lorenson & Cline 1987) and Region Growing (Sapidis & Besl 1995) were designed to automatically segment data sets into areas of similar material properties. However, due to the poor clarity of medical images and the close proximity and complexity of the organs, the extraction of surfaces with the use of image processing is still a developing process, and human intervention is almost always required.

This has led to the development of semi-automatic fitting techniques such as guide point fitting of Hedley (1998) and the voxel classification of Budgett (1995). Hedley (1998) used a combination of manually entered guide points and image analysis to construct a finite element left ventricle model from short and long axis MRI images. Budgett (1995) used MRI data to extract voxel elements. From the MRI images the fat, trunk, lung, heart, great blood vessels, liver and spine were extracted. The images were filtered to enhance particular tissues and heuristic information was included about the relative location of each of the organs. This involved a semi-automated approach where user interaction is included at several stages in the classification process.

Automatic extraction of surface information from volume data sets is still a developing field. This process is particularly difficult for features such as the endocardial surfaces, where there is not a high contrast between the blood masses and myocardium, and the right ventricle, which has a thin free wall. Despite manual digitisation of images being subject to human judgement, it is considered to be the most stable method of surface classification. The geometric models produced in this thesis were produced from manually digitised images.



Structures such as papillary muscles within the heart are usually ignored when modelling the electrical activity within the heart. They are unlikely to cause significant effects on the torso surface potentials but can be included as another source of error in the modelling process. By taking a boundary element modelling approach, including complex geometries, such as bone, would dramatically increase the problem complexity. Previously studies by Klepfer, Johnson & MacLeod (1997) had found that the addition of bone structures has little effect on the forward computed torso surface potentials.

The surface data can be used to create surface or volume meshes. To create  $C^1$  bicubic Hermite surfaces meshes the geometric data fitting procedure described in Bradley et al. (1997) was employed. Each surface of the model was considered independently, but care was taken to ensure that the surfaces did not intersect, especially when the surfaces are located in close proximity to each other (*e.g.*, the lung surfaces surrounding the heart).

To minimise the fitting time, it was desirable to use an initial mesh which provided a close approximation to the data. To obtain the initial mesh, advantage was made of the fact that data were arranged in slices with a constant  $z$  elevation. For each surface, the minimum number of nodes in the circumferential direction was chosen which could still suitably represent the desired complicated shape. The number of nodes in the longitudinal direction was chosen such that resulting elements remained relatively square.

For each surface of interest, a number of uniformly spaced slices were chosen and a two-dimensional mesh was constructed from nodes uniformly spaced circumferentially around the slice. Care was taken to ensure that the position of each node lined up with the corresponding nodes from the slice above and below. Initial derivatives were set from a straight line approximation between nodes. Using the fitting procedure of Bradley et al. (1997), a two-dimensional mesh was fitted with cubic Hermite elements.

These two-dimensional meshes were then stacked on top of one another. Bicubic Hermite elements were created by joining corresponding nodes between each of the slices. Initial derivatives in the circumferential direction were obtained from the two-dimensional slices and calculated from straight line approximations in the longitudinal direction and cross derivatives initially set to zero. The fitting procedure was then applied to the full mesh to obtain the final three-dimensional mesh for each surface.



### 4.3 Generic Male Torso Model

The generic male torso model used in this thesis was based on the Bradley et al. (1997) high order coupled FEM-BEM model. This model consisted of six regions: epicardium, left and right lungs, skeletal muscle, subcutaneous fat and the outer torso layer. The homogeneous regions (epicardium and lungs) were modelled using BEM while the anisotropic fat and muscle layer were modelled using FEM. The data for this model was obtained from a healthy, 19 year old volunteer. It consisted of a series of 120 MRI images at 5 mm intervals. This is the same data set from which the Utah Torso model was constructed (MacLeod, Johnson & Ershler 1991, Johnson et al. 1992).

The activation based formulations for the forward and inverse problems of electrocardiology require both the endocardial and epicardial surfaces to be explicitly modelled. Lack of detail in the original MRI images prevented these surface being extracted so it was necessary to incorporate a new ventricular heart model into the torso model. Therefore, the Auckland heart model, based on the work of Nielsen, Le Grice, Smaill & Hunter (1991) and Le Grice et al. (1997) was used. The use of this canine mesh allows the inclusion of the detailed fibre and sheet information obtained by Le Grice et al. (1995) in the future.

The new heart model is a rectangular-Cartesian heart mesh is based on the 60 element prolate mesh of Le Grice et al. (1997) and the mesh fitted to their surface geometry data, using the positions of the nodes in their mesh as initial values in the fitting process. The epicardial and endocardial surfaces were artificially closed off at the valve plane with smooth surfaces to create an enclosed domain for the boundary element mesh to surround. The size of the heart was then scaled by a factor of  $1^{1/3}$  in each direction to provide a heart of proportions more suited to a human.

Shown in Figure 4.1a is the epicardial surface from Bradley et al. (1997). This was less geometrically accurate when compared to the new heart model shown in Figure 4.1b. Details such as the inter-ventricular groove and endocardial surfaces are included in the new model. The previous model was described by 37 nodes while the new epicardial surface was modelled with 62 nodes. Both of these meshes were defined by bicubic Hermite basis functions.

The results from the fitting process are shown in Table 4.1 and the final fitted model shown in Figure 4.2.

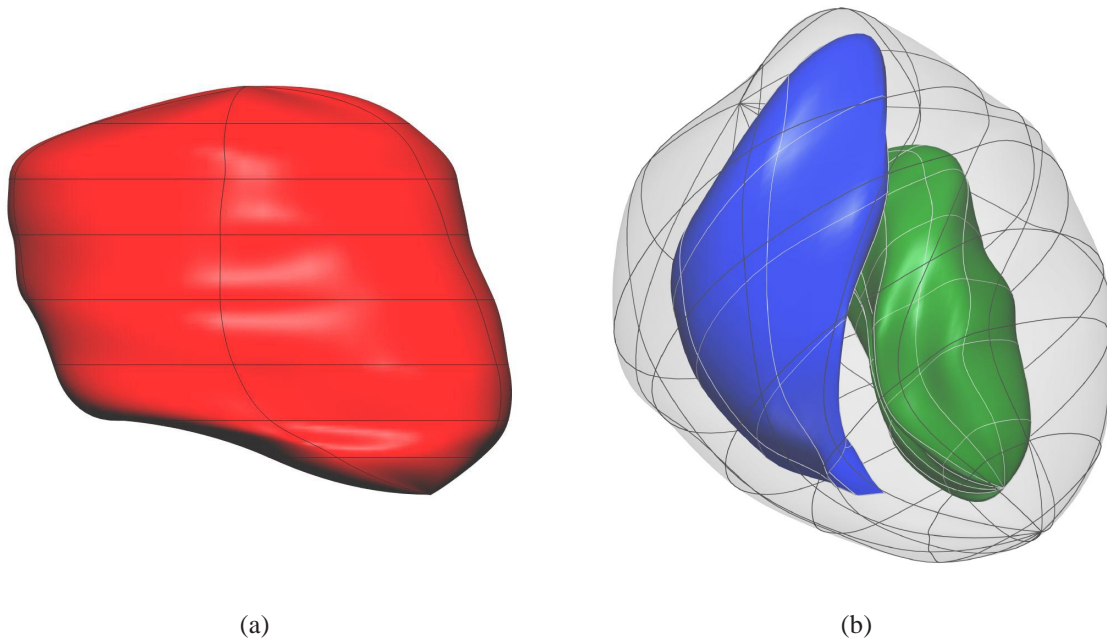


**Figure 4.1:** Anterior views of generic human heart models shown from the same perspective. Shown in (a) is the epicardial surface model created by Bradley et al. (1997) from human MRI scans. Shown in (b) is the new rectangular-Cartesian canine surface model created from data of Le Grice et al. (1997). The canine model contains both endocardial surfaces while the MRI model only contains epicardial surface information. The epicardial surface is shown in red in (a) and the transparent surface in (b), the left endocardial surface in green and the right endocardial surface in blue.

SURFACE	NUMBER OF NODES	NUMBER OF DATA POINTS	RMS ERROR (mm)
EPICARDIUM	62	802	1.37
LEFT VENTRICLE	62	770	2.18
RIGHT VENTRICLE	38	846	1.74
LEFT LUNG	74	2766	1.66
RIGHT LUNG	74	2750	1.69
OUTER TORSO	439	11966	1.43
TOTAL	749	19908	1.68

**Table 4.1:** Summary of the generic male torso fitting results obtained by fitting piecewise bicubic Hermite surfaces to digitised data. The RMS errors are between digitised data points and their orthogonal projections onto the fitted surfaces. The lungs and outer torso surfaces were the same as those constructed by Bradley et al. (1997), while heart data was obtained from the data of Le Grice et al. (1997).

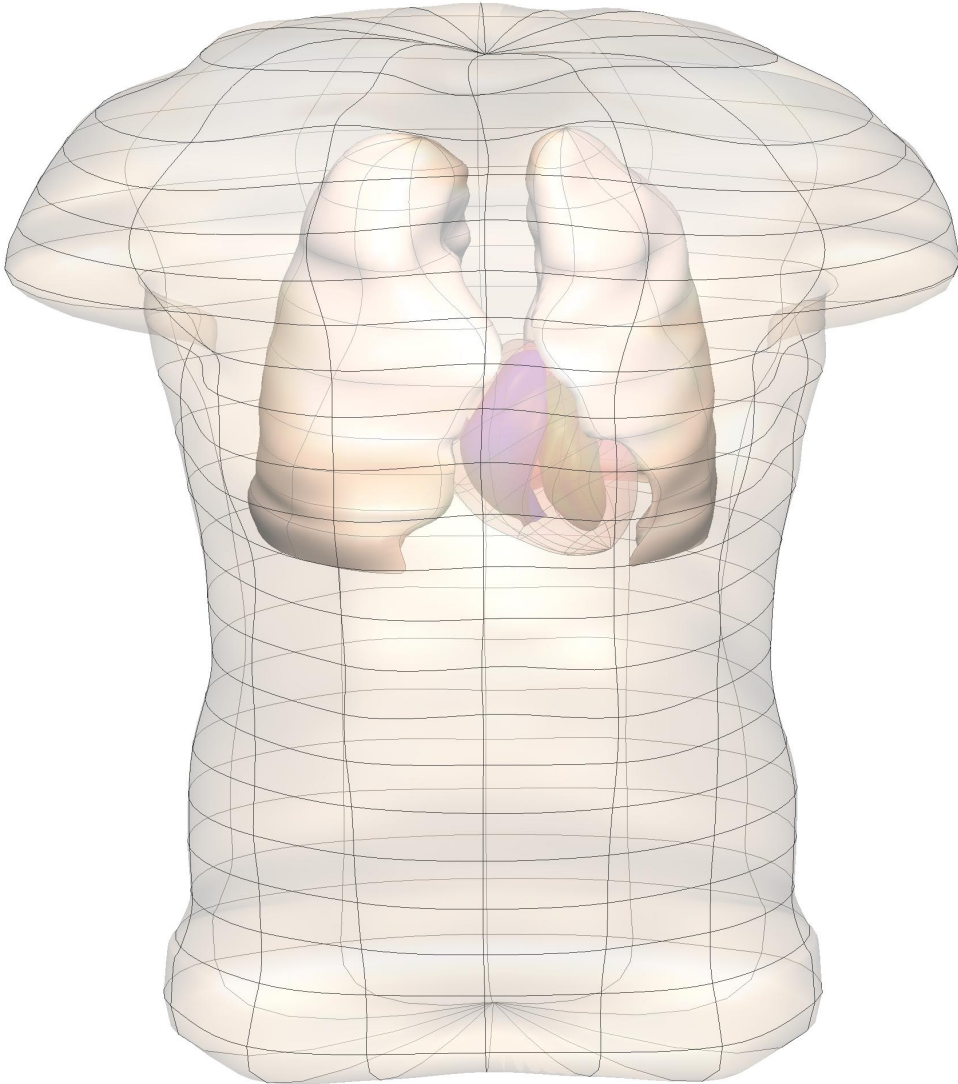


**Figure 4.2:** The full generic male model from an anterior perspective. Shown are the six boundary element regions: epicardium (pale red), left and right ventricular chambers (green and blue respectively), left and right lungs (beige) and the skin surface.

## Origin and Coordinate System

A rectangular Cartesian coordinate system was used to represent the data and the model. The origin was located at the bottom of the Xiphoid process, on the back surface of the torso. This was chosen so the coronal ( $x-z$ ) plane will be the same as the table on which the subject is expected to lie during a normal procedure. The  $x$  axis is positive to the model's left, the  $y$  axis positive towards the posterior of the torso and the  $z$  axis is positive towards the head.

## 4.4 Generic Porcine Model

The validation of numerical methods is crucial to their common acceptance. One method of validating a non-invasive electrical imaging algorithm is by obtaining concurrent measurements at the heart level and on the torso surface. Such validation experiments are possible on some animals and is currently being performed on pigs at the University of Oxford (Nash et al. 2000*b*). For the purpose of analysing these experiments a generic porcine model was required.

To construct the generic pig model, a sequence of cross-sectional CT torso images of a 20 kg pig was obtained at the University of Oxford. CT scanning is a radiographic method that was introduced in 1972 for neurological applications. It uses a rotating ultra thin X-ray beam with a detector mounted on the opposite side. As the X-ray and detector make one revolution, the detector takes numerous snapshots or profiles of the attenuated X-ray beam. Each profile is subdivided spatially into a two-dimensional slice. Substances of different density are displayed at different greyscales for visualisations of the internal structures. Bone, muscle and fat tissues absorb different levels of the X-ray producing an attenuation coefficient that varies with density. High density bone materials produce white pixels, whilst darker shades represent lower density fat and muscle. An example of such a two-dimensional slice is shown in Figure 4.3.

The CT images were acquired from the deceased animal which was slowly ventilated. Each slice was then acquired with the lungs fully inflated to simulate breath-hold in a live animal, as would occur in the practice in the *in-vivo* experiments. The generic model was created from 99 CT images, each 5 mm apart.

The porcine CT images were then digitised to provide a three-dimensional data set of six key surfaces: epicardium, left and right endocardial chambers, left and right lungs and skin surfaces.

Due to the leanness of the pig, the fat layer was not explicitly modelled and due to difficulty in determining the base plane of the heart, both the ventricles and atria have been modelled as one surface. These data were then used with the non-fitting procedure described in (Bradley et al. 1997), to form piecewise  $C^1$  continuous cubic Hermite elements of the above surfaces.

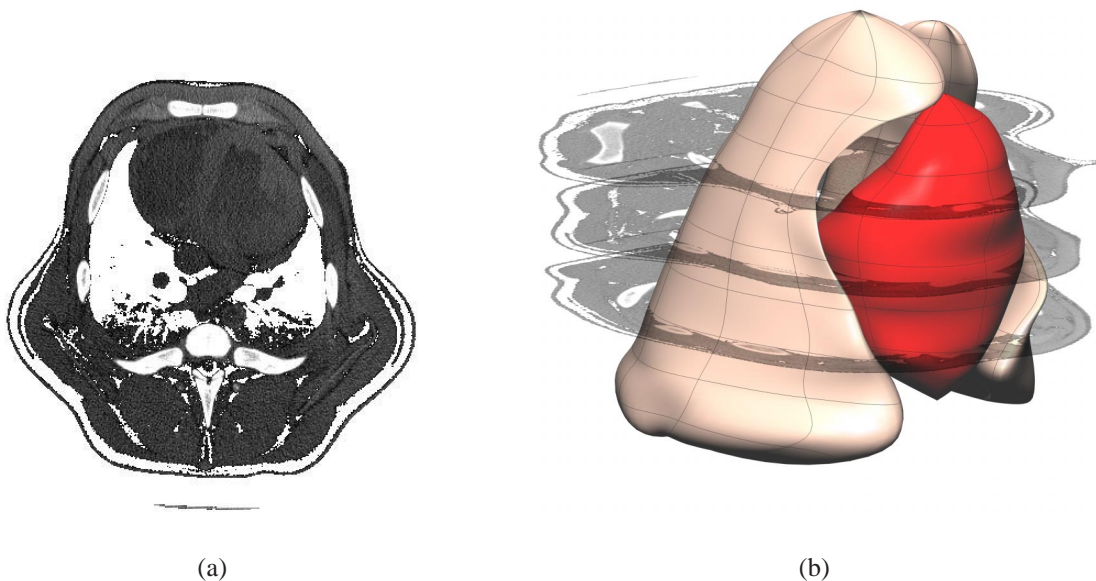


**Figure 4.3:** A CT image slice (a) of the generic pig at mid-heart level. Shown in white are the lungs, bones and fat layer. The muscle, myocardium and blood masses are shown as dark regions. (b) is a closeup of the epicardium and lungs of the pig model with three of the CT image slices from which the model was created overlaid at 25 mm intervals.

### Origin and Coordinate System

The origin and coordinate system of the pig model is the same as that of the human torso. The origin is located on the back surface of the pig in the supine position (*i.e.*, on the surgical table) and on the centreline of the pig. This is to account for the fact that the pig will be lying on a table during an *in-vivo* experiment. The coronal ( $x-z$ ) plane is equivalent to the table surface. The  $x$  axis was positive to the model's left, the  $y$  axis positive towards the posterior and the  $z$  axis was positive towards the head.

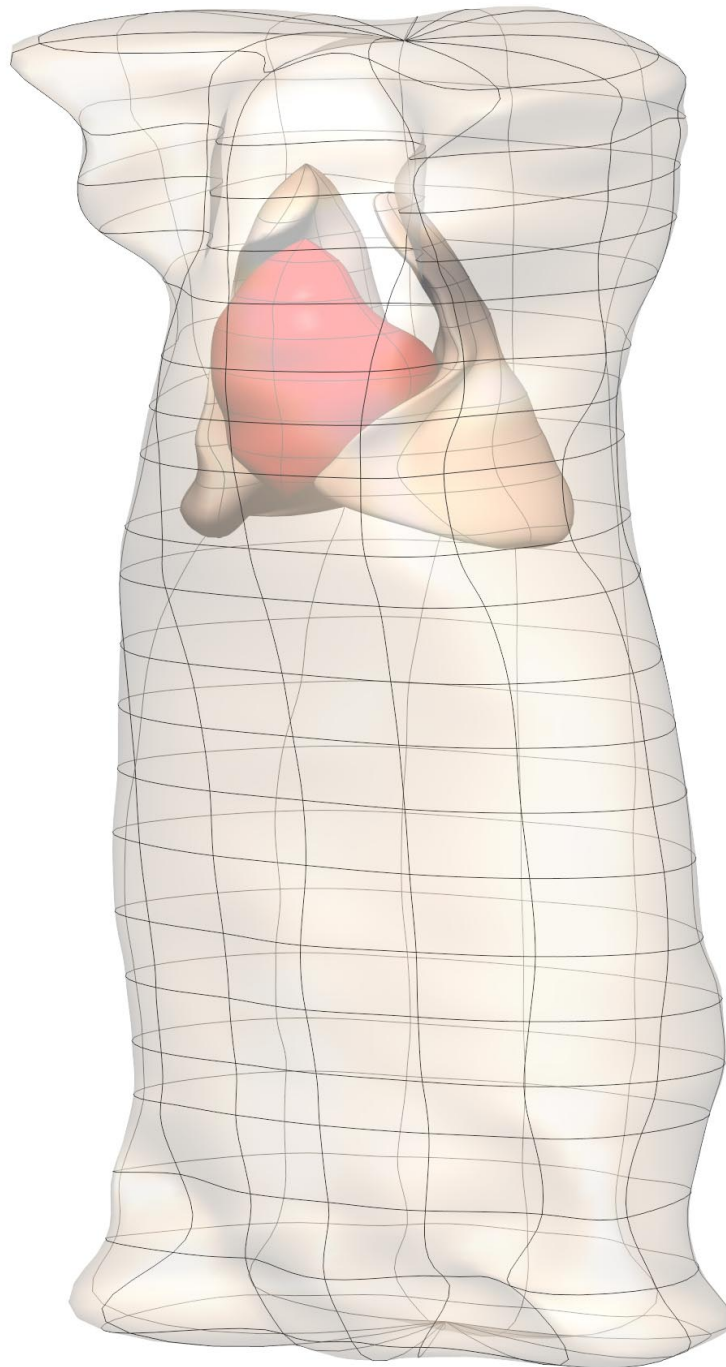


**Figure 4.4:** Generic porcine model created from digitised CT images (shown in Figure 4.3). Shown are the skin surface (transparent), left and right lungs (beige) and the epicardial surface (red). The ventricular chambers are not shown.



### 4.4.1 Fitting Results

The six surfaces of the generic pig torso were fitted independently. The number of nodes for each region was selected such that a good geometric representation of the surface could be achieved while minimising the number of nodes. The final fitted model is shown in Figure 4.4 and the fitting results in Table 4.2.

This generic model is referred to later as the model with level 0 refinement (see Table B.1) and provides a framework on which to validate certain aspects of the whole procedure (*e.g.*, the appropriate mesh resolution to use in the computational forward model).

SURFACE	NUMBER OF NODES	NUMBER OF DATA POINTS	RMS ERROR (mm)
EPICARDIAL	37	1603	1.23
LEFT VENTRICLE	27	500	1.47
RIGHT VENTRICLE	38	892	1.13
LEFT LUNG	74	2011	2.14
RIGHT LUNG	74	2640	2.71
OUTER TORSO	439	2417	2.47
TOTAL	689	10071	1.86

**Table 4.2:** Summary of the generic porcine fitting results obtained by fitting piecewise bicubic Hermite surfaces to digitised CT slices of a particular pig. The RMS errors are between digitised data points and their orthogonal projections onto the fitted surfaces.

## 4.5 Material Properties

In addition to the geometric description of a computational model, the electrical conductivities of the various torso inhomogeneities must be specified to provide a complete description of the model. At a microscopic level, the discrete nature of cell structures dictate that all tissue is anisotropic. However, at a macroscopic level, many tissues can be approximated as being electrically isotropic.

For the simulation studies conducted during the course of this research, the exact values of the conductivities was felt not to be too critical. The sensitivity of the inverse solutions to the material properties are investigated in Section 7.4.

A range of passive conductivities obtained experimentally and used in numerical simulations is summarised in Table 4.3 while published bidomain conductivities are shown in Table 4.4. The passive heart conductivity was used in the epicardial potential approach described in Section 5.6.2 while the bidomain conductivities in Section 4.5.2 are used for the activation approach described in Section 5.6.3 .

### 4.5.1 Passive Electrical Conductivities

The passive conductivities used for this thesis were derived from a number of published experimental papers (Rush, Abildskov & McFee 1963, Geddes & Baker 1967, Foster & Schwan 1989). These conductivities were measured experimentally, mostly on dogs. The electrical properties of the tissue are characterised by electrical conductivities parallel to (L) and perpendicular to (T) the fibre distribution in the myocardium. However, by assuming the myocardium to be electrically isotropic, an intermediate value must be used. This assumption also greatly reduces the problem size of the inverse procedures described in Chapter 6.

The differences in material conductivities can be attributed to the fact that they were obtained experimentally from a number of sources and under different conditions. Furthermore, the measurements were performed using tissue samples, which may not represent the true impedance of the living *in-vivo* tissue. Thus, there exists an uncertainty regarding the correct values of the tissue conductivities. However, a more important contribution may emerge from the fact that tissue conductivity may be different between species and may change due to many physiological and pathological conditions such as temperature, posture changes and when electrolytic or water balance of the body



is disturbed (Hyttinen, Puurtinen, Kauppinen, Nousiainen, Laarne & Malmivuo 2000, Rosenthal, Restieaux & Feig 1971).

In addition to the experimentally measured conductivities, the conductivities used in numerical simulations were also considered (Fischer, Tilg, Wach, Modre, Leder & Nowak 1999, Bradley, Pullan & Hunter 2000, Hyttinen et al. 2000). It should be noted that the conductivity value for heart of Bradley et al. (2000) was increased to account for the fact that the model did not contain blood masses.

The passive material conductivities were chosen to be consistent with the trends of multiple sources presented in Table 4.3 rather than with an individual paper. The conductivity values used throughout this thesis are shown in the last column of Table 4.3.

TISSUE	RUSH	GEDDES	FOSTER	FISCHER	BRADLEY	HYTTINEN	THIS THESIS
BLOOD	0.617	0.667	0.600	0.60	—	0.667	0.63
HEART	—	0.104	—	—	0.50	0.22	0.30
HEART (L)	0.397	—	—	—	—	—	—
HEART (T)	0.178	—	—	—	—	—	—
LUNGS	0.048	0.046	0.089	0.04	0.05	0.075	0.05
TORSO	0.216	0.241	0.239	0.20	0.22	0.25	0.22

**Table 4.3:** Passive electrical conductivities ( $\text{mS mm}^{-1}$ ) obtained experimentally by Rush et al. (1963), Geddes & Baker (1967) and Foster & Schwan (1989). Electrical conductivities used in computational simulations by Fischer et al. (1999), Bradley et al. (2000), Hyttinen et al. (2000) and those used in this thesis. The index *L* denotes conductivity in a longitudinal direction and *T* the conductivity in the transverse direction with respect to fibre orientation.

Heart conductivities vary greatly depending on the fibre direction within the myocardium. Transverse heart conductivities were determined to be  $0.178 \text{ mS mm}^{-1}$  while longitudinal conductivities were determined to be  $0.397 \text{ mS mm}^{-1}$  by Rush et al. (1963). The blood conductivities within the ventricular chambers were fairly constant with values ranging from  $0.6$  to  $0.667 \text{ mS mm}^{-1}$ . This is probably a result of the homogeneous nature of the medium and the ease with which experimental samples can be obtained. A value of  $0.63 \text{ mS mm}^{-1}$  was chosen for the simulations. The lung conductivities vary depending to the degree to which a lung is inflated. The conductivities had a range of  $0.042$ – $0.089 \text{ mS mm}^{-1}$ . The lung conductivity for this thesis was chosen to be  $0.05 \text{ mS mm}^{-1}$ . The torso conductivities were generally obtained from human subjects and had values between  $0.216$  and  $0.241 \text{ mS mm}^{-1}$  and a value of  $0.22$  was chosen for this thesis.

## 4.5.2 Bidomain Conductivities

The bidomain model (Tung 1978, Henriquez 1993) is a volume averaged model of the electrical properties of cardiac tissue which models two inter-penetrating domains – the intracellular and extracellular space. The electrical properties of the tissue are characterised by electrical conductivities parallel to (L) and perpendicular to (T) the myocardial fibres in the intracellular ( $i$ ) and extracellular space ( $e$ ). The values of these conductivities determine much of the electrical behaviour of the tissue. No consensus exists regarding the correct values of these parameters for mammalian ventricular muscle. The bidomain conductivities have been measured experimentally (Clerc 1976, Roberts, Hersch & Scher 1979, Roberts & Scher 1982) but as summarised in Table 4.4, the data is inconsistent. Roth (1997) determined a general rule for determining the ratios of the bidomain conductivities where the intracellular conductivity is approximately the same and the extracellular conductivity and the longitudinal conductivity was determined to be ten times greater than the extracellular conductivity.

DOMAIN	CLERC	ROBERTS <sup>79</sup>	ROBERTS <sup>82</sup>	SKOUIBINE	FISCHER	THIS THESIS
$\sigma_i$ (L)	0.17	0.28	0.34	0.375	—	—
$\sigma_i$ (T)	0.019	0.026	0.06	0.0375	—	—
$\sigma_i$	—	—	—	—	0.04	0.3
$\sigma_e$ (L)	0.62	0.22	0.12	0.375	—	—
$\sigma_e$ (T)	0.24	0.13	0.08	0.0214	—	—
$\sigma_e$	—	—	—	—	0.16	0.3

**Table 4.4:** Summary of bidomain conductivities ( $\text{mS mm}^{-1}$ ). Conductivities were obtained experimentally in (Clerc 1976, Roberts et al. 1979, Roberts & Scher 1982) and the values used in numerical simulations (Skouibine et al. 1999, Fischer et al. 1999) and those used in this thesis. The indices (L and T) are defined in Table 4.3

As with the passive material conductivities, the bidomain conductivities were chosen to be an average of the multiple sources presented in Table 4.4 rather than with an individual paper. As with the passive conductivities, the myocardium was assumed to be electrically isotropic, so averaged intracellular and extracellular conductivity was used. The conductivity values used throughout this thesis are shown in the last column of Table 4.4.

## 4.6 Cardiac Sources

It is necessary to have an accurate mathematical representation of the electrical activity of the heart to model the electrical activity throughout the torso. The highly variable and dynamic nature of

a normal and abnormal cardiac cycle is difficult to represent using a single mathematical cardiac ‘source’ model. The cardiac source is an essential and critical component of an accurate computational model. It has been shown that not only the type of the cardiac source but the point of the heart cycle at which analysis of results occur is critical in the understanding of the forward and inverse problems of electrocardiology (Hytinen et al. 2000).

The two predominant source descriptions are a potential distribution on the epicardial surface and the transmembrane potential gradient (essentially the activation wavefront during ventricular activation). To model the electrical activity within the torso, a cardiac source which specifies the electrical distribution within the heart is usually required. This source description may either be recorded by invasive means, approximated using electrical models or approximated using recordings from sources thought to represent the potential distribution from a heart inside a torso. Throughout this thesis a number of different heart sources are used. As these sources are merely approximations of what is actually occurring within a heart, it is hoped that the different sources will cover a number of aspects of cardiac activation.

In order to fully simulate both the activation sequence of the heart and clinically important pathological conditions, a heart model needs to incorporate a detailed ionic current membrane model and structures which affect the ionic currents (*e.g.*, the Purkinje fibres and the myocardial fibre and sheet structures). This must then be coupled into a detailed torso model so that the currents flowing between the heart and torso can be correctly matched with the underlying ionic currents which generate them (*e.g.*, Buist & Pullan 2001, Pullan & Buist 1998). This process is, however, extremely complicated and computationally expensive. It is also not feasible to recreate what is happening at the cellular level given only measurements on the torso surface.

Despite significant similarities in heart structure and function between pigs and humans and that pigs are considered to be the ideal animal for human heart transplants, there still exists significant differences between the two species. The duration of activation time is significantly shorter in a pig compared to a human as indicated by the much higher heart rates in pigs. The hearts in pigs are also oriented in line with the major axis of the torso as opposed to humans which have the heart long axis typically oriented in the lower left/upper right quadrant of the thorax.

Normal activation sequences in human and pigs which have been measured in experiments are described in Section 4.6.1 and Section 4.6.1. Sections (4.6.2)–(4.6.5) contain descriptions of the cardiac sources which are used throughout the rest of this thesis. The sources include a simple constant current dipole source, a simulated activation field derived from an eikonal solution, an

activation field derived by specifying seed points which represent initial activation sites and a source derived from an experimentally recorded epicardial potential distribution.

### 4.6.1 Normal Ventricular Activation Sequence

Although the ultimate aim of non-invasively imaging the heart is the diagnosis of abnormal heart rhythms, the ability to model a normal activation sequence is essential as part of the validation process. Presented below are descriptions of the normal activation sequences which occur in humans and pigs. Using these normal activation sequences as guidelines, the cardiac source models described in Sections (4.6.2)–(4.6.5) were created. These source models are used in the forward and inverse simulations described in Chapters (5)–(7).

#### Human Ventricular Activation

A normal human ventricular activation is considered to have a duration of around 100 ms. Experimental measurements of the ventricular activation durations have been found to vary between subjects but inversely computed activation times from experimentally measured body surface potentials have values of between 80–120 ms (Tilg et al. 1999, Fischer et al. 1999).

The most comprehensive investigation into the distribution of the excitation process of the human heart is that of Durrer, van Dam, Freud, Janse, Meijler & Arzbaecher (1970). In this study, seven individual hearts with no previous history of heart disease were examined. The isolated hearts were perfused and continued beating in a spontaneous sinus rhythm for a period ranging from 4 to 6½ hours. The electrical activity of the heart was recorded from epicardial and intramural electrodes. The QRS duration of the hearts varied from 70–80 ms. It is possible that the regions of the heart to be activated latest are small enough that they contribute little to the QRS complex. Thus, the total excitation time may appear to be longer than the QRS measured from electrocardiograms.

The general pattern of excitation did not change after isolation of the heart. However, total excitation in the perfused heart was completed earlier than in the *in-situ* heart. Measurements in the normal human heart, performed during surgical interventions, indicate a conduction velocity of about  $0.3 \text{ mm ms}^{-1}$ . In the isolated perfused human heart, a maximum conduction velocity of  $0.45 \text{ mm ms}^{-1}$  was found (Durrer et al. 1970).

The duration of ventricular activation for natural sinus and pacemaker-generated rhythms are of similar. This has been shown by comparing ECG recordings on the torso surface (Sands, Cheng & Pullan 2000). However, the different initial activation sites means that the torso surface potential patterns are significantly different.

### **Porcine Ventricular Activation**

Porcine epicardial activation times for sinus rhythms have been measured to have a duration in the range of 15–25 ms while torso surface signals are usually in the range of 30–40 ms. This information was gathered from 127 epicardial sock electrodes and 256 torso surface electrodes in the *in-vivo* experiments of Nash et al. (2000*b*).

From the *in-vivo* experiments it has been found that the duration of ventricular activation can be significantly altered in pigs depending on the site of initial activation (Cheng, Nash, Bradley, Pullan & Paterson 2000, Nash, Bradley, Cheng, Pullan & Paterson 2000*a*). A natural sinus rhythm had a ventricular activation duration of 20 ms while beats paced from the epicardial surface had a duration of up to 53 ms.

To date, there has been limited detailed analysis of *in-vivo* analysis of the myocardial activation pattern in pigs. There is some work which has been performed by Roshchevsky from the Russian Academy of Sciences, however, this work is published in Russian. There are also the studies performed by Nash et al. (2000*b*). This data only includes *in-vivo* measurements on the epicardial surface, but concurrent endocardial measurements are intended to be obtained soon. The epicardial measurements of one subject are used in Section 4.6.5 to produce an experimentally derived activation source.

#### **4.6.2 Single Dipole Source**

A traditional approach to modelling the electrical activity within the heart involves the use of dipoles. This typically involves specifying one, or more, moving or static dipoles within the heart. From this dipole the resulting epicardial potentials can be calculated.

The use of a single dipole restricts the potential on the epicardial surface to contain only one maxima and one minima, which is known to be physiologically unrealistic in a normal heart. Due

to its simplicity, this results in a smooth activation pattern. The use of multiple dipoles means that multiple maxima and minima may exist and can result in a more complex cardiac source than with a single dipole.

A single moving dipole source provides a simple, temporally varying potential distribution over the heart surface. To calculate the dipole orientation throughout the cardiac cycle a Frank vectorcardiograph (VCG) was recorded from a healthy male volunteer at Green Lane Hospital, Auckland. This was used to produce a single cardiac cycle of length 600 ms at a frequency of 1 kHz. This is the same cardiac source which was used by Bradley et al. (2000).

### 4.6.3 Eikonal Activation Profile

Using an eikonal equation, the myocardial excitation wavefront propagation was modelled in a 180 element tricubic Hermite finite element mesh of the Auckland canine ventricular model (see Section 4.3) by Tomlinson, Pullan & Hunter (1999). Similar methods had been previously conducted by Colli Franzone, Gueeri, Penacchio & Taccardi (1998) and Keener (1991). Using this approach, the spreading of excitation in the ventricular myocardium was modelled by treating the thin region of rapidly depolarising tissue as a propagation wavefront. The Petrov-Galerkin finite element method was used to solve the eikonal-diffusion equation and used to determine tissue activation times throughout the myocardium. The model included the effects of wavefront orientation in the myocardial structure and wavefront curvature. Further details about the solution process of the original cardiac source can be found in Tomlinson (2000).

From the excitation time solution, the resulting activation field was then transformed to the geometry of the porcine heart model by orthogonal projections onto the surface and fitting the field in a least squares sense.

The original canine activation profile and the fitted porcine activation profile are illustrated in Figure 4.5. Comparing the differences between the canine solution and fitted solution gave an RMS error of 2.0 ms and a similarity index of 0.99. The activation field of the canine model had a duration of 55 ms while the porcine model had a duration of 52 ms. These differences were attributed to the large geometric differences between the two heart models.

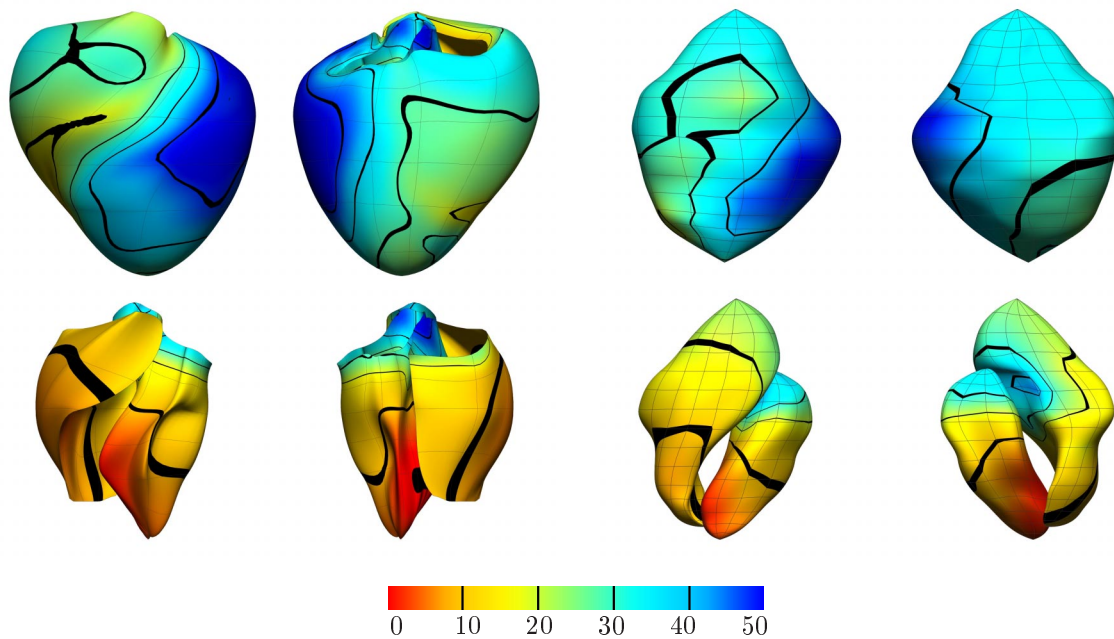


**Figure 4.5:** The activation field (ms) generated from an eikonal equation model of ventricular activation (first two columns) and the fitted activation field on the porcine heart model (last two columns). The colour field represents activation time ranging from 0 to 50 ms, with red being earliest and blue latest activation. The anterior surfaces are shown in the first and third columns and the posterior in the second and last columns. The endocardial surfaces shown in bottom row have been displaced below the epicardial surfaces in the top row for display purposes.

#### 4.6.4 Point Stimulus Activation Profile

An activation map can be created by specifying seed points at certain locations and then using a distance relationship between points on the heart surface to the seed point as a weighting on the activation time. Each seed point effectively represents an ectopic focus or a point stimulus from a catheter. A single seed point produces a spherical evolving wavefront, while the addition of more seed points can result in more complicated patterns. The approach preserves the main features of a true activation map and contains distinct points of initial activation. This approach is similar to that of a Huygen's wavefront theory based on the propagation of wavefronts in space where conduction is considered to be isotropic. Okajima, Fujino, Kobayashi & Yamada (1968) used this theory to specify the activation process of a block of tissue depending on its distance from all neighbouring active regions.

The activation field shown in Figure 4.6 was created from two seed points (represented by purple spheres) located near the left and right epicardial free walls. The seed near the right ventricular



free wall was located further away resulting in a slight delay in activation compared to the other seed point.

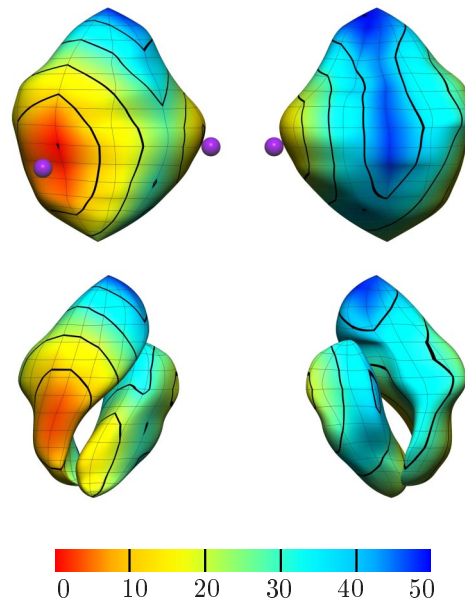


**Figure 4.6:** Cardiac source activation field (ms) generated from two activation seed points, shown by purple spheres. The colour field represents activation times up to 50 ms, with red being earliest activation and blue being latest activation. The anterior surfaces are shown on the left and the posterior on the right. The endocardial surfaces in the bottom row have been displaced below the epicardial surfaces in the top row for display purposes.

#### 4.6.5 Experimentally Derived Activation Profile

An experimentally derived heart source provided an attempt to test the computational algorithms with a cardiac source which closely represented cardiac activity in reality. The experimental procedure, outlined in Nash et al. (2000b), was used to obtain *in-vivo* data. The experimental procedure recorded concurrent epicardial, and torso surface potential recordings in domestic pigs. This is achieved through the use of a sock around the ventricles, a basket catheter within the ventricles and a vest on the torso surface, although, to date, these have not been obtained concurrently. The elastic sock (Biomedical Instruments Designers, Montreal) contained 127 unipolar stainless steel electrodes with intra-electrode spacing of approximately 5–10 mm. The Mercator High Density Array Catheter (Cardiac Pathways Corporation 2000), with 64 electrodes on eight flexible arms was used to obtain endocardial measurements and the custom elastic vest with 256 electrodes at a spacing of approximately 15 mm was placed over the torso surface.



Endocardial recordings could not be reliably obtained, therefore the data set contained only epicardial and torso surface potential recordings. For this data set, heart and torso geometries were not accurately obtained, and as such, the data could not be directly used for forward or inverse analysis. For use in the activation inverse approaches, the activation times must be known on the endocardial surfaces as well. The cardiac source was therefore constructed using a combination of the inverse procedures described in Section 6.3 and the fitting process described in Section 3.2.

The fitting procedure of Section 3.2 was used to recreate the information provided by the epicardial sock. To obtain the locations of the epicardial electrodes, the chest of the pig was re-opened and as many electrodes as possible (approximately 40%) were digitised using a FARO Arm (Faro Technologies Incorporated 2000) mechanical digitiser. The remaining unknown epicardial electrode locations were estimated using the predefined electrode topography of the epicardial sock. The electrodes were aligned with the generic heart using known landmarks such as the LAD, and then orthogonally projected onto the epicardial surface. The RMS distances of projecting the measured electrode positions onto the generic heart mesh was 0.6 mm.

Using the linear field fitting procedure described in Section 3.2 a full potential field was created for the epicardial surface. Figure 4.7 shows the experimentally recorded and the fitted signals at four locations on the epicardial surface. Due to inaccuracies in the geometric locations of the electrodes and the complex nature of epicardial potentials the fitting procedure was unable to exactly represent the measured potentials, with the most obvious location in the areas of high gradients.

Activation times were determined to lie at the maximum negative downstroke calculated using a moving finite difference scheme. The presence of multiple downstrokes in the epicardial signals may lead to some errors in determining the activation time. The effect of these errors are further discussed in Section 7.7. It should be noted, however, that the activation times for the fitted and original data have been largely unaffected for this data set.

Using a combination of the linear field fitting procedure outlined in Section 3.2 and the activation inverse procedure described in Chapter 6, the activation field on the entire epicardial surface and the endocardial surface was derived. The full fitted field on the epicardial surface is shown in Figure 3.4, while the activation field on both surfaces used in the inverse simulations in Section 6.4.2 and Section 7.6 is shown in Figure 4.8.

By comparing the fitted activation field at the electrode locations with experimentally recorded signals, there was an RMS error of 1.5 ms and a similarity index of 0.95. The range of the recorded

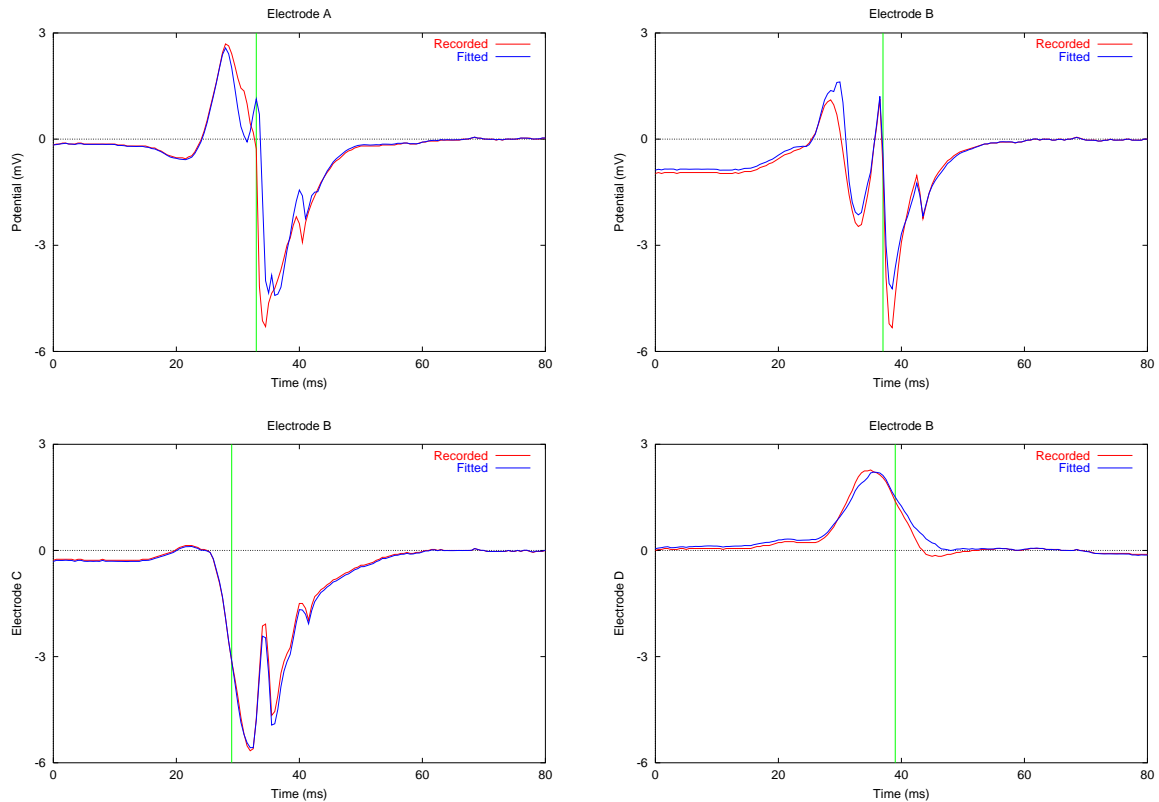


**Figure 4.7:** Potential traces from four typical electrodes, A–D, recorded from the epicardial sock (red) and their fitted representations (blue). The activation time, shown by the vertical green line, was determined from the maximum negative slope, calculated using a moving finite difference interval. This remains relatively constant between the fitted and raw signals. The fitted activation field from the 127 electrodes along with the locations of electrodes A–D is shown in Figure 3.4.

activation times at the electrodes was 16 ms compared with 15 ms for the entire fitted field. This showed that the fitted field provided an accurate representation of the recorded *in-vivo* data. The activation duration for the entire field is 20 ms compared to 15 ms for the duration of epicardial surface as measured experimentally.

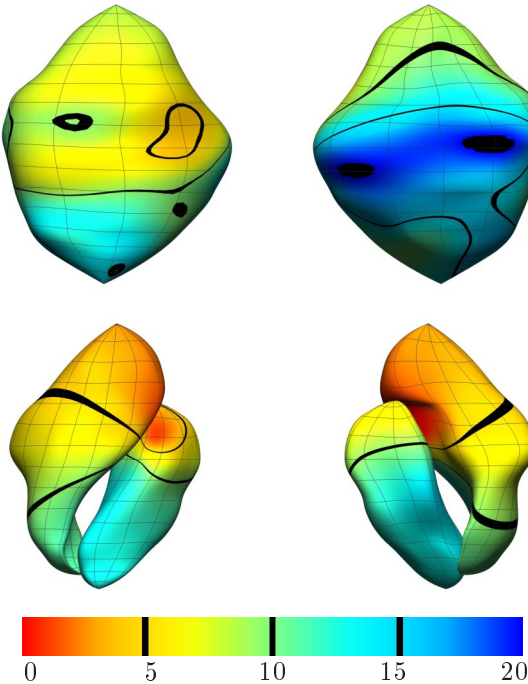


**Figure 4.8:** Experimental activation field (ms) derived from experimental data measured directly on the epicardial surface shown in Figure 3.4. Layout as described in Figure 4.6.



# 5 *The Forward Problem of Electrocardiology*

Computation of the linear relationship between measured potentials at the body surface and an appropriate cardiac source constitutes the forward problem of electrocardiology. The ultimate goal of the theory and models developed in this thesis is in the study of the clinically useful inverse problem of electrocardiology. However, accurately solving the forward problem is the first step of such a task.

The two predominant inverse source formulations are the epicardial potential and myocardial activation source formulations. Although both attempt to obtain an electrical image of the heart, each of their solutions are distinctly different.

The sources of torso surface potentials are largely confined to the heart and quasi-static conditions apply, since capacitive and inductive effects of the passive torso organs are insignificant (Plonsey 1969). Therefore, a generalised Laplace's equation is used to model the electrical activity in the regions external to the heart. The epicardial potential formulations model the passive electrical events from the epicardium through to the torso surface. The potentials on the body surface can be non-invasively measured while those on the epicardium are generally unknown but provide a clearer indication of the electrical activity occurring within the heart.

An alternative source formulation involves the activation times within the myocardium. These are more directly related to the actual sources which generate the torso surface potentials. Using the bidomain concept the source can be expressed in terms of the gradient of the transmembrane potential (Yamashita & Geselowitz 1985).

## 5.1 Governing Equations

A two-dimensional transverse slice through the torso is shown in Figure 5.1, identifying the main regions which are of interest from an electrocardiographic viewpoint. Illustrated from the centre of the schematic are the two ventricular blood masses surrounded by the myocardium, the two lungs and the outer torso surface. All regions, except for the myocardium, were assumed to be electrically passive.

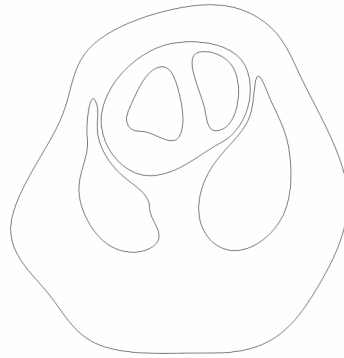


**Figure 5.1:** A transverse slice through a pig torso at heart level. Shown, from the centre of the diagram, are the left and right endocardial, epicardial, left and right lung and the skin surfaces.

The problems of electrocardiology, and other electro-magnetic problems, are governed by Maxwell's equations

$$\nabla \times \mathbf{E} + \frac{\partial \mathbf{B}}{\partial t} = 0 \quad (5.1)$$

$$\nabla \times \mathbf{H} - \frac{\partial \mathbf{D}}{\partial t} = \mathbf{J} \quad (5.2)$$

where  $\mathbf{E}$  is the electric field intensity,  $\mathbf{B}$  is the magnetic induction,  $\mathbf{H}$  is the magnetic field intensity,  $\mathbf{D}$  is electric displacement and  $\mathbf{J}$  is the current density.

These equations can be simplified by taking into account the electrical properties of biological tissues and the nature of heart cycles. The properties of the passive regions of biological tissue mean that inductive, capacitative and propagation effects can be ignored. This means that the problem can be thought of as being *quasi-static* (Plonsey 1969) with the torso approximated as a passive volume conductor. In practice, respiratory motion and physical movement will result in electrical activity in the skeletal muscle. The effects of these additional electrical sources are minimised by lying in a relaxed state when electrical recordings are being made and are assumed to be negligible.

Neglecting the effects of the time dependent terms results in

$$\frac{\partial \mathbf{B}}{\partial t} = 0 \quad \frac{\partial \mathbf{D}}{\partial t} = 0 \quad (5.3)$$

The current density  $\mathbf{J}$  can be found from the sum of any conductive currents and any impressed currents in that region, *i.e.*,

$$\mathbf{J} = \boldsymbol{\sigma} \mathbf{E} + \mathbf{J}_i \quad (5.4)$$

where  $\boldsymbol{\sigma}$  is the conductivity tensor of the surrounding tissue and  $\mathbf{J}_i$  is the impressed source current density.

As  $\mathbf{J}$  is solenoidal due to the conservation of current, taking the divergence of both sides of Equation (5.4) and using current conservation, results in

$$\begin{aligned} \nabla \cdot \mathbf{J} &= \nabla \cdot (\boldsymbol{\sigma} \mathbf{E} + \mathbf{J}_i) \\ &= 0 \end{aligned} \quad (5.5)$$

From Narayana (1972), the electric field is irrotational and conservative (*i.e.*,  $\nabla \times \mathbf{E} = 0$ ) and there must be an electric potential scalar  $\phi$  that satisfies the equation,

$$\nabla \phi = -\mathbf{E} \quad (5.6)$$

Substituting Equation (5.6) into Equation (5.5) results in the Poisson equation

$$\nabla \cdot (\boldsymbol{\sigma} \nabla \phi) = -\nabla \cdot \mathbf{J}_i \quad (5.7)$$

### 5.1.1 Generalised Laplace's Equation

By considering regions external to the epicardium and assuming that there are no current sources from skeletal muscle or other external sources (*i.e.*,  $\mathbf{J}_i = 0$ ), the Poisson equation specified in Equation (5.7) collapses to a generalised Laplace's equation

$$\nabla \cdot (\boldsymbol{\sigma} \nabla \phi) = 0 \quad (5.8)$$

Equation (5.8) is the governing equation for the epicardial potential based formulations for the problems of electrocardiology.

### 5.1.2 Poisson Equation

By using an activation based formulation, it is necessary to model the electrical activity within the myocardium as well. The bidomain source model (Henriquez 1993) is the basis of this formulation. The micro-structure of cardiac muscle is comprised of coupled cells enveloped by collagen, fluid and blood vessels. The bidomain model takes a continuous approach and represents groups of cells as discrete points, each with a portion of intracellular space and extracellular space. Quasi-static assumptions and Ohm's Law imply that the current density at all bidomain locations must satisfy

$$\mathbf{J} = -\boldsymbol{\sigma}_i \nabla \phi_i - \boldsymbol{\sigma}_e \nabla \phi_e \quad (5.9)$$

where  $\boldsymbol{\sigma}_i$  and  $\boldsymbol{\sigma}_e$  are the conductivity tensors of the intra- and extracellular space and  $\phi_i$  and  $\phi_e$  are the intra- and extracellular potentials.

The Poisson equation defined in Equation (5.7) has its source term derived from the transmembrane potential which is defined as the potential difference between the intra- and extracellular spaces (*i.e.*,  $\phi_m = \phi_i - \phi_e$ ). A temporally varying transmembrane potential (or action potential) of a single cardiac cell, as shown in Figure 1.4, is well documented by experiments and computational models which numerically simulate the activity of a cell. These models range from being simple empirical models (Hunter, McNaughton & Noble 1975) to detailed ionic current models (Beeler & Reuter 1977, Luo & Rudy 1994, Noble, Varghese, Kohl & Noble 1998).

By using Equation (5.5) and substituting the definition of the transmembrane potential into Equation (5.9), the bidomain equation is given by

$$\nabla \cdot [(\boldsymbol{\sigma}_i + \boldsymbol{\sigma}_e) \nabla \phi_e] = -\nabla \cdot (\boldsymbol{\sigma}_i \nabla \phi_m) \quad (5.10)$$



### 5.1.3 Boundary Conditions

The boundary conditions for the forward and inverse problems are prescribed potentials on the body and/or the heart surface, and no current (flux) leaving the body surface, *i.e.*,

$$\phi_H = f(\mathbf{x}, t) \quad \text{on } \Gamma_H \quad (5.11)$$

$$\phi_B = g(\mathbf{y}, t) \quad \text{on } \Gamma_B \quad (5.12)$$

$$\frac{\partial \phi_B}{\partial \mathbf{n}} = 0 \quad \text{on } \Gamma_B \quad (5.13)$$

$$\phi_B(\mathbf{y}_i) = 0 \quad \text{on } \Gamma_B \quad (5.14)$$

where  $\phi_H$  are the potentials located on the heart,  $\phi_B$  are the potentials on the torso surface,  $t$  is a measure of time,  $\mathbf{x}$  are points located on the heart surface  $\Gamma_H$ ,  $\mathbf{y}$  are points located on the torso surface  $\Gamma_B$ ,  $\mathbf{y}_i$  is a point on the torso surface chosen to be the reference potential and  $\mathbf{n}$  is the outward normal direction.

If the problem is modelled using activation source model and Equation (5.10) is solved then there is an additional boundary condition that restricts the transmembrane potential to the myocardium

$$\frac{\partial \phi_m}{\partial \mathbf{n}} = 0 \quad \text{on } \Gamma_H \quad (5.15)$$

In most cases, only the torso surface potential values for Equation (5.12) are known and the heart potentials in Equation (5.11) are unknown. A no flux boundary condition can be imposed on the torso surface/air interface as the conductivity of the air is effectively zero. Equation (5.14) corresponds to a location on the torso surface to which all other potential values are referenced. In the simulations in this thesis, the reference point is taken to be the near the right hip, which is the common position used for right leg grounding in electrocardiographic recordings.

## 5.2 Coupling Regions

When modelling organs with distinctly different material or physical properties, it is convenient to model each organ as distinct *regions*. These regions can then be modelled using the appropriate numerical methods and assigned appropriate conductivity values.

Regions such as the myocardium and skeletal muscle contain a complex fibre distribution which greatly affect its electrical properties while regions such as the blood masses and the lungs can be approximated as having homogeneous conductivities. The anisotropic nature of these regions can be explicitly modelled using the FEM. To ensure continuity of current and potentials at the interface between each region, continuity conditions are placed upon the nodes on these surfaces. Such a method was employed by Bradley et al. (1997) for the coupled FEM/BEM human torso, which used boundary elements to model isotropic regions and finite elements to model the anisotropic skeletal muscle regions. At this stage, isotropic material properties are assumed throughout and all regions are modelled using BEM so all coupling involves a BEM-BEM interface. This is because there is currently no detailed fibre information for the skeletal muscle or the myocardium of a pig model and introducing anisotropy in the myocardium greatly increases the complexity of the problem.

In each boundary element region  $r$ , a system of equations can be constructed in the form

$$\mathbf{P}_r \boldsymbol{\phi}_r = \mathbf{Q}_r \mathbf{q}_r \quad (5.16)$$

where the vector  $\boldsymbol{\phi}_r$  contains the unknown node based potentials in region  $r$ , and  $\mathbf{q}_r$  the unknown normal currents (fluxes), and  $\mathbf{P}$  and  $\mathbf{Q}$  are the boundary element potential and flux matrices.

Consider a domain consisting of two annuli. The first region, shown as dark grey in Figure 5.2, covers the space surrounded by the inner circle defined by nodes 1–8. The second annulus, shown in Figure 5.2 unshaded, is defined by nodes 5–12.

The systems in each of the two regions shown in Figure 5.2, modelled using linear basis functions, can be written as

$$\mathbf{P}_1 \begin{bmatrix} \phi_1^1 \\ \vdots \\ \phi_1^8 \end{bmatrix} = \mathbf{Q}_1 \begin{bmatrix} q_1^1 \\ \vdots \\ q_1^8 \end{bmatrix} \quad \text{and} \quad \mathbf{P}_2 \begin{bmatrix} \phi_2^5 \\ \vdots \\ \phi_2^{12} \end{bmatrix} = \mathbf{Q}_2 \begin{bmatrix} q_2^5 \\ \vdots \\ q_2^{12} \end{bmatrix} \quad (5.17)$$

where  $\mathbf{P}_r$  and  $\mathbf{Q}_r$  are the boundary element potential and flux matrices for region  $r$  and  $\phi_r^n$  and  $q_r^n$  are the potential and flux nodal values for region  $r$  and global node  $n$ .

By adopting a global numbering system for the entire problem any number of  $r$  matrices can be

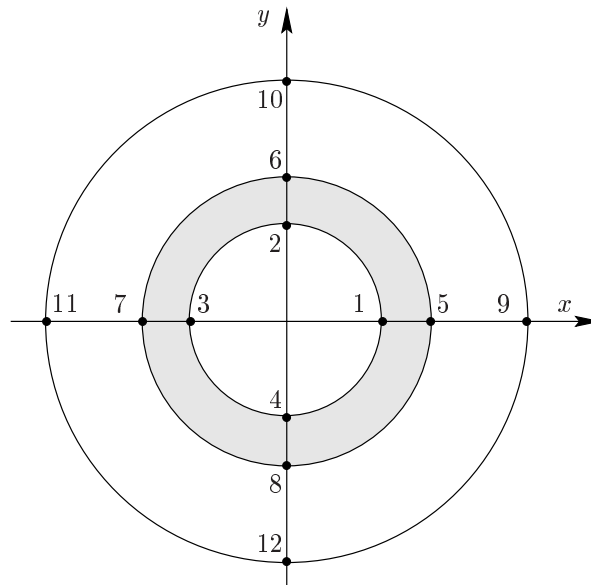


**Figure 5.2:** Coupling of two boundary element regions. The first region is the shaded annulus and is defined by nodes 1–8. The second annulus is defined by nodes 5–12. The regions are coupled by setting continuity conditions on the normal currents and potentials on the nodes at the interface surfaces (i.e., nodes 5–8).

assembled into a single set of matrix equations of the form

$$\mathbf{P}_{\text{global}} \boldsymbol{\phi} = \mathbf{Q}_{\text{global}} \mathbf{q} \quad (5.18)$$

where the global matrices contain the  $\mathbf{P}_r$  and  $\mathbf{Q}_r$  sub-matrix blocks which are fully populated and unsymmetric.

For the example shown in Figure 5.2, there are 32 unknowns (a total of 16 nodes in all regions, each with two DOF) and only 16 equations. In order to reduce the number of unknowns and couple the two regions together the interface conditions for potential and current are used.

$$\phi_1^n = \phi_2^n \quad (5.19)$$

$$q_1^n = -q_2^n \quad (5.20)$$

for nodes,  $n = 5, \dots, 8$ .

By applying boundary conditions involving potential or normal current to the 8 boundary nodes,

the system is reduced to a standard  $16 \times 16$  system of the form

$$\mathbf{R}\mathbf{u} = \mathbf{s} \quad (5.21)$$

where  $\mathbf{R}$  is the reduced global matrix,  $\mathbf{u}$  is the vector of global unknowns and  $\mathbf{s}$  is the known RHS vector.

### 5.3 Transfer Matrices From a Boundary Element Point of View

Three different, but consistent, transfer matrices can be generated which map potentials between different surfaces within the torso. Two map from transmembrane potentials to epicardial or torso surface potentials. The third transfer matrix maps potentials from the epicardial surface to the torso surface. These transfer matrices are able to provide consistent potentials throughout the torso given a single heart source (*i.e.*, from an activation heart source, corresponding epicardial and torso surface potentials are able to be produced) to enable direct comparison between the potential and activation based inverse approaches.

The partial differential equation defined in Equation (5.10) can be solved using a weighted residuals approach with  $w$  a (as yet unspecified) weighting function. Then, from weighted residuals

$$\int_{\Omega_H} \nabla \cdot ([\boldsymbol{\sigma}_i + \boldsymbol{\sigma}_e] \nabla \phi_e) w d\Omega + \int_{\Omega_H} \nabla \cdot (\boldsymbol{\sigma}_i \nabla \phi_m) w d\Omega = 0 \quad (5.22)$$

where  $\Omega_H$  is the domain of the heart (*i.e.*, the myocardium).

Using Green's theorem gives

$$\int_{\Gamma_H} w [\boldsymbol{\sigma}_i + \boldsymbol{\sigma}_e] \nabla \phi_e \cdot \mathbf{n} d\Gamma - \int_{\Omega_H} [\boldsymbol{\sigma}_i + \boldsymbol{\sigma}_e] \nabla \phi_e \cdot \nabla w d\Omega + \int_{\Omega_H} \nabla \cdot (\boldsymbol{\sigma}_i \nabla \phi_m) w d\Omega = 0 \quad (5.23)$$

where  $\mathbf{n}$  is the unit outward normal and  $\Gamma_H$  are the surfaces of the heart.

Applying Green's theorem to the second integral again gives

$$\begin{aligned} \int_{\Gamma_H} w [\boldsymbol{\sigma}_i + \boldsymbol{\sigma}_e] \nabla \phi_e \cdot \mathbf{n} d\Gamma - \int_{\Gamma_H} \phi_e [\boldsymbol{\sigma}_i + \boldsymbol{\sigma}_e] \nabla w \cdot \mathbf{n} d\Gamma \\ + \int_{\Omega_H} \nabla \cdot ([\boldsymbol{\sigma}_i + \boldsymbol{\sigma}_e] \nabla w) \phi_e d\Omega + \int_{\Omega_H} \nabla \cdot (\boldsymbol{\sigma}_i \nabla \phi_m) w d\Omega = 0 \quad (5.24) \end{aligned}$$

This is the standard boundary integral equation for Poisson's equation with a general source term. For the special case of the source being given by  $-\nabla \cdot (\boldsymbol{\sigma}_i \nabla \phi_m)$  it is possible to apply a similar procedure to that above on this term, *i.e.*,

$$\begin{aligned} \int_{\Omega_H} \nabla \cdot (\boldsymbol{\sigma}_i \nabla \phi_m) w d\Omega &= \int_{\Gamma_H} w \boldsymbol{\sigma}_i \nabla \phi_m \cdot \mathbf{n} d\Gamma - \int_{\Omega_H} \boldsymbol{\sigma}_i \nabla \phi_m \cdot \nabla w d\Omega \\ &= \int_{\Gamma_H} w \boldsymbol{\sigma}_i \nabla \phi_m \cdot \mathbf{n} d\Gamma - \int_{\Gamma_H} \phi_m \boldsymbol{\sigma}_i \nabla w \cdot \mathbf{n} d\Gamma \\ &\quad + \int_{\Omega_H} \nabla \cdot (\boldsymbol{\sigma}_i \nabla w) \phi_m d\Omega \quad (5.25) \end{aligned}$$

Substituting Equation (5.25) into Equation (5.24) results in

$$\begin{aligned} \int_{\Gamma_H} w [\boldsymbol{\sigma}_i + \boldsymbol{\sigma}_e] \nabla \phi_e \cdot \mathbf{n} d\Gamma - \int_{\Gamma_H} \phi_e [\boldsymbol{\sigma}_i + \boldsymbol{\sigma}_e] \nabla w \cdot \mathbf{n} d\Gamma \\ + \int_{\Omega_H} \nabla \cdot ([\boldsymbol{\sigma}_i + \boldsymbol{\sigma}_e] \nabla w) \phi_e d\Omega + \int_{\Gamma_H} w \boldsymbol{\sigma}_i \nabla \phi_m \cdot \mathbf{n} d\Gamma \\ - \int_{\Gamma_H} \phi_m \boldsymbol{\sigma}_i \nabla w \cdot \mathbf{n} d\Gamma + \int_{\Omega_H} \nabla \cdot (\boldsymbol{\sigma}_i \nabla w) \phi_m d\Omega = 0 \quad (5.26) \end{aligned}$$

which is a generalisation of Equation 31 from (Yamashita & Geselowitz 1985).

To this point, no assumptions have been made on  $w$ ,  $\boldsymbol{\sigma}_i$  or  $\boldsymbol{\sigma}_e$  (apart from differentiability and integrability) so Equation (5.26) is totally general. Yamashita & Geselowitz (1985) assumed that

$w$  was a Green's function satisfying

$$\nabla \cdot ([\boldsymbol{\sigma}_i + \boldsymbol{\sigma}_e] \nabla w) + \delta(\mathbf{x}_0) = 0 \quad (5.27)$$

and

$$\boldsymbol{\sigma}_e \nabla w \cdot \mathbf{n} = 0 \text{ on } \Gamma_B \quad (5.28)$$

where  $\delta(\mathbf{x}_0)$  is the Dirac delta distribution centred at a point  $\mathbf{x}_0$  within the torso and  $\Gamma_B$  is the surface of the torso. This resulted in the removal of the first volume integral in Equation (5.26).

In practice, such a Green's function for the heart cannot be found analytically, since both  $\boldsymbol{\sigma}_i$  and  $\boldsymbol{\sigma}_e$  are in general anisotropic and inhomogeneous. By assuming that they are homogeneous, both conductivity tensors can be represented by constant  $3 \times 3$  matrices, which are diagonal in the coordinate system defined by the myocardial fibres and sheets. The fibre and sheet orientation in the heart is very complex and this anisotropy means that it is not possible to solve Equation (5.27) analytically, even under the assumption of equal anisotropy ratios. This is true irrespective of whether a proper Green's function is used (*i.e.*, impose Equation (5.28)) or merely look for a freespace Green's function (also known as a fundamental solution) which is a solution of Equation (5.27) with appropriate boundary conditions at infinity (*i.e.*, the no-flux condition on  $\Gamma_B$  is ignored).

By further assuming that the heart domain is isotropic in both the extra and intracellular domains, it is possible to apply a standard boundary element procedure to Equation (5.26). For this  $w$  is taken to be the freespace Green's function, *i.e.*, a solution of

$$\nabla \cdot (\nabla w) + \delta(\mathbf{x}_0) = 0 \quad (5.29)$$

where  $\mathbf{x}_0$  is now an arbitrary point in space and  $w$  vanishes at infinity. In three-dimensions, the solution of this equation is

$$w(\mathbf{x}, \mathbf{x}_0) = \frac{1}{4\pi R} \quad (5.30)$$

where  $R = \|\mathbf{r}\|_2 = \|\mathbf{x} - \mathbf{x}_0\|_2$  is the distance measured from  $\mathbf{x}_0$ .

With  $w$  defined in Equation (5.30),  $\mathbf{x}$  inside  $\Omega_H$  and assuming material isotropy (*i.e.*,  $\boldsymbol{\sigma}_i = \sigma_i \mathbf{I}$ ,  $\boldsymbol{\sigma}_e = \sigma_e \mathbf{I}$  and  $\sigma_i = k\sigma_e$  where  $k$  is a constant) Equation (5.29) can be used to simplify the domain

integrals in Equation (5.26) so that

$$\begin{aligned} \int_{\Omega_H} \nabla \cdot ([\boldsymbol{\sigma}_i + \boldsymbol{\sigma}_e] \nabla w(\mathbf{x}, \mathbf{x}_0)) \phi_e(\mathbf{x}) d\Omega(\mathbf{x}) &= (1+k) \sigma_e \int_{\Omega_H} \nabla \cdot (\nabla w(\mathbf{x}, \mathbf{x}_0)) \phi_e(\mathbf{x}) d\Omega(\mathbf{x}) \\ &= -(1+k) \sigma_e \phi_e(\mathbf{x}_0) \end{aligned} \quad (5.31)$$

$$\begin{aligned} \int_{\Omega_H} \nabla \cdot (\boldsymbol{\sigma}_i \nabla w(\mathbf{x}, \mathbf{x}_0)) \phi_m(\mathbf{x}) d\Omega(\mathbf{x}) &= k \sigma_e \int_{\Omega_H} \nabla \cdot (\nabla w(\mathbf{x}, \mathbf{x}_0)) \phi_m(\mathbf{x}) d\Omega(\mathbf{x}) \\ &= -k \sigma_e \phi_m(\mathbf{x}_0) \end{aligned} \quad (5.32)$$

Thus, Equation (5.26) becomes

$$\begin{aligned} (1+k) \sigma_e \int_{\Gamma_H} w(\mathbf{x}, \mathbf{x}_0) \nabla \phi_e(\mathbf{x}) \cdot \mathbf{n}(\mathbf{x}) d\Gamma(\mathbf{x}) \\ - (1+k) \sigma_e \int_{\Gamma_H} \phi_e(\mathbf{x}) \nabla w(\mathbf{x}, \mathbf{x}_0) \cdot \mathbf{n}(\mathbf{x}) d\Gamma(\mathbf{x}) - (1+k) \sigma_e \phi_e(\mathbf{x}_0) \\ + k \sigma_e \int_{\Gamma_H} w(\mathbf{x}, \mathbf{x}_0) \nabla \phi_m(\mathbf{x}) \cdot \mathbf{n}(\mathbf{x}) d\Gamma(\mathbf{x}) \\ - k \sigma_e \int_{\Gamma_H} \phi_m(\mathbf{x}) \nabla w(\mathbf{x}, \mathbf{x}_0) \cdot \mathbf{n}(\mathbf{x}) d\Gamma(\mathbf{x}) - k \sigma_e \phi_m(\mathbf{x}_0) = 0 \end{aligned} \quad (5.33)$$

The equation of more interest is the case when  $\mathbf{x}_0 \in \Gamma_H$  (*i.e.*,  $\mathbf{x}_0$  on the boundary of the domain). To derive this equation,  $\mathbf{x}_0$  is considered to be at a smooth point on the boundary of  $\Omega_H$  and a hemispherical region of radius  $\varepsilon$  centred at  $\mathbf{x}_0$  constructed.  $\Omega'_H$  was defined to be the extended region (*i.e.*,  $\Omega_H$  plus the hemispherical region). Then  $\mathbf{x}_0$  is interior to  $\Omega'_H$  so Equation (5.33) is valid with  $\Gamma_H$  replaced by  $\partial\Omega'_H$ . If this equation is considered as  $\lim_{\varepsilon \downarrow 0}$ , if  $\Gamma_\varepsilon$  is the boundary of the hemispherical region, and  $\Gamma_{-\varepsilon}$  the boundary of that part of  $\Omega_H$  that is outside the hemisphere (so

$\partial\Omega'_H = \Gamma_\epsilon \cup \Gamma_{-\epsilon}$ ) then as long as the surface at  $\mathbf{x}_0$  has a unique tangent plane

$$\begin{aligned} \lim_{\epsilon \downarrow 0} \int_{\Gamma_\epsilon} \phi_e(\mathbf{x}) \nabla w(\mathbf{x}, \mathbf{x}_0) \cdot \mathbf{n}(\mathbf{x}) d\Gamma(\mathbf{x}) &= \lim_{\epsilon \downarrow 0} \frac{-1}{4\pi R^2} 2\pi R^2 \phi_e(\gamma) \\ &= -\frac{\phi_e(\mathbf{x}_0)}{2} \end{aligned} \quad (5.34)$$

where  $\gamma$  is some point on the hemisphere of radius  $\epsilon$  and the mean value theorem has been applied.

Similarly,

$$\begin{aligned} \lim_{\epsilon \downarrow 0} \int_{\Gamma_\epsilon} \phi_m(\mathbf{x}) \nabla w(\mathbf{x}, \mathbf{x}_0) \cdot \mathbf{n}(\mathbf{x}) d\Gamma(\mathbf{x}) &= \lim_{\epsilon \downarrow 0} \frac{-1}{4\pi R^2} 2\pi R^2 \phi_m(\gamma) \\ &= -\frac{\phi_m(\mathbf{x}_0)}{2} \end{aligned} \quad (5.35)$$

It can also be shown that

$$\lim_{\epsilon \downarrow 0} \int_{\Gamma_\epsilon} w(\mathbf{x}, \mathbf{x}_0) \nabla \phi_e(\mathbf{x}) \cdot \mathbf{n}(\mathbf{x}) d\Gamma(\mathbf{x}) = 0 \quad (5.36)$$

and

$$\lim_{\epsilon \downarrow 0} \int_{\Gamma_\epsilon} w(\mathbf{x}, \mathbf{x}_0) \nabla \phi_m(\mathbf{x}) \cdot \mathbf{n}(\mathbf{x}) d\Gamma(\mathbf{x}) = 0 \quad (5.37)$$

As  $\lim_{\epsilon \downarrow 0} \Gamma_{-\epsilon} \rightarrow \Gamma_H$  and while the integrands are singular when  $\mathbf{x}_0$  is on  $\mathbf{x}$ , the integrals exist in the standard sense, so

$$\lim_{\epsilon \downarrow 0} \int_{\Gamma_{-\epsilon}} (\text{each integrand}) d\Gamma = \int_{\Gamma_H} (\text{same integrand}) d\Gamma \quad (5.38)$$

Substituting Equations (5.34)–(5.38) into Equation (5.33) and dividing through by  $(1+k)\sigma_e$ , the



general boundary integral equation is defined as

$$\begin{aligned}
& c(\mathbf{x}_0) \phi_e(\mathbf{x}_0) + \int_{\Gamma_H} \phi_e(\mathbf{x}) \nabla w(\mathbf{x}, \mathbf{x}_0) \cdot \mathbf{n}(\mathbf{x}) d\Gamma(\mathbf{x}) \\
& + \frac{k}{1+k} c(\mathbf{x}_0) \phi_m(\mathbf{x}_0) + \frac{k}{1+k} \int_{\Gamma_H} \phi_m(\mathbf{x}) \nabla w(\mathbf{x}, \mathbf{x}_0) \cdot \mathbf{n}(\mathbf{x}) d\Gamma(\mathbf{x}) \\
& = \int_{\Gamma_H} \frac{w(\mathbf{x}, \mathbf{x}_0)}{\sigma_i + \sigma_e} q_e(\mathbf{x}) d\Gamma(\mathbf{x}) + \frac{k}{1+k} \int_{\Gamma_H} w(\mathbf{x}, \mathbf{x}_0) \nabla \phi_m(\mathbf{x}) \cdot \mathbf{n}(\mathbf{x}) d\Gamma(\mathbf{x}) \quad (5.39)
\end{aligned}$$

where

$$c(\mathbf{x}_0) = \begin{cases} 1 & \text{if } \mathbf{x}_0 \in \Omega_H \\ \frac{1}{2} & \text{if } \mathbf{x}_0 \in \Gamma_H \text{ and } \Gamma_H \text{ smooth at } \mathbf{x}_0 \\ \frac{\text{internal solid angle}}{4\pi} & \text{if } \mathbf{x}_0 \in \Gamma_H \text{ and } \Gamma_H \text{ not smooth at } \mathbf{x}_0 \\ 0 & \text{if } \mathbf{x}_0 \text{ outside } \Omega_H \end{cases} \quad (5.40)$$

and  $q_e(\mathbf{x}) = \nabla \phi_e(\mathbf{x}) \cdot \mathbf{n}(\mathbf{x})$  is the extracellular normal current at the point  $\mathbf{x}$ .

Equation (5.39) relates  $\phi_e$  and  $\phi_m$  at the point  $\mathbf{x}_0$  to the values of  $\phi_e$ ,  $\phi_m$ ,  $q_e$  and  $\nabla \phi_m \cdot \mathbf{n}$  everywhere on  $\Gamma_H$ . On  $\Gamma_H$ ,  $\nabla \phi_m \cdot \mathbf{n}$  is 0 since transmembrane potentials are confined to the heart, which removes the last integral in Equation (5.39).

External to the heart, there are assumed to be no electrical sources so the governing equation collapses from a Poisson equation to the generalised Laplace's equation defined in Equation (5.8).

Continuity of extracellular potential and current across the myocardial boundaries provides the links between Equation (5.8) and Equation (5.39). In the usual way, it is possible to discretise the boundaries of all regions involved and assemble the following matrices, as described in Section 5.2

$$\begin{pmatrix} \text{all coefficients} \\ \text{of potentials from} \\ \text{Equation (5.39)} \\ \text{and Equation (5.8)} \end{pmatrix} \begin{pmatrix} \phi_m \\ \phi_e^H \\ \phi_e^1 \\ \vdots \\ \phi_e^N \end{pmatrix} = \begin{pmatrix} \text{all coefficients} \\ \text{of currents from} \\ \text{Equation (5.39)} \\ \text{and Equation (5.8)} \end{pmatrix} \begin{pmatrix} \mathbf{q}_e^H \\ \mathbf{q}_e^1 \\ \vdots \\ \mathbf{q}_e^N \end{pmatrix} \quad (5.41)$$

where

- $N$  is the number of tissue regions outside the heart
- $\phi_e^i$  is a vector of nodal values of  $\phi_e$  in region  $i$
- $\phi_m$  is a vector of nodal values of  $\phi_m$  on the heart
- $\phi_e^H$  is a vector of nodal values of  $\phi_e$  on the heart
- $\mathbf{q}_e^i$  is a vector of nodal values of  $q_e$  on the surface of region  $i$
- $\mathbf{q}_e^H$  is a vector of nodal values of  $q_e$  on the heart surface

The coefficient matrices include all the continuity constraints. Also, since  $\frac{\partial \phi_m}{\partial \mathbf{n}}$  is 0 on  $\Gamma_H$ , this term is not present in Equation (5.41). It is worth noting that the coefficients of  $\phi_m$  in Equation (5.39) are just  $\frac{k}{k+1}$  times the coefficients of  $\phi_e$  in that equation. Use of this fact allows the speed up of the assembly of Equation (5.41).

Equation (5.41) can be considered to be an implicit relationship between the transmembrane potentials  $\phi_m$  and the torso potentials  $\phi_B$ . To construct an explicit transfer matrix,  $\mathbf{A}$ , use is made of the definition of the transfer matrix, *i.e.*,

$$\phi_B = \mathbf{A}\phi_m \quad (5.42)$$

Using this relationship,  $\phi_m$  can be set to be the vector  $e_k$  (*i.e.*, a unit vector that is zero everywhere except at the  $k^{\text{th}}$  position) and Equation (5.41) solved. The resulting solution for  $\phi_B$  corresponds to the  $k^{\text{th}}$  column of  $\mathbf{A}$ . Alternatively the transfer matrix which maps from  $\phi_m$  through to  $\phi_e^H$  can be constructed by suitable rearrangement of Equation (5.41).

The construction of the transfer matrix described previously has assumed homogeneity and isotropy in the myocardium from Equation (5.31) onwards. It is worth pointing out that the assumptions of homogeneity and isotropy are not required to use the activation imaging algorithm of Huiskamp & Greensite (1997). It is also possible to construct a transfer matrix relating activation times to torso potentials without these assumptions. However, the transfer matrix construction under anisotropic conditions becomes significantly more difficult. The bidomain equations (or a weak form of them, such as that given in Equation (5.26)) have to be solved throughout the heart (using some volume-discretisation procedure representing the full myocardial-fibre orientation) and coupled to solutions of Equation (5.8) outside the heart. This dramatically increases the problem size. Work on this is progressing (*e.g.*, Pullan & Buist 1998, Buist & Pullan 2001) but at this stage homogeneity and isotropy is assumed.

## 5.4 Activation Function

The transfer matrix described in Section 5.3 is capable of mapping from heart transmembrane potentials to torso surface potentials. To relate the torso surface potentials directly to the underlying activation wavefront, an additional mapping from transmembrane potentials to activation times (or *vice versa*) is required. To achieve this mapping the underlying physiology of an ventricular action potential is modelled.

The activation phase of a normal ventricular action potential contains a sharp region of depolarisation which corresponds to the time at which the activation wave passes that point (*i.e.*, the activation times). By assigning an activation time to each node on the heart surface, transmembrane potentials can be calculated using an arctan function (Tilg 1998) or via the Heaviside step function

$$\phi_m = a + bH(t - \tau(\mathbf{x})) \quad (5.43)$$

where  $t$  is the current solution time step and  $\tau(\mathbf{x})$  is the activation time at a point on the heart surface,  $a$  is the resting transmembrane potential and  $b$  is the height of the transmembrane jump.

Shown in Figure 5.3 is a comparison between the ventricular action potential (solid line) and its Heaviside step function approximation overlaid with a dashed line.

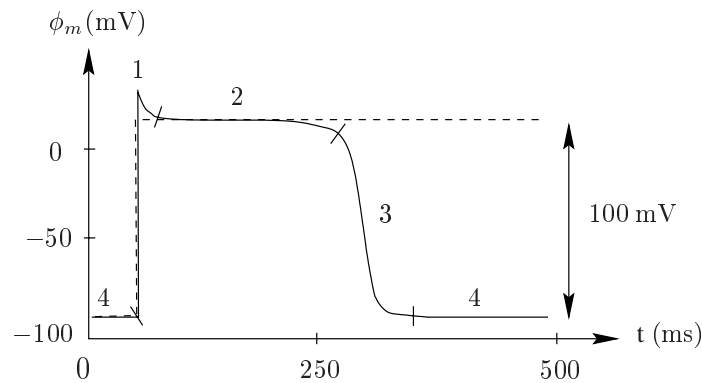


**Figure 5.3:** A schematic ventricular action potential (solid line) and the Heaviside approximation (dashed line). The four phases of the action potential are labelled; 1: upstroke, 2: plateau, 3: recovery, 4: rest. The resting potential is typically around -80 mV and this rises to a peak of approximately 20 mV (*i.e.*, a transmembrane jump of approximately 100 mV). The duration of the entire action potential typically lasts for 300 ms.

The Heaviside step function models an elementary source at a point on the heart surface  $\mathbf{x}$ , activated at time  $\tau(\mathbf{x})$  which remains activated until the entire domain has been activated. Since only the QRS interval of the ECG is modelled (*i.e.*, the activation phase) in this thesis the recovery phase

(phase 3) of the action potential was not considered. Ventricular repolarisation can be modelled using a similar process but calculating recovery times instead of activation times. However, the modelling of ventricular repolarisation introduces the additional complications of the mechanical motion of the heart. During the recovery stage of the cardiac cycle the geometry of the ventricles cannot be assumed to be fixed. Also, as shown in Figure 5.3, repolarisation occurs over a relatively long time period so it is difficult to define a distinct recovery time unlike the activation time which is defined by a sharp upstroke.

If the sources are switched ‘on’ at discrete locations on the heart surface (*i.e.*, the nodal positions), then the resultant simulated potentials are discontinuous. This gives rise to body surface potentials that are not continuous with respect to the activation times. For use in the optimisation phase of the activation inverse procedure (see Section 6.3.1) it is more desirable to deal with functions which are continuous and the speed of convergence is greatly aided by continuous derivatives as well (Huiskamp & van Oosterom 1988).

To account for this, Equation (5.43) was approximated by the sigmoid function,  $S(t - \tau)$  shown in Figure 5.4. This results in values of  $\phi_m$  that are smooth and continuous but still contain the general features of the activation phase of a ventricular action potential.

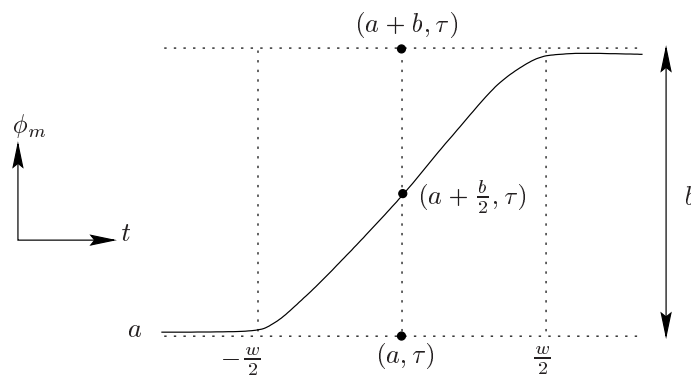


**Figure 5.4:** Approximation of the Heaviside step function by a sigmoidal function. This function contains the parameters  $\omega$  and  $b$  to determine its shape. The  $\omega$  parameter controls the width or window of the activation upstroke (*i.e.*, the duration of the depolarisation) while the  $b$  parameter controls the height of the transmembrane jump, *i.e.*, the difference between the resting potential ( $a$ ) and the maximum systolic potential. Time is shown on the horizontal axis and the transmembrane potential on the vertical axis.

In this function, the  $a$  and  $b$  parameters again represent the transmembrane resting potential and the transmembrane jump respectively. The smooth function is created by gradually activating the sources over a timespan of  $\omega$ .

If  $u$  is defined as  $t - \tau(\mathbf{x})$  the smooth activation function can be represented mathematically by the function

$$S(u) = \begin{cases} a & u \leq -\frac{\epsilon}{2} \\ a + \frac{b}{2} \left(\frac{2}{\omega}u + 1\right)^2 & -\frac{\epsilon}{2} < u \leq 0 \\ b - \frac{b}{2} \left(\frac{2}{\omega}u - 1\right)^2 & 0 < u < \frac{\epsilon}{2} \\ a + b & u \geq \frac{\epsilon}{2} \end{cases} \quad (5.44)$$

The derivatives of the torso surface potential with respect to the activation times for use in the optimisation phase are given by

$$\frac{\partial \hat{\phi}_B}{\partial \tau} = \mathbf{A} \cdot (-1) \begin{cases} 0 & u \leq -\frac{\epsilon}{2} \\ b \left(\frac{2}{\omega}u + 1\right) \frac{2}{\omega} & -\frac{\epsilon}{2} < u \leq 0 \\ -b \left(\frac{2}{\omega}u - 1\right) \frac{2}{\omega} & 0 < u < \frac{\epsilon}{2} \\ 0 & u \geq \frac{\epsilon}{2} \end{cases} \quad (5.45)$$

## 5.5 Analytic Test Cases

Analytic solutions to mathematical problems have been used for many years to study the behaviour of electrocardiographic problems (*e.g.*, Wilson & Bayley 1950, Brody 1956, McFee & Rush 1968). In most cases, the use of analytic solutions has required simplifying assumptions to be made, so that a qualitative understanding of the problem may be gained. However, analytic solutions are still vitally important in modern computational studies. As computational techniques are only ever approximations of real solutions, they inherently contain modelling errors. To quantify the component of error which corresponds to the numerical solution method, it is necessary to be able to compare the computed solution with an exact or analytic solution. To make the test as realistic as possible, it is desirable to perform the test on a problem that is similar to the ‘real world’ scenario.

The standard approach for the finite and boundary element methods when testing a computational procedure is to compare the results generated against some known analytical solutions so that errors in the method can be quantified. It is also standard practice to perform a convergence analysis in which the error in a particular problem is investigated as the problem size is systematically increased (*i.e.*, element mesh size decreased).

The numerical error associated with a finite or boundary element method can be reduced by *refining* the mesh as described in Section 2.5. By refining the elements once in each  $\xi$  direction the element size is reduced by a factor of 4. This also introduces an increased number of solution DOF used to solve the problem and as a result the mesh is able to better represent the solution field.

The standard approach for *convergence analysis* of a finite and boundary element methods is to compare the solutions as the element sizes are reduced. With a stable numerical procedure, the error will decrease as the solution DOF is increased. If the numerical method is stable, refining the mesh will result in a fixed rate of decrease in error. If this is the case, the convergence results should produce a straight line on a  $\log - \log$  plot of the measure of error versus a measure of the problem size. The slope of this line provides an indication of the rate of convergence.

To quantify the degree of refinement two measures are used, characteristic element size ( $h$ ) and the number of solution DOF. To calculate the characteristic element size in irregular meshes,  $h$  is defined to be the square root of the average element areas for two-dimensional surface elements. The number of solution DOF is a parameter which provides a consistent size of the computational problem.

The Normalised Integral Difference Squared (NIDS) error metric, defined in Equation (5.46) provides a relative measure of the differences between two solutions.

$$\text{NIDS} = \sqrt{\frac{\int_{\Gamma} (\phi_{\text{analytic}} - \phi_{\text{numeric}})^2 d\Gamma}{\int_{\Gamma} (\phi_{\text{analytic}})^2 d\Gamma}} \quad (5.46)$$

The RMS measure as defined in Equation (3.7) was also used to provide a measure of the absolute difference between two solutions.

### 5.5.1 Laplace's Equation Analytic Test Problem

A dipole in a concentric sphere problem is a common analytic solution to Laplace's equation. As the electrical activity external to the heart is governed by the generalised Laplace's equation,

this analytic solution ensures that the epicardial to body surface potential transfer matrix defined in Section 5.3 has been constructed correctly. Additional analytic test problems which solved for eccentric dipoles and normal currents on the outer spheres (by setting potential boundary conditions on the outer surfaces) have previously been thoroughly tested by Harris (1996) and Bradley et al. (1997).

The dipole in a sphere problem consists of finding the potential and current distribution inside  $N$  homogeneous concentric spheres with a single dipole located at an arbitrary position inside the spheres. A test problem with a static dipole in a concentric sphere problem was performed with physically realistic boundary conditions of no normal current flow was imposed on the surface of the outer sphere.

### Governing Equations & Boundary Conditions

By considering a concentric sphere setup, as shown in Figure 5.5, where the domains for both spheres are governed by the generalised Laplace's equation, we have a simplified representation of a heart in a torso. The surface of the inner sphere represents the epicardial surface and the surface of the outer sphere, the torso surface. The problem is defined in the spherical polar coordinate system  $(r, \theta, \zeta)$ , with  $0 \leq \theta \leq 2\pi$  for the circumferential coordinate and  $0 \leq \zeta \leq \pi$  for the azimuthal coordinate, although numerical solutions were carried out in a rectangular Cartesian framework.

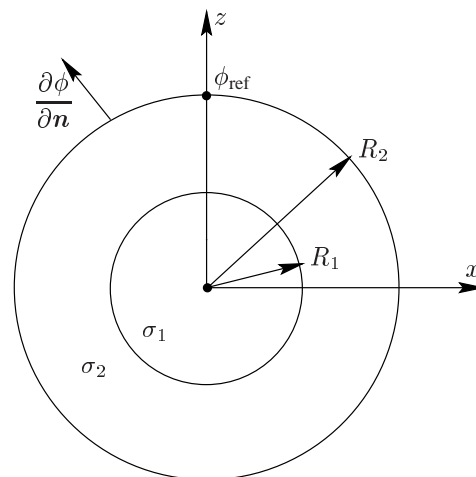


**Figure 5.5:** Schematic of Laplace's equation analytic solution. The setup consists of two concentric spheres of radius  $R_1$  and  $R_2$  with varying conductivities ( $\sigma_1$  and  $\sigma_2$ ). A dipole is located at the origin. A no flux boundary condition is applied to the outer surface as well as a reference potential at one node. Potentials are computed on both surfaces and normal currents on the inner surface.

The governing equations are subject to the boundary conditions which closely represent those of an epicardial potential formulation for the problem of electrocardiology. Equation (5.47) and Equation (5.48) ensure continuity of potential and current on the interface surface between the two regions. Equation (5.49) specifies a no-flux boundary condition on the outer surface representing the torso surface/air interface and a reference potential is specified with Equation (5.50).

$$\phi^{out} = \phi^{in} \quad \text{at } r = R_1 \quad (5.47)$$

$$\sigma_{in} \frac{\partial \phi^{in}}{\partial r} = \sigma_{out} \frac{\partial \phi^{out}}{\partial r} \quad \text{at } r = R_1 \quad (5.48)$$

$$\frac{\partial \phi^{out}}{\partial r} = 0 \quad \text{at } r = R_2 \quad (5.49)$$

$$\phi^{out} = 0 \quad \text{at } r = R_2, \zeta = 0 \quad (5.50)$$

### General Solution for Laplace's Equation

The general solutions to the three-dimensional Laplace's equation in polar coordinates is given by

$$\phi(r, \theta, \zeta) = \sum_{n=0}^{\infty} \sum_{m=0}^n (A_{mn} \cos(m\theta) + B_{mn} \sin(m\theta)) \left( C_{mn} r^n + \frac{D_{mn}}{r^{n+1}} \right) P_n^m(\cos \zeta) \quad (5.51)$$

where  $P_n^m(\cos \zeta)$  is the associate Legendre polynomials of degree  $n$  and order  $m$  as specified below:

Associate Legendre Polynomials	
	$P_0^0(x) = 1$
	$P_1^0(x) = x$
	$P_1^1(x) = - (1 - x^2)^{\frac{1}{2}}$
	$P_2^0(x) = \frac{1}{2} (3x^2 - 1)$
$P_n^m(x) = (-1)^m (1 - x^2)^{\frac{m}{2}} \frac{d^m}{dx^m} P_n(x)$	

where  $P_n(x)$  is the Legendre polynomial of degree  $n$  as specified by Rodrigues' formula,



Legendre Polynomials	
$P_n(x) = \frac{1}{2^n n!} \frac{d^n}{dx^n} (x^2 - 1)^n$	$P_0(x) = 1$
	$P_1(x) = x$
	$P_2(x) = \frac{1}{2} (3x^2 - 1)$
	$P_3(x) = \frac{1}{2} (5x^3 - 3x)$

Considering a dipole inside  $N$  concentric spheres problem, if  $i$  is used to denote the region between, or inside, adjacent concentric shells (*i.e.*,  $i = 1$  is the inner sphere,  $2 \leq i \leq N$  are the concentric shells and  $i = N + 1$  is the domain outside the sphere) then Equation (5.51) can be applied in each region, *i.e.*,

$$\phi^i(r, \theta, \zeta) = \sum_{n=0}^{\infty} \sum_{m=0}^n (A_{mn}^i \cos(m\theta) + B_{mn}^i \sin(m\theta)) \left( C_{mn}^i r^n + \frac{D_{mn}^i}{r^{n+1}} \right) P_n^m(\cos \zeta) \quad (5.52)$$

### Dipole in an Infinite Medium

If a region contains a dipole, the dipole solution can be written in the same form as Equation (5.51)

$$\phi(r, \theta, \zeta) = \sum_{n=0}^{\infty} \sum_{m=0}^n (E_{mn} \cos(m\theta) + F_{mn} \sin(m\theta)) \left( G_{mn} r^n + \frac{H_{mn}}{r^{n+1}} \right) P_n^m(\cos \zeta) \quad (5.53)$$

where  $E_{mn}$ ,  $F_{mn}$ ,  $G_{mn}$  and  $H_{mn}$  are known constants for the particular dipole location and orientation.

The potential field due to a dipole (up to an additive constant) is given by Plonsey & Barr (1988) as

$$\phi(\mathbf{x}) = \frac{\boldsymbol{\rho} \cos \gamma}{4\pi\sigma \|\mathbf{x}_d^2\|} \quad (5.54)$$

where  $\mathbf{x}$  is the observation position,  $\boldsymbol{\rho}$  is the magnitude and orientation of the dipole,  $\gamma$  is the angle between the dipole observation orientation and the observation point, and  $\mathbf{x}_d$  the vector from the dipole centre to the observation point.

For a centric dipole inside a sphere, Equation (5.54),  $\|\mathbf{x}_d\|$  is the radius ( $r$ ) of the observation point and Equation (5.54) becomes

$$\phi(\mathbf{x}) = \frac{\boldsymbol{\rho} \cos \gamma}{4\pi\sigma r^2} \quad (5.55)$$

Considering the Cartesian components of  $\boldsymbol{\rho}$  (*i.e.*,  $\rho_x, \rho_y, \rho_z$ ), the potential for a centric dipole in an infinite medium is

$$\phi(r, \theta, \zeta) = \frac{\rho_x \cos \theta \sin \zeta + \rho_y \sin \theta \sin \zeta + \rho_z \cos \zeta}{4\pi\sigma r^2} \quad (5.56)$$

By comparing Equation (5.56) and Equation (5.53), the separated coefficients are

$$E_{01} = \frac{\rho_z}{4\pi\sigma} \quad E_{11} = \frac{-\rho_x}{4\pi\sigma} \quad F_{11} = \frac{-\rho_y}{4\pi\sigma} \quad H_{01} = H_{11} = 1$$

with all other coefficients equal to zero.

### Coefficient Evaluation

Once the expression for the potential due to a dipole in an infinite domain has been found, this may be used in conjunction with the boundary conditions of continuity of potential and current across surfaces. If there are  $N$  spheres in the problem (where  $N \geq 1$ ), then we can generate  $N - 1$  equations from continuity considerations, and  $N$  equations from conservation of current. There is one coefficient for the centre sphere and two coefficients for each of the  $N - 1$  shells surrounding it. In total, this gives us  $2N - 1$  equations and  $2N - 1$  unknowns. From this a system of linear equations can be generated for each  $m, n$  spherical harmonic pair. Further details can be found in Bradley et al. (1997).

### Source Term Due to a Dipole

To allow for dipolar source terms to be included, a source term must be included in the boundary integral equations. For a dipole with magnitude and direction given by the vector  $\boldsymbol{\rho}$ , located at the point  $\boldsymbol{\rho}_0$ , this source term is given by

$$V(\mathbf{x}, \boldsymbol{\rho}, \boldsymbol{\rho}_0) = \frac{\mathbf{r} \cdot \boldsymbol{\rho}}{4\pi\sigma r^3} \quad (5.57)$$

where  $r = \|\mathbf{r}\|_2 = \|\boldsymbol{\rho}_0 - \mathbf{x}\|_2$  and  $\sigma$  is the conductivity of the space (Plonsey & Barr 1988, Bradley 1998).

This yields a matrix system of the form

$$\mathbf{P}\phi + \mathbf{d} = \mathbf{Q}\mathbf{q} \quad (5.58)$$

where  $\mathbf{P}$  is the boundary element global dependent variable matrix and  $\mathbf{Q}$  is the boundary element global flux variable matrix and  $\mathbf{d}$  is the source vector due to any dipoles.

### Convergence Analysis

A particular solution to the generalised Laplace's equation with the setup as illustrated in Figure 5.5 was investigated. The inner sphere had unit radius and the second sphere radius 2. The static dipole was centred at the origin with strength of 1.7, 1.2, 2.2. The inner sphere had a conductivity of  $0.3 \text{ mS mm}^{-1}$  while the outer sphere had a conductivity of  $0.2 \text{ mS mm}^{-1}$ .

The problem was solved with bilinear Lagrange basis functions (the same basis functions used for the forward and inverse simulations). The initial mesh consisted of  $4 \times 4$  elements in the circumferential and azimuthal directions. Further refinement (*i.e.*, once in each  $\xi$  direction) resulted in  $8 \times 8$ ,  $16 \times 16$  and  $32 \times 32$  elements in each direction.

Shown in Figure 5.6 is the convergence analysis of the potential distribution at 28 nodal positions on both spheres. These nodal positions are uniformly distributed and correspond to the node locations at the lowest mesh resolution ( $4 \times 4$ ). Shown in Figure 5.7 is the convergence analysis of the current distribution at each of the nodal positions. In both cases the numerical solutions have been compared to the analytical solutions using the comparison metrics RMS and NIDS defined in Equation (3.7) and Equation (5.46), respectively. From the convergence plots, as the mesh resolution (and therefore solution DOF) increases, the deviation between the numerical and analytical results reduced, indicating a linear rate of convergence.

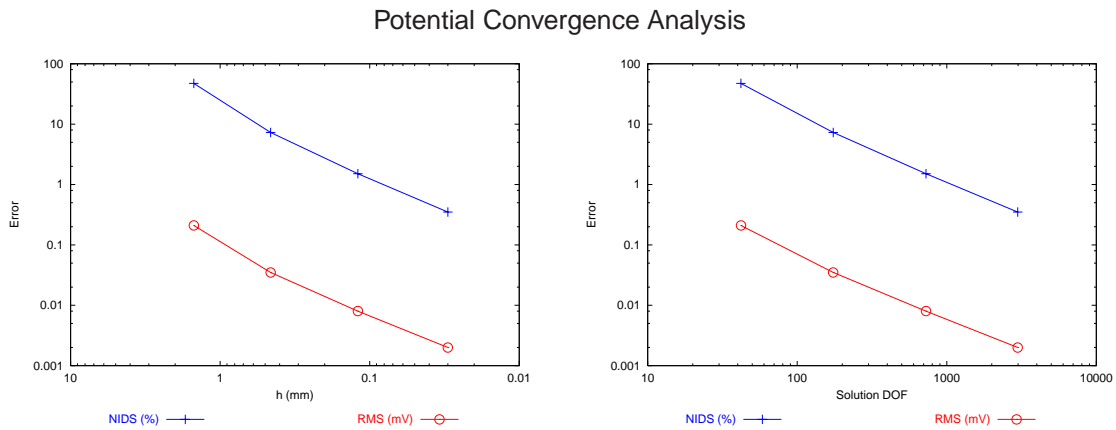


**Figure 5.6:** Convergence analysis of potential on both spheres due to a dipole in the Laplace's equation setup shown in Figure 5.5.

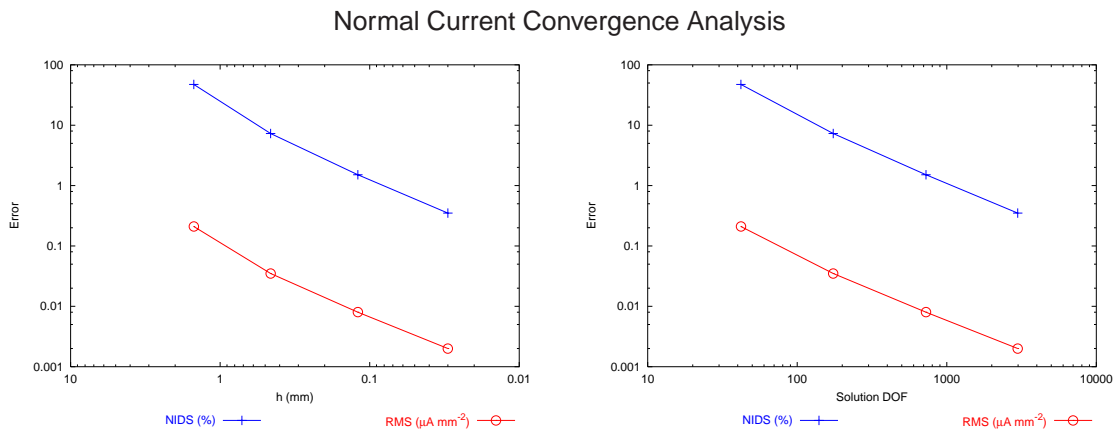


**Figure 5.7:** Convergence analysis of the current on the inner sphere due to a dipole in the Laplace's equation setup shown in Figure 5.5.

## 5.5.2 Poisson Equation Analytic Test Problem

If the electrical activity within the myocardium is to be modelled through to the torso surface, Equation (5.10) must be solved. Presented here is a bidomain based analytic solution which ensures that the transfer matrix mapping from transmembrane potential to torso surface potentials, as described in Section 5.3, has been constructed correctly.

In order to verify the results computed by the numerical solutions, an analytic solution that combined a bidomain and a generalised Laplace's equation setup was calculated for a simplified test geometry. Two concentric spheres representing the myocardium enclosed by a torso of homogeneous conductivity were defined. On the inner sphere surface a known transmembrane potential distribution was applied to depict the excitation wavefront at a particular time instant and on the

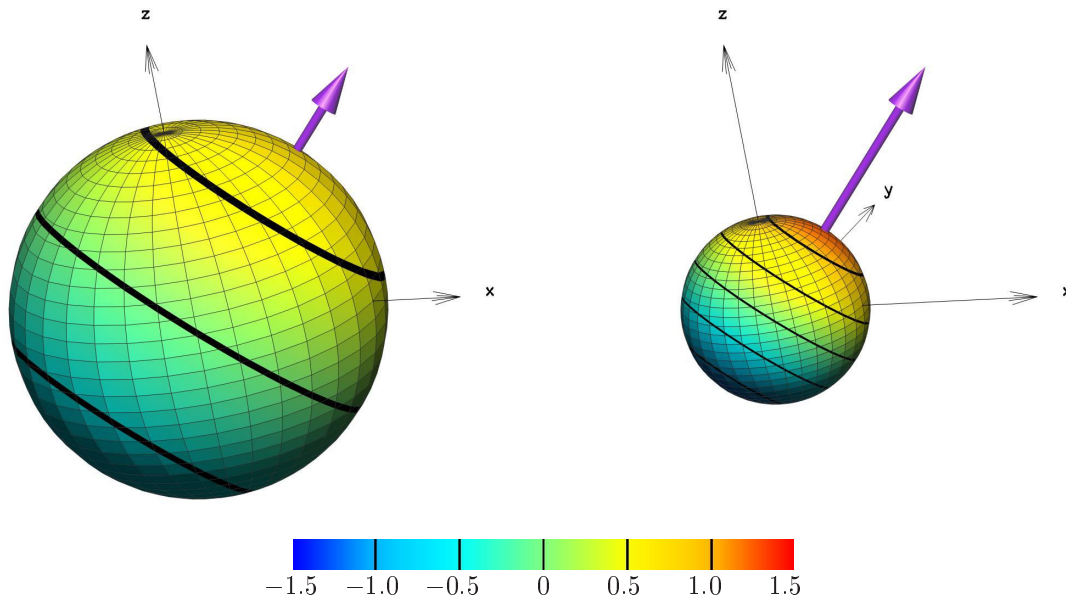


**Figure 5.8:** Potential (mV) generated by a dipole (purple arrow) of strength 1.7, 1.2, 2.2 in the Laplace's equation setup shown in Figure 5.5. The inner sphere of unit radius has a conductivity of  $0.3 \text{ mS mm}^{-1}$  and the outer sphere of radius 2 has a conductivity of  $0.2 \text{ mS mm}^{-1}$ .

outer surface, the resultant potentials were determined.

### Governing Equations & Boundary Conditions

By considering the solutions to the bidomain and generalised Laplace's equation within a concentric sphere setup as shown in Figure 5.9, the governing equations can be specified as

$$\nabla \cdot [(\sigma_i + \sigma_e) \nabla \phi_e^{in}] = -\nabla \cdot (\sigma_i \nabla \phi_m) \quad (5.59)$$

$$\nabla \cdot (\sigma \nabla \phi_e^{out}) = 0 \quad (5.60)$$

where Equation (5.59) is the governing equation for the inner sphere and Equation (5.60) is the governing equation in the outer sphere and  $\phi_e^{in}$  and  $\phi_e^{out}$  are the extracellular potentials located on the inner and outer spheres respectively.

This setup provides a simplified representation of a heart in a torso. The inner sphere represents the epicardial surface and the outer sphere represents the torso surface. The problem was defined in the spherical polar coordinate system with coordinates  $(r, \theta, \zeta)$ , with  $0 \leq \theta \leq 2\pi$  for the circumferential coordinate and  $0 \leq \zeta \leq \pi$  for the azimuthal coordinate, although numerical solutions

were carried out in a rectangular Cartesian framework. This creates a situation where an analytic solution can be generated which closely represents the true problem of solving for activation times in a human torso.

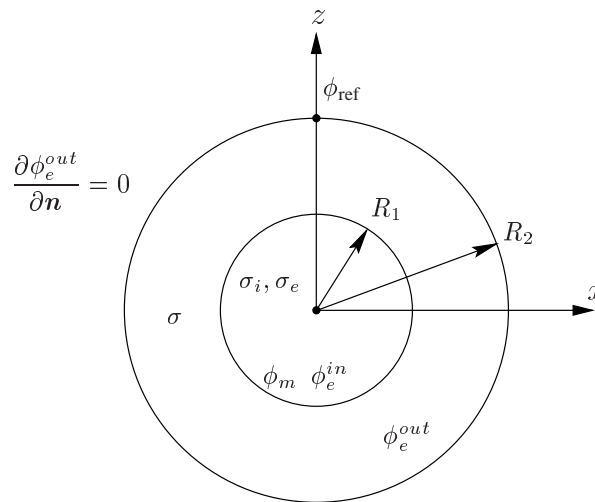


**Figure 5.9:** Schematic of analytic bidomain problem setup, with inner sphere of radius  $R_1$  and outer sphere of radius  $R_2$ . Bidomain conductivity parameters of  $\sigma_i$  and  $\sigma_e$  in the inner sphere and passive conductivity of  $\sigma$  in the outer sphere were specified. The transmembrane potential  $\phi_m$  on the inner surface was specified by Equation (5.67) and a no flux boundary condition was specified on the outer surface as well a reference potential at the top of the outer sphere,  $(R_2, \theta, 0)$ . The extracellular potential ( $\phi_e^{in}$ ) on the inner surface and extracellular ( $\phi_e^{out}$ ) on the outer surface as well as the normal derivatives were solved for.

The governing equations are subject to the boundary conditions which closely represent those of the true boundary conditions encountered within a torso. At the inner surface, there is a no-flux boundary condition for the transmembrane potential, as specified by Equation (5.61). The interface between the inner and outer surfaces must have the same values of extracellular potential and continuity of current across the boundary. These are enforced by the boundary conditions Equation (5.62) and Equation (5.63). The boundary condition, Equation (5.64), ensures that there is a no flux boundary condition on the outer surface which represents the torso surface/air interface on a human. An additional boundary condition of a reference potential was chosen in Equation (5.65)

and arbitrarily to be located at  $(R_2, \theta, 0)$  (*i.e.*, at the top of the outer sphere) and set to 0.

$$\frac{\partial \phi_m}{\partial r} = 0 \quad \text{at } r = R_1 \quad (5.61)$$

$$\phi_e^{out} = \phi_e^{in} \quad \text{at } r = R_1 \quad (5.62)$$

$$(\sigma_i + \sigma_e) \frac{\partial \phi_e^{in}}{\partial r} = \sigma \frac{\partial \phi_e^{out}}{\partial r} \quad \text{at } r = R_1 \quad (5.63)$$

$$\frac{\partial \phi_e^{out}}{\partial r} = 0 \quad \text{at } r = R_2 \quad (5.64)$$

$$\phi_e^{out} = 0 \quad \text{at } r = R_2, \zeta = 0 \quad (5.65)$$

### Analytic Transmembrane Potentials

From Equation (5.59) within the inner sphere (*i.e.*, for  $0 < r \leq R_1$ )

$$\nabla^2 \left( \phi_e^{in} + \frac{\sigma_i}{\sigma_i + \sigma_e} \phi_m \right) = 0 \quad (5.66)$$

In polar spheroidal coordinates, if  $\phi_m$  is defined to be the potential field generated by a centric dipole of magnitude, in the rectangular Cartesian coordinate system,  $\boldsymbol{\rho} = (\rho_x, \rho_y, \rho_z)$  inside a sphere of radius  $R_1$  with a no-flux boundary condition set on the outer sphere at  $R_1$ , then,

$$\phi_m(r, \theta, \zeta) = \frac{(R_1^3 + 2r^3)}{R_1^3 r^2} (\rho_x \cos \theta \sin \zeta + \rho_y \sin \theta \sin \zeta + \rho_z \cos \zeta) \quad (5.67)$$

With  $\phi_m$  chosen as such, Equation (5.61) is satisfied and  $\phi_m$  is itself a solution to Laplace's equation inside the inner sphere (except at the origin).

### Analytic Extracellular Potentials

From Equation (5.66), if  $\phi_m$  is a solution to Laplace's equation then it is necessary to find  $\phi_e^{in}$  such that  $\phi_e^{in} + \frac{\sigma_i}{\sigma_i + \sigma_e} \phi_m$  satisfies Laplace's equation inside the first sphere. The general solution to Laplace's equation in polar spheroidal coordinates is given by

$$\phi_e^{in} = \sum_{n=0}^{\infty} \sum_{m=0}^n (A_{mn} \cos(m\theta) + B_{mn} \sin(m\theta)) \left( C_{mn} r^n + \frac{D_{mn}}{r^{n+1}} \right) P_n^m(\cos \zeta) \quad (5.68)$$

where  $P_n^m(\cos \zeta)$  is the associate Legendre polynomials of degree  $n$  and order  $m$ , as defined in Section 5.5.1,

If the extracellular potentials are first considered on the surface of the inner sphere, from the orthogonality of spherical harmonic functions the choice of  $\phi_m$  only contains the  $mn$  coefficients: 00, 01 and 11. The general expression for  $\phi_e^{in}$  thus need only contain these coefficients, *i.e.*,

$$\begin{aligned} \phi_e^{in}(r, \theta, \zeta) = & (A_{11} \cos \theta + B_{11} \sin \theta) \left( C_{11}r + \frac{D_{11}}{r^2} \right) \sin \zeta \\ & + A_{01} \left( C_{01}r + \frac{D_{01}}{r^2} \right) \cos \zeta + A_{00} \left( C_{00} + \frac{D_{00}}{r} \right) - \left( \frac{\sigma_i}{\sigma_i + \sigma_e} \right) \phi_m \end{aligned} \quad (5.69)$$

Grouping the coefficients

$$\begin{aligned} C_0 &= A_{00}C_{00} & C_1 &= A_{01}C_{01} \\ D_0 &= A_{00}D_{00} & D_1 &= A_{01}D_{01} \end{aligned}$$

the extracellular potential for the inner sphere is given by

$$\begin{aligned} \phi_e^{in}(r, \theta, \zeta) = & (A_{11} \cos \theta + B_{11} \sin \theta) \left( C_{11}r + \frac{D_{11}}{r^2} \right) \sin \zeta \\ & + \left( C_1r + \frac{D_1}{r^2} \right) \cos \zeta + \left( C_0 + \frac{D_0}{r} \right) - \frac{\sigma_i}{\sigma_i + \sigma_e} \phi_m \end{aligned} \quad (5.70)$$

Next, the extracellular potentials on the outer sphere are considered. In the outer sphere, Laplace's equation for  $\phi_e^{out}$  must be satisfied. The general solution to Laplace's equation in spherical polar coordinates is given by

$$\phi_e^{in} = \sum_{n=0}^{\infty} \sum_{m=0}^n (E_{mn} \cos(m\theta) + F_{mn} \sin(m\theta)) \left( G_{mn}r^n + \frac{H_{mn}}{r^{n+1}} \right) P_n^m(\cos \zeta) \quad (5.71)$$

From orthogonality of spherical harmonic functions the general solution for the outside sphere is hence

$$\begin{aligned} \phi_e^{out} = & (E_{11} \cos \theta + F_{11} \sin \theta) \left( G_{11}r + \frac{H_{11}}{r^2} \right) \sin \zeta \\ & + E_{01} \left( G_{01}r + \frac{H_{01}}{r^2} \right) \cos \zeta + E_{00} \left( G_{00} + \frac{H_{00}}{r} \right) \end{aligned} \quad (5.72)$$



Grouping the coefficients

$$\begin{aligned} G_0 &= E_{00}G_{00} & G_1 &= E_{01}G_{01} \\ H_0 &= E_{00}H_{00} & H_1 &= E_{01}H_{01} \end{aligned}$$

the expression for the extracellular potential in the outer sphere is given by

$$\begin{aligned} \phi_e^{out}(r, \theta, \zeta) &= (E_{11} \cos \theta + F_{11} \sin \theta) \left( G_{11}r + \frac{H_{11}}{r^2} \right) \sin \zeta \\ &+ \left( G_1r + \frac{H_1}{r^2} \right) \cos \zeta + \left( G_0 + \frac{H_0}{r} \right) \end{aligned} \quad (5.73)$$

Thus, from Equation (5.70) and Equation (5.73), the general expression for  $\phi_e$  throughout the domain is therefore given by

$$\phi_e(r, \theta, \zeta) = \begin{cases} \left( A_{11} \cos \theta + B_{11} \sin \theta \right) \left( C_{11}r + \frac{D_{11}}{r^2} \right) \sin \zeta \\ \quad + \left( C_1r + \frac{D_1}{r^2} \right) \cos \zeta + C_0 + \frac{D_0}{r} - \frac{\sigma_i}{\sigma_i + \sigma_e} \phi_m(r, \theta, \zeta) & 0 < r \leq R_1 \\ \left( E_{11} \cos \theta + F_{11} \sin \theta \right) \left( G_{11}r + \frac{H_{11}}{r^2} \right) \sin \zeta \\ \quad + \left( G_1r + \frac{H_1}{r^2} \right) \cos \zeta + G_0 + \frac{H_0}{r} & R_1 < r \leq R_2 \end{cases} \quad (5.74)$$

By applying boundary conditions specific to this problem setup to the general solution specified in Equation (5.74), it is now possible to obtain a specific solution.

By substituting Equation (5.74) into Equation (5.62), continuity of potential across the inner sphere

surface implies

$$G_0 + \frac{H_0}{R_1} = C_0 + \frac{D_0}{R_1} \quad (5.75)$$

$$E_{11} \left( G_{11} R_1 + \frac{H_{11}}{R_1^2} \right) = A_{11} \left( C_{11} R_1 + \frac{D_{11}}{R_1^2} \right) - \frac{3\sigma_i}{R_1^2 (\sigma_i + \sigma_e)} \rho_x \quad (5.76)$$

$$F_{11} \left( G_{11} R_1 + \frac{H_{11}}{R_1^2} \right) = B_{11} \left( C_{11} R_1 + \frac{D_{11}}{R_1^2} \right) - \frac{3\sigma_i}{R_1^2 (\sigma_i + \sigma_e)} \rho_y \quad (5.77)$$

$$G_1 R_1 + \frac{H_1}{R_1^2} = C_1 R_1 + \frac{D_1}{R_1^2} - \frac{3\sigma_i}{R_1^2 (\sigma_i + \sigma_e)} \rho_z \quad (5.78)$$

By substituting Equation (5.74) into Equation (5.63), continuity of current across the inner sphere boundary implies

$$\frac{\sigma H_0}{R_1^2} = \frac{(\sigma_i + \sigma_e) D_0}{R_1^2} \quad (5.79)$$

$$\sigma E_{11} \left( G_{11} - \frac{2H_{11}}{R_1^3} \right) = (\sigma_i + \sigma_e) A_{11} \left( C_{11} - \frac{2D_{11}}{R_1^3} \right) \quad (5.80)$$

$$\sigma F_{11} \left( G_{11} - \frac{2H_{11}}{R_1^3} \right) = (\sigma_i + \sigma_e) B_{11} \left( C_{11} - \frac{2D_{11}}{R_1^3} \right) \quad (5.81)$$

$$\sigma \left( G_1 - \frac{2H_1}{R_1^3} \right) = (\sigma_i + \sigma_e) \left( C_1 - \frac{2D_1}{R_1^3} \right) \quad (5.82)$$

Substituting Equation (5.74) into Equation (5.64), the no-flux boundary condition across the outer surface implies

$$G_{11} - \frac{2H_{11}}{R_2^3} = 0 \quad (5.83)$$

$$G_1 - \frac{2H_1}{R_2^3} = 0 \quad (5.84)$$

$$-\frac{H_0}{R_2^2} = 0 \quad (5.85)$$

Substituting Equation (5.74) into Equation (5.65), specification of the reference potential at the top of the outer sphere  $(R_2, \theta, 0)$  implies

$$\phi_{\text{ref}} = G_1 R_2 + \frac{H_1}{R_2^2} + G_0 + \frac{H_0}{R_2} \quad (5.86)$$

By applying the boundary conditions to Equation (5.74), two sets of independent linear equations are formed. The first set contains the five equations, Equations (5.76)–(5.77) and Equations (5.80)–(5.81) and Equation (5.83). These equations involve eight unknowns  $A_{11} - H_{11}$ , all with ‘11’ coefficients. The second set contains the equations Equation (5.75), Equations (5.78)–(5.79) and Equations (5.84)–(5.86). These seven equations involve the eight unknowns  $C_0, C_1, D_0, D_1, G_0, G_1, H_0$  and  $H_1$ , all with either ‘0’ or ‘1’ coefficients.

To solve these under-determined systems of linear equations, three coefficients in the first system and one coefficient in the second system must be fixed. It is desirable to have the resultant circumferential variation directly dependent on the underlying dipole orientation that is generating  $\phi_m$ , so the  $C_{11}, D_{11}$  and  $H_{11}$  coefficients were chosen so as to normalise the equations in the radial direction.

From Equations (5.80) and (5.81)

$$E_{11} = \frac{(\sigma_i + \sigma_e) R_2^3 (R_1^3 C_{11} - 2D_{11})}{2\sigma (R_1^3 - R_2^3) H_{11}} A_{11} = \alpha A_{11} \quad (5.87)$$

$$F_{11} = \frac{(\sigma_i + \sigma_e) R_2^3 (R_1^3 C_{11} - 2D_{11})}{2\sigma (R_1^3 - R_2^3) H_{11}} B_{11} = \alpha B_{11} \quad (5.88)$$

and thus by combining Equations (5.76) and (5.77)

$$A_{11} = \frac{-3\sigma_i R_2^3}{(\sigma_i + \sigma_e) (\alpha (2R_1^3 + R_2^3) H_{11} - R_2^3 (C_{11} R_1^3 + D_{11}))} \rho_x = \beta \rho_x \quad (5.89)$$

$$B_{11} = \frac{-3\sigma_i R_2^3}{(\sigma_i + \sigma_e) (\alpha (2R_1^3 + R_2^3) H_{11} - R_2^3 (C_{11} R_1^3 + D_{11}))} \rho_y = \beta \rho_y \quad (5.90)$$

For the second set of equations, it should be noted that  $H_0$  (and thus  $D_0$  from Equation (5.79)) can not be fixed as it is implicitly zero from Equation (5.85). It should also be noted that if  $C_0$  or  $G_0$  is fixed the resulting expression for  $\phi_e$  in the outer sphere will not depend on the dipole source generating  $\phi_m$ . For this reason, and to be consistent with the choice of coefficients from the first set of equations,  $C_1$  was the coefficient chosen to be fixed. Thus, from Equation (5.85),  $H_0 = 0$  and therefore from Equation (5.79)  $D_0 = 0$ . This gives, from Equation (5.75),  $C_0 = G_0$ .

Equation (5.84) can be rearranged into the form

$$G_1 = \frac{2H_1}{R_2^3} \quad (5.91)$$

and thus from Equations (5.78) and (5.82) the  $D_1$  and  $H_1$  coefficients are defined by

$$D_1 = \frac{3(2R_1^3 + R_2^3)((\sigma_i + \sigma_e)R_1^3 C_1 - 2\sigma_i \rho_z)}{2((2\sigma_i + 2\sigma_e + \sigma)R_1^3 + (\sigma_i + \sigma_e - \sigma)R_2^3)} - R_1^3 C_1 + \frac{3\sigma_i \rho_z}{\sigma_i + \sigma_e} \quad (5.92)$$

and

$$H_1 = \frac{3R_2^3((\sigma_i + \sigma_e)R_1^3 C_1 - 2\sigma_i \rho_z)}{2((2\sigma_i + 2\sigma_e + \sigma)R_1^3 + (\sigma_i + \sigma_e - \sigma)R_2^3)} \quad (5.93)$$

The final coefficient can then be obtained from Equation (5.86), *i.e.*,

$$G_0 = \phi_{\text{ref}} - \frac{9R_2((\sigma_i + \sigma_e)R_1^3 C_1 - 2\sigma_i \rho_z)}{2((2\sigma_i + 2\sigma_e + \sigma)R_1^3 + (\sigma_i + \sigma_e - \sigma)R_2^3)} \quad (5.94)$$

Using Equations (5.75)–(5.86) an analytic test solution for a specific situation is presented in Section 5.5.2.

### Singularity at the Origin

It should be noted that as both  $\phi_m$  and  $\phi_e^{in}$  only exist within the inner sphere, which is centred at the origin, the  $\frac{1}{r^2}$  terms in Equation (5.67) and Equation (5.74) contain singularities when  $r = 0$ . The effect of these singularities must be taken into account when performing an integration of the type in Equation (5.22). The  $\frac{1}{r}$  terms contained in Equation (5.74) do not result in a singularity as the coefficients  $H_0$  and  $D_0$  are implicitly zero.

The resulting singularity from  $\phi_e^{in}$ , when integrated with the weighted function, acts like a dipole source as in the generalised Laplace's formulation in Section 5.5.1. The correction factor that needs to be added to the LHS of Equation (5.39) can be determined by considering two sources  $S$  and

$S^+$  with their strengths defined as

$$\phi_s = \frac{I_t}{\|\mathbf{r}\|} \quad (5.95)$$

$$\phi_s^+ = \frac{I_t}{\|\mathbf{r} - \eta\boldsymbol{\rho}\|} \quad (5.96)$$

where  $I_t$  is the total injected current,  $\boldsymbol{\rho}$  is a direction and  $\eta \in \mathbb{R}$  and  $\eta > 0$

The potential field that results from a dipole that is created from such two sources when they are brought towards each other is given by

$$\begin{aligned} \phi_m &= \lim_{\eta \rightarrow 0} \left\{ \frac{1}{\eta} (\phi_s^+ - \phi_s) \right\} \\ &= \lim_{\eta \rightarrow 0} I_t \left\{ \frac{1}{\eta} \left( \frac{1}{\|\mathbf{r} - \eta\boldsymbol{\rho}\|} - \frac{1}{\|\mathbf{r}\|} \right) \right\} \\ &= \lim_{\eta \rightarrow 0} I_t \left\{ \frac{r - \sqrt{\mathbf{r}^2 - 2\eta\mathbf{r} \cdot \boldsymbol{\rho} + \eta^2\|\boldsymbol{\rho}\|^2}}{\eta r \|\mathbf{r} - \eta\boldsymbol{\rho}\|} \right\} \\ &= \lim_{\eta \rightarrow 0} I_t \left\{ \frac{1 - \sqrt{1 - 2\eta\frac{\mathbf{r} \cdot \boldsymbol{\rho}}{r^2} + \eta^2\frac{\|\boldsymbol{\rho}\|^2}{r^2}}}{\eta \|\mathbf{r} - \eta\boldsymbol{\rho}\|} \right\} \\ &= \lim_{\eta \rightarrow 0} I_t \left\{ \frac{1 - \left( 1 - \eta\frac{\mathbf{r} \cdot \boldsymbol{\rho}}{r^2} + O(\eta^2) \right)}{\eta \|\mathbf{r} - \eta\boldsymbol{\rho}\|} \right\} \\ &= I_t \frac{\mathbf{r} \cdot \boldsymbol{\rho}^*}{r^3} \end{aligned} \quad (5.97)$$

where  $\boldsymbol{\rho}^* = (A_{11}D_{11}, B_{11}D_{11}, D_1)$  and is the pseudo-dipole singularity source which is derived from the coefficients for each directional component of Equation (5.70).

### Convergence Analysis

A particular solution to the Poisson equation with the setup as illustrated in Figure 5.9 was investigated, with the inner sphere of radius 1 and the outer sphere of radius 3, the dipole specified by  $\boldsymbol{\rho} = (1, 2, 1)$ , the bidomain conductivities given by  $\sigma_i = 2$  and  $\sigma_e = 4$  and the passive conductivity

set to  $\sigma = 2$ . By specifying four coefficients to create a fully determined system

$$C_{11} = 1 \quad D_{11} = 1 \quad H_{11} = 1 \quad C_1 = 1$$

the system of equations can be solved. The full set of 16 coefficients were

$$\begin{array}{llll} C_0 = -\frac{27}{122} & D_0 = 0 & G_0 = -\frac{27}{122} & H_0 = 0 \\ C_1 = 1 & D_1 = \frac{87}{122} & G_1 = \frac{3}{61} & H_1 = \frac{81}{122} \\ A_{11} = \frac{52}{17} & B_{11} = \frac{104}{17} & C_{11} = 1 & D_{11} = 1 \\ E_{11} = \frac{81}{17} & F_{11} = \frac{162}{17} & G_{11} = \frac{2}{27} & H_{11} = 1 \end{array}$$

The general solution for  $\phi_e$ , subject to the boundary conditions specified by Equations (5.61)–(5.65) was found to be

$$\phi_e = \begin{cases} \left( \frac{52}{17} \cos \theta + \frac{104}{17} \sin \theta \right) \left( r + \frac{1}{r^2} \right) \sin \zeta + \left( r + \frac{87}{122r^2} \right) \cos \zeta \\ \quad - \frac{(2r^3 + 1)}{3r^2} (\cos \theta \sin \zeta + 2 \sin \theta \sin \zeta + \cos \zeta) - \frac{27}{122} & 0 \leq r \leq 1 \\ \left( \frac{81}{17} \cos \theta + \frac{162}{17} \sin \theta \right) \left( \frac{2}{27}r + \frac{1}{r^2} \right) \sin \zeta + \left( \frac{3r}{61} + \frac{81}{122r^2} \right) \cos \zeta - \frac{27}{122} & 1 \leq r \leq 3 \end{cases} \quad (5.98)$$

and the normal derivatives given by

$$\frac{\partial \phi_e}{\partial \mathbf{n}} = \begin{cases} \left( \frac{52}{17} \cos \theta + \frac{104}{17} \sin \theta \right) \left( 1 - \frac{2}{r^3} \right) \sin \zeta + \left( 1 - \frac{174}{122r^3} \right) \cos \zeta \\ \quad - \frac{2(r^3 - 1)}{3r^3} (\cos \theta \sin \zeta \sin \theta \sin \zeta + \rho_z \cos \zeta) & 0 \leq r \leq 1 \\ \left( \frac{81}{17} \cos \theta + \frac{162}{17} \sin \theta \right) \left( \frac{2}{27} - \frac{2}{r^3} \right) \sin \zeta + \left( \frac{3}{61} - \frac{162}{122r^3} \right) \cos \zeta & 1 \leq r \leq 3 \end{cases} \quad (5.99)$$

The numerically calculated solutions for this problem were compared to the analytic solution pro-

vided by Equation (5.98) and Equation (5.99) using the RMS and NIDS comparison metrics, defined in Equation (3.7) and Equation (5.46) respectively.

The problem was solved using bilinear Lagrange basis functions (the same basis functions used for the forward and inverse simulations) with the mesh systematically refined in each  $\xi$  direction. The convergence plots for potential and normal currents on both surfaces are shown in Figure 5.10 and Figure 5.11. The error measures are plotted against the average characteristic element size ( $h$ ), defined as the square root of the average surface area of each element, and the solution DOF. The slopes of the convergence plots in Figure 5.10 and Figure 5.11 indicate the problem has a linear rate of convergence.

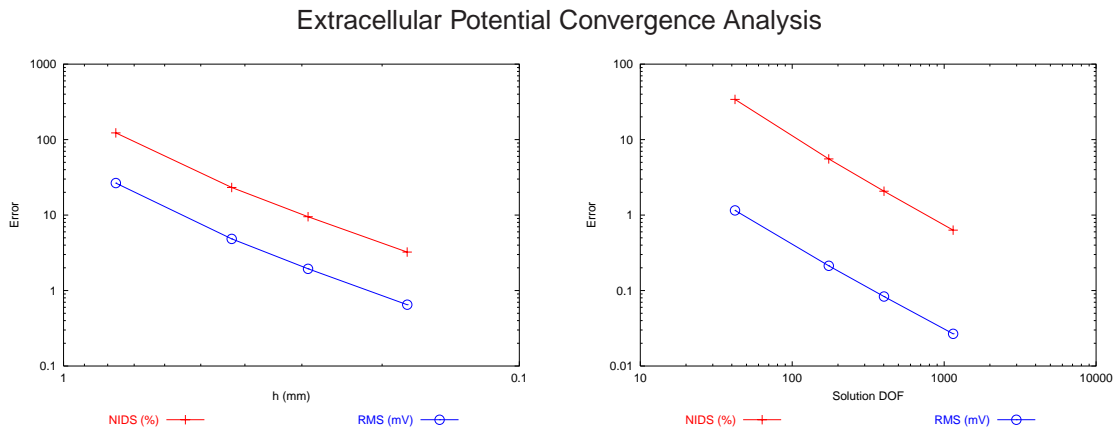


**Figure 5.10:** Convergence analysis for the extracellular potentials on both surfaces generated by the dipole in Equation (5.67) subject to the conditions specified by Equations (5.61)–(5.65).

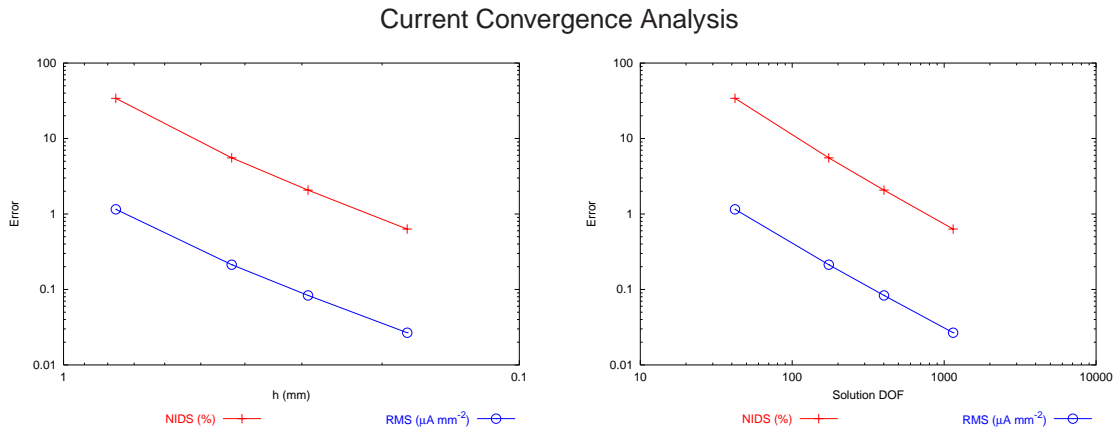


**Figure 5.11:** Convergence analysis for the normal current on the inner sphere generated by the dipole in Equation (5.67) subject to the boundary conditions specified by Equations (5.61)–(5.65).

Figure 5.12 shows the potential and the normal current at five evenly spaced points, by specifying  $\theta = 0$  and varying  $\zeta$  from 0 to  $\pi$ . Effectively this is a slice from the top to the bottom of the sphere

with the points corresponding to nodes at the lowest resolution mesh. The left plot shows the potential on the outer surface ( $r = R_2$ ) and the right plot the current at the inner surface ( $r = R_1$ ). Note that the reference potential is set to 0 mV at  $\zeta = 0$ . It can be seen that as the mesh is refined, the solution approaches the analytic solution.

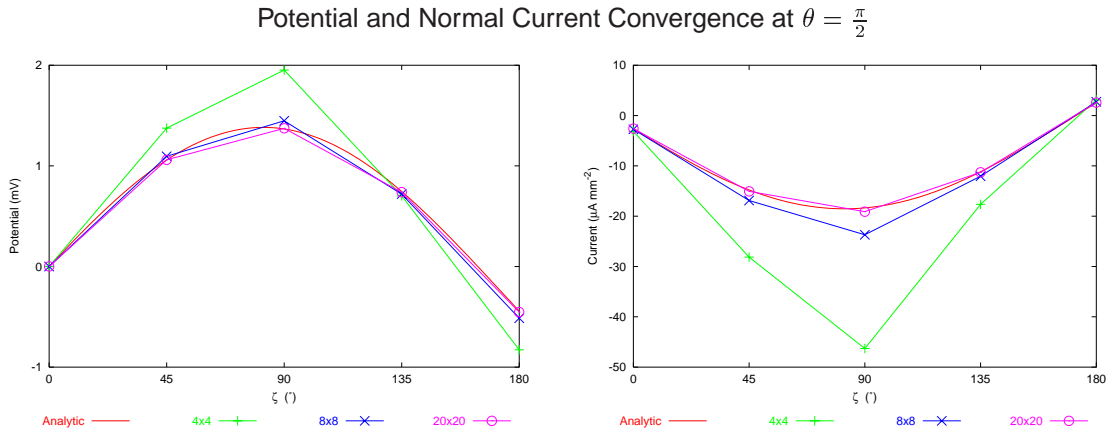


**Figure 5.12:** Comparison between the analytic and the numerical extracellular potentials at  $r = R_2$  and the currents at  $r = R_1$ . The analytic potential is specified by Equation (5.98) and the analytic normal current is specified by Equation (5.99)



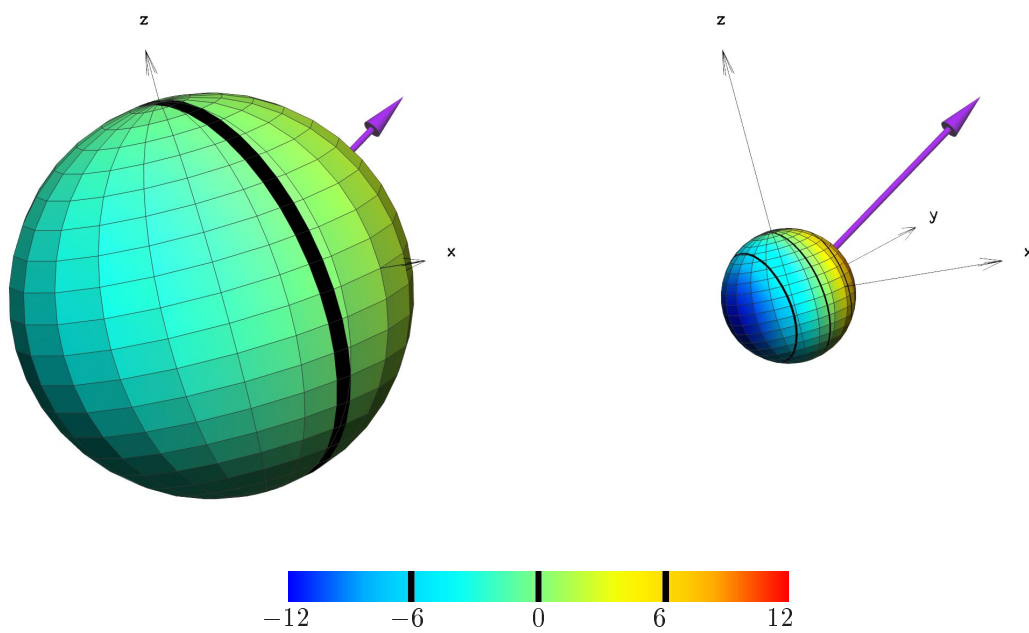


**Figure 5.13:** Analytic extracellular potential (mV) solutions at a refinement level of  $20 \times 20$  (20 elements in the circumferential and azimuthal directions with a total of 400 elements for each of the two surfaces). The purple arrow represents the dipole strength and orientation  $(1, 2, 1)$ .

## 5.6 Convergence Analysis of Generic Model

The generic porcine model, described in Section 4.4, was constructed with the minimum number of DOF necessary to accurately represent the geometric shape of the torso. However, to accurately represent a changing potential field further refinement may be required. At the heart level there are high potential gradients caused by the rapidly moving wavefront and the sharp upstroke in a ventricular action potential. To be able to resolve such rapidly varying fields a relatively fine mesh resolution is required. On the torso surface, the potential fields are the low resolution projection of the electrical activity occurring within the heart. The signal magnitudes have been attenuated and the potentials are also distributed over a larger physical area. Typically a lower resolution mesh is required there than on the heart. The torso model must be systematically refined to a point where the change in solution upon further refinement is below an acceptable level.

Shown in Figure 5.14 is the effect of refining the model once in each  $\xi$  direction. Further details about the refinement of each surface is given in Table B.1. The average characteristic element sizes ( $h$ ) of the left ventricular surface have reduced from 13 mm to 7 mm while the average characteristic element size for the right ventricle has reduced from 14.8 mm to 7.4 mm.

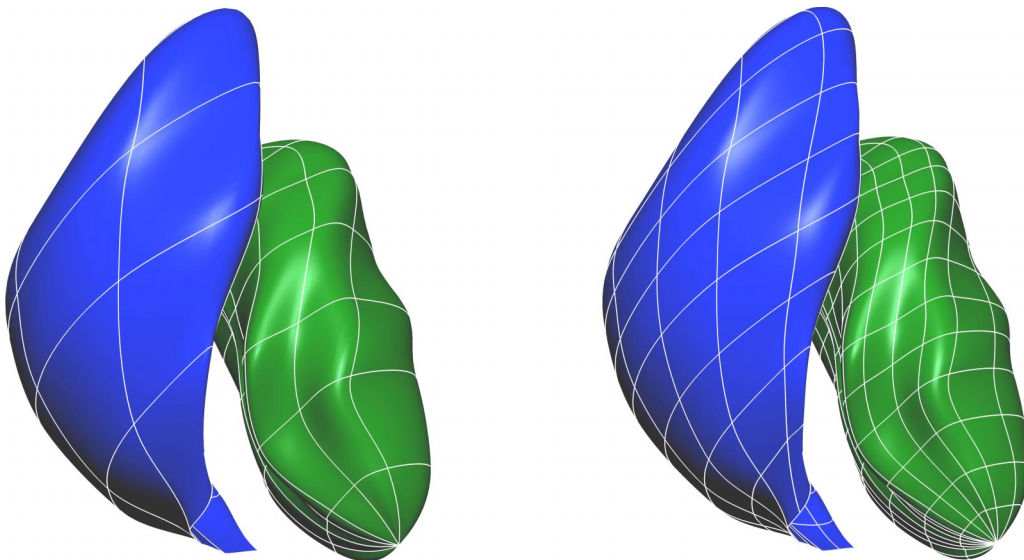


**Figure 5.14:** The result of refining the endocardial surfaces once in each direction. The left endocardial surface is shown in green, the right endocardial surface is blue and white lines show the element borders. On the left is the heart model created by fitting the geometric data and on the right, the computational model needed for a converged forward solution.

The geometric model described Section 4.4 was used to test the refinement level required for a converged forward solution. This was performed using the heart sources described in Sections 4.6.2

and 4.6.3 and imposing the boundary conditions described in Section 5.1.3.

### 5.6.1 Mesh Resolution

The full reference porcine model consisted of six regions. As explained in Section 4.4, the epicardial, left and right endocardial, left and right lung and skin surfaces were modelled. The full list of information about each surface of the model as it was refined is shown in Table B.1. One level of refinement is defined as refinement at  $\xi = 0.5$  once in each  $\xi$  direction.

A factorial design was used to determine the appropriate level of refinement for each of the regions. Each surface was refined while all other surfaces remained constant and the resulting solutions examined. More detailed information about each surface is shown for the different refinement levels of each surface is shown in Table B.1.

### 5.6.2 Potential Based Convergence

The potential based formula is governed by the generalised Laplace's equation throughout the entire domain. The dynamic dipole source described in Section 4.6.2 was used to calculate potentials on the epicardial surface. These potential distributions were then mapped through to the torso surface via a traditional epicardial potential to torso surface potential transfer matrix. Using this setup a range of simulations at different refinement levels were performed to quantify the effect of mesh resolution on solution convergence.

Since the use of the dipole source was to determine the appropriate mesh resolution for a traditional potential inverse, no blood masses were included in the forward simulations involving this source. Both endocardial surfaces were removed with this cardiac source and the passive material conductivities defined in Table 4.3 were used in the remaining four regions.

To quantify the changes between refined meshes only the potentials at the nodal positions from the least refined case (level 0) were used for the refinement comparisons. There were 37 sites on the epicardium and 254 sites on the torso surface used for comparisons.

Key events in the cardiac cycle were used as temporal markers for comparisons. They were peak P,

peak R, peak T and the QRS interval. These times and intervals were determined by solving the forward problem and examining the resultant signals on the dominant chest leads such as those shown in Figure 5.16.

An isoparametric formulation was used in the forward solutions, *i.e.*, the dependent variable (potential) was approximated using the same basis functions used for the geometry (cubic Hermite interpolation). Epicardial potentials were then calculated from the dipole source inside the heart as part of the solution and these potentials changed with heart mesh refinement. Therefore for this analysis, epicardial and torso surface potentials were compared.

To test whether a model with a certain refinement level had converged, a particular region was progressively refined until there was no significant change in the solution. To determine the appropriate resolution of the entire mesh, this process needed to be repeated with the other regions in the mesh at various levels of refinements as well. From this large number of simulations, a reference model was chosen which had each region at an appropriate resolution for a converged forward solution using bicubic Hermite elements. Detailed results of this series of simulations are presented in Tables (B.2)–(B.7).

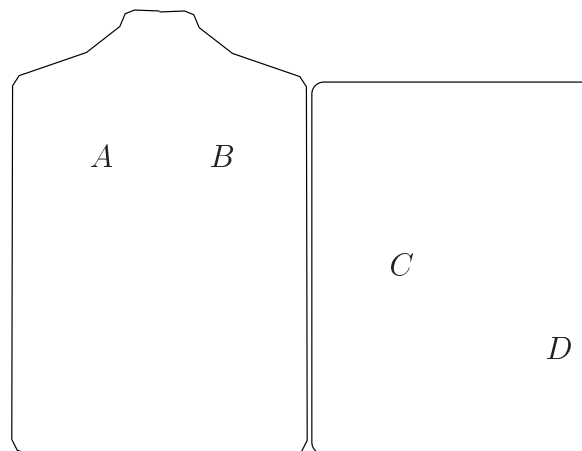


**Figure 5.15:** Four typical torso surface signals are shown for potential and activation forward convergence analysis simulations. Their locations on the torso surface are shown schematically above. These signals are shown graphically in Figure 5.16 and Figure 5.19. Layout as described in Figure 3.5.

For all cases, refining each of the surfaces had minimal effect upon the resultant torso surface potentials. In each of the simulations, if only the torso surface potentials were examined, then a converged solution was obtained with the first level refinement for each surface. However, by also examining the epicardial surface potentials a very different trend is encountered. As each

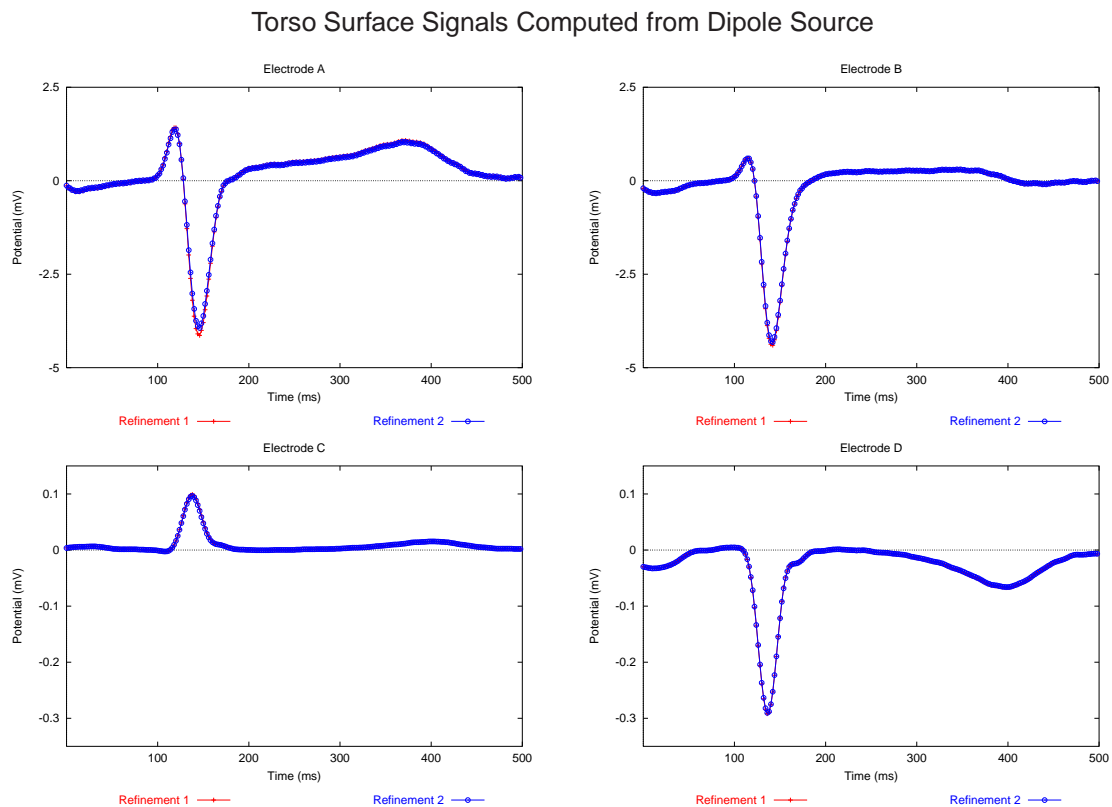


**Figure 5.16:** Torso surface signals using the dipole source described in Section 4.6.2. The resultant solutions with the heart refined once (red) and refined twice (blue) have been overlaid. All other regions are at the converged resolutions. The location of each electrode is shown schematically in Figure 5.15.

surface is systematically refined the magnitudes of the epicardial surface potentials changed greatly. The patterns of the signals (as shown by the similarity index error metric) are unchanged for all refinement levels but the magnitudes of the signals slowly converge as each surface is systematically refined.

The final converged model contains the epicardium refined to level 2, the left and right lung and the torso refined to level 1. This resulted in an average characteristic element size of approximately 5 mm for the epicardial surface, 10 mm for the lung surfaces and 18 mm for the torso surface. Torso potentials generated using this reference model 140 ms into the simulation are shown in Figure 5.17.

The convergence analysis was repeated using bilinear Lagrange basis functions (the interpolation which is eventually used in the inverse simulations). Similar trends were obtained when compared to the bicubic Hermite simulations and the same refinement was required to obtain a converged

solution. The results from these simulations are summarised in Table B.8 and Table B.9. Both interpolation functions show a linear rate of convergence as shown in Figure 5.18.

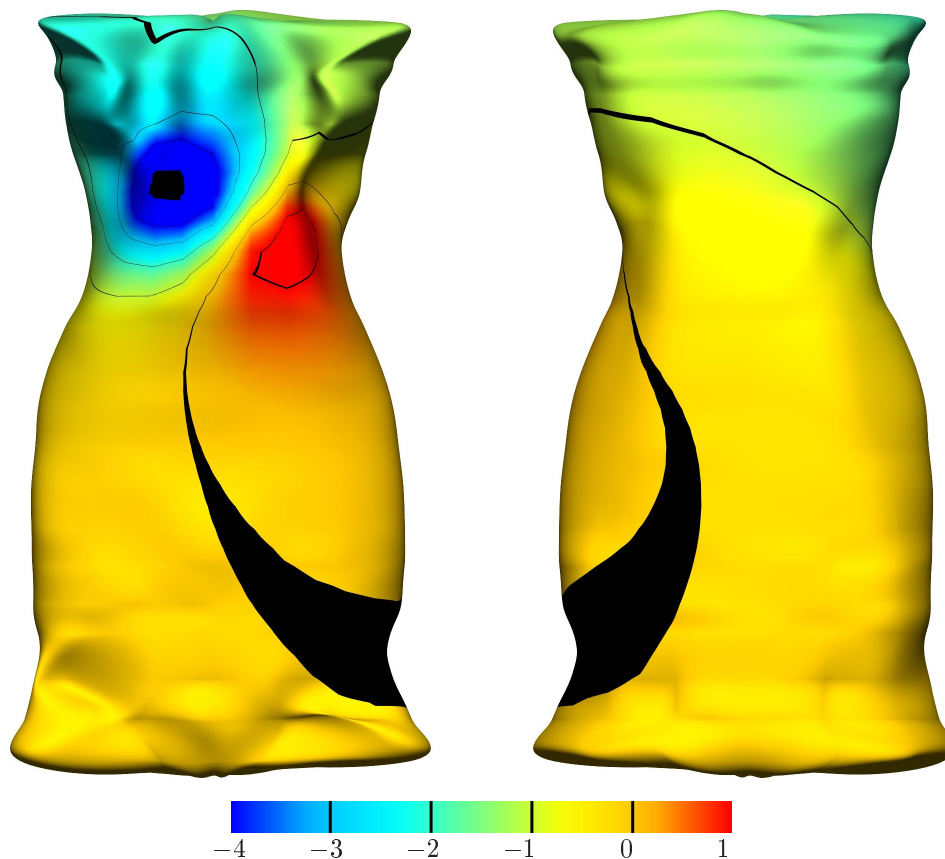


**Figure 5.17:** Torso surface potential fields (mV), 140 ms into the simulation, created by solving the forward problem and using the dipole source described in Section 4.6.2. The problem was solved using the converged mesh resolution, with all surfaces refined once in each direction, except the epicardial surface which was refined twice in each direction. Corresponding torso surface signals are shown in Figure 5.16. The anterior view is shown on the left and the posterior on the right.

The use of a dipole source meant that the epicardial potentials were calculated as part of the solution procedure. As the epicardial surface was refined, the potentials calculated at the epicardial nodal positions also changed. This was not the case when an activation cardiac source was used, as in Section 5.6.3, where the activation times are not numerically calculated for each refinement level.

## Convergence Comparison Between Bicubic Hermite and Bilinear Lagrange Basis Functions

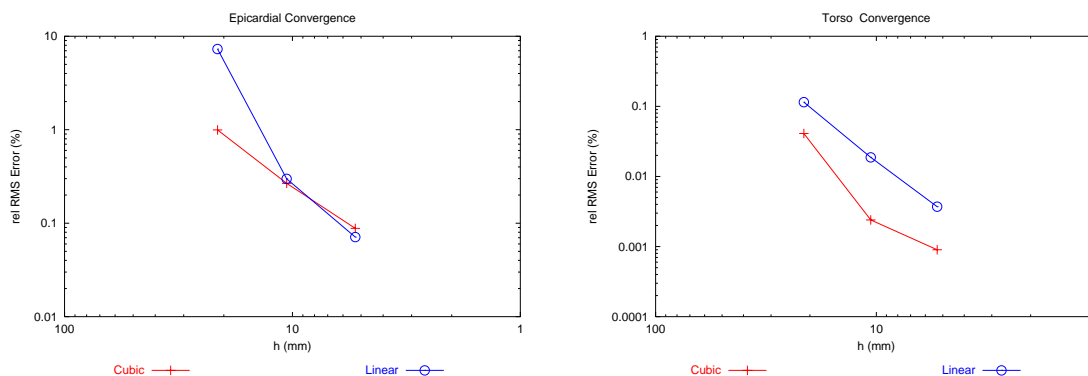


**Figure 5.18:** Forward convergence of generic model with dipole source using bilinear Lagrange and bicubic Hermite basis functions. The effect of refining the epicardial surface on the computed epicardial potentials (left) and the torso surface potentials (right) are compared when using different interpolating basis functions. The relative RMS error metric defined in Equation (3.8) is plotted against the average characteristic element size.

### 5.6.3 Activation Based Convergence

The activation based formulation maps activation times from the epicardial and endocardial surfaces through to the torso surface via a transmembrane to torso surface potential transfer matrix and from the epicardial and endocardial surfaces through to the epicardial surface via a transmembrane to epicardial surface potential transfer matrix. The same convergence analysis process described in Section 5.6.2 was repeated using the eikonal activation profile described in Section 4.6.3 except that only linear Lagrange interpolation was used. This interpolation scheme is the same as that used by the inverse procedures described in Chapter 6 and the inverse simulations presented in Chapter 7. The model contained all six surfaces and the conductivities defined in Tables 4.3 and 4.4 were used.

Since the activation sequence was derived from a ventricular model (Tomlinson 2000), only the QRS interval of the cardiac cycle was considered. As outlined in Section 4.6.3, the activation sequence had a duration of 52 ms. Key events of the QRS interval were used as temporal markers for comparisons. They were peak Q, peak R, peak S and the QRS interval. These times were again determined by solving the forward problem and examining the resultant signals in the dominant chest leads on the torso surface such as those shown in Figure 5.19.

As with Section 5.6.2, to quantify the changes between refined meshes the potentials at the nodal positions on the epicardial (37 sites) and torso surface of the unrefined model (254 sites) were used. Again, convergence was determined by altering the refinement level of a given region while holding

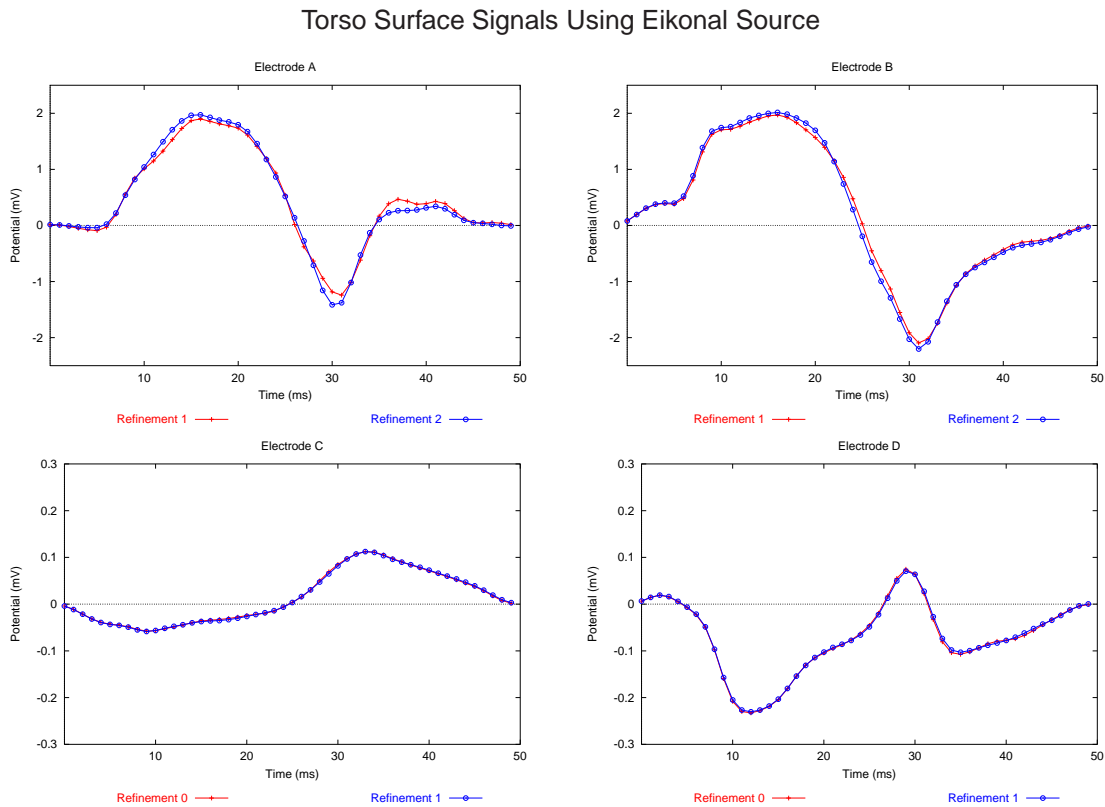


**Figure 5.19:** Torso surface signals using the eikonal source described in Section 4.6.3. The resultant solutions with the generic heart (red) and refined once (blue) have been overlaid. All other regions are at the converged resolutions. The location of each electrode is shown schematically in Figure 5.15.

all other regions constant. Detailed results for convergence analysis with an activation source are shown in Tables (B.11)–(B.19).

When using the activation based approach with the eikonal source, the solutions converged at a faster rate than the epicardial potential forward simulations with the dipole source. After one level of refinement all surfaces had an average error of less than 1% on both the computed epicardial and torso surface potentials. The final converged solution using the activation source required a single refinement in each  $\xi$  direction for each of the six surfaces. This resulted in an average characteristic element size of approximately 18 mm for the torso surface and 10 mm for the epicardial, ventricular chamber and lung surfaces. A potential map for the converged model 10 ms into the simulation is shown in Figure 5.20.



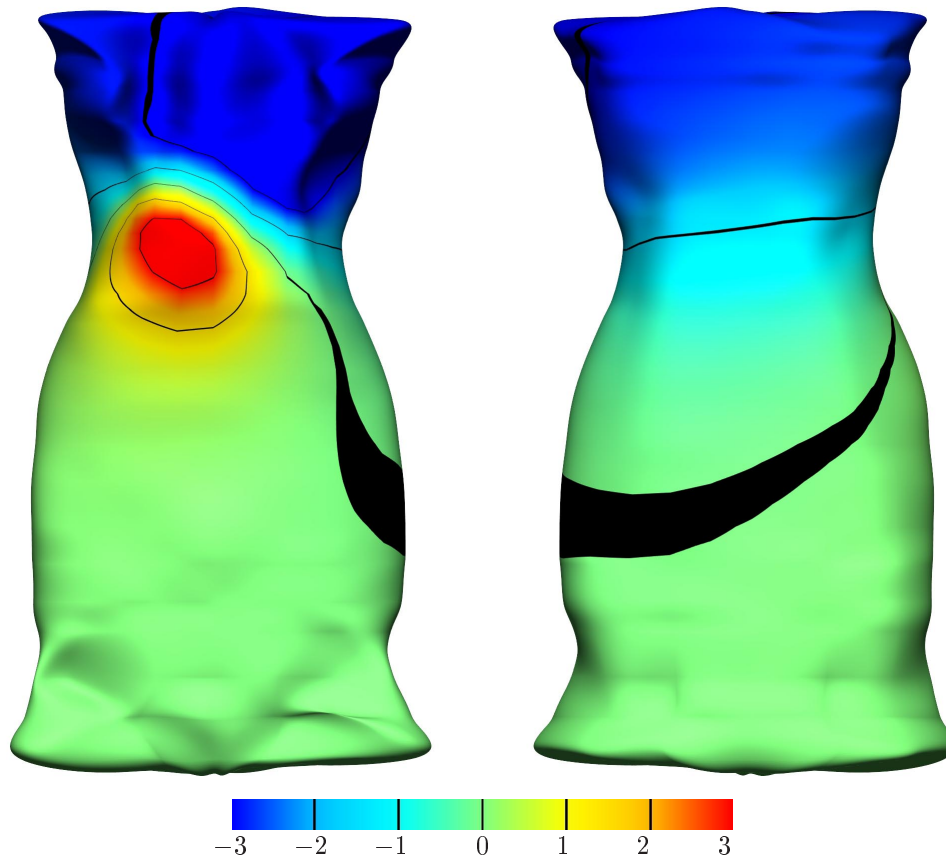


**Figure 5.20:** Torso surface potential map (mV), 10 ms into the simulation, created by solving the forward problem and using the eikonal activation source described in Section 4.6.3. The converged mesh resolution, with all surfaces refined once in each direction, was used. Corresponding torso surface signals are shown in Figure 5.19. Layout as described in Figure 5.17.

#### 5.6.4 Convergence Summary

The forward convergence analysis was performed using a dipole source and an activation cardiac source. Convergence was determined by performing a series of forward simulations and comparing the resultant epicardial and torso surface signals at common locations.

The dipole source calculated epicardial potentials as part of the solution process and used an epicardial to torso surface transfer matrix to calculate the torso surface potentials. Both bicubic Hermite and bilinear Lagrange basis functions were used as the interpolation function for the solution, with each producing similar results. To obtain a converged solution with the dipole source each surface was refined once in each direction and the epicardial surface was refined twice in each direction.

With the activation source, bilinear Lagrange basis functions were used as the interpolation function. This is the same basis function that is used with the inverse procedures described in Chapter 6. Epicardial potentials were calculated using a transmembrane to epicardial surface potential transfer matrix while torso surface potentials were generated using a transmembrane to torso surface potential transfer matrix. To obtain a converged solution with the activation source each surface only needed to be refined once in each direction despite only using a linear Lagrange basis function used to interpolate the solution.

# 6 *The Inverse Problem of Electrocardiology*

Quantitative interpretation of the multiply sampled ECG signals in terms of the underlying cardiac source generator is an inverse problem and various mathematical algorithms have been developed over the years in an attempt to solve this electrical imaging problem (*e.g.*, Barr & Spach 1978, Gulrajani, Roberge & Savard 1984, Martin, Pilkington & Morrow 1975, Oster & Rudy 1992). To date, none of these have been proven to be reliable and stable enough to be routinely used in a clinical situation.

Unless the inverse problem is posed in a particular manner, it is not uniquely determined (*i.e.*, there exist multiple cardiac electrical generator configurations that can give rise to the same thoracic ECGs). Earlier approaches to the inverse problem modelling the heart as a combination of a small number of fixed or moving dipoles (*e.g.*, Miller & Geselowitz 1978, Huiskamp 1998). This non-uniqueness has hampered attempts at solving the inverse problem and the resulting dipoles, also provide poor insight into the underlying cardiac function.

Currently, the most widely used formulation of the inverse problem of electrocardiology involves determining the epicardial potentials. It has been recognised that by posing the problem in terms of reconstructing epicardial potentials, the problem is uniquely determined (Yamashita 1982, Martin & Pilkington 1972), however the problem also becomes ill-posed. This means that the presence of any noise (which always exists in practice), will be amplified in the computed solution in an unknown and uncontrolled fashion.

The emergence of a general theory for such ill-posed problems (Tikhonov & Arsenin 1977) and the introduction of the ideas behind constraining the mathematical solutions have resulted in the large number of variants of the inverse algorithms in existence today in the field of electrocardiographic imaging. Regularised solutions to the inverse problem of electrocardiography first appeared in

the mid-70s (Barr & Spach 1978). Since then, considerable effort has been put into finding more reliable and controllable inverse solutions. Initially, much of this effort went towards studying the effects of various regularisation constraints and the choice of the regularisation parameter. It has now been recognised that there is an increasing need to impose some form of temporal constraint on the solutions (Gulrajani 1998) due to the poor performances of algorithms which only regularise in the spatial domain and also the ability to make use of the temporal correlation of solutions at adjacent time steps. Recently, elaborate regularisation techniques which combine both spatial and temporal constraints on the solutions have been developed (Oster & Rudy 1992, Greensite & Huiskamp 1998, Brooks, Ahmad, MacLeod & Maratos 1999). One of the main problems with a regularisation technique is that it is not known *a priori* the degree of regularisation to apply. With a known solution, it is possible to obtain an optimal regularisation parameter which will optimally reconstruct the desired solution. However, since many of the regularisation techniques are based on a general mathematical approach for ill-posed problems they fail to account for the underlying physiological processes governing the generation of the body surface potentials (namely an evolving wave of activation) and are lacking in reliability.

When dealing with epicardial potentials, there exist sharp gradients between the unpolarised and depolarised regions (*i.e.*, at the site of the activation wavefront). These sharp transition zones mean that the problem must be solved at a resolution capable of capturing this detailed information. These regions are also not well handled by the standard regularisation techniques described in Section 6.2. In addition, many of the algorithms construct the inverse solution by treating each time instance independently, which, at least theoretically, is not the optimal way to proceed with such temporally correlated information as is present in ECG signals (Oster & Rudy 1992, Greensite & Huiskamp 1998).

The principal interest in electrically imaging the heart is to estimate the real electrical generators present within the myocardium. Due to the proximity of the epicardial potentials to the actual electrical source they are able to provide a close representation of the electrophysiological processes occurring within the myocardium (Spach & Barr 1975). However, it is clear that even if the inverse problem can be accurately and reliably solved in terms of the epicardial potentials, the results need to be interpreted in a form which is clinically useful as a diagnostic aid. Reconstruction of the myocardial activation times is a formulation which is still close to the underlying physiology of the problem and inherently more stable than the epicardial potential approach. By posing the problem in terms of activation times, the solution domain can be reduced from temporally and spatially varying potentials to just spatially varying activation times and thus there exists the possibility of a better-posed problem – while still maintaining what is, in some regards, the most physiologically

important feature of the solutions (Brooks & MacLeod 1997). In addition, by following an activation based approach, the solution no longer possesses sharp gradients (which makes the problem mathematically difficult) as it is essentially representing a continuous evolving wavefront. The solution method using the activation based formulation is described in detail in Section 6.3.

## 6.1 Singular Value Decomposition

Singular Value Decomposition (SVD) is a mathematical technique which can determine the principal components of the information contained within a matrix (Press, Teukolsky, Vetterling & Flannery 1992). If an SVD is applied to a transfer matrix  $\mathbf{A}$ , then the transfer matrix can be rearranged to be of the form

$$\begin{aligned}\mathbf{A} &= \mathbf{U}\mathbf{\Sigma}\mathbf{V}^T \\ &= \sigma_i \mathbf{u}_i \mathbf{v}_i^T\end{aligned}\tag{6.1}$$

where  $\mathbf{U}$  and  $\mathbf{V}$  are orthogonal matrices (their columns are orthonormal) and  $\mathbf{\Sigma}$  contains the weighting singular values while  $\mathbf{u}_i$  and  $\mathbf{v}_i$  are vectors forming the orthogonal matrices and  $\sigma_i$  are the singular values with  $i = 1, \dots, N$ . The singular values are typically sorted in decreasing order with the larger values corresponding to principal components of the  $\mathbf{A}$  matrix. The eigenvectors corresponding to small singular values are assumed to correspond to random noise space and are often discarded to create a more stable system of equations.

To understand how regularisation can stabilise an inverse problem, Hansen (1992) rearranged the standard inverse problem formulation to be of the form

$$\begin{aligned}\phi_H &= (\mathbf{A}^T \mathbf{A} + \lambda \mathbf{I})^{-1} \mathbf{A}^T \phi_B \\ &= \left( \frac{\sigma_i}{\sigma_i^2 + \lambda^2} \right) v_i u_i^T \phi_B\end{aligned}\tag{6.2}$$

where  $(\mathbf{A}^T \mathbf{A} + \lambda \mathbf{I})^{-1}$  is defined as the pseudo inverse (further explained in Section 6.2),  $\lambda$  is a regularisation parameter and  $\mathbf{I}$  is the identity matrix.

By examining Equation (6.2), when  $\sigma_i$  is small, the solution becomes unstable due to the presence of the  $\sigma_i^2$  term in the denominator. This can be overcome by two methods. The regularisation term  $\lambda$  can be increased to help to stabilise the solution, especially for values of  $\sigma \gg \lambda$ . This technique is further explained in Section 6.2.1. An alternative approach involves totally removing the effects

of the equations which correspond to small singular values as explained in Section 6.2.2. Both the truncation and regularisation techniques are employed in the activation based inverse approaches in Section 6.3, and by Greensite's spatial and temporal potential regularisation technique described in Section 6.2.3.

An SVD can also be applied to the torso surface signal data matrix  $\Phi_B$  (which stores the signal information in each row of the matrix and the potentials each time instant in the columns of the matrix) to determine its principal components. This factorises the spatial eigenvectors into  $U$  and the temporal eigenvectors into  $V$ . The columns of  $U$  and  $V$  corresponding to small singular values are assumed to correspond to Gaussian noise and typically removed (Huiskamp & Greensite 1997).

The method of determining when the singular values corresponding to noise space can be estimated by plotting the log of the ordered singular values against the rank of the matrix. This typically results in a characteristic 'L' shaped curve as shown in Figure 6.1. It has been postulated that the points below which the curve levels off corresponds to noise space (Huiskamp & Greensite 1997). A number of different methods are used for determining the best place at which to cut off the singular values such as the Akaike Information Criterion (Akaike 1974) and the point of steepest curvature. However, none of these have been found to be truly reliable in practice. The points selected as the cutoff of the singular values are given in Figure 6.1 by the horizontal and vertical green lines. The upper left quadrant corresponds to the significant singular values and the lower right quadrant the small singular values which are discarded.

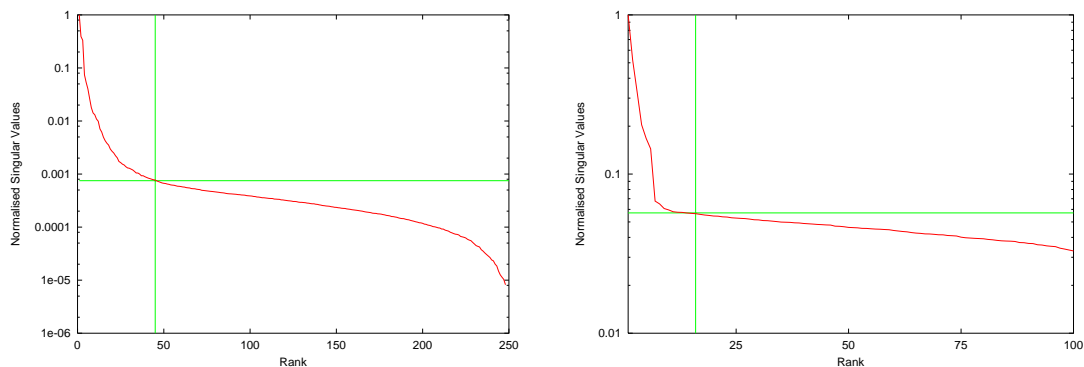


**Figure 6.1:** Singular value spectra of two different torso surface signal matrices. On the left are the singular values from a signal matrix recorded from a normal male volunteer and on the right simulated signals from the double point cardiac source described in Section 4.6.4. The singular values have been normalised and plotted on a log scale to emphasise the curvature in the singular values. The lower right quadrant (as defined by the vertical and horizontal green lines) correspond to the ranks and singular values which have been considered to correspond to noise.

## 6.2 Epicardial Potential Formulation

The standard solution approach to solving the epicardial inverse problem of electrocardiography is based on solving a set of independent quasi-static problems of the form given by

$$\Phi_B = \mathbf{A}\Phi_H \quad (6.3)$$

where  $\mathbf{A}$  is the geometric noise-corrupted transfer matrix and  $\Phi_B$  is a noise-corrupted body surface potential distribution and  $\Phi_H$  is the unknown epicardial potential solution. If only the depolarisation phase of the heart cycle is modelled then  $\mathbf{A}$  it is valid to assume this remains constant as the heart does not contract during this period. As the potential distributions on the torso and heart vary temporally, the solutions can be stored as corresponding columns in each matrix.

By treating every individual equation independently and solving each time step (or column)  $\phi_B$  of  $\Phi_B$  for its corresponding solution for  $\phi_H$ , results in

$$\phi_H = \mathbf{A}_{\lambda_t}^{\dagger} \phi_B \quad (6.4)$$

where  $\mathbf{A}_{\lambda_t}^{\dagger}$  is the regularised (either Tikhonov or Truncated Singular Value Decomposition (TSVD)) pseudo inverse of  $\mathbf{A}$  at time  $t$ . These two families of regularisation methods are currently the most widely used in solving the epicardial inverse problem of electrocardiology. These two spatially regularising families as well as the temporally and spatially regularised solution method of Greensite & Huiskamp (1998) are further described in Sections (6.2.1)–(6.2.3).

### 6.2.1 Tikhonov Regularisation

The least squares solution to inverse problem using a Tikhonov regularisation scheme is given by

$$\phi_H = \min \|\phi_B - \mathbf{A}\phi_H\|_2 + \lambda \|\mathbf{R}\phi_H\|_2 \quad (6.5)$$

where the first term of Equation (6.5) is the least squares solution to Equation (6.3) and the second term regularises the solution by imposing a penalty function on the solution via the regularisation matrix  $\mathbf{R}$  and the weighting term  $\lambda_t \in \mathbb{I}$  and positive.

which determines the amount of regularisation to be applied.

The regularisation matrix changes depending on the type of Tikhonov regularisation used. For zero-order Tikhonov regularisation,  $\mathbf{R} = \mathbf{I}$  (the identity matrix) for first-order Tikhonov  $\mathbf{R} = \mathbf{G}$  (the surface gradient) and for the second-order Tikhonov  $\mathbf{R} = \mathbf{L}$  (the surface Laplacian). Each of the regularisation methods constrains the solution in different ways. The amplitude of the solution is constrained with the use of the zero-order Tikhonov, the surface gradient for the first-order and the surface curvature of the second-order Tikhonov methods. The  $\lambda$  parameter may be altered to vary between different time steps as denoted by the subscript  $t$ . Thus the pseudo inverse for each time step is given by

$$\mathbf{A}_{\lambda_t}^\dagger = (\mathbf{A}^T \mathbf{A} + \lambda_t^2 \mathbf{R}^T \mathbf{R})^{-1} \mathbf{A}^T \quad (6.6)$$

It has previously been found using an eccentric sphere model that the zero-order Tikhonov regularisation method performs as well as those of higher order (Messinger-Rapport & Rudy 1988), therefore the zero-order Tikhonov technique has widely been adopted as the standard Tikhonov technique for the epicardial potential inverse methods.

The solution to Equation (6.3) using zero-order Tikhonov regularisation can be written as

$$\begin{aligned} \phi_H &= (\mathbf{A}^T \mathbf{A} + \lambda_t^2 \mathbf{I})^{-1} \mathbf{A}^T \phi_B \\ &= \sum_{n=1}^N f_n(t) \frac{\langle u_{A,n}, \phi_B \rangle}{\sigma_{A,n}} v_{A,n} \end{aligned} \quad (6.7)$$

where  $\langle \cdot, \cdot \rangle$  is the inner product of two column vectors,  $u_{A,n}$  and  $v_{A,n}$  are the  $n^{\text{th}}$  vectors from the SVD of  $\mathbf{A}$ ,  $\sigma_{A,n}$  is the  $n^{\text{th}}$  singular value from the SVD of  $\mathbf{A}$  and  $f_n(t)$  are the Tikhonov filter factors given by

$$f_n(t) = \frac{\sigma_{A,n}^2}{\sigma_{A,n}^2 + \lambda_t^2} \simeq \begin{cases} 1 & \sigma_{A,n} \gg \lambda_t \\ \sigma_{A,n}^2 / \lambda_t^2 & \sigma_{A,n} \ll \lambda_t \end{cases} \quad (6.8)$$

Hence the filter factors filter out the contribution of  $\phi_H$  corresponding to the small singular values less than the value defined by  $\lambda_t$  whilst leaving the SVD components corresponding to large singular values almost unaffected. For values of  $\sigma \simeq \lambda_t$ , the solution begins to be damped by the regularisation.



## 6.2.2 Truncated SVD Regularisation

Another method of treating the ill-conditioned nature of the transfer matrix  $\mathbf{A}$  is to derive a new problem with a well-conditioned rank-deficient transfer matrix (Hansen & O'Leary 1993). A rank-deficient matrix which theoretically does not contain information pertaining to noise and error can be obtained by truncating the SVD expansion defined in Section 6.1, *i.e.*,

$$\mathbf{A}_{\lambda_t} = \sum_{n=1}^{\lambda_t} \mathbf{u}_n \sigma_n \mathbf{v}_n^T \quad \lambda_t \leq N \quad (6.9)$$

where  $N$  is the full rank of the matrix and the size of  $\lambda_t$  determines the level of regularisation for time  $t$  and  $\lambda_t \in \mathbb{I}$  and positive.

The TSVD solution is then obtained by minimising the objective function,

$$\phi_H = \min \|\mathbf{A}_{\lambda_t} \phi_H - \phi_B\|_2 \quad (6.10)$$

The pseudo inverse for the problem is given by

$$\mathbf{A}_{\lambda_t}^\dagger = \tilde{\mathbf{V}} \tilde{\Sigma} \tilde{\mathbf{U}}^T \quad (6.11)$$

where  $\tilde{\mathbf{U}}$  and  $\tilde{\mathbf{V}}$  contain the first  $\lambda_t$  columns of the orthogonal matrices and  $\tilde{\Sigma}$  are the first  $\lambda_t$  singular values.

Thus the solution to Equation (6.3) using TSVD regularisation is given by

$$\begin{aligned} \phi_H &= \tilde{\mathbf{V}} \tilde{\Sigma} \tilde{\mathbf{U}}^T \phi_B \\ &= \sum_{n=1}^{\lambda_t} \frac{\langle \mathbf{u}_{A,n}, \phi_B \rangle}{\sigma_{A,n}} \mathbf{v}_{A,n} \end{aligned} \quad (6.12)$$

This formulation is similar to that of the Tikhonov regularisation method defined in Equation (6.7) where the terms up to and including  $\lambda_t$  are included in the summation and have a filter factor of one whilst the remaining terms have a filter factor of zero.

### 6.2.3 Greensite Temporal & Spatial Regularisation

Standard regularisation techniques have achieved only limited success in solving the inverse problem of electrocardiology (Brooks et al. 1999). The major drawback with these regularisation schemes is that they impose non-physiological constraints on the problem and ignore the temporal dependency of the data.

The method of Greensite & Huiskamp (1998) regularises both the temporal and the spatial domains of the problem. The equations associated with each time point are regularised, based on the idea (and proved theoretically in Greensite & Huiskamp (1998)) that a solution based on optimal regularisation of each integral equation associated with each *principle component* of the data will be more accurate than a solution based on the optimal regularisation of each integral equation associated with each *time point*. By imposing no additional *a priori* constraints, this new method addresses uncorrelated noise only and with the presence of dominating correlated noise such as geometric error it may only be successful in producing a cleaner signal (Greensite 1992).

Instead of treating each column (or time step) of  $\Phi_B$  independently, they are treated as a family of solutions. The SVD of the body surface potentials are given by

$$\begin{aligned}\Phi_B &= U_B \Sigma_B V_B^T \\ &= \sum_i \mathbf{u}_{B,i} \sigma_{B,i} \mathbf{v}_{B,i}\end{aligned}\quad (6.13)$$

where  $U_B$  represents the spatial components,  $V_B$  the temporal components and  $\Sigma_B$  the singular values of the signal matrix.

Thus Equation (6.3) can be solved by

$$\begin{aligned}\Phi_H &= A_{\lambda_i}^\dagger \Phi_B \\ &= \sum_i \sigma_{B,i} A_{\lambda_i}^\dagger \mathbf{u}_{B,i} \mathbf{v}_{B,i}\end{aligned}\quad (6.14)$$

where  $A_{\lambda_i}^\dagger$  is the pseudo inverse for each individual equation  $i$  determined either from Tikhonov regularisation with regularisation parameter  $\lambda_i$  or TSVD regularisation with a truncation rank  $\lambda_i$ .

The solution to Equation (6.14) is obtained by solving a two step problem. Initially a system of

linear equations for each equation  $i$  is solved, *i.e.*,

$$\mathbf{u}_{B,i} = \mathbf{A}\boldsymbol{\gamma}_i \quad (6.15)$$

whose solution is obtained by

$$\boldsymbol{\gamma}_i = \mathbf{A}_{\lambda_i}^\dagger \mathbf{u}_{B,i} \quad (6.16)$$

*i.e.*, a traditional Tikhonov or TSVD inverse applied to  $\mathbf{u}_{B,i}$ , the spatial basis vector, rather than  $\boldsymbol{\phi}_B$ . In the context of a zero-order Tikhonov regularisation, the solution to Equation (6.16) is given by

$$\boldsymbol{\gamma}_i = \sum_{n=1}^N \langle \mathbf{u}_{A,n}, \mathbf{u}_{B,i} \rangle \frac{\sigma_{A,n}}{\sigma_{A,n}^2 + \lambda_i^2} \mathbf{v}_{A,n} \quad (6.17)$$

and similarly for the TSVD regularisation technique

$$\boldsymbol{\gamma}_i = \sum_{n=1}^{\lambda_i} \frac{\langle \mathbf{u}_{A,n}, \mathbf{u}_{B,i} \rangle}{\sigma_{A,n}} \mathbf{v}_{A,n} \quad (6.18)$$

Finally, the solution to Equation (6.3) is given by

$$\boldsymbol{\Phi}_H = \sum_i \sigma_{B,i} \boldsymbol{\gamma}_i \mathbf{v}_{B,i} \quad (6.19)$$

#### 6.2.4 Determining the Regularisation Parameter

Determining the level of regularisation to apply to a solution has been found to be critical in obtaining an appropriate solution (Hansen 1998). This typically involves determining the value to assign to  $\lambda_i$ . If too much regularisation is introduced the solution will be over-damped while if insufficient regularisation is used, the solution will be too noisy.

There exist a number of *a posteriori* methods to obtain the ‘best’ regularisation parameter. Commonly accepted methods are generalised cross validation (GCV) method of Golub, Heath & Wahba (1979), the L-Curve curve method of Hansen & O’Leary (1993), the zero-crossing method of Johnston & Gulrajani (1997) and the Composite RESidual and Smoothing Operator (CRESO) criterion

of Colli Franzone, Guerri, Taccardi & Viganotti (1985). If the heart solution is also known (which is not usually the case in practice) then it is possible to compute the optimal regularisation parameter using the optimal criterion to compute a theoretical optimal solution given each regularisation technique.

### Optimal Criterion

The optimal criterion, although not feasible except in simulation studies, places a theoretical limit on the optimal performance of a given regularisation scheme and thus leads to a valid comparison measure between different regularisation approaches. It uses the known heart solution to determine the optimal regularisation parameter which best matches the known solution.

The optimal solution for Tikhonov and TSVD regularisation schemes can be obtained by choosing the optimal regularisation parameters  $\lambda_t$  at time  $t$  for the solution to Equation (6.4). The optimal regularisation parameter is determined as the parameter which minimises

$$\left\| \phi_{H,i} - \hat{\phi}_{H,i} \right\|_2 \quad (6.20)$$

where  $\hat{\phi}_{H,i}$  is the  $i^{\text{th}}$  regularised solution and forms the  $i^{\text{th}}$  column of the regularised solution.

The optimal regularised solution to Greensite's potential method can be obtained by regularising every  $i^{\text{th}}$  equation individually since the columns of  $\mathbf{U}_B$  are orthogonal, hence are linearly independent. Thus for every solution  $\gamma_i$  of Equation (6.16) the optimal regularisation parameter is the value which minimises

$$\left\| \sigma_{B,i} \gamma_i v_{B,i} - \Phi_H \right\|_F \quad (6.21)$$

where  $\| \cdot \|_F$  is the Frobenius norm.

### L-Curve Criterion

The L-Curve method uses a plot of all valid regularisation parameters ( $\lambda$ ) of the regularisation objective function ( $\mathbf{R}\phi_H$ ) against the corresponding residual objective function ( $\mathbf{A}\phi_H - \phi_B$ ). This determines a value of  $\lambda$  which provides a balance between the two components which are minimised in Equation (6.5). For discrete ill-posed problems it turns out that the L-curve, when

plotted on a log-log scale, often has a characteristic L-shaped appearance with a corner separating the vertical and horizontal components of the curve as shown in Figure 6.2. The point of maximum curvature (or the corner of the plot) is used to determine the optimal regularisation parameter to use. As long as the uncorrelated Gaussian noise present in  $\phi_B$  dominates the correlated geometric noise, in  $\mathbf{A}$ , this curve is in the form of an ‘L’. However, with high quality recording systems the Gaussian noise levels are typically low and there are difficulties in obtaining the point of highest curvature.

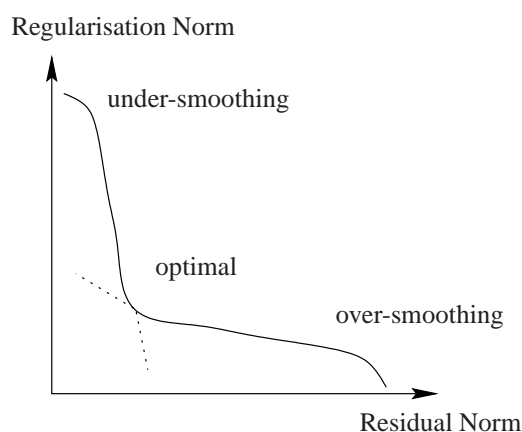


**Figure 6.2:** The L-curve is a log-log plot of the residual norm,  $\log \left\| \mathbf{A} \hat{\phi}_H - \phi_B \right\|_2$ , against the regularisation norm,  $\log \left\| \mathbf{R} \hat{\phi}_H \right\|_2$ . This plot is typically of the form of an ‘L’. The corner of the ‘L’ strikes a balance between the residual of the solution and the regularisation norm.

With little regularisation introduced, the solution is dominated by the residual norm. This situation is called under-smoothing and corresponds to the upper left component of the curve as shown in Figure 6.2. When a large amount of regularisation is introduced, then the solution is dominated by the regularisation error. This situation is called over-smoothing and corresponds to the lower right portion of the plot.

The plot basically consists of two components which intersect at what is considered an optimal value to choose for  $\lambda$ . For low values of the regularisation parameters, corresponding to the vertical section of the L-curve, the solution is sensitive to small changes in the value of  $\lambda$ . When large amounts of regularisation are introduced, the solution becomes dominated by the residual norm. This corresponds to the horizontal section of the L-curve which is not sensitive to changes in the regularisation value.

### CRESO Criterion

The Composite RESidual and Smoothing Operator (CRESO) criterion, proposed by Colli Franzone et al. (1985), finds the regularisation parameter for which the difference between the derivative of the residual term and the derivative of the smoothing term is maximised. The CRESO regularisation parameter is determined as the smallest value of  $\lambda^2$  that results in a relative maximum of the function,

$$C(\lambda_t) = \|\phi_H\|_2^2 + 2\lambda_t^2 \frac{d}{d\lambda_t} \|\phi_H\|_2^2 \quad (6.22)$$

where the  $C(\lambda_t)$  is the derivative of the function  $B(\lambda_t)$ , where

$$B(\lambda_t) = \lambda_t^2 \|\phi_H\|_2^2 - \|\mathbf{A}\phi_H - \phi_B\|_2^2 \quad (6.23)$$

As the CRESO function is only strictly defined for a continuous regularisation parameter it cannot be used for the discrete TSVD approximation.

### Zero-Crossing Criterion

The zero-crossing criterion of Johnston & Gulrajani (2000) is another method of determining the corner of the L-Curve. It aims to find the appropriate regularisation parameter by solving the function  $B(\lambda_t) = 0$  given in Equation (6.23) for the smallest value of  $\lambda_t$ . It has the advantage that it is simpler to compute and has previously been found to perform as well and sometimes better than the CRESO criterion or L-curve methods (Johnston & Gulrajani 1997).

## 6.3 Myocardial Activation Time Formulation

The formulation of the inverse problem in terms of myocardial activation times was first performed by Cuppen & van Oosterom (1984). The recent development of a new algorithm by Huiskamp & Greensite (1997) has led to further development in this field. For diagnosing arrhythmias, activation times provide a better representation of the electrical activity of the heart than epicardial potentials. The problem size has been reduced by a dimension only timing information is modelled on the heart surfaces. By tracking the activation wavefront instead of the potential values throughout the

heart, a lower resolution mesh is typically required. This smaller problem size allows the possibility of a better posed problem than that provided by a standard potential approach.

### 6.3.1 Determining & Refining the Activation Sequence

The inverse problem can be formulated as an optimisation problem which attempts to determine an appropriate cardiac source which matches the known torso surface potentials. By using the relationships defined in Section 5.4, the derivatives of the torso surface potentials with respect to the activation times on the heart can be calculated. Using an initial activation sequence, as estimated by the critical point algorithm, an optimisation loop can be used to solve multiple forward problems and adjust the heart activation times to minimise the differences between the known and computed torso surface potentials. This is used to iteratively refine the activation sequence.

The ultimate test of the accuracy of an inverse algorithm is a direct comparison between the known input and the inversely computed cardiac activation field  $\tau(\mathbf{x})$ . However, without invasive measurements these are not available for comparison. Typically, only the torso surface potentials are known and the only measure of error which can be used for a solution is a difference measure between the recorded and calculated torso surface signals.

The most simple and common approach is to use the sum of squares difference between the recorded and calculated torso surface potentials as the error measure (Huiskamp & Greensite 1997, Fischer 1999), *i.e.*,

$$\left\| \phi_B - \hat{\phi}_B \right\|_2^2 \quad (6.24)$$

where  $\phi_B$  are the recorded body surface potentials and  $\hat{\phi}_B = \mathbf{A} \tau(\mathbf{x})$  are the computed body surface potentials generated from the activation field on the myocardial surfaces for each time step.

Alternative choices for the residual vectors include using a similarity index (as defined in Equation (3.9)) as a measure of the differences between the two sets of torso surface potentials. As the goal is to maximise the similarity index between the two signal sets, the residual function can then be formulated as

$$\left\| 1 - \text{SI}(\phi_B, \hat{\phi}_B) \right\|_2^2 \quad (6.25)$$

A better objective function may involve employing both of these residuals (or additional ones) in the form,

$$\left\| \left( \phi_B - \hat{\phi}_B \right) \right\|_2^2 + \lambda_1 \left\| \left( 1 - \text{SI} \left( \phi_B, \hat{\phi}_B \right) \right) \right\|_2^2 \quad (6.26)$$

where  $\lambda_i$  are parameters controlling the degree of weighting of each residual component.

It is also possible to optimise the parameters which define the shape of the activation function (*e.g.*,  $\omega$ ,  $a$  and  $b$ ) as defined in Equation (5.4) and the passive and bidomain conductivity values of the model. However, in practice, these values are not altered as part of the optimisation procedure as the problem becomes ill-posed with too many DOF being optimised.

### 6.3.2 Estimation of the Activation Sequence

The optimisation approach for determining the activation times as described in Section 6.3.1 requires an initial estimate which is then gradually improved and refined according to the forward projected body surface potentials. An accurate initial estimate of the activation field is crucial to prevent the optimisation phase converging to a local minimum (Huiskamp & van Oosterom 1988). The quality of the initial estimate will be related to the quality of the final solution. The critical point algorithm provides a good initial estimate of the activation field on the heart surfaces.

This algorithm revolves around the identification of the critical points and times of the surface activation function (*i.e.*, epicardial and endocardial breakthrough/termination points and times) (Huiskamp & Greensite 1997). The approach involves the use of a modified MUSIC (Multiple Signal Classification) algorithm from antenna theory (Schmidt 1986). It arises from the observation that when an evolving cardiac activation wavefront intersects the endocardial or epicardial surface a ‘hole’ develops in the wavefront. The ‘holes’ developed in the propagating wavefront, when it intersects the epicardial surface, results in a changed slope in the temporal ECG, leading to a step discontinuity or ‘jump’ in the first derivative of the ECG traces (Greensite 1992). The times at which these discontinuities occur identify the critical times associated with the critical points.

If  $\tau(\mathbf{x})$  is defined to be the activation time on the heart surface ( $\Gamma_H$ ) at location  $\mathbf{x}$  and if the wavefront breaks through at location  $\mathbf{x}'$ , then  $\nabla\tau(\mathbf{x}') = 0$  and this point is considered to be a critical point. This time  $\tau(\mathbf{x}')$  at which this breakthrough occurs is the critical time corresponding to the critical point.



The critical points  $\mathbf{x}'$  correspond to extrema sites on the map of the heart surface activation times (*i.e.*, minima, maxima or saddle points). The epicardial breakthrough of the transmural wavefront arriving from the endocardium is identified by a minimum in the epicardial activation maps, sites where the epicardial wavefront dies out would be a maximum and a collision of two epicardial wavefronts would constitute a saddle point.

### 6.3.3 Critical Points & Times

Following considerable mathematical manipulation (Greensite 1995), this critical point observation leads to two important results:

1.  $\mathbf{x}'$  is a critical point of  $\tau(\mathbf{x})$  with critical time  $\tau(\mathbf{x}')$   $\iff \mathbf{a}$  is in the space spanned by the spatial eigenvectors of  $\phi_B$ , where  $\mathbf{a}$  is the column of the transfer matrix from  $\phi_m$  to  $\phi_B$  corresponding to the point  $\mathbf{x}'$ .
2. With all critical points of  $\tau(\mathbf{x})$  determined, the computation of  $\tau(\mathbf{x})$  (on both the epicardial and endocardial surfaces) is a well-posed problem.

Examples of critical points in a simulated activation wavefront are shown in Figure 6.3. They show the activation wavefront (gold surface) computed by Tomlinson (2000) as it collides with the epicardial and endocardial surfaces. The heart is viewed from the apex with the epicardial surface displayed with a transparent material, the left ventricular surface in green and the right ventricular surface in blue. The left-most image shows the initial activation sites representing the Purkinje sites, followed by the first and second critical points near the right ventricular wall in the middle and right images.

The key assumption required to prove the first point above is that the change in transmembrane potential as the activation wavefront passes each point is modelled as a uniform step jump, as shown in Equation (5.4) and Figure 5.4. This is not a practical restriction for normal hearts, but does imply that the maximal temporal resolution is the duration of a transmembrane upstroke and the maximal spatial resolution is the width of the activation wavefront.

To compute the critical points and times, two inputs are required: the ‘recorded’ torso surface potential matrix  $\Phi(\mathbf{y}, t)$  and the transfer matrix  $\mathbf{A}(\mathbf{x}, \mathbf{y})$  which maps from transmembrane potentials to body surface potentials. The signal matrix  $\Phi(\mathbf{y}, t)$  is of size number of electrodes  $\times$  time steps, where  $\mathbf{y}$  is a point on the torso surface,  $t \in [1, T]$  and  $T$  is the total number of time steps in the

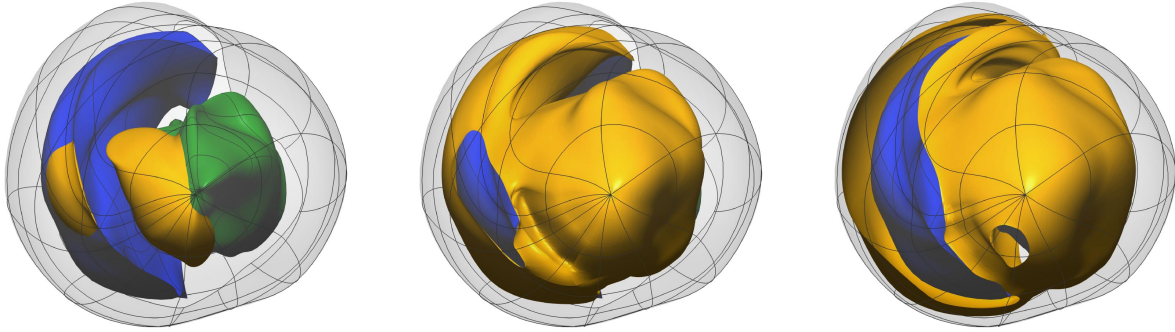


**Figure 6.3:** Critical points and times as an activation wavefront from Tomlinson (2000) collides with the heart walls. The left-most image shows the initial activation sites near the endocardial surfaces. The middle and right images show critical points as the activation wavefront (gold surface) collides with the epicardial surface and a hole is formed in the wavefront. The heart is viewed from the apex with the epicardium shown as a transparent surface, the left ventricular surface in green and the right ventricular surface in blue.

torso surface signals. Essentially each column of the matrix contains the potential information at each electrode at a particular instant in time and forms a body surface potential map as described in Section 1.3. Each row of the signal matrix corresponds to the potential recorded by a particular electrode over time. It is essentially storing an ECG trace for the electrode, similar to those shown in Figure 1.8.

The transmembrane potential to torso surface potential transfer matrix  $\mathbf{A}$  (as constructed in Section 5.3) maps from locations on the epicardial and endocardial surfaces ( $\mathbf{x}$ ) to points on the torso surface ( $\mathbf{y}$ ). This contains the geometrical and conductivity information of the model.

### 6.3.4 Critical Point Function

A reciprocal of distance from signal space (Greensite 1995) can be constructed by

$$M_1^T(\mathbf{x}) = \left( 1 - \sum_{r=1}^R [\bar{a}(\mathbf{x}, \mathbf{y}) \cdot \mathbf{u}_r(\mathbf{y})] \right)^{-1} \quad (6.27)$$

where  $\bar{a}(\mathbf{x}, \mathbf{y}) = \frac{\mathbf{A}(\mathbf{x}, \mathbf{y})}{\|\mathbf{A}(\mathbf{x}, \mathbf{y})\|}$  and  $\mathbf{u}_r$  is the  $r^{\text{th}}$  column of the spatial eigenvector matrix  $\mathbf{U}$  and  $\|\cdot\|$  is the  $L1$ -norm.

This measure exaggerates points which are close due to fact that  $\bar{a}(\mathbf{x}, \mathbf{y})$  is normalised and the entire function is inverted. This function thus emphasises  $\mathbf{x}$  points which are close to signal space. In practice, no singularities occur in  $M_1^T(\mathbf{x})$  due to noise and errors associated with the signal and transfer matrices.

To find the activation times corresponding to these critical points, the following functions are constructed

$$M^+(\mathbf{x}, t) = M_1^t(\mathbf{x}) \quad (6.28)$$

$$M^-(\mathbf{x}, t) = M_t^T(\mathbf{x}) \quad (6.29)$$

where  $1 < t < T$ . These two functions look at the distance from signal space where the signal space is restricted to  $[1, t]$  and  $[t, T]$  respectively. From these two functions, a zero-crossing matrix (of size number of heart nodes  $\times$  number of time steps) is constructed with

$$Z(\mathbf{x}, t) = M^+(\mathbf{x}, t) - M^-(\mathbf{x}, t) \quad (6.30)$$

Each row of the zero-crossing matrix corresponds to distance from signal space at a particular location on the heart. These functions are similar to step functions as shown in Figure 6.4, with high gradients at the point at which the  $x$ -axis is crossed. Theoretically, the critical point function corresponding to a critical point crosses zero at the critical time.

The statement of the critical point theorem relates to critical points only; therefore the activation field as estimated by the zero-crossing times of Equation (6.30) can be considered accurate at those points only. However, as the estimates of activation times are essentially generated as a distance measure, the critical point function estimate of activation times for points not corresponding to critical points are a reasonable estimate of the true activation sequences. As stated in Section 6.3.3, with all critical points and times accurately defined computing all the activation times is now, theoretically, a well-posed problem. The difficulty lies in the accuracy and reliability of the critical points and times generated by Equation (6.30) and imposing these in the optimisation.

One flaw in the critical point algorithm is that it cannot reliably distinguish between events on the epicardial and endocardial surfaces (possibly due to the fact that the myocardium is assumed to be a homogeneous region for this thesis). Endocardial timings merely seem to follow the corresponding timing found at the epicardium. This can be understood by considering two adjacent points on

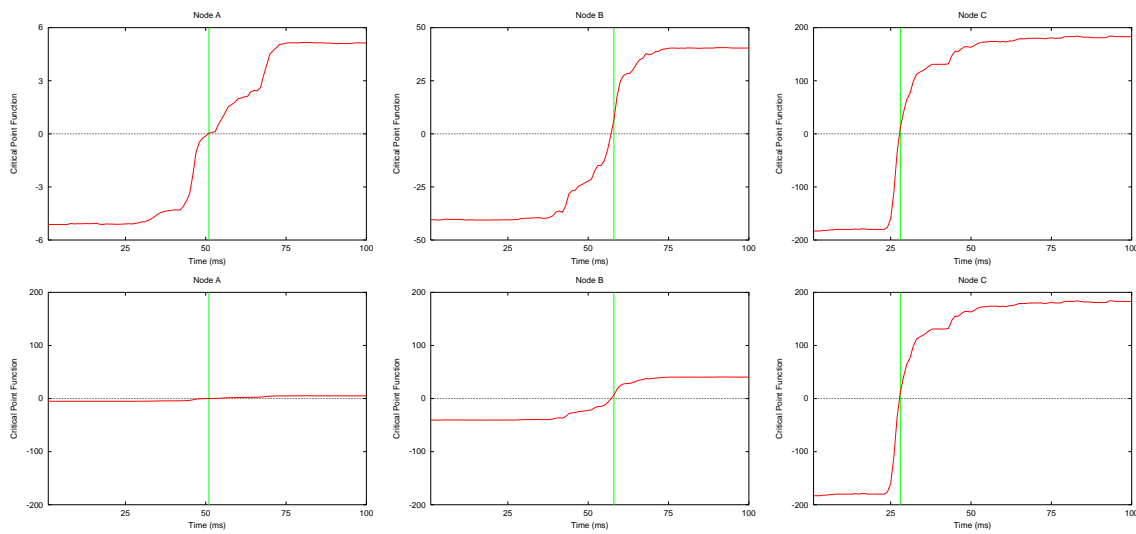


**Figure 6.4:** Comparison of critical point functions between critical and non-critical points. The top row shows the three functions individually scaled. Bottom row has all the functions scaled to the same ranges. The larger jump in the critical point function for node C indicates it corresponds to a critical point and time. The vertical green line marks the points at which the functions cross the horizontal axis and provide an estimate of the activation time at each location.

either side of the myocardium. The close proximity between these two points and the high correlation between the transfer matrix columns corresponding to the two points, means that an epicardial critical point could be incorrectly assigned to an endocardial point or *vice versa*. It is believed that the majority of critical points are located on the epicardial surface as activation on the endocardial surface in a normal heart is highly dominated by the distributed Purkinje network. In addition, the activation times as estimated by the critical point function tend to be compressed towards the centre of the time domain. As stated by Huiskamp & Greensite (1997), there is a “tendency for estimates of critical times to be restricted to a narrow time interval; the early events tend to come later, whereas the late events happen earlier”. This can possibly be overcome by the introduction of an anisotropic transfer matrix, however, as previously explained in Section 5.3, isotropy is assumed at this stage. Initial investigations have been performed on the creation of an anisotropic transfer matrix, however, this has been limited to the forward problem of electrocardiography (Fischer et al. 2000).

This can be understood by decomposing a signal into Gaussian noise and the pure signal components. For the Gaussian noise component, with little significant information, the critical point function will produce a slow ramping function, crossing zero halfway through the time interval. The signal component will produce a fast, steep ramp crossing at the critical time. When the two critical point functions are combined, the Gaussian noise contributions will drag the true activation

times closer to the centre of the time interval. This is illustrated on simulated signals in Figure 6.5, where the critical point estimates of the activations times for clean signals are compared to corresponding signals which have had  $100 \mu\text{V}$  RMS of Gaussian noise added.

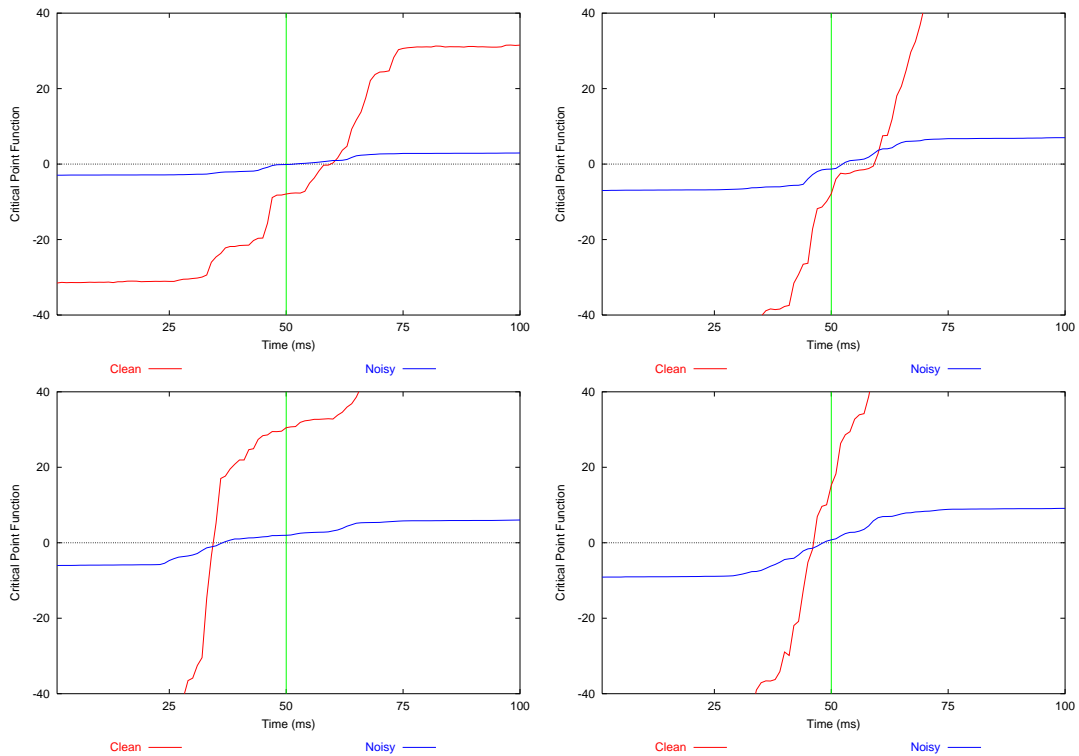


**Figure 6.5:** Estimates of activations as determined by the critical point algorithm. The activation times (as determined by the point at which the functions cross zero) are compared for ‘clean’ (red) and ‘noisy’ (blue) signals. The overlaid graphs show that with increased noise levels, the estimates are compressed towards the centre of the time domain (indicated by the green vertical line). The magnitudes of the functions are also reduced, indicating a reduced certainty in the solutions.

As the critical point algorithm only provides an estimate of the true activation sequence from the body surface signals, it is desirable to obtain a more accurate representation of the true activation sequence through the refinement process described in Section 6.3.1.

### 6.3.5 Myocardial Activation Regularisation Constraints

The activation based inverse formulation has had few developments when compared to the potential based formulation. The currently exists a vast array of regularisation methods for the epicardial potential based approaches. The activation approach is also believed to be more stable in a variety

of situations than the potential inverse methods (Brooks & MacLeod 1997). The most commonly used regularisation technique for the activation time formulation involves the inclusion of a surface Laplacian constraint as shown in Equation (6.5). The degree of regularisation which is applied is to the objective function is controlled by the regularisation parameter  $\lambda$ .

### Surface Laplacian Constraint

The surface Laplacian constraint is a second order Tikhonov constraint. However, unlike the use of this constraint in epicardial potential approaches, it has a physiological basis as the path of the surface activation wavefront is known to be continuous and smooth at a length scale greater than the size of cell.

The Laplacian constraint  $\mathcal{L}$  or penalty function forces the field (the activation wavefront) to have a smooth curvature, *i.e.*,

$$\mathcal{L} = \left( \frac{\partial^2 u}{\partial s_1^2} + \frac{\partial^2 u}{\partial s_2^2} \right) \quad (6.31)$$

where  $u$  is an unspecified scalar field and  $s_i$  are the local coordinates in the  $i^{\text{th}}$  direction.

A simple method of approximating the surface Laplacian at the nodal positions is by a finite difference technique. If a one-dimensional mesh is considered, with a point  $x_0$  with neighbours  $x_1$  and  $x_2$ . If  $u_i$  is defined to be the field at location  $x_i$  (*i.e.*,  $u(x_i)$ ) then a Taylor's series expansion by an amount  $h$  yields,

$$\begin{aligned} u(x_0 + h) = u(x_0) + h \left. \frac{du}{dx} \right|_{x=x_0} + \frac{h^2}{2!} \left. \frac{d^2u}{dx^2} \right|_{x=x_0} + \dots \\ + \frac{h^n}{n!} \left. \frac{d^n u}{dx^n} \right|_{x=x_0} + \frac{h^{n+1}}{n+1!} \left. \frac{d^{n+1}u}{dx^{n+1}} \right|_{x=\xi} \end{aligned} \quad (6.32)$$

where  $x_0 < \xi < x_0 + h$

Considering a non-uniform mesh, (*i.e.*,  $h$  is different in each direction) and defining  $\Delta x_a$  to be the distance between node  $n$  and  $a$  then node  $n$  represents the point which the Laplacian is centred around.

Combining the Taylor series expansion of  $u(x_0 - \Delta x_1)$  and  $u(x_0 + \Delta x_2)$  and rearranging for the

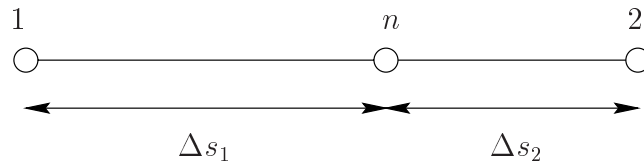


**Figure 6.6:** Central difference approximation to the second derivative at node  $n$ . The distances between node  $n$  and node  $i$  is given by  $\Delta s_i$

second derivative term results in

$$\frac{d^2u}{dx^2} \simeq 2 \cdot \frac{u_2 - 2u_i + u_1}{\Delta s_1^2 + \Delta s_2^2} \quad (6.33)$$

where  $u_n$  is defined as  $u(x_n)$ ,  $u_1$  is defined as  $u(x_n - \Delta x_1)$  and  $u_2$  is defined as  $u(x_n + \Delta x_2)$  and  $\Delta s_i$  is defined as  $\Delta x_i$ .

There is a slight error introduced as the first derivative terms do not exactly cancel due to the variations in adjacent elements. The magnitude of the error term is given by  $(\Delta s_1 - \Delta s_2) \frac{du}{dx}$ , where  $(\Delta s_1 - \Delta s_2)$  is a measure of the differences in size between neighbouring elements. This error term was assumed to be negligible due to the relatively regular sizes of the elements and the fact that only an approximation to the surface Laplacian is required.

For a two-dimensional surface, Equation (6.33) can be generalised to regularise the activation field,  $\tau(\mathbf{x})$ . If we consider a point  $i$  as shown in Figure 6.7 the surface Laplacian given at that point is given by,

$$\mathfrak{L}_i = \frac{\tau_A - 2\tau_i + \tau_B}{\Delta s_{i,A}^2 + \Delta s_{i,B}^2} + \frac{\tau_C - 2\tau_i + \tau_D}{\Delta s_{i,C}^2 + \Delta s_{i,D}^2} \quad (6.34)$$

where  $\mathfrak{L}_i$  is the surface Laplacian at node  $i$ , and  $\tau_n$  is the activation field at node  $n$  and  $\Delta s_{i,A}$  represents the Euclidian distance between nodes  $i$  and node  $A$ .

Equation (6.34) is a generalisation of the formulation proposed by Oostendorp & van Oosterom (1989). This was formulated as

$$\mathfrak{L}_i = \frac{n}{h^2} (\bar{\tau} - \tau_i) \quad (6.35)$$

where  $n$  is the number of nodes surrounding point  $i$ ,  $\bar{\tau}$  is the average field at each of the  $n$  points, and  $h$  the distance between each of these nodes and the central node  $i$ . In this case, the constant

distance  $h$  assumes that all surrounding nodes are equidistant from the central node. This is not the case for our geometric models.

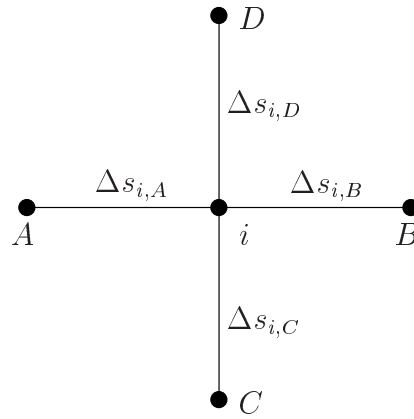


**Figure 6.7:** Schematic of a regular grid used for calculating the surface Laplacian at point  $i$ . The surface Laplacian for a given node is given in Equation (6.34). Points A, B, C and D are the nodes surrounding point  $i$  and the  $\Delta s_{i,A}$  is the Euclidean distance between point  $i$  and point A.

The derivative of this Laplacian constraint with respect to to the optimisation variables ( $\tau_i$ ) is given by,

$$\frac{\partial \mathcal{L}}{\partial \tau_i} = \frac{-4}{\Delta s_{i,A}^2 + \Delta s_{i,B}^2} + \frac{2}{\Delta s_{i,A}^2 + \Delta s_{i,A^*}^2} + \frac{2}{\Delta s_{i,B}^2 + \Delta s_{i,B^*}^2} \quad (6.36)$$

where the superscript  $\star$  indicates the next neighbouring node further away from point  $i$ .

### 6.3.6 Critical Point & Times Constraints

Parts of the activation sequence as determined by the critical point estimation in Section 6.3.2 can also be constrained during the optimisation process of Section 6.3.1. Critical points and/or times may be constrained to remain local maxima, minima or saddle points of  $\tau(\mathbf{x})$ , however, in practice, this has not been done in our simulations due to its questionable benefit and large number of variables already being optimised.



## 6.4 Control Inverse Simulations

The control (or reference) inverse simulations for the three cardiac sources (double point, eikonal and experimentally derived), described in Sections (4.6.3)–(4.6.5), are examined in detail in Sections (6.4.1)–(6.4.3). As the cardiac sources used are merely approximations of what is actually occurring within an *in-vivo* heart, it is necessary to use a number of different cardiac sources to capture the dynamic and variable nature of the electrical propagation within the heart. These cardiac sources are also used later in Chapter 7 for investigating the sensitivity of each of the inverse algorithms. The results from these control simulations provide a theoretical limit of the best results achievable by the activation based formulation.

Using the cardiac sources, the forward problem procedures outlined in Chapter 5 were used to compute torso surface signals. To replicate optimal experimental conditions, absolute Gaussian noise levels of  $10 \mu\text{V}$  RMS were applied to the torso surface signals. As it is technically impossible to achieve totally clean signals,  $10 \mu\text{V}$  RMS of Gaussian noise provides a lower bound on the noise levels which could be expected under optimal conditions. These known torso surface signals were then used as input for the inverse algorithm. No geometric or material property errors were included at this stage – the effect of these errors are examined in detail in Section 7.2.

The porcine model used in the control simulation is composed of all six surfaces (epicardial, left and right endocardial, left and right lungs and skin surface) refined once in each direction, the refinement required for a converged solution as determined in Section 5.6.3.

The inverse solution for each of the cardiac sources is presented graphically in the form of activation maps in Figures (6.8)–(6.10). Displayed for each cardiac source are graphical representations of (from left to right) the input source, the solution computed using the activation based formulation and the difference between the two solutions. The black regions in the difference map correspond to areas which have less than 1 ms difference between the input and computed solutions. A table of results for each simulation compares the known and computed activation fields ( $\tau$ ) and the corresponding known and computed torso surface potentials ( $\phi_B$ ) after the initial critical point algorithm (CPA) and after the refinement phase of the procedure (Final). In addition the differences between the known and computed activation fields on the epicardium (EPI) and the left (LV) and right (RV) endocardium are displayed. Three error measures, defined in Section 3.2.3, are used to compare the solutions: RMS, relative RMS and the similarity index. The RMS errors for the activation fields are given in ms and in mV for the torso surface potentials.

### 6.4.1 Double Point Stimulus Activation Profile

The double point activation profile, described in Section 4.6.4, was used as an input for the activation based inverse algorithm. Comparisons between the known activation fields and the computed fields are shown graphically in Figure 6.8 and numerically in Table 6.1 using error metrics defined in Section 3.2.3.

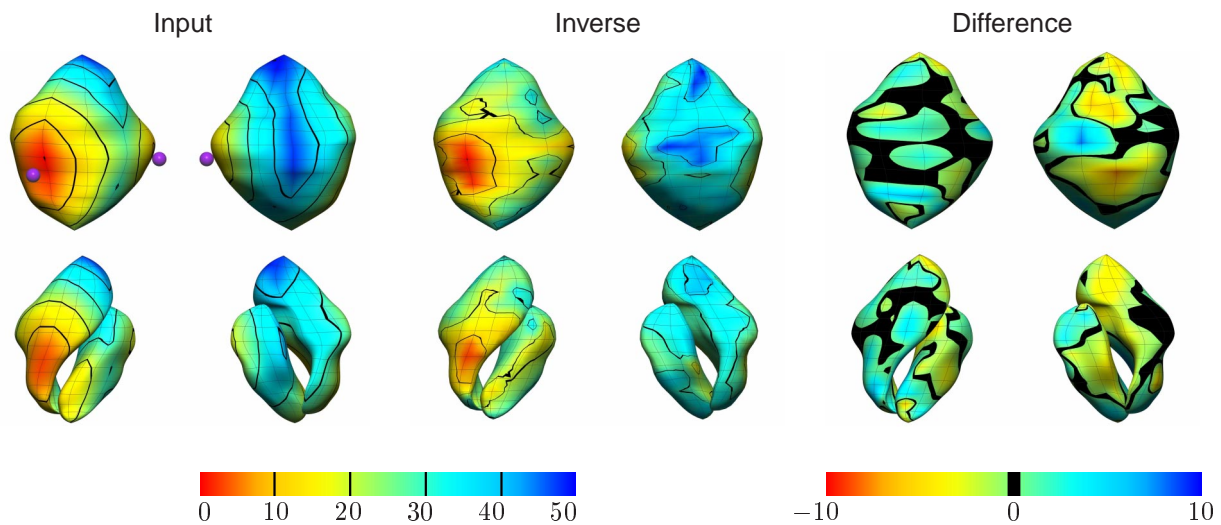


**Figure 6.8:** Activation and difference maps (ms) comparing the analytic double point source and the control inverse computed solution. Shown are the input activation field (left two columns) and the inverted activation field (middle two columns) and the differences between the two fields (right two columns). The coloured field represents the activation times in ms, with red being earliest activation and blue latest activation. Anterior views are shown in the first, third and fifth columns and posterior views in the second and fourth and sixth columns. The epicardial surfaces are shown in the top row and the endocardial surface on the bottom row. The purple spheres in the input source show the locations of the activation seed points used for generating the activation field. Black regions in the difference map indicate areas with error of less than 1 ms.

By examining the activation fields on each of the three surfaces, it can be seen that the error is evenly distributed throughout the heart mesh. There is a tendency for the activation times to be compressed towards the centre of the time domain (*i.e.*, early activation times occurring late and *vice versa*). It should be noted that on the left endocardial surface, the activation field worsened after the refinement stage of the algorithm despite the epicardial and right endocardial surfaces improving. This may possibly be due to the fact that the left endocardial surface had a better initial critical point estimate when compared to the other two surfaces.

		$\phi_B$	$\tau$	$\tau_{EPI}$	$\tau_{LV}$	$\tau_{RV}$
RMS	CPA	0.20	4.8	4.7	4.8	4.8
	FINAL	0.02	4.1	4.1	4.0	4.2
REL. RMS	CPA	0.79	0.09	0.09	0.09	0.10
	FINAL	0.07	0.08	0.08	0.08	0.08
SI	CPA	0.90	0.92	0.96	0.75	0.93
	FINAL	1.00	0.93	0.95	0.83	0.93
MAX.	CPA		12.6	12.5	12.6	12.6
	FINAL		12.5	12.5	10.4	11.1

**Table 6.1:** Comparison between the analytic double point source and the control inverse computed solution. Shown are the comparisons between the known and computed activation fields (ms) and the known and computed torso surface potentials (mV). The RMS, rel. RMS and similarity index error metrics defined in Section 3.2.3 as well as the maximum error are used to compare the estimate from the critical point algorithm and the optimised solutions for the torso surface signals ( $\phi_B$ ), the activation field ( $\tau$ ), and the activation field on the epicardial (EPI), left ventricular (LV) and right ventricular (RV) surfaces.

## 6.4.2 Eikonal Activation Profile

The eikonal activation profile, described in Section 4.6.3, was used as input for the activation based inverse algorithm. Comparisons between the known activation fields and the computed fields are shown graphically in Figure 6.9 and numerically using error metrics in Table 6.2.

		$\phi_B$	$\tau$	$\tau_{EPI}$	$\tau_{LV}$	$\tau_{RV}$
RMS	CPA	1.45	12.0	10.3	15.6	10.3
	FINAL	0.16	11.4	10.4	15.1	9.0
REL. RMS	CPA	1.01	0.46	0.30	0.76	0.57
	FINAL	0.11	0.44	0.30	0.74	0.49
SI	CPA	-0.34	0.35	0.50	0.35	0.51
	FINAL	0.99	0.50	0.48	0.34	0.54
MAX.	CPA		27.7	27.0	27.6	19.8
	FINAL		44.0	37.5	44.0	24.8

**Table 6.2:** Comparison between the analytic eikonal source and the control computed solution. Layout as described in Table 6.1.

The complex nature of this cardiac source (with endocardial the endocardial surface activating significantly earlier than the epicardial surface) meant that this activation field was the most difficult of the three cardiac sources to reconstruct. This source was the only source which was constructed using inhomogeneous material properties within the heart. However, in the inverse procedure, homogeneous material properties are assumed.

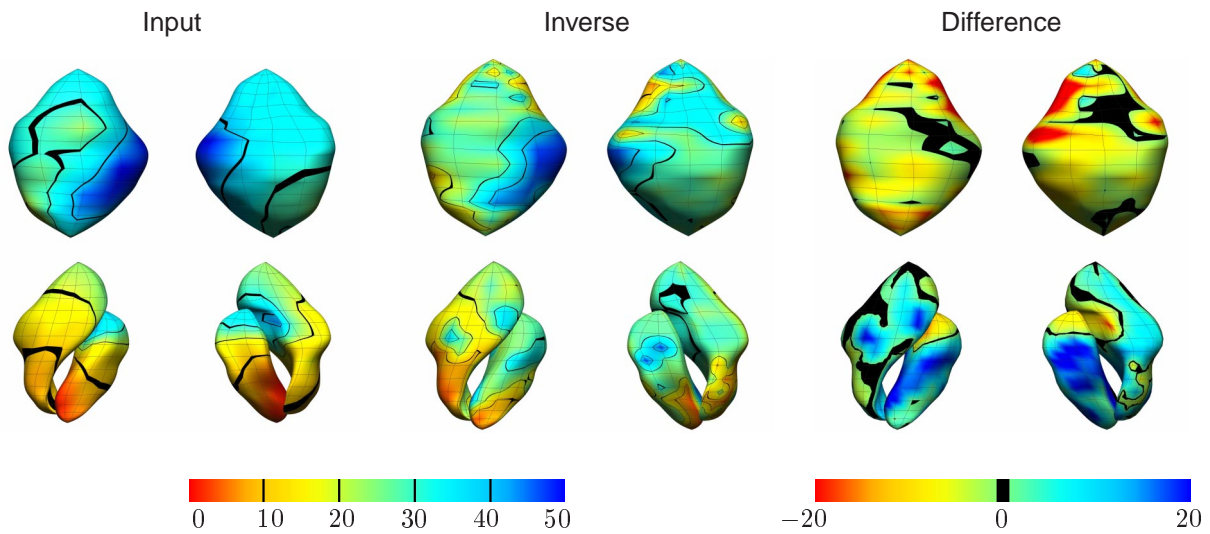


**Figure 6.9:** Activation and difference maps (ms) comparing the analytic eikonal source and the control inverse computed solution. Black regions in the difference map indicate areas with error of less than 1 ms. Layout as described in Figure 6.8.

The initial activation field as estimated by the critical point function was extremely poor with the corresponding torso surface signals having a relative RMS of 1.01 and a similarity index of  $-0.34$ . This can be attributed to the lack in ability for the critical point algorithm to distinguish between critical points occurring on the epicardial and endocardial surfaces. It should be noted that there were significant problems in reconstructing the activation field on the left ventricular surface. The activation field on this surface was reconstructed with an RMS error approximately 5 ms greater than on the epicardial and right endocardial surfaces. This is also reflected in the large increase in the maximum error on the left ventricular surface.

### 6.4.3 Experimentally Derived Activation Profile

The experimentally derived profile, described in Section 4.6.5, was used as input for the activation based inverse algorithm. Comparison between the known activation fields and the computed fields are shown graphically in Figure 6.10 and numerically using error metrics in Table 6.3.

The shorter duration of this cardiac source meant that the possibility for large errors to occur were reduced. Again the critical point function provided a poor initial estimate of the activation field with corresponding torso surface signals having a relative RMS of 1.00 and a similarity index of 0.09. The error in the reconstructed activation fields was evenly distributed over the each of the

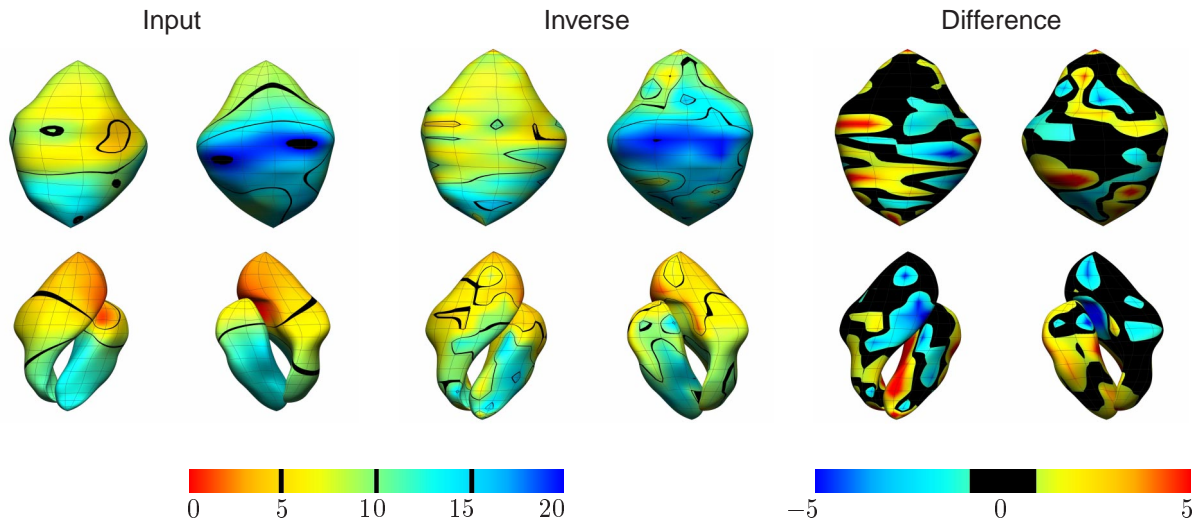


**Figure 6.10:** Activation and difference maps (ms) comparing the analytic experimentally derived source and the control computed solution. Black regions in the difference map indicate areas with error of less than 1 ms. Layout as described in Figure 6.8.

		$\phi_B$	$\tau$	$\tau_{EPI}$	$\tau_{LV}$	$\tau_{RV}$
RMS	CPA	0.83	2.7	2.3	2.7	3.1
	FINAL	0.02	2.4	2.3	2.6	2.3
REL. RMS	CPA	1.00	0.08	0.07	0.08	0.10
	FINAL	0.02	0.07	0.07	0.08	0.08
SI	CPA	0.09	0.68	0.79	0.60	0.70
	FINAL	1.00	0.77	0.76	0.74	0.72
MAX.	CPA		7.9	5.8	6.2	7.9
	FINAL		8.2	7.8	7.1	8.2

**Table 6.3:** Comparison between the analytic experimentally measured source and the control computed solution. Layout as described in Table 6.1.

three heart surfaces, with errors of around 2 ms occurring on each surface. Despite the RMS and SI errors indicating an improvement in the quality of the solutions during the optimisation phase of the algorithm, the maximum error increased for each of the three heart surfaces at the same time.

#### 6.4.4 Summary for Control Inverse Simulations

In general, all three of the cardiac sources behaved in similar ways. The torso surface potentials which were being minimised were dramatically improved from the critical point estimates, with all cases having similarity indexes greater than 0.99. The optimised activation fields on the heart surface were improved when compared to the critical point estimates but not significantly. In all

cases the activation fields were improved by less than 2 ms RMS.

There was also a tendency for the activation fields to be compressed towards the centre of the time domain (*i.e.*, early activation times occurring later than expected and vice versa). The refinement stage of the procedure addresses this to some extent but does not entirely remedy this problem.

The ‘patchy’ nature of the difference maps may indicate that insufficient regularisation was used in the solution process. However, it was found that the computed solutions were fairly insensitive to the degree of regularisation applied with general features remaining the same. When additional levels of regularisation were applied smoother activation fields were produced, but the damping of the maxima and minima meant that better solutions were not necessarily produced. This indicates that more elaborate regularisation schemes (such as those used in the potential based formulations) may need to be devised.

### 6.4.5 Effect of Refinement Level

To investigate the effect of the refinement level upon the inverse solutions, the same control simulations with the eikonal cardiac source performed with one lower and one higher level of refinement for the epicardial surface (*i.e.*, refinement level 0 and 2 as described in Table B.1).

The eikonal activation field was fitted, using the linear fitting techniques described in Section 3.3.1, to an epicardial mesh with refinement level 2. Torso surface potentials were then generated by solving the forward problem. These then used as input for inverse problem after applying 10  $\mu\text{V}$  RMS of noise (as with the control simulations described in Sections (6.4.1)–(6.4.3)).

The inverse simulations were performed using the under- and over-refined transfer matrices. With the lower refined transfer matrix, poor inverse solutions were obtained, due to the optimisation phase of the inverse procedure converging to the wrong solution. This can be attributed to the fact that the unconverged transfer matrix was producing incorrect and inconsistent torso surface potentials. The resulting solutions had an RMS error of 8 ms. When the over-refined transfer matrix was used, solutions were less than 1 ms RMS different to those obtained for the reference torso simulation shown in Table 6.2. These results are consistent with the forward convergence results described in Section 5.6.3 with the corresponding torso models.



# **7** *The Sensitivity of Inverse Solutions to Modelling Errors*

In practice, errors of one form or another will always be present in the modelling process. As a result of the ill-posed nature of both the potential and activation formulations of the inverse problem of electrocardiology, small errors can result in large inaccuracies in the final solution. For these algorithms and techniques to be reliably used in a clinical situation two key requirements must be addressed: the solutions must be accurate and defined in a physiologically meaningful sense, and perform reliability under the presence of both measurement noise, geometrical modelling errors and other uncertainties that are inevitable in a practical environment (MacLeod & Brooks 1998). It is essential to quantify the effects which these errors may cause on the computed solutions and the degree of accuracy required to obtain a stable solution. One of the key advantages of using a numerical modelling technique is the ability to easily adjust a wide variety of parameters. The effects of each of these parameters on the inverse solutions can therefore be carefully investigated in an isolated manner.

To date there has not been a detailed simulation study comparing activation and potential formulations and investigating a variety of modelling errors using a realistic geometry. Outlined in Section 7.1 are some previous attempts at addressing the effects of modelling errors on the inverse problem of electrocardiology. Presented in the remaining sections are a comprehensive study comparing the Tikhonov (Tikhonov & Arsenin 1977) and Greensite (Greensite & Huiskamp 1998) potential based formulations and an activation based formulation (Huiskamp & Greensite 1997), using a realistic geometric torso model and a number of different heart sources. The potential based TSVD method was also implemented but it was found to be extremely susceptible to any noise in all cases except for when optimal regularisation was used. For this reason, only the TSVD solutions with optimal regularisation parameters are presented.

## 7.1 Previous Investigations

There have been several studies investigating the effects of torso geometry on the solution of the inverse problem to date. However, there appears to be no comprehensive study on a large variety of modelling errors, with different cardiac sources, using realistic geometry. The majority of studies have only involved reconstruction of epicardial potentials using the traditional inverse methods described in Section 6.2.

Messinger-Rapport & Rudy (1986) used an idealised eccentric spheres model to analyse the effects of changes in torso geometry and conductivity on the recovery of epicardial potentials from electrical signals recorded on the torso surface. The eccentric spherical model is simple enough to be solved analytically yet contained sufficient information on geometric and conductivity factors to allow analysis of the effects of varying these parameters. The geometric parameters investigated by Messinger-Rapport & Rudy (1986) were the relative position and size of the heart within the torso. It was found that the inverse procedure was sensitive to variations in these geometric parameters with small changes in heart position resulting in a large loss in the resolution of calculated epicardial potentials. However, no regularisation techniques were used in the inverse procedure and it is expected that the use of such techniques would improve the resulting solution when geometrical errors are present.

The layered inhomogeneous eccentric spheres system was also used by Throne & Olson (1995) to look at the effect of errors in geometry and conductivities on solutions to the inverse problem of electrocardiography. Four different numerical methods were used to solve the inverse problem with two methods using a regularisation technique. Throne & Olson (1995) found that although the regularised methods performed better in the presence of geometric errors, small errors in heart size and position still had a significant effect on the resulting solution.

Inverse procedures were performed on realistic torso geometries by Huiskamp & van Oosterom (1989). The differences in the solutions were compared using a 'standard' realistic torso geometry and using the 'tailored' or actual geometry of the patient. Torso models were created for three subjects using contours from MRI images and a triangularisation technique. The models included an outer skin surface, lungs and a heart. The inverse problem was then solved with the corresponding patient ECG recordings. They then solved the inverse problem using mismatched ECG recordings and torso model to determine differences between using the actual geometric measurements and some standard model. Huiskamp & van Oosterom (1989) found that a fixed standard torso model gave unreliable results when used to solve the inverse problem. They concluded that a patient



specific model incorporating at least accurate torso size, heart orientation and position with respect to the ECG lead positions would be necessary for accurate inverse solutions. Similar results were obtained by Johnston & Kilpatrick (1995), who performed a similar study using 16 realistic torsos with varying heart sizes and positions.

Investigations into the effect of the number of torso residuals in the activation inverse to use and the complexity of the torso model were conducted by Modre (2000). In this study the number of electrodes was varied between 20, 41 and 62. The torso models were also varied by using a model with no lungs and using a torso model with similar geometry. With the electrode setups with 41 and 62 electrodes there was little variation, while when using 21 electrodes results were significantly poorer with both correct and incorrect geometry. However, the number of electrodes required is highly dependent upon the heart source which is being reconstructed.

Ramanathan & Rudy (2001*b*) studied the effects of torso inhomogeneities on reconstruction of epicardial potentials using zero-order Tikhonov methods. By solving the inverse problem with different torso configurations, it was found that the material properties have a minimal effect on the final inverse solutions. When Gaussian signal noise and electrode location error was added to the solution, an approximating the torso as being homogeneous resulted in more accurate solutions.

## 7.2 Simulation Study Overview

The modelling errors associated with an electrical imaging inverse problem can be categorised into three general classes. They consist of errors resulting from the torso surface signal data, the material conductivities and the geometric model. Errors in the signal data can be attributed to inaccurate measurements of the potential values (largely due to unavoidable presence of Gaussian noise) and uncertainty in the electrode locations. Material conductivities are known to vary between people and can vary from day to day (see Section 4.5.1). The geometrical model is usually a simplification of the true torso. Incorrect measurements may be made and not all regions are usually explicitly modelled (*e.g.*, bones, blood vessels, cardiac fat) or simplifications made about complex structures (*e.g.*, ignoring papillary muscles in the ventricles and the anisotropic nature of the myocardium). There are also assumptions and simplifications which are implied on the shape and duration of the activation wavefront.

Using the realistic porcine model described in Section 4.4 and the transfer matrices described in

Section 5.3 and a known activation field on the heart, corresponding epicardial and torso surface signals were computed. The torso surface signals and/or the transfer matrices were then subjected to varying amounts of modelling error and a series of inverse solutions computed using the corrupted input. The computed solutions can then be compared to the known cardiac source and the effect of the modelling errors on the computed solutions examined.

Using a modelling approach it is possible to carefully examine the sensitivity of the inverse algorithms with respect to a variety of modelling errors or a combination of these errors. The main input for the inverse algorithms is the torso surface signal information. The effects of errors associated with the potentials and the electrode locations on the inverse algorithms are investigated in Section 7.3. The torso model is defined by both the geometrical model and the material conductivities assigned to the various regions being modelled. With the activation inverse approach there are additional bidomain material properties which must also be set. The effect of material property errors are investigated in Section 7.4 while the effect of the errors in the surface description of the torso, incorrect size and/or orientation of the heart and lungs are investigated in Section 7.5.

For each of these simulations the double point heart source described in Section 4.6.4 was used as the cardiac source. For each simulation (except when electrical noise was applied), Gaussian noise levels of  $5 \mu V$  were applied to represent what are considered minimal experimental noise levels. Similar scales and layouts are used in each of these sections to enable accurate comparison between the different simulations.

As a test of the ability of the inverse algorithms to cope with realistic experimental errors which could be encountered in a real life situation, a number of different signal, geometric and material property errors were all combined in Section 7.6. In this series of simulations three different cardiac sources were used: the double point source described in Section 4.6.4, the eikonal source described in Section 4.6.3 and the experimentally derived source described in Section 4.6.5.

In order to compare the potential and activation based formulations directly, one of the solutions must be converted to a compatible form for comparison. Activation times are able to be extracted from the epicardial potentials to provide an equivalent solutions for comparison. The activation sequence was derived from an epicardial potential map by identifying, at each nodal site, the maximum negative slope using a moving finite difference interval. This time was then assigned as the activation time for that particular position (Oster, Taccardi, Lux, Ershler & Rudy 1998). However, there is error associated with this conversion process which is further discussed in Section 7.7.

As the endocardial surfaces are not explicitly modelled in the potential formulations, only the solutions on the epicardial surfaces were compared with the activation based solutions. The two measures which were used to compare the different activation time solutions were the RMS error (defined in Equation (3.7)) and the similarity index (defined in Equation (3.9)).

For each simulation, a series of eight plots, each displaying an error measure comparing the computed and known solutions against the level of applied modelling error, illustrates the results for each situation. The RMS error is used in the left column of plots and the similarity index is used on the right column of plots. The first row of plots shows the results for the activation based solutions, while the results for the potential based formulations are shown in the remaining three rows. For the activation based plots, each line represents the level of regularisation which was applied to the solutions. The degree of regularisation applied refers to the  $\lambda$  parameter defined in Equation (6.5). Each line on the potential based simulations corresponds to the method by which the regularisation parameter was computed. The results for each simulation are also presented in tabular form in Appendix C.

### 7.3 Effect of Signal Errors

Recorded potentials on the torso surface  $\Phi_B$  are almost certainly contaminated with errors of two main different forms: correlated and uncorrelated noise. This can be written as

$$\Phi_B = \hat{\Phi}_B + k\mathbf{E}_1 + \mathbf{E}_2 \quad (7.1)$$

where  $\Phi_B$  represents the recorded data,  $\hat{\Phi}_B$  is the true signal data,  $\mathbf{E}_1$  represents normalised, Gaussian (or uncorrelated) noise scaled by a factor  $k$  and  $\mathbf{E}_2$  represents correlated signal noise.

The correlated signal noise can arise from the recording equipment and errors resulting from incorrectly determining the locations of the recording electrodes, while uncorrelated noise usually results from recording background noise.

One method of simulating a noise corrupted signal it is to apply an absolute RMS voltage level of random noise to a ‘clean’ signal. This absolute noise is applied constantly across all signals independent of the peak to peak range of the signals. The other common methods of measuring noise levels are percentage noise levels (as defined in Equation (7.2)) and Signal-to-Noise ratio (as defined in Equation (7.3)). These are relative noise measures which give a measure of noise dependent on the peak to peak levels of the signal. Thus ‘small’ signals will typically have larger noise characteristics and ‘large’ signals will typically have small noise characteristics using this measure.

$$\text{Percentage Noise} = \frac{k\mathbf{E}_1 + \mathbf{E}_2}{\Phi_{\text{exact}}} \quad (7.2)$$

$$\text{Signal-to-Ratio (SNR)} = 20 \log_{10} \left( \frac{\|\Phi_{\text{exact}}\|_{\text{F}}}{\|k\mathbf{E}_1 + \mathbf{E}_2\|_{\text{F}}} \right) \quad (7.3)$$

The geometric model used for investigating the effect of signal errors contained all six regions and the same transfer matrix is used throughout as only the signal data matrix is being corrupted in different manners.

### 7.3.1 Effect of Uncorrelated Electrical Noise

The most common type of signal error which is conventionally investigated in inverse simulations is Gaussian electrical noise. It is traditionally thought to have the least effect upon the inverse solutions, possibly due to the ability of algorithms to distinguish Gaussian noise. Typical experimental recordings have noise levels in the range of 10–50  $\mu\text{V}$ . However, under optimal conditions, using active electrodes from BioSemi (2000) it is possible to achieve recordings with noise levels of 3  $\mu\text{V}$  (Tilg 1998).

Absolute RMS noise levels in the range of 1–100  $\mu\text{V}$  were applied to ‘clean’ simulated signals. A sample of four of the signal traces are shown in Figure 7.2. The location of the four sample electrodes on the torso surface are shown in Figure 7.1.

ELECTRODE	PEAK-TO-PEAK (mV)	ABS RMS ( $\mu\text{V}$ )	%	SNR (dB)
A	0.02	1	0.05	26.0
		10	0.5	6.02
		100	5	-14.0
B	0.02	1	0.05	26.0
		10	0.5	6.02
		100	5	-14.0
C	1.0	1	0.001	60.0
		10	0.01	40.0
		100	0.1	20.0
D	3.0	1	0.0003	70.5
		10	0.0033	49.6
		100	0.0333	29.6
256 ELECTRODES	4.0	1	0.0003	72.0
		10	0.0025	52.0
		100	0.025	32.0

**Table 7.1:** Noise levels applied to four sample electrodes. Absolute Gaussian noise was applied to each of the electrodes. The locations of the sample electrodes are shown in Figure 7.1 and their traces shown in Figure 7.2.

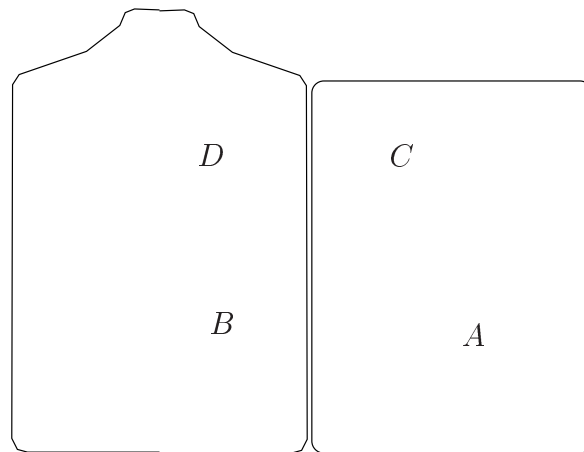


**Figure 7.1:** Schematic diagram illustrating the location of the electrodes A–D described in Figure 7.2 and Table 7.1. Layout as described in Figure 3.5

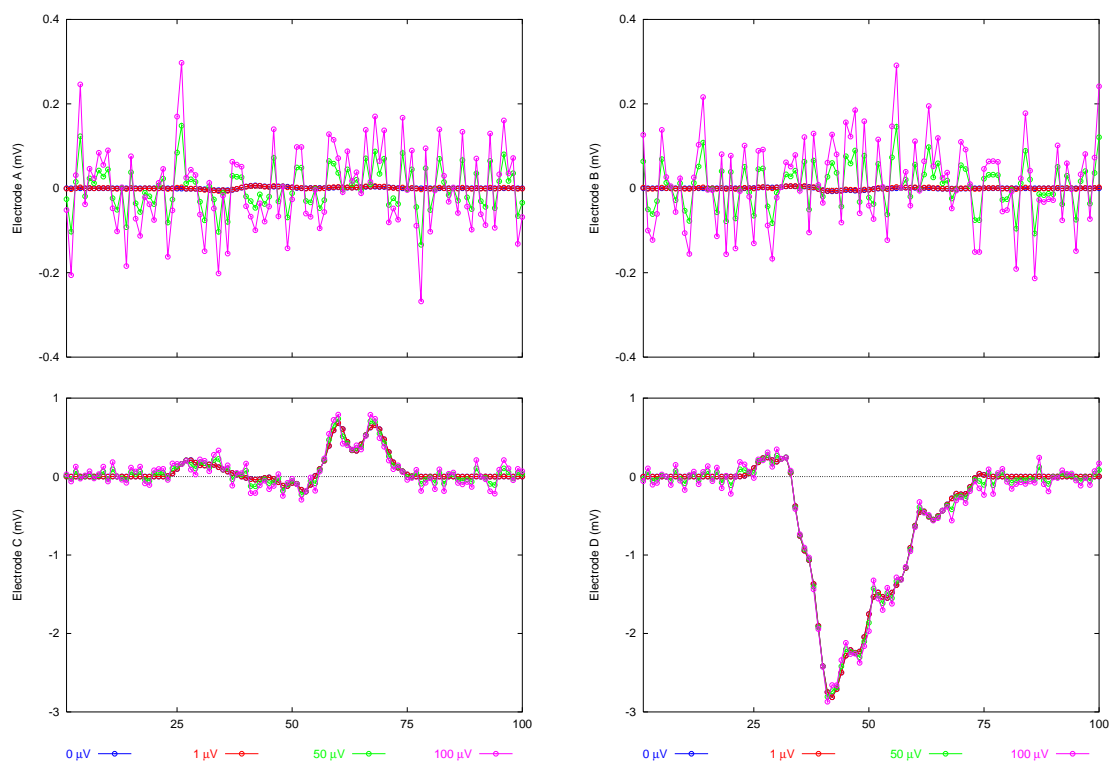


**Figure 7.2:** Applying Gaussian noise to simulated clean signals. Four typical signal traces are displayed – two ‘small’ signals (top row) and two ‘large’ signals (bottom row). The location of each electrode on the torso surface is shown in Figure 7.1. Time is shown on the horizontal axis in ms and potential on the vertical in mV. Note that the original signal with no applied noise is masked by the 1  $\mu$ V signal.

The inverse solutions for these corrupted signals are shown in Figure 7.3. They show that similar results were obtained for both potential and activation based approaches, with solution error gradually increasing with higher levels of applied noise. At noise levels less than  $50 \mu\text{V}$ , solution errors did not significantly increase, especially in the potential based formulations. Under optimal conditions, the potential based approaches provided better results than the activation formulation but results were similar for both approaches at noise levels greater than  $10 \mu\text{V}$ . With applied noise levels below  $10 \mu\text{V}$  there was a rapid increase in the solution error as shown by the sharp gradients in the plots in Figure 7.3.

The Greensite optimal and zero-crossing methods were almost identical, as were the Greensite CRESO and L-curve techniques at producing regularised solutions. All Tikhonov regularisation methods produced similar trends while the L-curve technique was marginally favoured over the zero-crossing method for determining the regularisation parameter.



## Gaussian Electrical Noise

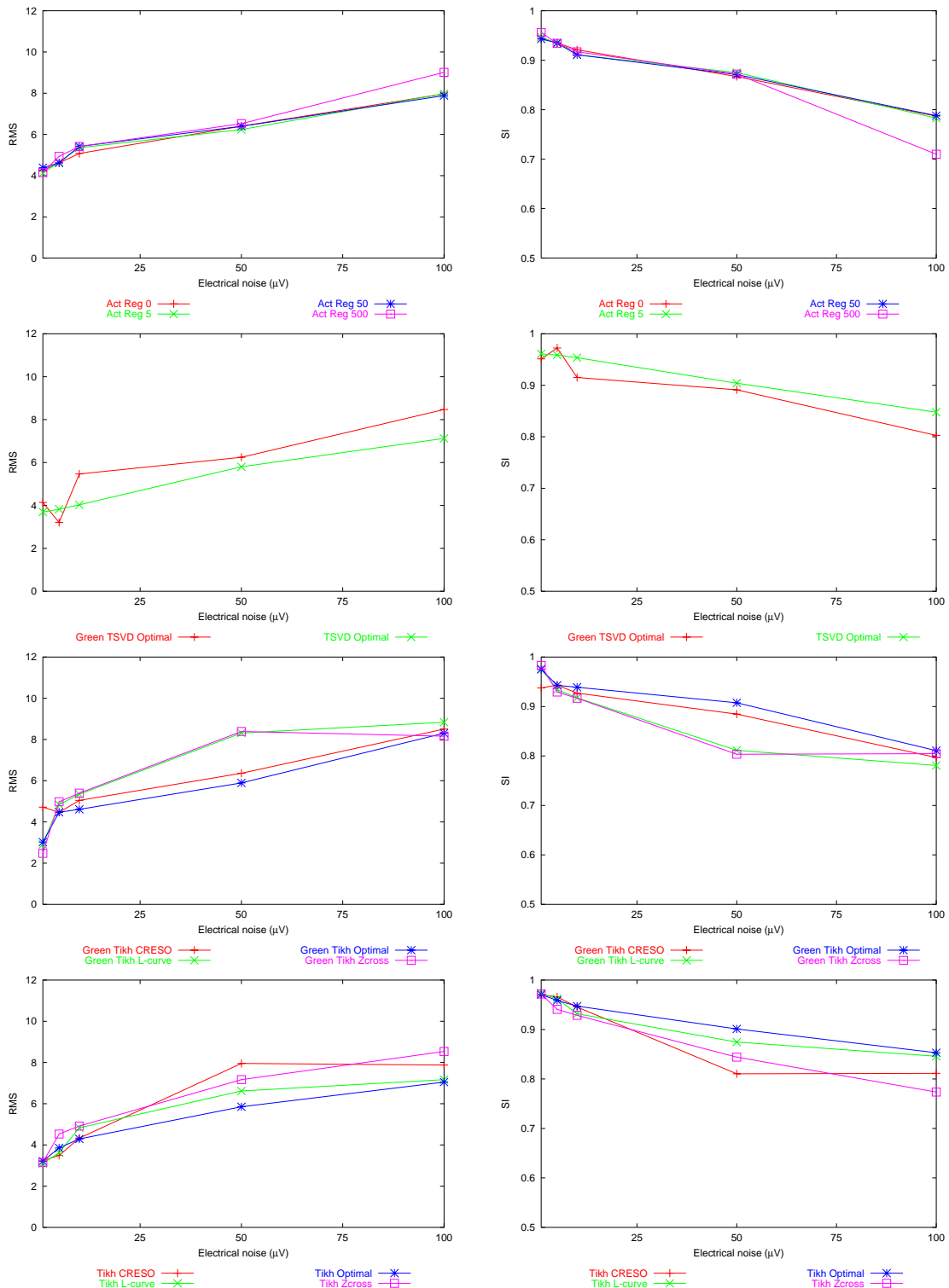


**Figure 7.3:** Effect of Gaussian electrical noise on activation and potential based formulations. The left column shows the comparisons between analytic and computed activation times using the RMS measure and the right column with a similarity index (SI) comparison. The first row corresponds to the activation based approach (Act) with different regularisation values and the last three rows correspond to the potential based approaches, Greensite TSVD (Green TSVD), Greensite Tikhonov (Green Tikh) and first order Tikhonov (Tikh).

### 7.3.2 Effect of Uncorrelated Electrode Displacement

To investigate the effect of uncorrelated electrode displacements, electrode positions were translated by 5, 10 and 15 mm in each of the three rectangular Cartesian axis directions using a normally distributed random number sequence. This resulted in electrode points in free space which were then orthogonally projected back onto the surface of the model to provide corrupted electrode positions. Using these new electrode positions, the potential field values were evaluated and then assigned to the original nodal positions. The resultant RMS displacements between the nodal positions and the corrupted electrode positions was calculated to be 7, 15 and 22 mm respectively.

Figure 7.4 shows the inverse solutions when the electrodes were displaced in an uncorrelated fashion. They show that the activation approaches provided more stable solutions, especially with higher regularisation parameters when electrodes were significantly displaced, with all solutions errors less than 2 ms different from the control simulations. When the electrodes were translated less than 7 mm results were similar to those obtained under control conditions.

The potential formulations provided less stable results, with even small electrode displacements resulting in immediate degradation of the inverse solutions. The Tikhonov potential approaches all provided similar trends but there was large variability between the different Greensite methods, with the CRESO method providing the best regularised solutions.

### Uncorrelated Electrode Displacement

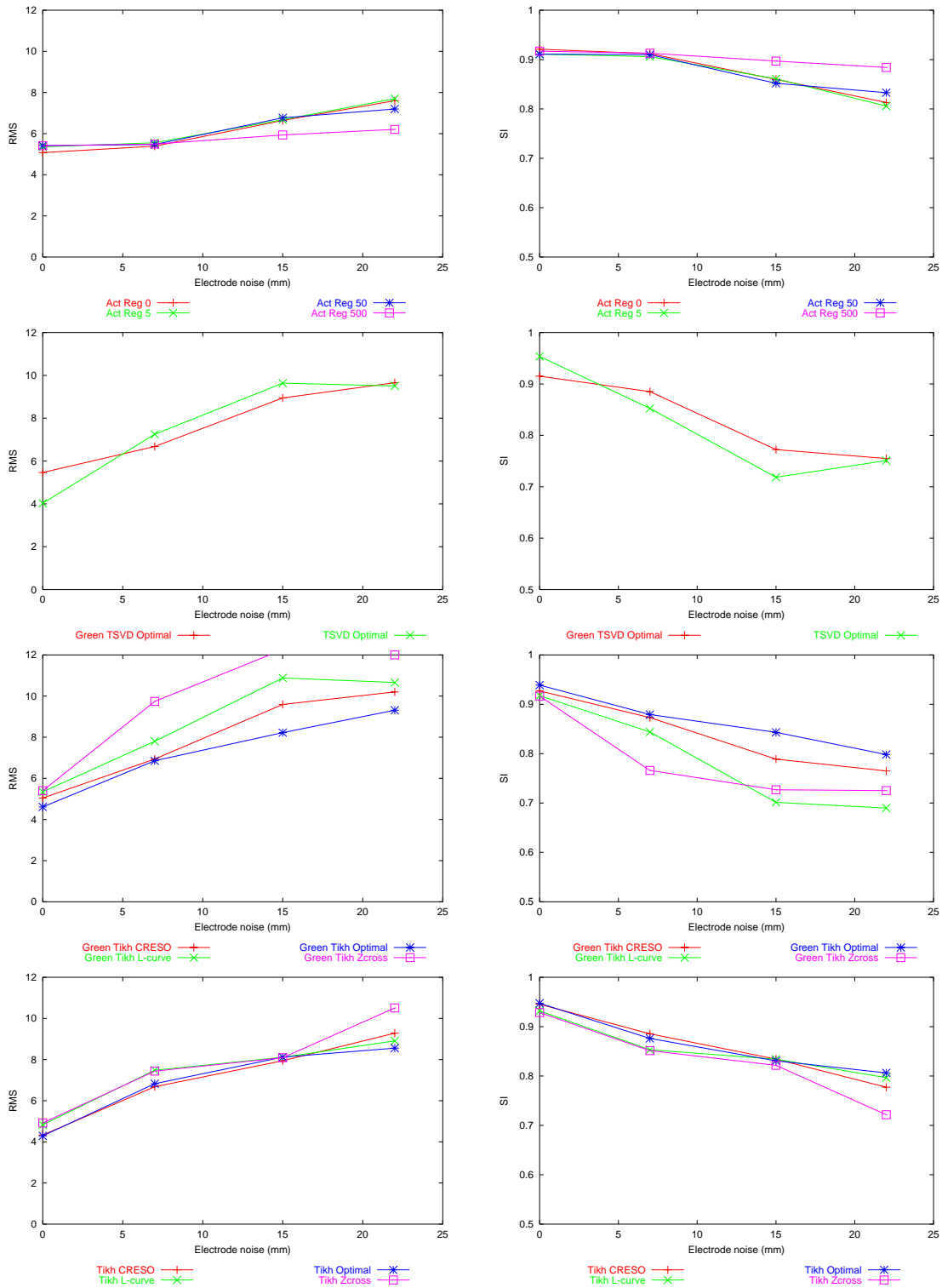


**Figure 7.4:** Effect of uncorrelated electrode displacement on activation and potential based formulations. Layout as described in Figure 7.3.

### 7.3.3 Effect of Correlated Electrode Displacement

To investigate the effect of correlated electrode displacement the electrodes were rotated about the sagittal plane ( $z$ -axis) in the clockwise (positive) and anti-clockwise (negative) directions. The rotations were  $-10$ ,  $-5$ ,  $5$  and  $10^\circ$ . These rotations corresponded to average RMS displacements of 15, 7.5, 7.5 and 15 mm for the electrodes. This sort of error could occur if the equipment used to record electrode positions was not correctly calibrated.

The activation approach provided similar results for all regularisation parameters. All solutions were within 1 ms of the control solutions when the electrode positions were rotated up to  $10^\circ$  in either direction in the coronal plane.

Both the Greensite and Tikhonov approaches had unstable results with significant errors resulting unless the optimal method was used to determine the regularisation parameter. With both the Greensite and Tikhonov approaches, the CRESO method failed when electrodes were rotated in anti-clockwise direction by  $10^\circ$ . The electrode positions must be known to within  $5^\circ$  to obtain solutions within 1 ms of the control solutions. Significant errors resulted if the electrode were displaced by more than  $5^\circ$  using the potential based formulations.

As the Gaussian noise is generated using a pseudo random number generator, to fully test the inverse algorithms and the randomness of the random number generator, the simulations were repeated multiple times with different sets of Gaussian corrupted signals. With each of the cases, near identical results were obtained.

### Correlated Electrode Displacement

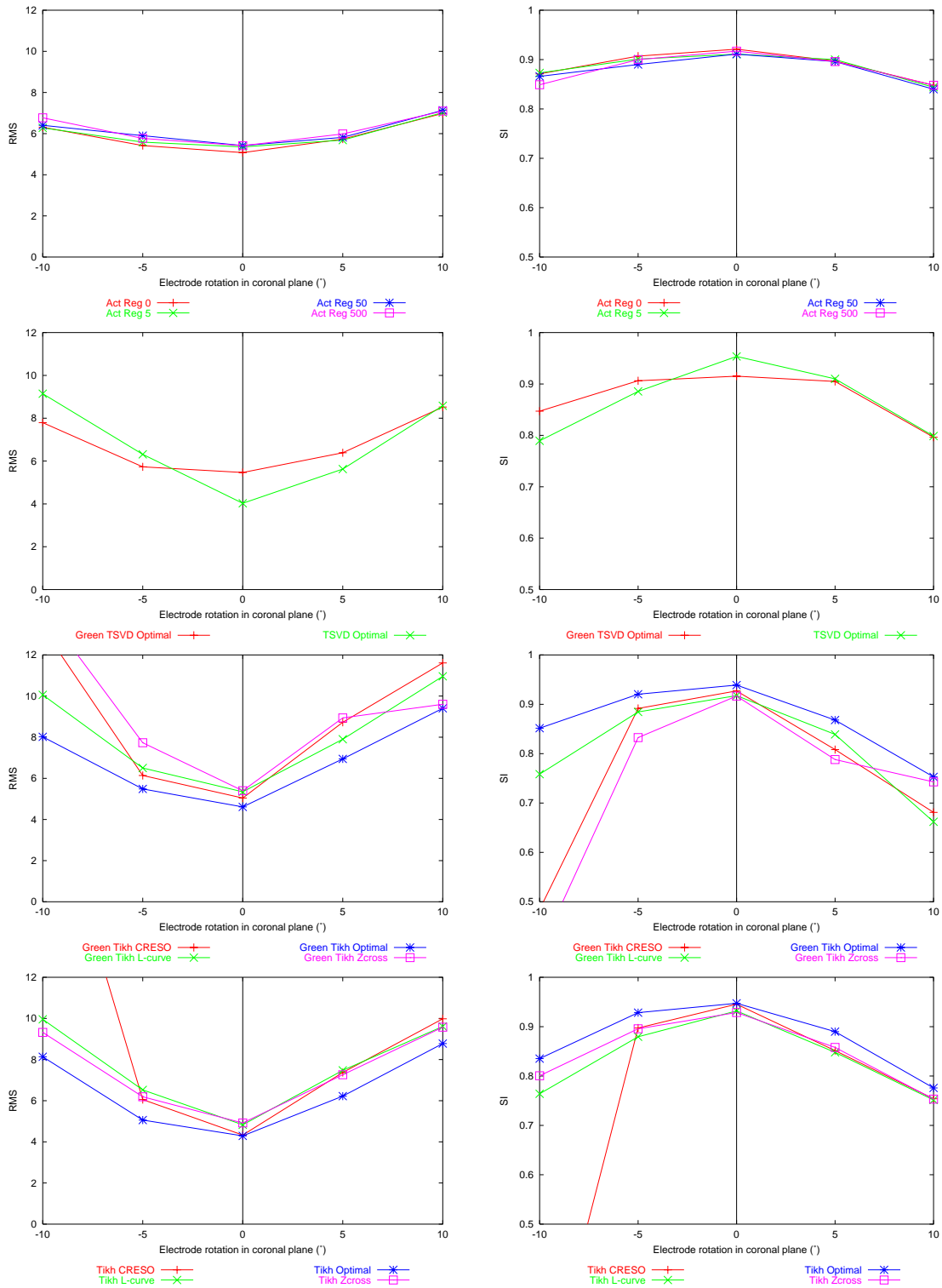


**Figure 7.5:** Effect of correlated electrode displacement on activation and potential based formulations. Layout as described in Figure 7.3.

## 7.4 Effect of Material Property Errors

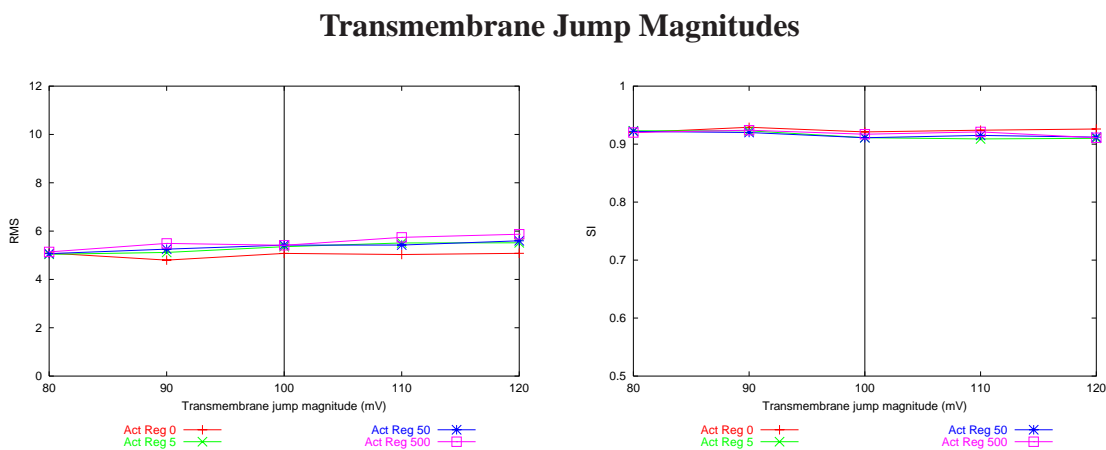
The effect which the material parameters have on the inverse solutions is investigated in this section. Activation based formulations are believed to be less susceptible to material conductivity values (Green, Taccardi, Ershler & Lux 1991) when compared to potential based approaches. The passive conductivities outside the heart should linearly scale the calculated torso potentials due to the conductivity scalar in the generalised Laplace's equation.

The full six region torso matrix with the same input signals are used, with the conductivity values varying the transfer matrices for each simulation run.

### 7.4.1 Effect of the Transmembrane Jump Magnitudes

The magnitude of the transmembrane jump as defined in Section 5.4 is a key component in the relationship between the transmembrane potential and the body surface potentials. Although the transmembrane jump of an action potentials is typically constant throughout the myocardium in a healthy heart, in cases such as ischaemia, the magnitude of the transmembrane jumps may vary in different regions of the heart (Holland & Brooks 1976, Holland & Brooks 1977).

The effect of this parameter was investigated by adjusting the magnitude from 80–120 mV when performing the inverse solutions with the default value for all other simulations set to 100 mV.



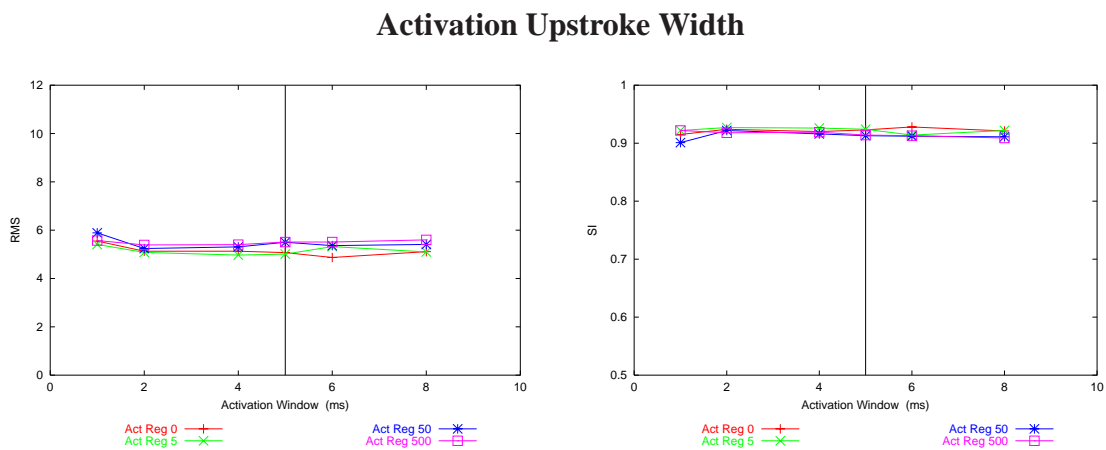
**Figure 7.6:** Effect of transmembrane jump magnitude on the activation based formulation. As potential based approaches do not contain a transmembrane jump parameter, only the activation based approaches were examined for this simulation.

Figure 7.6 shows there is almost no effect of adjusting the transmembrane jump magnitudes. When the magnitudes were adjusted in the range of 80–120 mV there was less than 1 mV change in all solutions compared to the control simulation.

### 7.4.2 Effect of the Width of the Activation Upstroke

As described in Section 5.4, the activation wavefront is modelled as a Heaviside step function which is then approximated as a sigmoid function. One of the key parameters of the function specified in Equation (5.44) is the activation width  $\omega$ . This parameter determines the transition zone between the activated and unactivated regions.

The effect of this parameter was investigated by adjusting the magnitude from 1–8 ms when performing the inverse solutions with the default value for all other simulations set to 5 ms.



**Figure 7.7:** Effect of width of the activation upstroke on the activation based formulation. As potential based approaches do not model the activation upstroke parameter, only the activation based approaches were examined for this simulation.

Figure 7.7 shows there is almost no effect of adjusting the width of the activation function. When the magnitudes were adjusted in the range of 1–8 ms there was less than 1 mV change in all solutions compared to the control simulation.

### 7.4.3 Effect of Lung Masses & Conductivities

The effect of the lung masses on the inverse solutions is investigated by varying the lung conductivities and also by setting the lungs conductivity to be the same as the surrounding torso cavity. The conductivities of the lungs were varied from 0.01–0.22 mS mm<sup>-1</sup>, where a conductivity value of 0.22 mS mm<sup>-1</sup> corresponded to the control torso cavity conductivity and the control lung conductivity was originally set to 0.05 mS mm<sup>-1</sup>. The remaining torso conductivities are the standard values specified in Section 4.5.1.

The inverse solutions with varying lung conductivities are shown in Figure 7.8. They show that in general, there was little change in the solution errors when the lung conductivities were changed in the inverse problem. The one exception was the potential based approaches which failed when the conductivities were reduced significantly below that of the normal control value. For all cases, when the conductivity levels were increased, the resultant solutions changed by less than 1 ms from the control solutions. The L-curve method was preferred over the other methods for determining the regularisation parameter in the potential based approaches, while the CRESO method failed with low conductivity values.

The lungs masses were also totally removed (*i.e.*, a homogeneous heart torso model was used) in a simulation. The solutions with this setup were similar to those obtained when the lung conductivities were set to be equal to the surrounding torso cavity with RMS errors of less than 1 ms.

This lack of effect of the changes in lung conductivities on the inverse solutions is in contrast to other forward problem simulations (Klepfer et al. 1997, van Oosterom & Huiskamp 1989, Bradley et al. 2000). In these simulations the resultant torso surface potentials have been found to change dramatically with changes in the surrounding tissue impedance.

The inverse study conducted by (Ramanathan & Rudy 2001a) has shown similar results which indicate that the inclusion of the lung inhomogeneities contribute little to the accuracy of the inverse solutions.



### Lung Conductivities

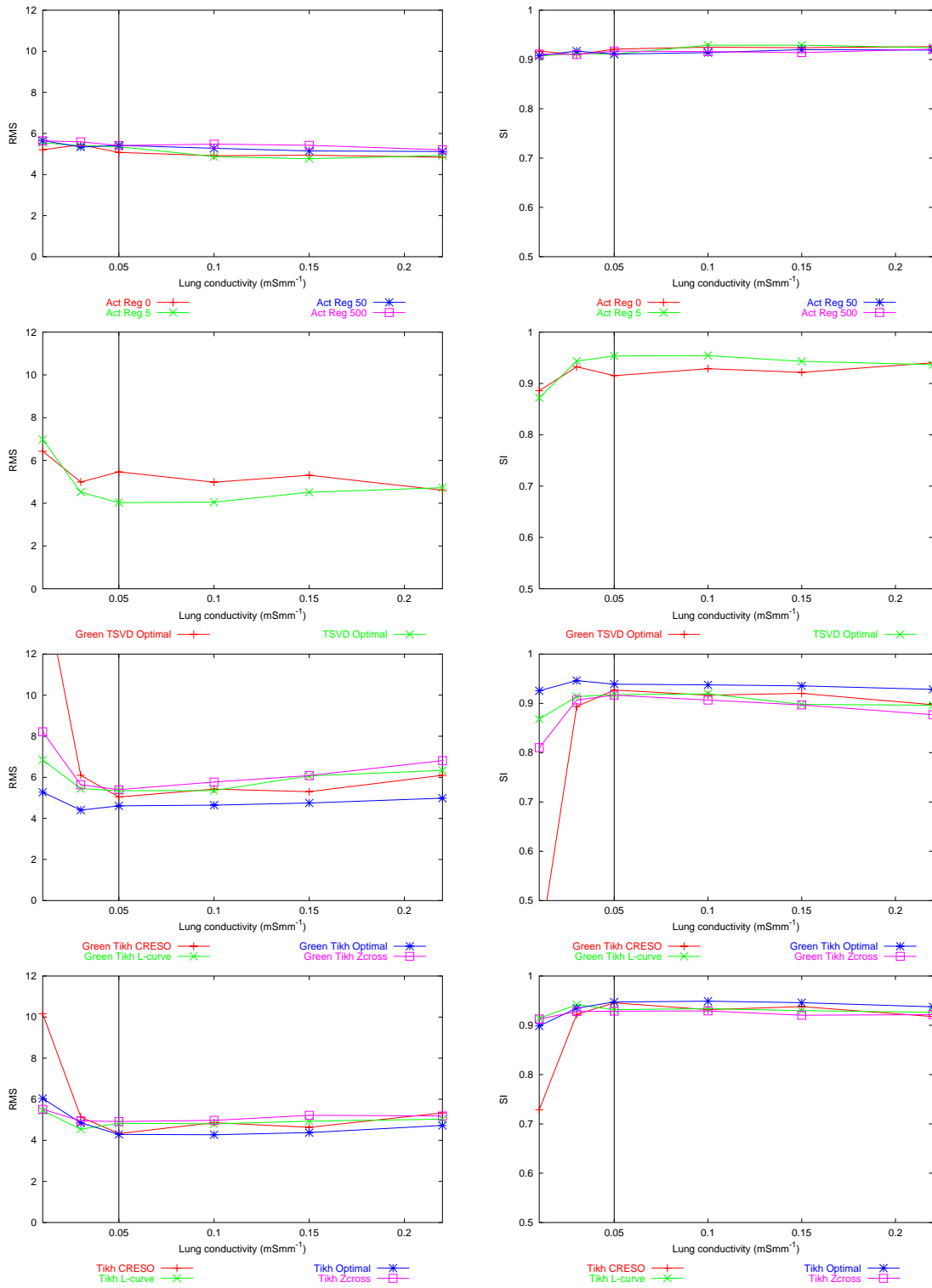


**Figure 7.8:** Effect of lung conductivities on activation and potential based formulations. Layout as described in Figure 7.3.

## 7.5 Effect of Geometric Errors

The relative positions between the heart and the torso surface plays an important role in determining the pattern of current flow, and hence the potential distribution on the torso surface. To quantify this and investigate the effect of errors in modelling the torso geometry, this section investigates the effect of heart size and position as well as torso size.

The close proximity of the lung and heart surfaces means it was necessary to omit the lungs from these simulations to avoid intersection between surfaces when the heart was moved and a four region model was used. Different transfer matrices were used with different geometric setups but the same signal data matrix was used for all simulation runs.

### 7.5.1 Effect of Heart Translation in the Lateral Directions

To investigate the effect of translating the heart in the lateral directions, the heart was translated up to 30 mm in the right lateral (negative) direction and up to 20 mm in the left lateral (positive) direction.

Figure 7.9 shows the inverse solutions when the heart was translated in the lateral directions.

The solution errors in both potential and activation approaches increased at a slower rate when the heart was translated in the right lateral direction when compared to translations in the left lateral direction. Figure 7.9 shows that, in general, the activation based approaches were affected less by the geometric error and the potential approaches were severely compromised when the heart was translated more than 10 mm in either direction.

All the different regularisation parameters produced similar results with the activation approach, however there was large variability with the potential based approaches. The Tikhonov methods provided the best results under control conditions. The L-curve and zero-crossing methods provided the best regularised solutions. Translations by less than 5 mm resulted in less than 1 ms error in the inverse solutions when using a potential based approach.

### Lateral Heart Translations

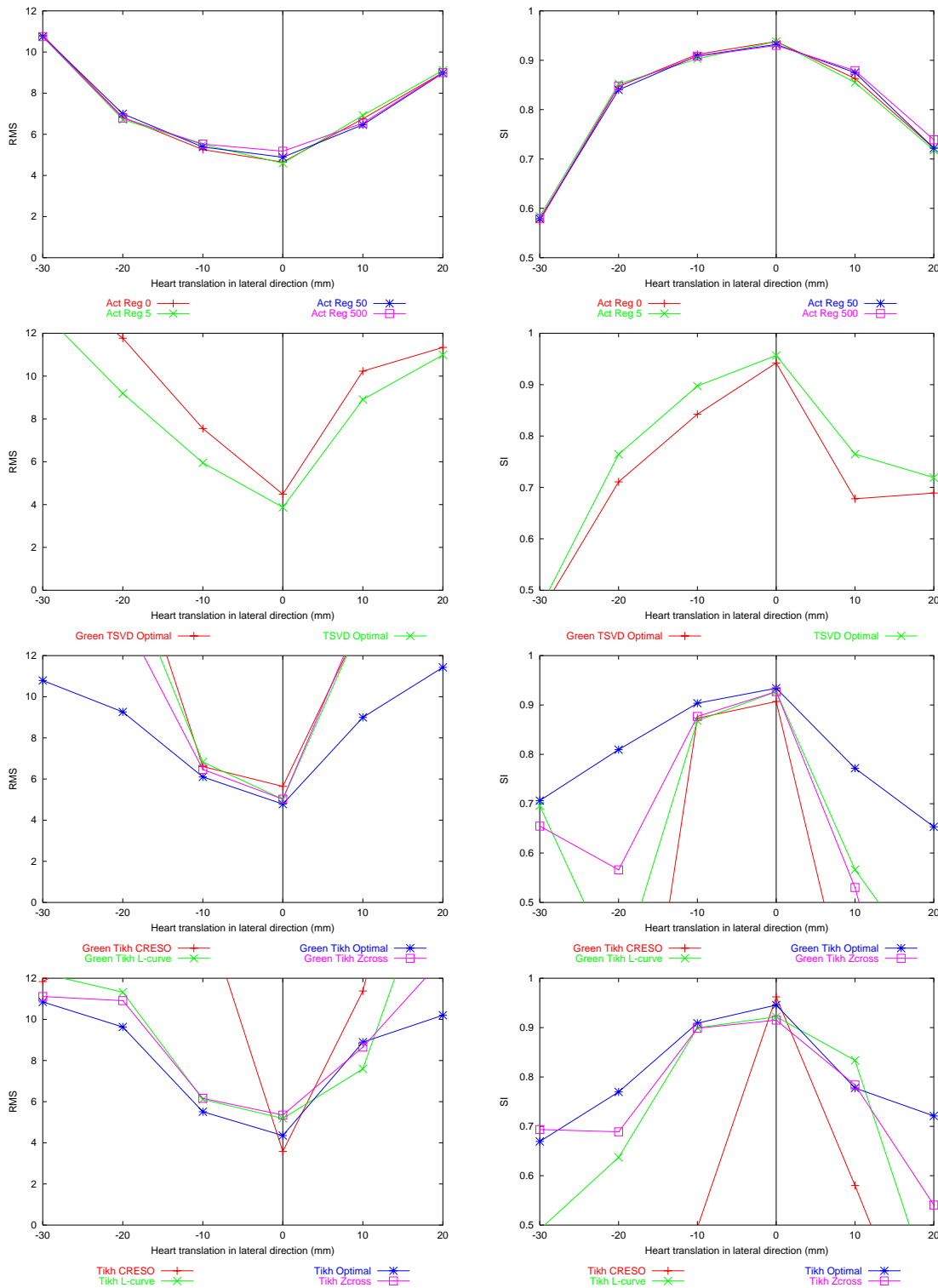


Figure 7.9: Effect of lateral heart translations on activation and potential based formulations. Layout as described in Figure 7.3.

### **7.5.2 Effect of Heart Translation in the Posterior-Anterior Directions**

To investigate the effect of heart translation in the posterior-anterior directions, the heart was translated up to 15 mm in the posterior (positive) direction and up to 20 mm in the anterior (negative) direction.

Figure 7.10 shows that the solutions errors increased at a lower rate when the heart was translated in the posterior direction for both activation and potential approaches.

The activation approaches provided similar results for all regularisation parameters except for when the heart was translated in extreme cases. It provided best results when the heart was translated less than 10 mm. The potential approaches provided acceptable results when the heart was translated less than 5 mm.

Under control conditions, the Tikhonov methods were able to produce the best results, while, when the heart was translated from the control position, the activation approaches, in general, provided better results than the potential approaches.

Posterior-Anterior Heart Translations

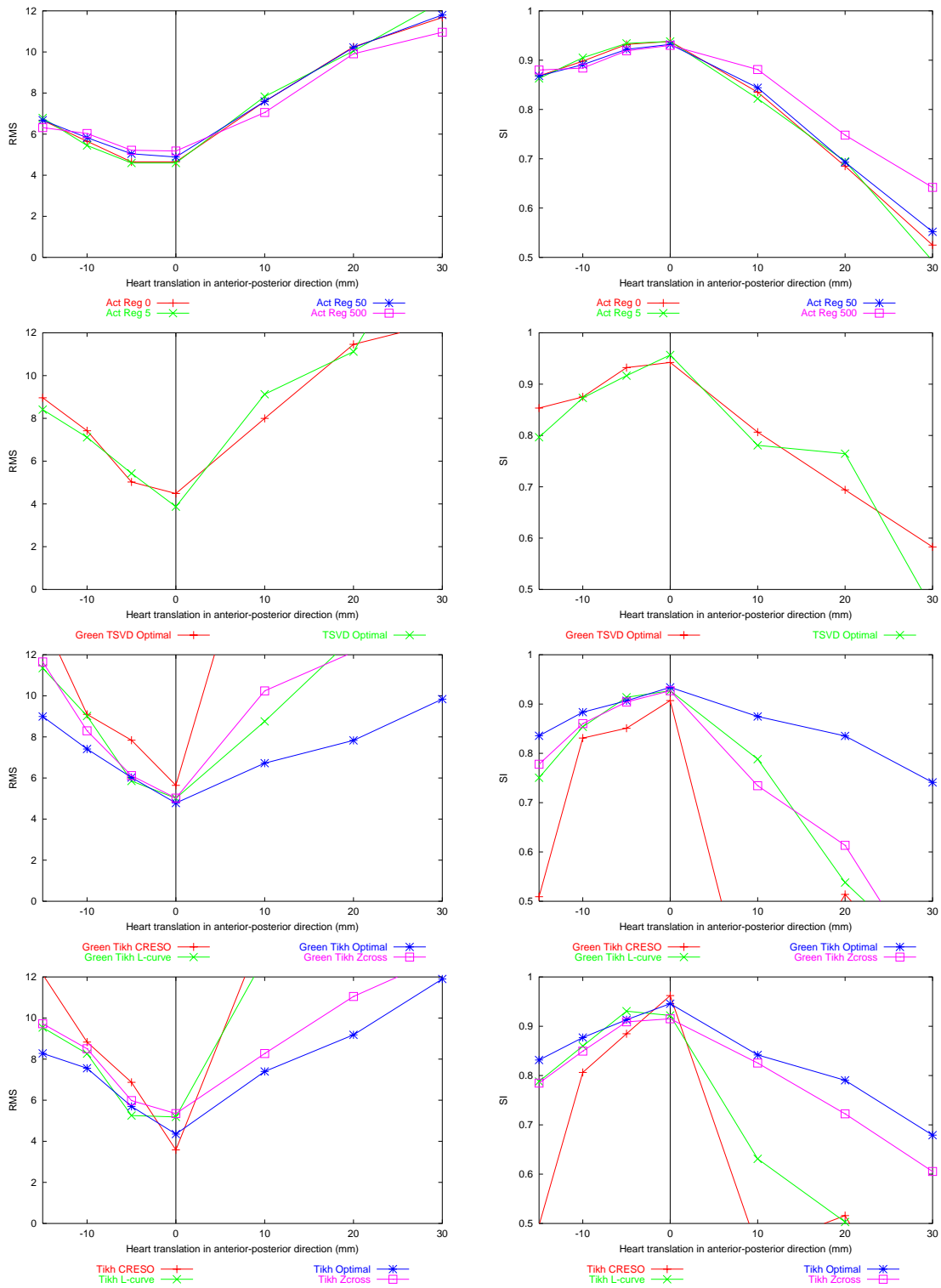


Figure 7.10: Effect of posterior-anterior heart translations on activation and potential based formulations. Layout as described in Figure 7.3.

### 7.5.3 Effect of Heart Translation in the Superior-Inferior Directions

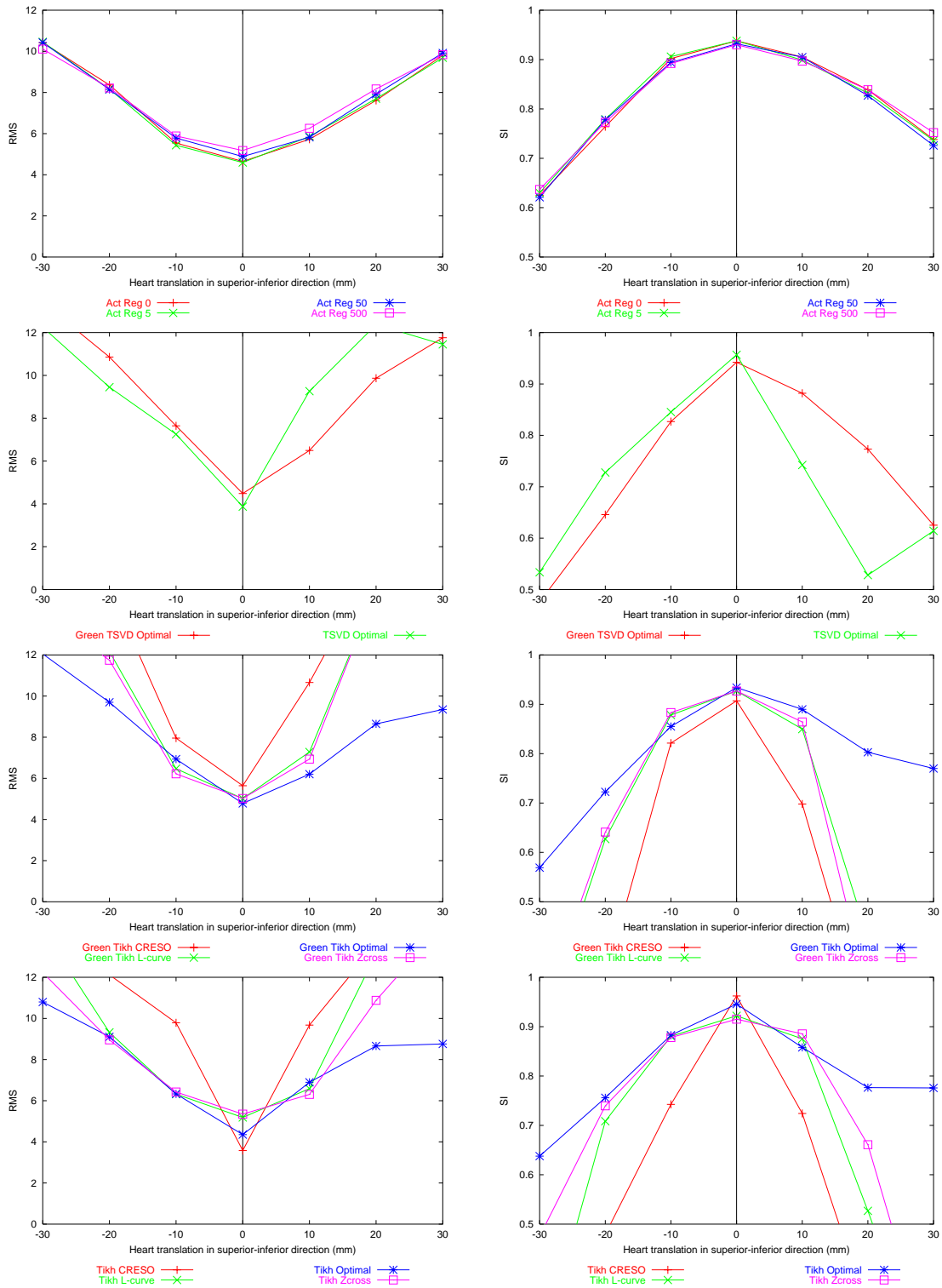
To investigate the effect of heart translation in the superior-inferior directions, the heart was translated up to 30 mm in both the superior (positive) and inferior (negative) directions.

Figure 7.11 shows that the errors increased at a slightly slower rate when the heart was translated in the inferior direction when compared to translations in the superior direction for both potential and activation approaches.

The activation approach produced similar results for all regularisation parameters and the heart was able to be displaced by up to 10 mm without the resultant solution deteriorating by more than 1 ms RMS. In general the activation approach was more stable to heart translations in the superior-inferior directions.

The potential approaches were also able to produce results within 1 ms RMS of the control simulations if the heart was translated less than 10 mm. However, large errors resulted with all methods of determining the regularisation parameters if the heart was further translated. The L-curve and zero-crossing methods provided the best solutions when the heart was displaced less than 10 mm.

### Superior-Inferior Heart Translations



**Figure 7.11:** Effect of superior-inferior heart translations on activation and potential based formulations. Layout as described in Figure 7.3.

### 7.5.4 Effect of Heart Rotation About the Coronal Plane

To investigate the effect of wrongly orientating the heart, the heart was rotated between  $-15-45^\circ$  about the coronal plane (*i.e.*, about the  $y$ -axis) with the centre of rotation defined as the centroid of the heart and the amount of rotation defined in degrees. A positive rotation was defined as an anti-clockwise rotation about the axis and a negative rotation a clockwise rotation from a superior perspective.

Figure 7.12 shows that the activation based approach provided solutions within 1 ms of the control simulation when the heart was rotated within  $15^\circ$  of the control position and produced similar results with different regularisation parameters. There was a near linear decrease in accuracy as the heart was further rotated from the control position.

The potential approaches were generally highly unstable with both the Greensite and Tikhonov methods providing similar results. The CRESO methods for determining the regularisation parameters failed for both Greensite and Tikhonov methods for at both  $15$  and  $45^\circ$  anti-clockwise rotations. In each of these cases infeasible solutions resulted. The L-curve method was preferred over the zero-crossing method for determining the regularisation parameter.

In general, the activation approaches provided more stable results than the potential based formulations, especially at higher levels of heart rotation.



### Heart Rotation about the Coronal Plane

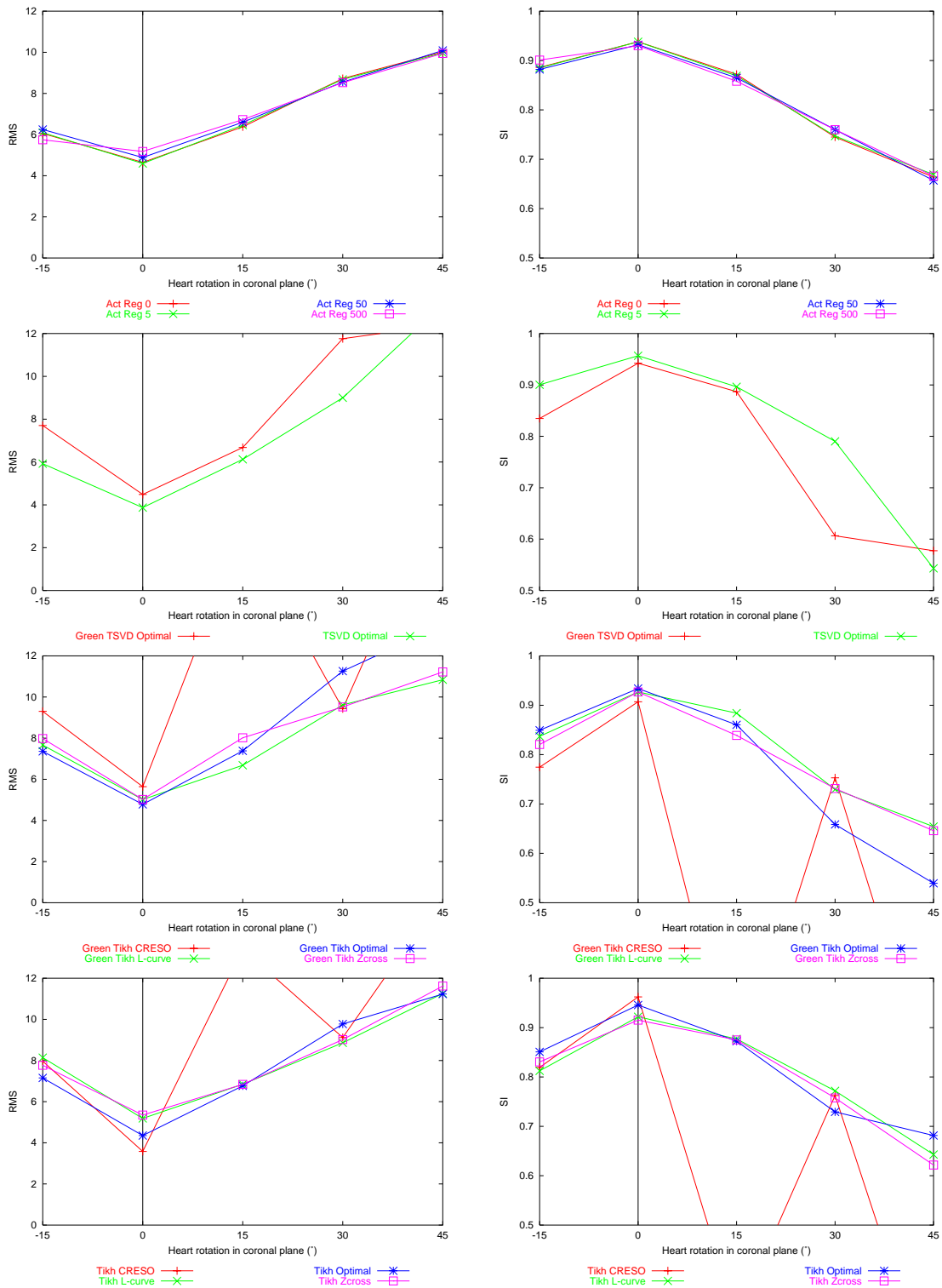


**Figure 7.12:** Effect of heart rotations about the coronal plane on activation and potential based formulations. Layout as described in Figure 7.3.

### 7.5.5 Effect of Heart Rotation About the Sagittal Plane

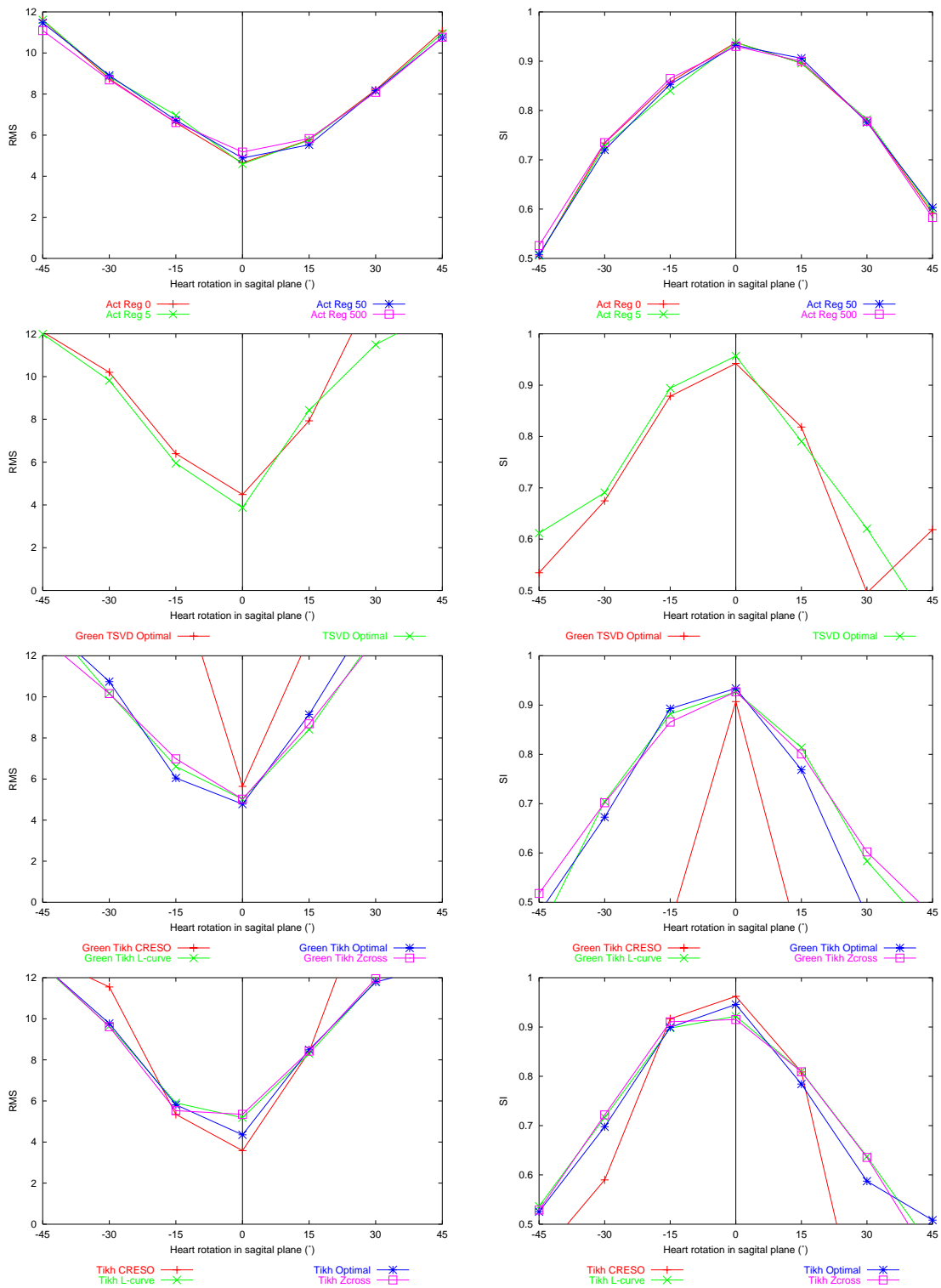
To investigate the effect of misorientating the heart, the heart was rotated clockwise (positive) and anti-clockwise (negative) about the sagittal plane (*i.e.*, about the  $z$ -axis) with the centre of rotation defined as the centroid of the heart and the amount of rotation was in the range of  $-45$ – $45^\circ$ .

Figure 7.13 shows that using the activation based formulation, errors increased at a lower rate when the heart was rotated in the clockwise direction while it increased at a lower rate with the potential based formulations when the heart was rotated in the anti-clockwise direction.

The regularisation parameter had minimal effect on the activation approach solutions. For the potential formulations, the L-curve and zero-crossing methods for determining the regularisation parameters produced similar results. The CRESO method for determining the regularisation parameter failed for all heart rotations with the Greensite method and failed when the heart was rotated more than  $15^\circ$  with the Tikhonov methods. In each of these cases infeasible solutions resulted.

In general, the Tikhonov methods produced the best results under control conditions positions and the activation approach was favoured especially if the heart was rotated in the clockwise direction.

### Heart Rotation about the Sagittal Plane



**Figure 7.13:** Effect of heart rotations about the sagittal plane on activation and potential based formulations. Layout as described in Figure 7.3.

### 7.5.6 Effect of Heart Size

To investigate the effect of incorrectly determining the heart size, simple scaling of the heart was used. The heart volume was altered by scaling the distance between each heart node and the origin of the mesh in each direction. The change in heart volume was measured as a ratio between the volume of the control heart mesh and each corrupted heart volume, *i.e.*,

$$\text{Volume change} = \frac{V}{V_0} \quad (7.4)$$

where  $V_0$  is the volume of the control mesh and  $V$  is the new volume.

The changes in epicardial volumes for each run of the simulation are shown in Table 7.2. The heart volumes were varied by between 0.65 and 1.43 times the epicardial control mesh. The heart was not scaled in the  $y$  direction to prevent the heart surfaces intersecting with the torso surface.

SIMULATION	A	B	C	D	E
SCALE FACTORS	0.8 0.8 0.8	0.9 0.9 0.9	1.0 1.0 1.0	1.1 1.0 1.1	1.2 1.0 1.2
VOLUME (mm <sup>3</sup> )	$7.55 \times 10^4$	$9.51 \times 10^4$	$1.17 \times 10^5$	$1.41 \times 10^5$	$1.67 \times 10^5$
$V/V_0$ RATIO	0.65	0.81	1.00	1.21	1.43

**Table 7.2:** Heart scaling parameters used to alter the volume of the heart mass. The shaded column represents the control simulation.

The activation based approaches produced similar results for all regularisation parameters and results within 1 ms RMS of the control case were obtained when the size of the heart was altered by up to 20%.

The potential based approaches were generally stable when the heart size was reduced by 20% but failed if the heart size was reduced further. The CRESO method was unstable especially when the size of the heart was under-estimated while the L-curve method was slightly favoured over the zero-crossing method for determining the regularisation parameter.

Both activation and potential based methods continued to produce favourable results when the heart was 20% smaller than the control heart size. The activation approach was able to produce better solutions than the potential based methods when the heart volume was over-estimated.

Heart Size

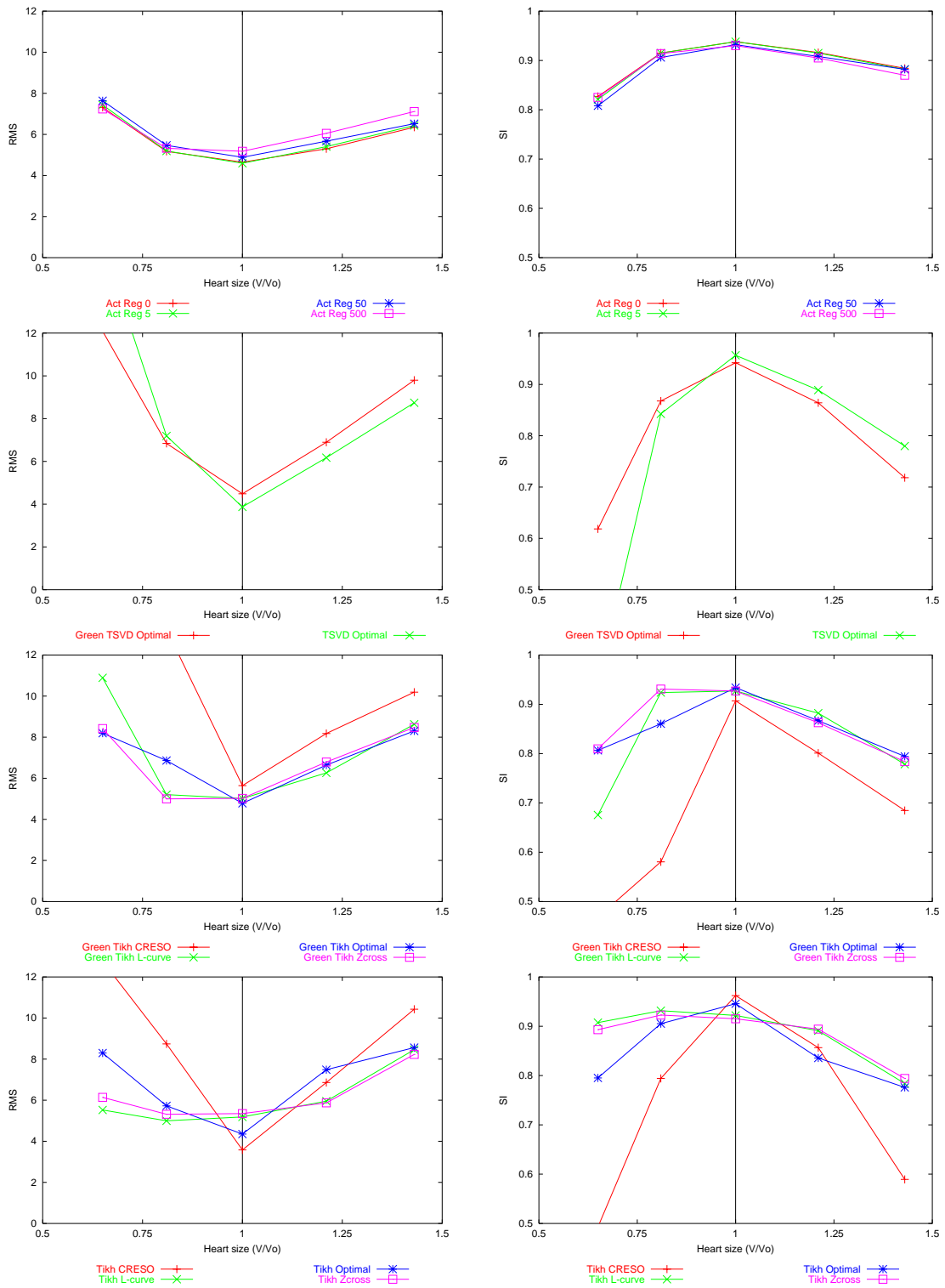


**Figure 7.14:** Effect of heart size on activation and potential based formulations. Layout as described in Figure 7.3.

### 7.5.7 Effect of Torso Size

To investigate the effect of the size of torso cavity on the inverse solutions, simple scaling of the torso surface was used to create known errors in the transfer matrices. The measure of torso cavity changes were the same as that used to measure the changes in heart volume as specified in Equation (7.4).

The torso cavity volumes were varied between 0.64 and 1.72 times the volume of the control mesh. The sizes of the torso volumes for each run of the simulation are shown in Table 7.3. The torso size was not reduced in the  $y$  direction to prevent intersection of the heart and torso surfaces.

SIMULATION	A	B	C	D	E
SCALE FACTORS	0.8 1.0 0.8	0.9 1.0 0.9	1.0 1.0 1.0	1.1 1.1 1.1	1.2 1.2 1.2
VOLUME (mm <sup>3</sup> )	$7.98 \times 10^6$	$1.01 \times 10^7$	$1.25 \times 10^7$	$1.65 \times 10^7$	$2.15 \times 10^7$
$V/V_0$ RATIO	0.64	0.81	1.00	1.32	1.72

**Table 7.3:** Torso scaling parameters used to alter the volume of the torso mass. The shaded column represents the control simulation.

Figure 7.15 shows that the activation based approaches tended to favour under-estimating the torso size. When the torso size was within 20% of the actual size results remained within 1 ms RMS of the control simulations.

The potential based approaches failed when the incorrect torso sizes were used. Errors rapidly increased as the torso size was increased or decreased from the control. The zero-crossing method for both potential approaches provided the best choice of regularisation parameter.

Torso Size

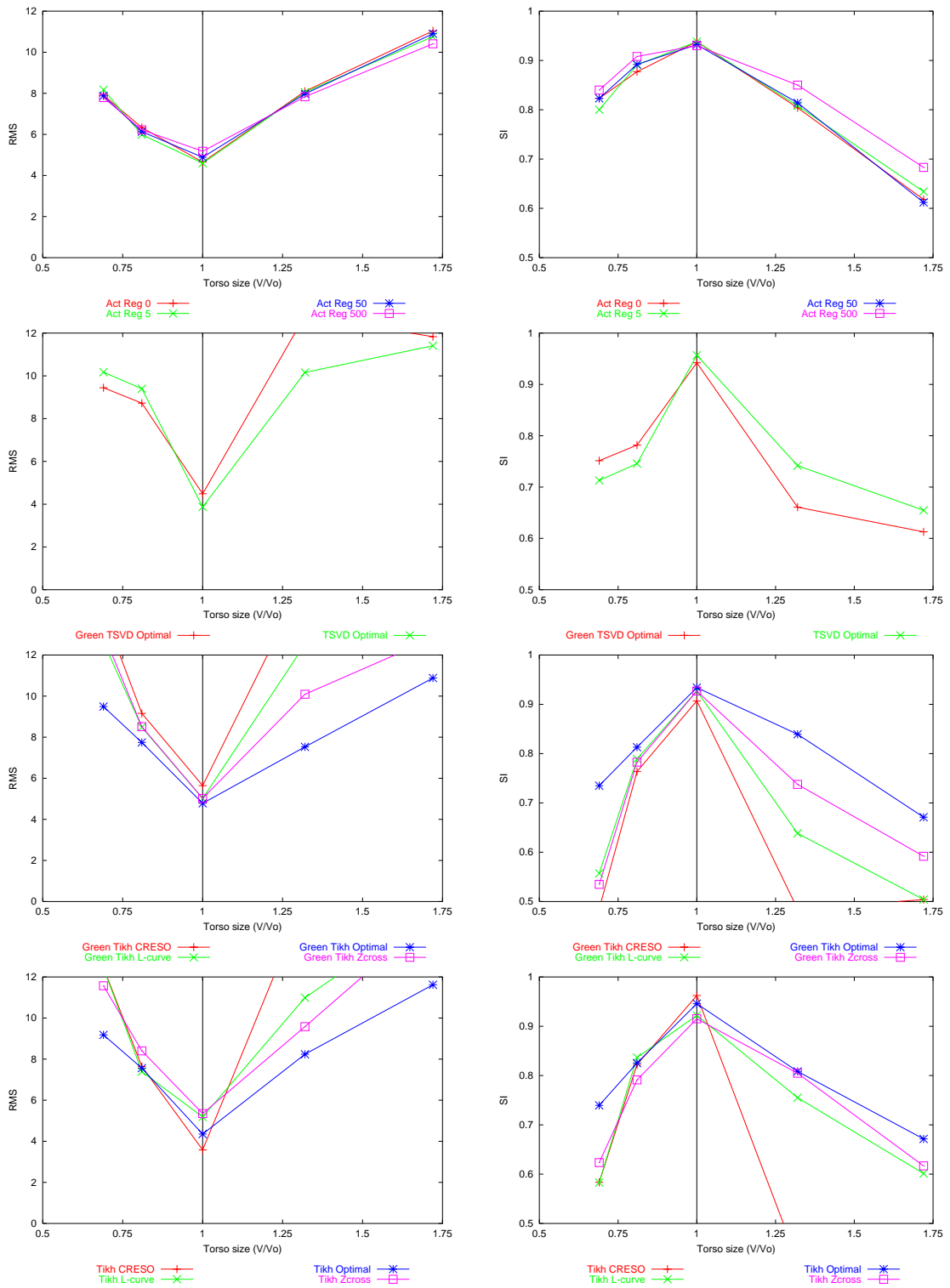


Figure 7.15: Effect of torso size on activation and potential based formulations. Layout as described in Figure 7.3.

## 7.6 Effect of Realistic Experimental Errors

To simulate the conditions which may occur in a realistic clinical or experimental situation, a variety of the errors, previously considered, were combined into a single simulation. The non-linearity of the inverse problem means that the solutions will not be a linear combination of all the previous simulations where individual errors were applied and also why a number of different source models were investigated.

Again, due to the proximity of the heart and lung surfaces, the lungs have been removed for this series of simulations. Using the double point, eikonal and the experimentally derived cardiac sources as described in Sections (4.6.4)–(4.6.5), corresponding torso surface potentials were computed.

To add the combined modelling errors to the inverse simulations, geometric errors were first applied to the heart position and size. The heart was scaled using the coefficients defined in Table 7.2 by 1.1, 1.05, 1.05 and translated by (5, 8, -4) mm. The heart was then rotated about the coronal plane ( $y$  axis) by  $5^\circ$  and then about the sagittal plane ( $z$  axis) by  $5^\circ$ . The signal data was corrupted by  $50 \mu\text{V}$  RMS of Gaussian noise and the physical locations of electrodes then were displaced by a distance of 7 mm RMS. In addition, the magnitude of the transmembrane jump was increased from 100 mV to 110 mV.

The results of the inverse results for each of the three cardiac sources is illustrated in Figures (7.16)–(7.20). For each cardiac source there is a series of eight plots with the same layouts as described in Section 7.2. Along with the plots, the solutions are shown graphically with activation maps and difference maps. The top row of each figure contains (from left to right) the input cardiac field followed by the computed solutions for the activation and the Greensite potential inverse approach. The second row of each figure contains the difference maps between the input cardiac source and the computed solutions. The black regions on the difference maps correspond to areas which have less than 1 ms difference between the input and computed solutions.

With the double point and experimentally derived heart source, the activation approach outperformed all the potential based approaches under control and realistic conditions. With the eikonal heart source, the potential based approaches outperformed the activation based approaches under control conditions. However, when typical errors were added to the simulations, the activation based approaches consistently outperformed all the potential based approaches.

By examining the difference maps it can be seen that with the eikonal and experimentally derived



cardiac sources, for both activation and potential based formulations, the computed solutions tended to move towards the centre of the activation ranges (*i.e.*, regions which should have activated early, activated later than expected and vice versa). This feature is exhibited with the activation based solution with the double point source but not by the Greensite potential based solution.

Applying different levels of regularisation to the activation based formulation did not significantly improve the computed solutions. With higher levels of regularisation, smoother activation fields were produced, however, the magnitudes of the minima and maxima were adversely affected resulting in poor solutions.

The different methods for determining the regularisation parameters for the potential formulations tended to produce comparable results with no method performing consistently better. Despite sometimes failing when subjected to the individual errors (*e.g.*, Figure 7.12 from the simulation where the heart was rotated about the coronal plane) and generally performing poorly, when subjected to the combined errors, the CRESO method was slightly favoured when using a standard Tikhonov regularisation method. The zero-crossing method was slightly favoured when using the Greensite regularisation method, however, in general, all methods for determining the regularisation parameter performed similarly.

### Realistic Simulation with Double Point Cardiac Source

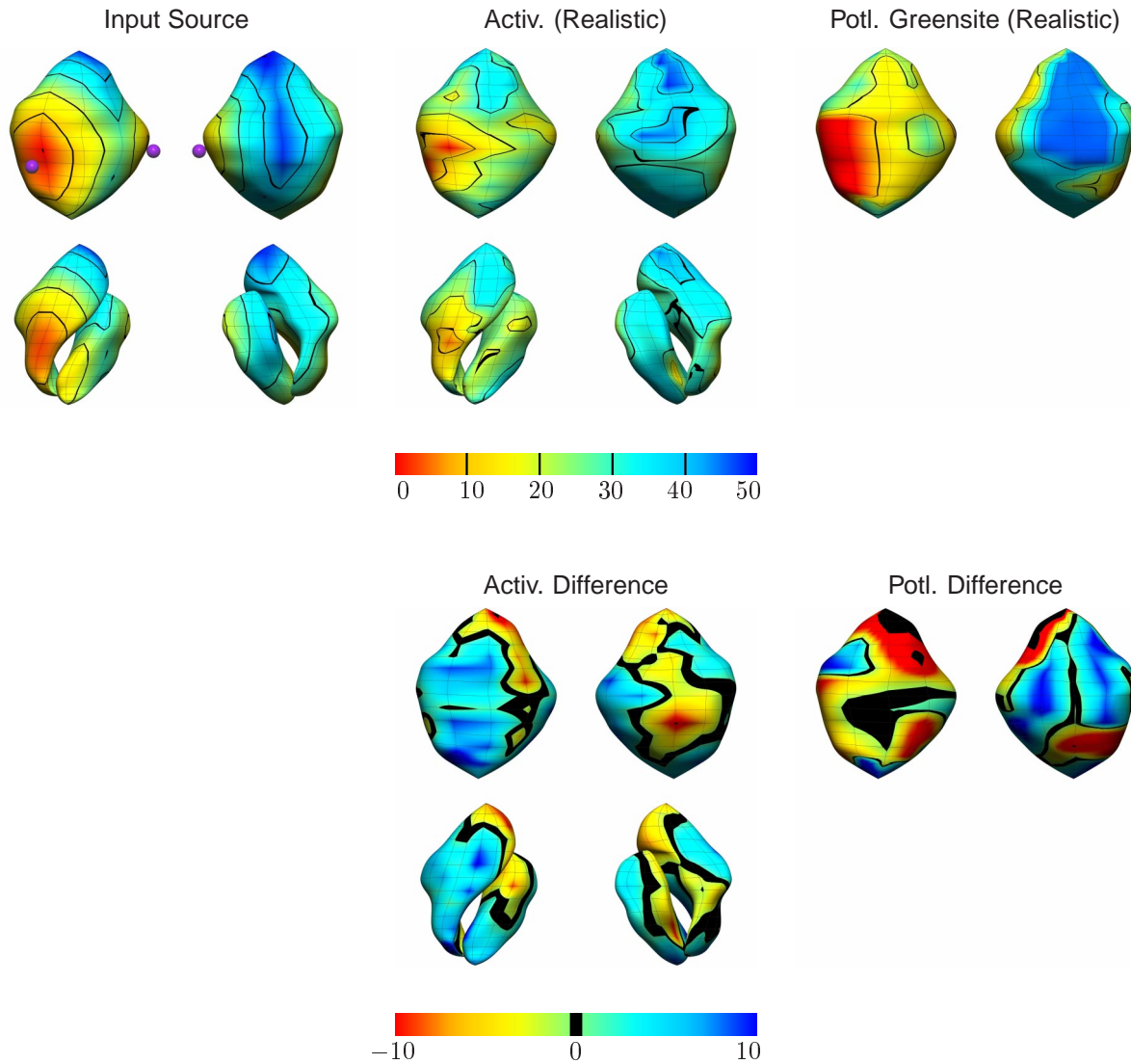


**Figure 7.16:** Comparison between the activation based and potential based formulations (ms) using the double point cardiac source with realistic experimental errors. Shown on the top row from the left is the input activation source, the computed activation field using the activation based formulation and the computed activation field using the Greensite potential method. The second row shows the activation difference maps between the input source and each of the computed solutions. Each subfigure shows the activation field on the epicardial surface (top) and any associated endocardial views (bottom) and anterior views in the left columns and posterior views in the right columns. Note that the potential based methods only compute solutions on the epicardial surfaces, and thus do not have any solutions on the endocardial surfaces associated with them.

Realistic Simulation with Double Point Cardiac Source

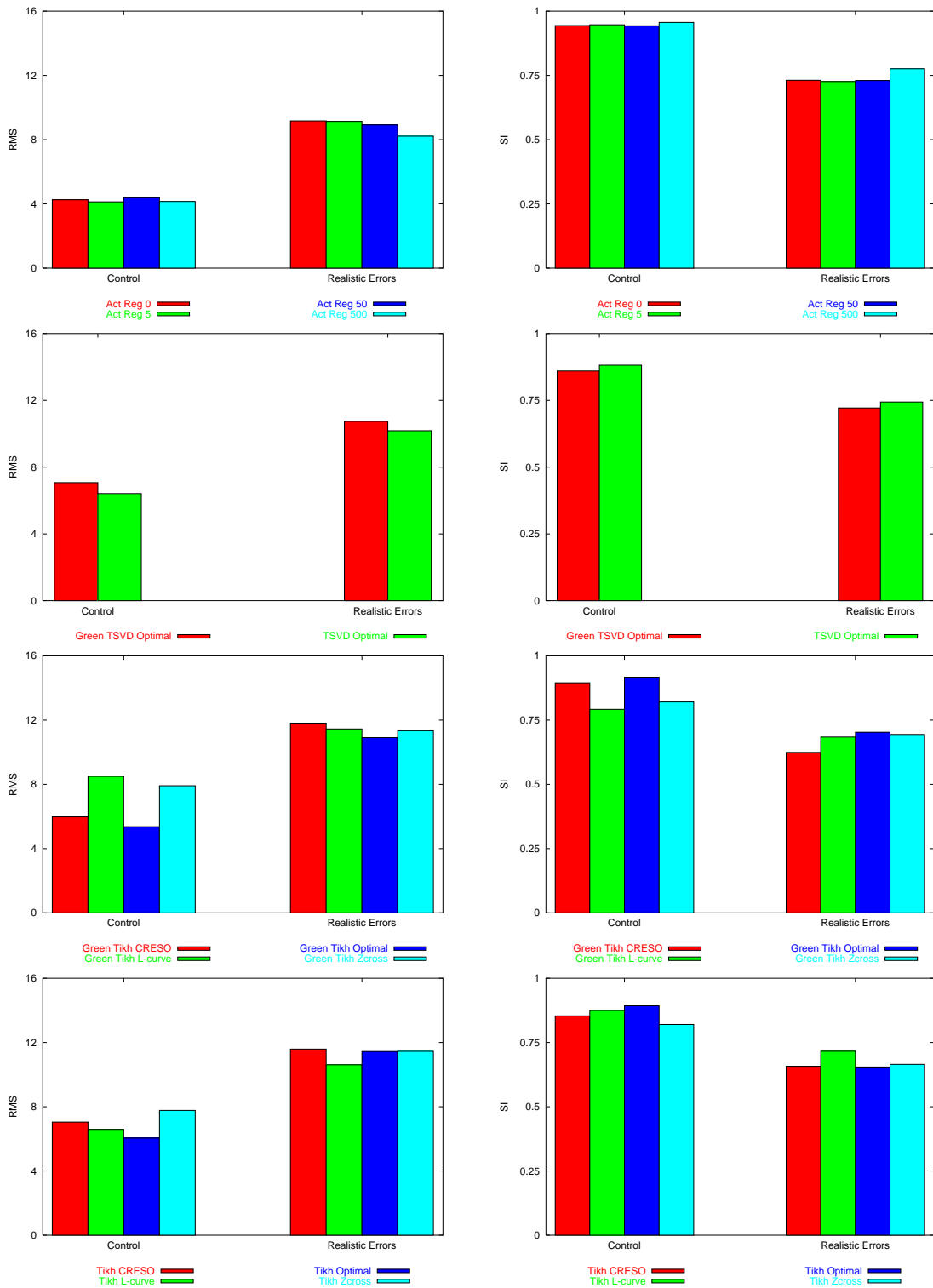
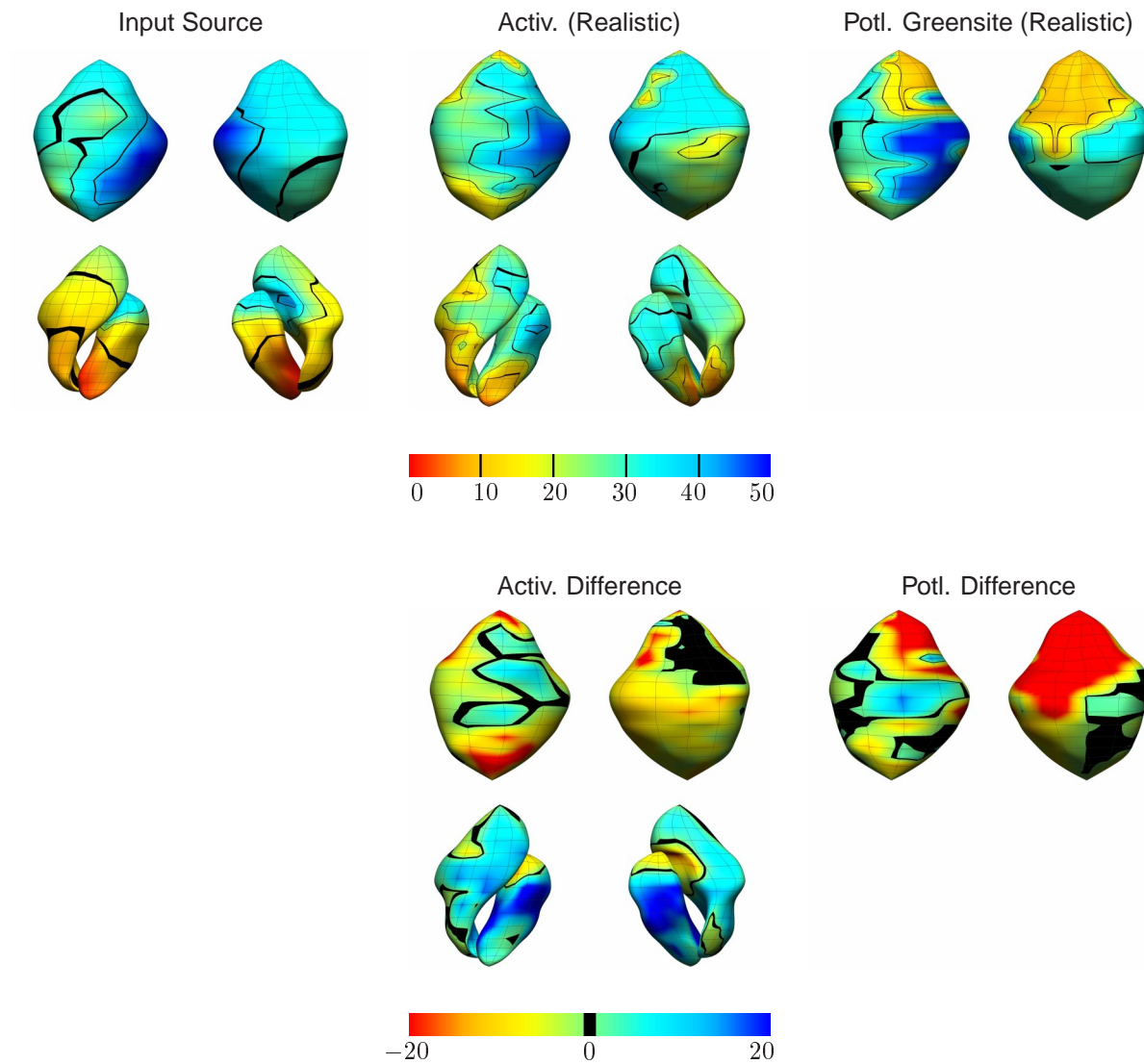


Figure 7.17: Effect of realistic errors on activation and potential based formulations with double point cardiac source. Layout as described in Figure 7.3.

**Realistic Simulation with Eikonal Cardiac Source**

**Figure 7.18:** Comparison between the activation and potential based formulations (ms) using the eikonal cardiac source with realistic experimental errors. Layout as described in Figure 7.16.

Realistic Simulation with Eikonal Cardiac Source

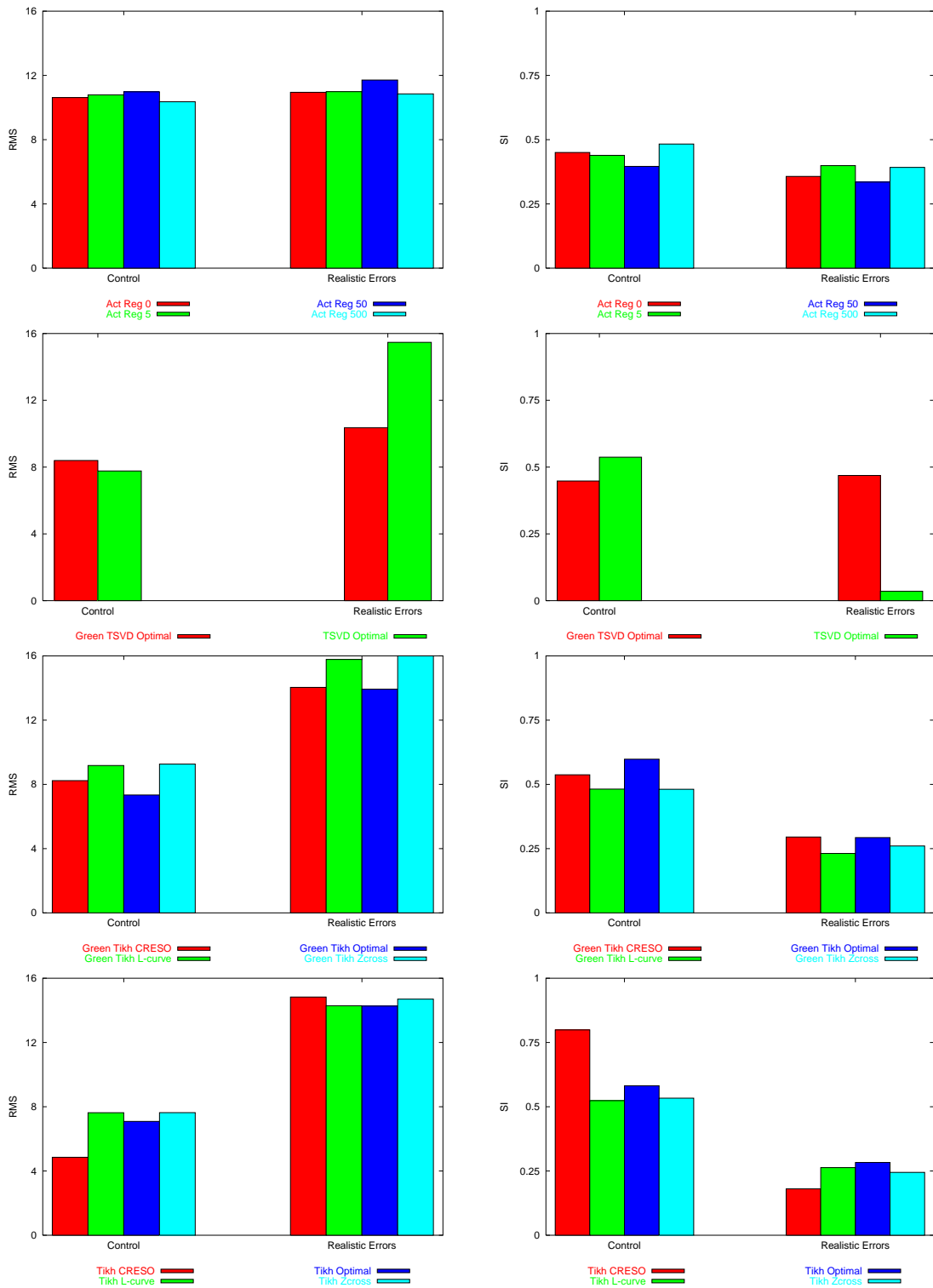
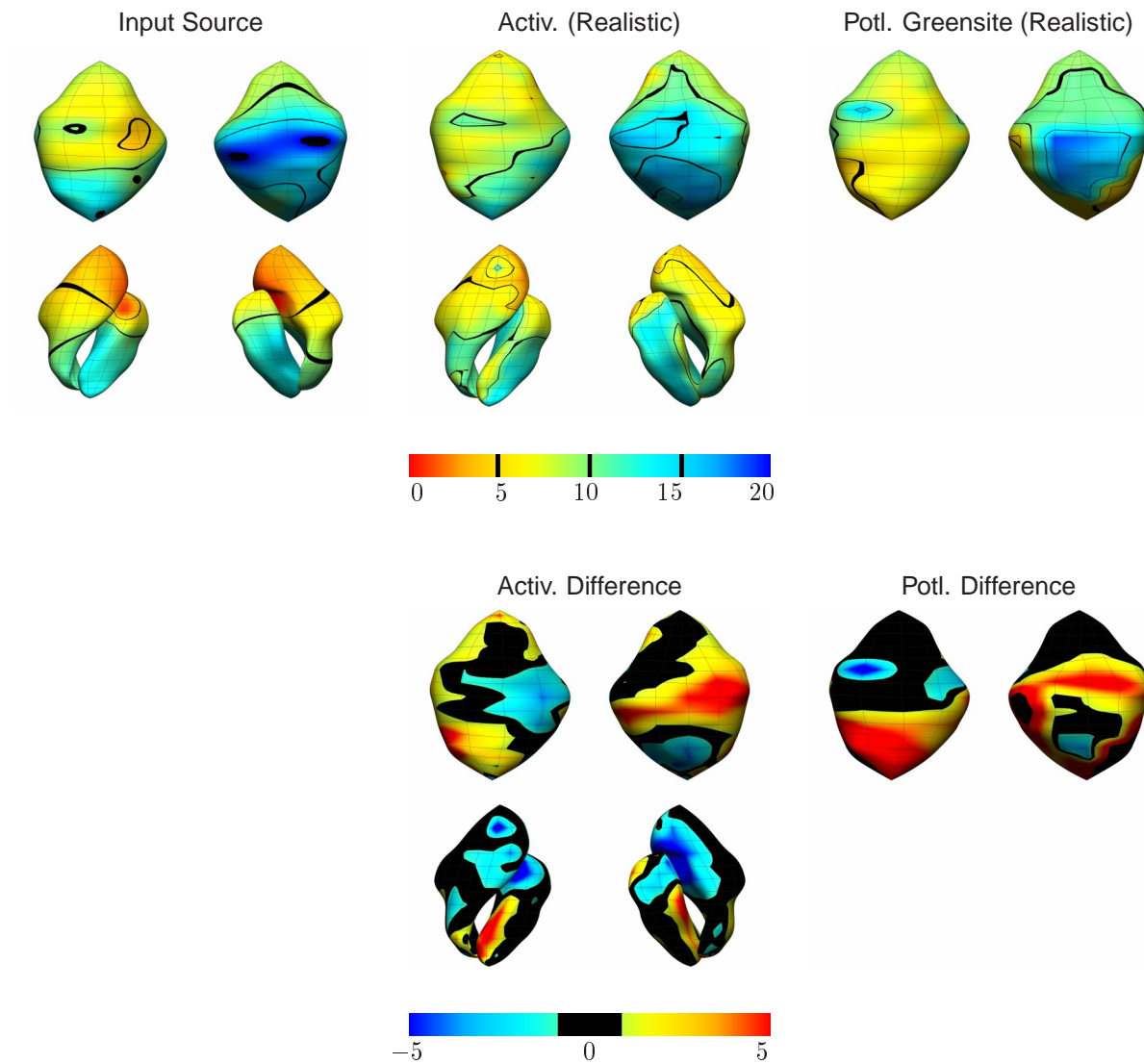


Figure 7.19: Effect of realistic errors on activation and potential based formulations with eikonal cardiac source. Layout as described in Figure 7.3.

## Realistic Simulation with Experimentally Derived Source



**Figure 7.20:** Comparison between the activation and potential based formulations (ms) using the experimentally derived cardiac source with realistic experimental errors. Layout as described in Figure 7.16.

Realistic Errors with Experimentally Derived Cardiac Source

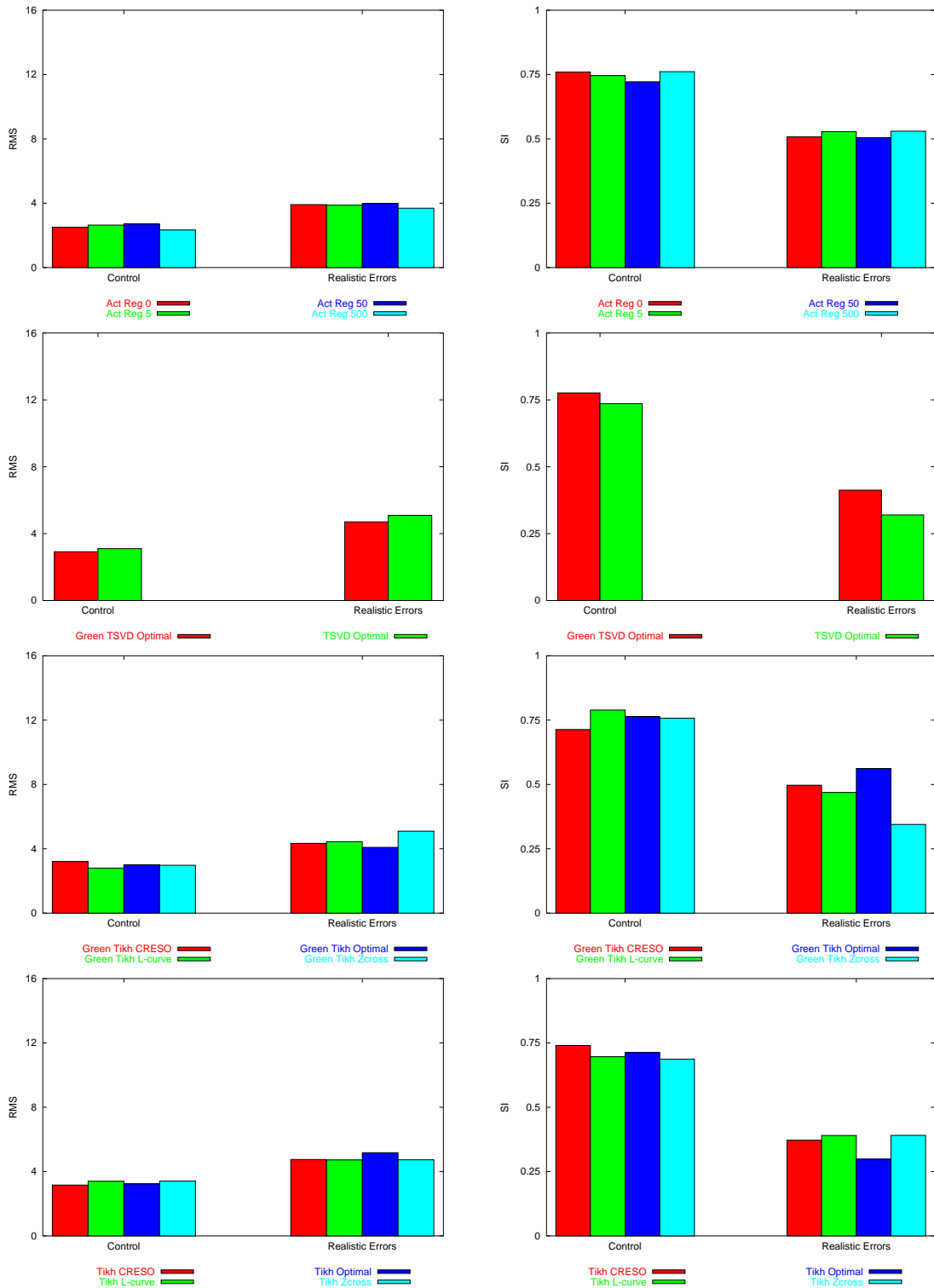


Figure 7.21: Effect of realistic errors on activation and potential based formulations with experimentally derived cardiac source. Layout as described in Figure 7.3.

## 7.7 Comparisons Between Activation & Potential Formulations

As explained in Section 7.2, in order to directly compare the potential and activation formulations, the temporally varying potentials were converted to activation times by assigning the point of maximum negative slope to be the activation time. By converting the potential solutions to an activation based solution, only the point of maximum downstroke needs to be accurately modelled. A large amount of information contained within the signal is effectively lost and the extracted portion corresponding to the maximum negative slope may not necessarily be a true representation of the true signal correlation. With this conversion process errors resulted, even when the exact epicardial distribution was used.

Due to the vast number of signals produced in such a comprehensive simulation study, it was not feasible to manually validate the activation times as determined from the maximum negative slope from the moving finite difference scheme. The moving finite difference method was sufficient for simple traces where only one region of negative slope exists but can lead to significant errors with more complex traces. This conversion process can be dramatically improved with more elaborate methods of determining the appropriate activation times.

Table 7.4 and Figure 7.22 illustrate cases of error resulting from deriving activation times from the exact epicardial solution for three different cardiac sources. Another source of error associated with epicardial inverse activation times is that the activation times were calculated at discrete time intervals and hence an error of up to 0.5 ms can be associated at each heart node.

CARDIAC SOURCE	RMS (ms)	SI
DOUBLE POINT	1.14	1.00
EIKONAL	2.34	0.95
EXPERIMENTALLY DERIVED	2.23	0.88

**Table 7.4:** Comparison between the original activation times and those derived from the corresponding epicardial potential distributions using a moving finite difference calculation. The three cardiac sources correspond to those used in the realistic error simulations described in Section 7.6 while the RMS and similarity index error metrics are defined in Section 3.2.3. Figure 7.22 shows graphically the minimum, median and maximum error associated with the conversion process for one source.

The fact that, occasionally, with the potential inverse solutions (*e.g.*, the geometric error simulations in Section 7.5), the optimal regularisation schemes did not produce the best solutions is an indicator



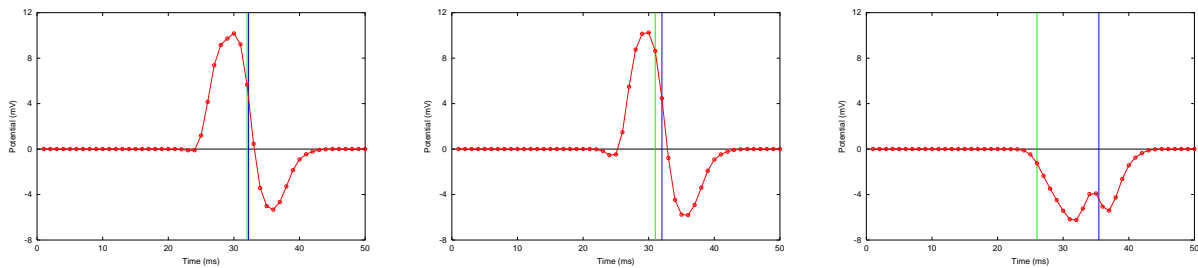


**Figure 7.22:** Exact epicardial traces which represents the minimum, median and maximum error associated with the derived activation times from the experimentally derived activation sequence. The vertical blue line represents the activation time derived from the maximum negative slope and the green vertical line represents the activation time from which the signals were generated. The differences between the original and derived activation times for each signal (from left to right) are 0.23, 1.01 and 9.44 ms. The errors associated with the epicardial surface for three cardiac sources used in the realistic error simulations in Section 7.6 are given in Table 7.4.

of the difficulty of directly comparing the activation and potential based formulations.

### 7.7.1 Effect of Individual Errors

Applying signal errors had a moderate effect on the inverse solutions. Under uncorrelated signal errors (potential recordings and electrode position measurements) the CRESO criterion for determining the regularisation parameter performed close to optimal for both standard and Greensite Tikhonov regularisation. However, under all forms of correlated error the CRESO criterion performed poorly. This can be explained due to the algorithm choosing the wrong relative maximum for the regularisation parameter. This can result in an under- or over-regularised solution. It has been postulated that a better approach would be to choose the relative maxima that results in a feasible solution rather than the first relative maxima which satisfies the CRESO criteria (Johnston & Gulrajani 2000).

The material properties, in general, only had a minor effect on the inverse solutions. Altering the transmembrane jump magnitude within the range of 80–120 mV as with adjusting the width of the activation upstroke had minimal effects on the inverse solutions.

It was found that due to the non-linear optimisation process, even when the magnitude of the transmembrane jump was set to the control value 100 mV, the best results were not necessarily obtained. Varying the lung conductivities resulted in little difference in both the activation and potential in-

verse solutions. By increasing the lung conductivities to the same value as the surrounding torso conductivities, similar results were obtained. If necessary, the lungs could be completely removed and a homogeneous torso region used, resulting in reduced computation in the generation of the transfer matrix.

Torso and heart geometry, as expected, had the greatest effects on the inverse solutions. In general, the heart needed to be positioned within 5 mm to obtain results within 2 ms RMS of the control simulations.

Translating the heart closer to the centre of the torso in the posterior direction (negative  $y$ -axis) produced significantly worse errors in comparison to translating the heart towards the anterior body surface wall. Translation along the right lateral directions (negative  $x$ -axis) and the inferior direction (negative  $z$ -axis) resulted in similar observations but to a lesser extent.

A larger heart and smaller torso size should be favoured if in doubt of the true geometry as solutions errors tended to increase at a lower rate when these sizes were underestimated.

Table 7.5 shows a summary of the preferred algorithms under different categories of applied errors. This is a general summary with the preferred algorithm dependent upon the levels of error introduced into the system. The individual results for each simulation should be examined for more detailed analysis. However, the results provide an indication of the strength of each algorithm when subjected to a moderate level of error and indicate that the activation based method was the preferred inverse algorithm when ever correlated errors were introduced into the system.

APPLIED ERROR	METHOD 1	METHOD 2
SIGNAL NOISE	GREENSITE-TIKHONOV, CRESO	TIKHONOV, L-CURVE
ELECTRODE DISPLACEMENT	ACTIVATION	GREENSITE-TIKHONOV, L-CURVE
CONDUCTIVITY	ACTIVATION	TIKHONOV, L-CURVE
HEART POSITION	ACTIVATION	TIKHONOV, ZERO-CROSSING
HEART SIZE	ACTIVATION	GREENSITE-TIKHONOV, ZERO-CROSSING

**Table 7.5:** Summary of preferred inverse algorithms for typical levels of modelling errors. The applied errors have been grouped into signal, material property and geometric errors. The two most preferred algorithms (excluding optimal based methods) for each type of modelling error are listed.

### 7.7.2 Effect of Combined Errors

When the various signal, material and geometric errors were combined to form realistic modelling errors which could be encountered in an experimental or clinical situation, different trends than with individual errors were observed. In all cases, when typical errors were applied, the activation based solutions still out performed the potential based approaches, but the different regularisation schemes for the potential approaches all provided similar results. There was no significantly favoured method for determining the regularisation parameter, but unlike when errors were applied individually, the CRESO criterion performed on par with the L-curve and zero-crossing methods. The zero-crossing method may be slightly favoured over the other two methods for determining the regularisation parameter.

Although with the control simulations with an eikonal cardiac source both the activation and potential inverse simulations produced poor results (RMS error of 8 ms and SI value of 0.5), the potential inverse solutions were significantly worse under realistic conditions.

For the experimentally derived activation sequence under realistic conditions, all the potential based inverse solutions produced stable solutions. The activation inverse results had an RMS error approximately 1 ms smaller than the potential based inverse.

### 7.7.3 General Comparisons

The Laplacian constraint for the activation based formulation did not greatly improve the solution accuracy. The regularisation parameter which controls the weight given to the body surface residual and activation sequence curvature did provide smoother activation patterns, as would be expected in a normal activation sequence. However, the solution error did not decrease as the maxima and minima in the solutions were usually smoothed out, increasing the error.

Under nearly all circumstances the optimal Tikhonov schemes outperformed the optimal TSVD schemes which reinforced the decision to base the study on a Tikhonov family of regularisation schemes. The L-curve and zero-crossing criterion were the best *a posteriori* methods and resulted in similar comparison metrics. The reason for this is that the zero-crossing criterion is similar to the L-curve minimal-product criterion (Johnston & Gulrajani 2000).

In general the L-curve and zero-crossing criterion produced better results under most protocols for both Tikhonov and Greensite Tikhonov regularisation. Despite the fact that no one potential regularisation scheme produced consistently stable and accurate results over a range of geometric and signal noise encountered, the L-curve method tended to provide the best regularisation solutions except for the cases where size of the heart or torso was adjusted. The zero-crossing method for determining the regularisation parameter may be slightly favoured over the L-curve method as it generally performed well with both individual and combined errors as found by Johnston & Gulrajani (1997).

The Greensite Tikhonov and TSVD methods outperformed the standard techniques only under recording noise error. Both approaches performed on par with one another under uncorrelated measurement noise. However, the Greensite techniques should always be preferred over the more widely accepted spatial regularisation formulations since Greensite's method will always result in a smoother solution set and a reduced variation in the temporal domain.

Only under Gaussian electrical noise did the potential based inverse supersede the activation inverse approach. In all other cases the activation based solutions showed more stable and ordered solutions trends than the more volatile potential inverse approaches. It can be concluded that for activation comparison the myocardial activation inverse is preferred over the potential based solutions. However, error introduced when extracting an activation sequence from an epicardial potential distribution means it is difficult to make a clear comparison between the two inverse regimes.

# 8 *Conclusions, Validation & Future Developments*

There is a general expectation that myocardial electrical source images can be obtained of sufficient accuracy and reliability for them to be useful as an aid for clinical assessment of the heart. The initial steps for determining the reliability and ability for non-invasive electrical imaging algorithms to produce maps of the epicardial and endocardial surfaces which can be of use as a diagnostic tool have been presented.

The methods for efficiently creating a patient specific heart and torso model and the necessary tools for creating and analysing an electrical image of the heart have been developed. Using these tools, a comprehensive inverse simulation study with realistic geometry and several different cardiac sources was performed using both potential and activation based inverse formulations. In addition, a large variety of individual modelling errors as well as a combination of realistic errors which could be expected to be encountered in an experimental or clinical situation were imposed on the simulations.

The simulation study aims to improve the understanding of the inverse problem. Despite being the largest known study to date of the effects of experimental and modelling errors, it still contains a number of weaknesses. Even though a number of heart sources were used, due to the non-linearity of the problem, different heart sources may result in different trends. There are also difficulties in comparing the results between the different solution types, and further errors are introduced in the conversion between potential and activation based solutions. Only one set of combined errors was investigated and different sets of combined errors may lead to slight different trends in terms of relative performance of the various algorithms. Thus, despite the large study, definitive statements about relative performances in real situations cannot be made. Rather, these results can be used to indicate likely trends.

Despite these shortcomings of the simulation study, it is possible to obtain a number of key findings. It was found that the relative positions between the heart and torso is critical in computing an accurate solution. Signal errors also have a moderate effect upon the final outcome of the solution. Material property errors were however, found to have an almost negligible effect upon the inverse solutions. The minimal effect of the lung masses indicates that it may not be necessary to include these in the geometric model for future inverse studies. The inverse algorithms found the presence of correlated errors (such as the geometric errors) that had the largest effects on the final solutions.

It was found that the activation based solutions produced the most stable and consistent results, with Greensite's method the most favoured of the potential based formulations. The zero-crossing and L-curve methods were the best methods for determining the regularisation parameters, with the zero-crossing method slightly favoured when applying individual errors and when typical experimental errors were applied. The surface Laplacian regularisation had minimal effect upon the final solution error metrics for the activation based inverse solutions despite smoother (and more feasible) solutions being obtained. More elaborate regularisation techniques would improve this situation.

Although the activation based formulations produced more accurate and stable results under the majority of conditions, the potential based formulations are computationally much more efficient. In a clinical situation, where solutions must be generated, ultimately, in 'real-time', the potential based solutions will undoubtedly play a significant role.

## 8.1 Validation of Numerical Methods

Despite comparing simplified problems against known analytic solutions and performing a vast variety of inverse simulations with encouraging results, simulations alone will never be sufficient to determine the viability of an electrical imaging procedure in a clinical situation. To quantitatively validate the performance of the inverse procedures, numerical results must be directly compared with experimentally obtained data under conditions which closely match those which would be encountered in a clinical situation.

One approach to obtain such data is to perform *in-vitro* experiments on perfused hearts in a torso tank. Data from such *in-vitro* experiments from perfused canine hearts in a homogeneous cylindrical tank have been collected (Oster & Rudy 1992, Oster, Taccardi, Lux, Ershler & Rudy 1997, Oster

et al. 1998). Similar experiments have been performed under control conditions and with acute ischaemia (MacLeod et al. 1995). These experiments provide a high level of experimental control from which accurate data can be acquired. However, they do not provide a true representation of the *in-vivo* situation.

Of particular use for validating both potential and activation based inverse algorithms would be simultaneously recorded epicardial, endocardial and torso surface potentials. Until recently, only two sets of *in-vivo* data have ever been collected, one in a chimpanzee (Spach, Barr, Lanning & Tucek 1977) and one in a dog (Barr & Spach 1978). Three groups are currently attempting to obtain detailed *in-vivo* data. They are located at the University Laboratory of Physiology, Oxford, the Bioimaging group at the Graz University of Technology and the Bioengineering Research Group at The University of Auckland.

The Graz group have obtained data from human subjects to both validate and further refine an activation-based imaging approach (Tilg et al. 1999). They aim to supplement the information that is currently available to a cardiologist faced with the task of curing a person of a cardiac arrhythmia via a catheterisation procedure. During the procedure, 62 ECG leads are used to acquire torso surface potentials while an electro-anatomical catheter mapping system (Biosense Webster 2000) is used to record endocardial potentials at known geometrical locations. One major disadvantage of this system is that data from only one one recording site can be obtained at a time. To obtain an image of one surface of heart, multiple beats must be used to ‘build up’ an image of the heart. Using this system, it is therefore, not possible to validate irregular beats.

An alternative approach being used at Oxford involves invasive experiments on pigs with simultaneously densely sampled torso and cardiac potential information (Nash et al. 2000*b*). A vest with 256 electrodes with approximately 15 mm spacing is placed on the torso surface and an epicardial sock with 127 electrodes with approximately 7 mm spacing placed around the ventricles. It is also hoped to include the use of an endocardial basket catheter system with 64 electrodes (Cardiac Pathways Corporation 2000) to obtain concurrent endocardial information. In the procedure pigs are thoracotomised and an epicardial electrode sock is placed inside of the pericardium. The chest is then re-closed with the epicardial electrode wires exiting near the diaphragm and the chest cavity filled with saline to eliminate air pockets. Apart from normal sinus rhythms, abnormal beats can be also initiated, either by pacing down any of the epicardial electrodes, via the injection of drugs or by closing and opening of ligates around one of the major coronary arteries. Further information about this process can be found in Nash et al. (2000*b*).

Finally, the ultimate set of data for validation would involve collecting data for single beat analysis from human subjects. At Green Lane Hospital in Auckland, human volunteer subjects already undergoing catheter ablation surgery are candidates for gathering such data (Sands et al. 2000). At the conclusion of a successful procedure, the heart will be paced at single or multiple sites using a catheter. Electrical activity can be recorded at any of the remaining catheters within the heart and a 256 electrode vest similar to that used at the University of Oxford.

Each of the three groups attempting to produce the necessary data for validation of the inverse algorithms presented have their advantages and disadvantages. The data from the Oxford group provides the greatest quantity of information with measurements on epicardial, endocardial and torso surface potential recordings. However, the ultimate validation will need to be performed on *in-vivo* human data for the methods to be clinically accepted. The data obtained from the Graz group is able to provide an activation field on an entire endocardial surface while the Auckland data will only contain discrete measurements, possibly, from multiple endocardial surfaces. However, using the beat averaging method of the Carto system, the Graz group cannot obtain data from unstable arrhythmias. By recording data from each beat individually, the Auckland group is able to capture complex arrhythmias and attempt to analyse this data.

## 8.2 Future Developments

To increase the acceptance of non-invasive electrical imaging of the heart for use in a clinical situation, development of a reliable scheme for obtaining *in-vivo* data from which validation of numerical results is required. Undoubtedly, further hurdles will eventuate when these methods are used in a clinical situation, but this can only be remedied once this process is performed in a routine situation.

Improvement of the initial estimate of the activation field provided by the critical point algorithm is desirable. The activation timings, as provided by the critical point functions, tend to be compressed towards the centre of the temporal domain and difficulties exist in distinguishing between events on the endocardial and epicardial surfaces. A possible solution involves coupling of the critical point algorithm with a reliable potential inverse algorithm to obtain a better initial estimate of the activation times. The simulation study has shown that the Greensite spatial and temporal regularisation method is the preferred potential inverse approach.



The models presented in this thesis have assumed isotropic material properties. This is not a valid assumption within the skeletal muscle region and within the myocardium where electrical conductivities are greatly affected by the fibres within these regions. These isotropic assumptions may have led to the poor performance of the inverse algorithms with the eikonal cardiac source as it was derived from a simulation within a ventricular model with anisotropic material properties. The benefits of the inclusion of a detailed anisotropic heart model are unknown at this stage (and the material property simulations indicate that they have little effect upon the final solution) but may enable more accurate results with experimental and clinical data. The inclusion of heart fibre information may possibly help to overcome the problem with distinguishing critical points on the endocardial and epicardial surfaces. Even if it is shown that inclusion of the fibre information was beneficial it is difficult to obtain fibre information on a patient specific basis, with the most common method using generic information and rule based method for assigning the fibre distribution (Sachse, Frech, Werner & Dössel 1999).

Use of more detailed cardiac source models in the heart, solving directly from cell to body surface, such as the work of Buist & Pullan (2001), may be desired. This would enable more detailed analysis at the cellular level, however, the detail required for accurate solutions is unknown. There is the possibility that a less complex cardiac model such the eikonal equation approach of Tomlinson et al. (1999) may be sufficient.

As discussed in Section 7.7, errors are introduced when temporally and spatially varying potential based solutions are converted to spatially varying activation times. As activation times are believed to be clinically more informative, they are the preferred method of describing the electrical activity within the heart. At present a simple moving average finite difference scheme is used to automatically calculate the maximum negative slope. Due to the vast number of signals produced in such a comprehensive simulation study, it was not feasible to manually check each activation time as automatically determined. This method is sufficient for simple traces where only one region of negative slope exists but can lead to significant errors with more complex traces. This conversion process can be dramatically improved with more elaborate methods of determining the appropriate time of activation.

It is also necessary to reduce the computational time of the algorithms, if such methods are intended for use in a 'real-time' clinical situation. Using a precomputed transfer matrix and torso model, the activation approach is an order of magnitude slower than the potential based inverse solutions (minutes compared to seconds). With further refinement of the code it should be possible to have both potential and activation based formulations automated and obtain an accurate solution in less

than 10 minutes.

A more robust method for determining the heart geometry is also required. Three-dimensional ultrasound is easily accessible and relatively cheap, however, the large variability in quality of cardiac images between subjects will undoubtedly mean that an alternative imaging modality will need to be investigated once the value and reliability of the inverse algorithms have been proven. At this point in time MRI is the leading candidate for providing the most reliable images of the heart. It is however, relatively expensive and time consuming to obtain all the necessary data.

The simulations under both control and realistic conditions showed that the accuracy of the inverse solutions are highly dependent on the cardiac source which is being recovered. Further simulations should be performed with a larger variety of more realistic cardiac sources.

To be able to model re-entrant arrhythmias it is necessary to be able to model the repolarisation phase of the cardiac wavefront. Some work has been performed by Tilg (1998) using similar methods to model the activation phase of the cardiac cycle. However, the modelling of this phase of the cardiac cycle is significantly different to modelling the activation wavefront. Unlike the activation phase the repolarisation phase does not contain a sharp jump. However, one of the key assumptions of the critical point theorem is that it can be approximated as a uniform step jump, which is not the case with recovery wavefront. In addition, during the recovery phase (unlike the activation phase) the heart is subject to motion as it is in its systolic phase of the cardiac cycle.

# **A** *Laplace's & Poisson Equation Analytic Test Solutions*

The results for the analytic test solutions for the generalised Laplace's equation problem described in Section 5.5.1 are presented in tabular form in Appendix A.1 and the solutions to the Poisson equation problem described in Section 5.5.2 presented in Appendix A.2.

The generalised Laplace's equation test problem corresponds to the setup of an epicardial to torso surface transfer matrix while the Poisson equation problem test the transmembrane to epicardial surface and the transmembrane to torso surface transfer matrices.

## **A.1 Convergence of Analytic Laplace's Equation Problem**

The derivation of the general solution to the Laplace's equation along with a specific case is presented in Section 5.5.1. The numerical solutions are compared to the analytic solutions using the error metrics defined in Section 3.2.3 as the mesh was systematically refined.

Table A.1 and Table A.2 show the reduction in error between the numerical and analytic solution as the mesh is refined. The results are also shown graphically in Figures (5.6)–(5.8).

REFINEMENT	NODES	ELEMENTS	AVERAGE CHARACTERISTIC ELEMENT SIZE	RMS (mV)	NIDS (%)
4×4	28	32	1.5	0.210	47.30
8×8	116	128	0.46	0.035	7.28
12×12	484	512	0.12	0.008	1.51
20×20	1988	2048	0.03	0.002	0.35

**Table A.1:** Convergence analysis of potential for Laplace's equation problem. The numerical results have been compared to the analytic solution using the comparison metrics defined in Section 3.2.3.

REFINEMENT	NODES	ELEMENTS	AVERAGE CHARACTERISTIC ELEMENT SIZE	RMS ( $\mu\text{A mm}^{-2}$ )	NIDS (%)
4×4	28	32	1.5	0.124	85.90
8×8	116	128	0.46	0.024	18.56
12×12	484	512	0.12	0.006	4.35
20×20	1988	2048	0.03	0.001	1.05

**Table A.2:** Convergence analysis of normal current for Laplace's equation problem. The numerical results have been compared to the analytic solution using the comparison metrics defined in Section 3.2.3.

## A.2 Convergence of Analytic Poisson Equation Problem

The derivation of the general solution to the Poisson equation along with a specific case is presented in Section 5.5.2. The numerical solutions are compared to the analytic solutions using the error metrics defined in Section 3.2.3 as the mesh was systematically refined.

Table A.3 and Table A.4 show the reduction in error between the numerical and analytic solution as the mesh is refined. The variation of the extracellular potential and normal currents as the mesh is refined is shown Table A.5 and Table A.6. The results are also shown graphically in Figures (5.10)–(5.13).

### A.2.1 Convergence Analysis of Potential and Normal Current

REFINEMENT	NODES	ELEMENTS	AVERAGE CHARACTERISTIC ELEMENT SIZE	RMS (mV)	NIDS (%)
4×4	28	32	0.77	26.54	122.8
8×8	116	128	0.43	4.84	23.2
12×12	484	512	0.30	1.94	9.5
20×20	1988	2048	0.18	0.65	3.2

**Table A.3:** Convergence analysis of the extracellular potential for Poisson equation problem. The numerical results have been compared to the analytic solution specified by Equation (5.98) using the comparison metrics defined in Section 3.2.3.

REFINEMENT	NODES	ELEMENTS	AVERAGE CHARACTERISTIC ELEMENT SIZE	RMS ( $\mu\text{A mm}^{-2}$ )	NIDS (%)
4×4	28	32	0.77	1.15	34.1
8×8	116	128	0.43	0.21	5.5
12×12	484	512	0.30	0.08	2.1
20×20	1988	2048	0.18	0.03	0.6

**Table A.4:** Convergence analysis of the normal current for Poisson equation problem. The numerical results have been compared to the analytic solution specified by Equation (5.99) using the comparison metrics defined in Section 3.2.3.

### A.2.2 Comparison of Potential and Normal Current with Analytic Solution

POINT	ANGLE	ANALYTIC	4×4	8×8	20×20
1	0	0.00	0.00	0.00	0.00
2	45	1.06	1.38	1.11	1.07
3	90	1.37	1.95	1.45	1.39
4	135	0.75	0.70	0.72	0.73
5	180	-0.44	-0.83	-0.514	-0.45

**Table A.5:** Extracellular potentials (mV) calculated from the analytic solution to Case 1, given by Equation (5.98), on the outer sphere. The potentials have been evaluated at the plane of  $\theta = \frac{\pi}{2}$  at five equally spaced locations.

POINT	ANGLE	ANALYTIC	4×4	8×8	20×20
1	0	-2.56	-3.13	-2.74	-2.60
2	45	-14.79	-28.13	-16.89	-15.07
3	90	-18.35	-46.29	-23.69	-19.09
4	135	-11.17	-17.64	-12.06	-11.29
5	180	2.56	3.12	2.74	2.59

**Table A.6:** Current distributions ( $\mu A \text{ mm}^{-2}$ ) calculated from the analytic solution to the Poisson equation problem given by Equation (5.99), on the inner sphere. The potentials have been evaluated at the plane of  $\theta = \frac{\pi}{2}$  at five equally spaced locations.

# ***B*** *Convergence Analysis of Generic Porcine Model*

As the FEM and the BEM are numerical methods which solve problems by discretising the domain, error results from the size of each discretisation unit. The appropriate refinement level required for the generic porcine was determined by conducting a series of forward problem simulations.

Two sets of convergence simulations were conducted using different source models. They were the dipole source used by Bradley et al. (2000) and the eikonal activation source used throughout this thesis. Both of these sources are described in detail in Section 4.6. Further details about the forward simulations can be found in Section 5.6.

Further information about the different refinement levels used in the forward simulations are shown in Appendix B.1 while the convergence results when using the dipole source are given in Appendix B.2 and the results when using the activation source are given in Appendix B.3.

## B.1 Porcine Model Surface Information

SURFACE	REFINEMENT LEVEL	NUMBER OF NODES	NUMBER OF ELEMENTS	GEOMETRIC DOF PER COORDINATE	CHARACTERISTIC ELEMENT SIZE ( $h$ ) mm
EPICARDIUM	0	37	40	142	21.3
	1	152	160	602	10.6
	2	622	640	2658	5.3
	2.5	1242	1280	5114	3.8
LEFT LUNG	0	74	80	290	17.9
	1	306	320	1218	8.9
	2	1250	1280	4994	4.5
RIGHT LUNG	0	74	80	290	20.4
	1	306	320	1218	10.2
	2	1250	1280	4994	5.1
LEFT VENTRICLE	0	27	30	102	13.0
	1	112	120	442	7.0
	2	462	480	1842	3.4
RIGHT VENTRICLE	0	38	42	146	14.8
	1	158	168	626	7.4
	2	650	672	2594	3.7
SKIN	0	254	264	1010	37.3
	1	1034	1056	4130	18.6
	2	4178	4224	16706	9.3

**Table B.1:** Mesh statistics for each surface of the generic porcine model at different refinement levels. Refinement level 0 refers to the surfaces created from geometric fitting. Each higher refinement level involves refining the surface uniformly in each  $\xi$  direction. The epicardial refinement of 2.5 corresponds to 3 levels of refinement in the  $\xi=1$  direction and 2 levels of refinement in the  $\xi=2$  direction.



## B.2 Forward Simulation with Dipole Source

The convergence results for forward simulations with the dipole source using bicubic Hermite interpolation are displayed in Tables (B.2)–(B.7). Table B.8 and Table B.9 summarise the results for the forward simulations using bilinear Lagrange interpolation. These results are analysed in detail in Section 5.6.2.

The reference converged torso model was composed of the epicardial, lungs and torso surfaces with each surface refined once in each direction except the epicardial surface which was refined twice in each direction.

The epicardial potentials and torso surface potentials for each simulations were compared with those from the reference simulation. To compare solutions between different refinement levels, the epicardial potentials were compared at 37 common locations and the torso surface potentials at 254 common locations. These locations corresponded to the nodal positions at the lowest level of refinement.

The signals were compared using the error metrics defined in Section 3.2.3. Key events in the cardiac cycle were used as temporal markers for comparisons. They were Peak P, Peak R, Peak T and QRS interval. These times were determined by solving the forward problem and examining the resultant signals on the dominant chest leads such as those shown in Figure 5.16.

**Effect of Refining the Epicardial Surface on Epicardial Surface Potentials  
using a Dipole Source with Bicubic Hermite Interpolation**

MEASURE	Refinement Level	Peak P	Peak R	Peak T	QRS Integral
REL. RMS	0 – 1	$1.016 \times 10^{+00}$	$9.940 \times 10^{-01}$	$9.730 \times 10^{-01}$	$9.951 \times 10^{-01}$
	1 – 2	$1.691 \times 10^{-01}$	$3.270 \times 10^{-01}$	$3.671 \times 10^{-01}$	$2.670 \times 10^{-01}$
	2 – 2.5	$5.795 \times 10^{-02}$	$8.466 \times 10^{-02}$	$4.502 \times 10^{-02}$	$8.759 \times 10^{-02}$
SI	0 – 1	1.000	1.000	1.000	1.000
	1 – 2	1.000	1.000	1.000	1.000
	2 – 2.5	1.000	1.000	1.000	1.000
MAX. $ \Delta\Phi $	0 – 1	$2.369 \times 10^{+00}$	$3.155 \times 10^{+01}$	$7.420 \times 10^{+00}$	$3.270 \times 10^{+02}$
	1 – 2	$5.444 \times 10^{-02}$	$9.653 \times 10^{-01}$	$2.401 \times 10^{-01}$	$9.968 \times 10^{+00}$
	2 – 2.5	$1.868 \times 10^{-02}$	$2.500 \times 10^{-01}$	$2.939 \times 10^{-02}$	$3.274 \times 10^{+00}$
MIN. $ \Delta\Phi $	0 – 1	$2.372 \times 10^{+00}$	$3.157 \times 10^{+01}$	$7.437 \times 10^{+00}$	$3.275 \times 10^{+02}$
	1 – 2	$5.454 \times 10^{-02}$	$9.680 \times 10^{-01}$	$2.397 \times 10^{-01}$	$1.001 \times 10^{+01}$
	2 – 2.5	$1.870 \times 10^{-02}$	$2.505 \times 10^{-01}$	$2.949 \times 10^{-02}$	$3.279 \times 10^{+00}$
MAX. $\Delta\Phi\%$	0 – 1	-83.130	-84.580	129.650	-81.460
	1 – 2	12.770	20.160	-12.400	15.460
	2 – 2.5	-4.380	-5.220	-1.520	-5.080
MIN. $\Delta\Phi\%$	0 – 1	-123.280	-117.640	83.460	-123.700
	1 – 2	10.860	16.970	-19.430	13.760
	2 – 2.5	-3.720	-4.390	-2.390	-4.510

**Table B.2:** Effect of refining the epicardial surface on the epicardial surface potentials using a moving dipole source. All regions, except the epicardial surface, are maintained at the refinement level set by the reference model (both lungs and torso at level 1 refinement). The different comparison metrics used are listed in the first column. The second column outlines the different levels of refinement used for each surface, while the remaining columns show the comparisons at different time instances.

**Effect of Refining the Epicardial Surface on Torso Surface Potentials  
using a Dipole Source with Bicubic Hermite Interpolation**

MEASURE	Refinement Level	Peak P	Peak R	Peak T	QRS Integral
REL. RMS	0 – 1	$3.199 \times 10^{-02}$	$4.719 \times 10^{-02}$	$1.049 \times 10^{-01}$	$4.103 \times 10^{-02}$
	1 – 2	$1.365 \times 10^{-03}$	$2.548 \times 10^{-03}$	$3.233 \times 10^{-03}$	$2.434 \times 10^{-03}$
	2 – 2.5	$1.487 \times 10^{-03}$	$7.081 \times 10^{-04}$	$2.500 \times 10^{-03}$	$8.687 \times 10^{-04}$
SI	0 – 1	1.000	0.999	0.997	0.999
	1 – 2	1.000	1.000	1.000	1.000
	2 – 2.5	1.000	1.000	1.000	1.000
MAX. $ \Delta\Phi $	0 – 1	$8.504 \times 10^{-03}$	$1.376 \times 10^{-01}$	$1.116 \times 10^{-01}$	$1.366 \times 10^{+00}$
	1 – 2	$5.888 \times 10^{-05}$	$9.803 \times 10^{-04}$	$2.286 \times 10^{-03}$	$7.715 \times 10^{-03}$
	2 – 2.5	$1.957 \times 10^{-04}$	$7.235 \times 10^{-04}$	$4.632 \times 10^{-04}$	$1.151 \times 10^{-02}$
MIN. $ \Delta\Phi $	0 – 1	$2.659 \times 10^{-03}$	$4.853 \times 10^{-02}$	$3.213 \times 10^{-02}$	$6.624 \times 10^{-02}$
	1 – 2	$4.000 \times 10^{-04}$	$1.279 \times 10^{-03}$	$1.156 \times 10^{-03}$	$4.415 \times 10^{-04}$
	2 – 2.5	$1.653 \times 10^{-04}$	$7.176 \times 10^{-04}$	$3.763 \times 10^{-04}$	$1.060 \times 10^{-02}$
MAX. $\Delta\Phi\%$	0 – 1	10.390	14.330	-12.000	8.150
	1 – 2	-0.070	-0.090	0.280	-0.040
	2 – 2.5	0.220	0.070	0.060	0.060
MIN. $\Delta\Phi\%$	0 – 1	0.560	0.900	-8.420	-0.100
	1 – 2	0.090	-0.020	0.280	0.000
	2 – 2.5	0.040	0.010	0.090	0.020

**Table B.3:** Effect of refining the epicardial surface on the torso surface potentials using a moving dipole source. All regions, except the torso surface, are maintained at the refinement level set by the reference model.

**Effect of Refining the Lung Surfaces on Epicardial Surface Potentials  
using a Dipole Source with Bicubic Hermite Interpolation**

MEASURE	Refinement Level	Peak P	Peak R	Peak T	QRS Integral
REL. RMS	0 – 1	$1.992 \times 10^{-01}$	$2.315 \times 10^{-01}$	$7.517 \times 10^{-02}$	$2.319 \times 10^{-01}$
	1 – 2	$1.018 \times 10^{-01}$	$1.116 \times 10^{-01}$	$9.441 \times 10^{-02}$	$1.194 \times 10^{-01}$
SI	0 – 1	1.000	1.000	1.000	1.000
	1 – 2	1.000	1.000	1.000	1.000
MAX. $ \Delta\Phi $	0 – 1	$6.387 \times 10^{-02}$	$6.465 \times 10^{-01}$	$4.881 \times 10^{-02}$	$8.265 \times 10^{+00}$
	1 – 2	$3.268 \times 10^{-02}$	$3.283 \times 10^{-01}$	$6.143 \times 10^{-02}$	$4.453 \times 10^{+00}$
MIN. $ \Delta\Phi $	0 – 1	$6.519 \times 10^{-02}$	$6.924 \times 10^{-01}$	$6.158 \times 10^{-02}$	$8.777 \times 10^{+00}$
	1 – 2	$3.292 \times 10^{-02}$	$3.315 \times 10^{-01}$	$6.212 \times 10^{-02}$	$4.492 \times 10^{+00}$
MAX. $\Delta\Phi\%$	0 – 1	14.980	13.500	2.520	12.820
	1 – 2	-7.660	-6.860	-3.170	-6.900
MIN. $\Delta\Phi\%$	0 – 1	12.980	12.140	4.990	12.070
	1 – 2	-6.550	-5.810	-5.030	-6.180

**Table B.4:** Effect of refining the the lung surfaces on the epicardial surface potentials using a moving dipole source. All regions, except the lung surfaces, are maintained at the refinement level set by the reference model.

**Effect of Refining the Lung Surfaces on Torso Surface Potentials  
using a Dipole Source with Bicubic Hermite Interpolation**

MEASURE	Refinement Level	Peak P	Peak R	Peak T	QRS Integral
REL. RMS	0 – 1	$7.622 \times 10^{-03}$	$8.798 \times 10^{-03}$	$1.165 \times 10^{-02}$	$9.335 \times 10^{-03}$
	1 – 2	$5.232 \times 10^{-04}$	$6.151 \times 10^{-04}$	$6.579 \times 10^{-04}$	$6.431 \times 10^{-04}$
SI	0 – 1	1.000	1.000	1.000	1.000
	1 – 2	1.000	1.000	1.000	1.000
MAX. $ \Delta\Phi $	0 – 1	$5.665 \times 10^{-03}$	$6.036 \times 10^{-02}$	$1.516 \times 10^{-03}$	$7.752 \times 10^{-01}$
	1 – 2	$2.160 \times 10^{-04}$	$2.925 \times 10^{-03}$	$3.936 \times 10^{-04}$	$3.719 \times 10^{-02}$
MIN. $ \Delta\Phi $	0 – 1	$1.434 \times 10^{-03}$	$5.511 \times 10^{-03}$	$3.660 \times 10^{-03}$	$5.219 \times 10^{-02}$
	1 – 2	$1.343 \times 10^{-04}$	$5.541 \times 10^{-04}$	$6.637 \times 10^{-05}$	$6.455 \times 10^{-03}$
MAX. $\Delta\Phi\%$	0 – 1	-6.270	-5.500	0.190	-4.270
	1 – 2	0.240	0.270	0.050	0.200
MIN. $\Delta\Phi\%$	0 – 1	-0.310	-0.100	0.880	-0.080
	1 – 2	0.030	0.010	-0.020	0.010

**Table B.5:** Effect of refining the the lung surfaces on the torso surface potentials using a moving dipole source. All regions, except the lung surfaces, are maintained at the refinement level set by the reference model.

**Effect of Refining the Torso Surface on Epicardial Surface Potentials  
using a Dipole Source with Bicubic Hermite Interpolation**

MEASURE	Refinement Level	Peak P	Peak R	Peak T	QRS Integral
REL. RMS	0 – 1	$1.735 \times 10^{-01}$	$5.208 \times 10^{-02}$	$3.306 \times 10^{-01}$	$6.216 \times 10^{-03}$
	1 – 2	$3.443 \times 10^{-01}$	$3.980 \times 10^{-01}$	$1.264 \times 10^{-01}$	$3.982 \times 10^{-01}$
SI	0 – 1	1.000	1.000	1.000	1.000
	1 – 2	1.000	1.000	1.000	1.000
MAX. $ \Delta\Phi $	0 – 1	$5.708 \times 10^{-02}$	$1.684 \times 10^{-01}$	$2.067 \times 10^{-01}$	$2.444 \times 10^{-01}$
	1 – 2	$1.111 \times 10^{-01}$	$1.178 \times 10^{+00}$	$8.362 \times 10^{-02}$	$1.491 \times 10^{+01}$
MIN. $ \Delta\Phi $	0 – 1	$5.506 \times 10^{-02}$	$1.479 \times 10^{-01}$	$2.179 \times 10^{-01}$	$3.648 \times 10^{-02}$
	1 – 2	$1.109 \times 10^{-01}$	$1.176 \times 10^{+00}$	$8.258 \times 10^{-02}$	$1.490 \times 10^{+01}$
MAX. $\Delta\Phi\%$	0 – 1	-13.390	-3.520	10.670	-0.380
	1 – 2	26.050	24.600	4.320	23.130
MIN. $\Delta\Phi\%$	0 – 1	-10.960	-2.590	17.660	0.050
	1 – 2	22.080	20.630	6.690	20.480

**Table B.6:** Effect of refining the torso surface on the epicardial surface potentials using a moving dipole source. All regions, except the torso surface, are maintained at the refinement level set by the reference model.

**Effect of Refining the Torso Surface on Torso Potentials  
using a Dipole Source with Bicubic Hermite Interpolation**

MEASURE	Refinement Level	Peak P	Peak R	Peak T	QRS Integral
REL. RMS	0 – 1	$4.899 \times 10^{-03}$	$6.529 \times 10^{-03}$	$9.835 \times 10^{-03}$	$6.919 \times 10^{-03}$
	1 – 2	$2.728 \times 10^{-04}$	$3.720 \times 10^{-04}$	$8.055 \times 10^{-04}$	$3.556 \times 10^{-04}$
SI	0 – 1	1.000	1.000	1.000	1.000
	1 – 2	1.000	1.000	1.000	1.000
MAX. $ \Delta\Phi $	0 – 1	$5.315 \times 10^{-04}$	$6.119 \times 10^{-03}$	$4.330 \times 10^{-03}$	$9.542 \times 10^{-02}$
	1 – 2	$3.889 \times 10^{-06}$	$2.418 \times 10^{-04}$	$3.214 \times 10^{-04}$	$3.393 \times 10^{-03}$
MIN. $ \Delta\Phi $	0 – 1	$1.616 \times 10^{-03}$	$2.833 \times 10^{-03}$	$1.758 \times 10^{-03}$	$5.529 \times 10^{-02}$
	1 – 2	$5.540 \times 10^{-05}$	$2.060 \times 10^{-04}$	$2.575 \times 10^{-04}$	$2.379 \times 10^{-04}$
MAX. $\Delta\Phi\%$	0 – 1	-0.590	-0.560	-0.530	-0.530
	1 – 2	0.000	0.020	0.040	0.020
MIN. $\Delta\Phi\%$	0 – 1	0.340	-0.050	-0.420	-0.080
	1 – 2	-0.010	0.000	0.060	0.000

**Table B.7:** Effect of refining the torso surface on the epicardial surface potentials using a moving dipole source. All regions, except the torso surface, are maintained at the refinement level set by the reference model.

**Effect of Refining the Epicardial Surface on Epicardial Surface Potentials  
using a Dipole Source with Bilinear Lagrange Interpolation**

MEASURE	Refinement Level	Peak P	Peak R	Peak T	QRS Integral
REL. RMS	0 – 1	$6.560 \times 10^{+00}$	$9.075 \times 10^{-01}$	$9.330 \times 10^{+00}$	$7.285 \times 10^{+00}$
	1 – 2	$3.151 \times 10^{-01}$	$3.474 \times 10^{-01}$	$3.160 \times 10^{-01}$	$2.980 \times 10^{-01}$
	2 – 2.5	$8.398 \times 10^{-02}$	$7.121 \times 10^{-02}$	$8.271 \times 10^{-03}$	$7.125 \times 10^{-02}$
SI	0 – 1	0.662	0.517	0.412	0.622
	1 – 2	0.998	0.998	0.997	0.999
	2 – 2.5	1.000	1.000	1.000	1.000
MAX. $ \Delta\Phi $	0 – 1	$1.987 \times 10^{+00}$	$2.580 \times 10^{+01}$	$2.275 \times 10^{+00}$	$2.591 \times 10^{+02}$
	1 – 2	$1.063 \times 10^{-01}$	$1.131 \times 10^{+00}$	$3.129 \times 10^{-01}$	$1.134 \times 10^{+01}$
	2 – 2.5	$2.849 \times 10^{-02}$	$2.327 \times 10^{-01}$	$9.663 \times 10^{-03}$	$2.736 \times 10^{+00}$
MIN. $ \Delta\Phi $	0 – 1	$4.416 \times 10^{+00}$	$5.417 \times 10^{+00}$	$7.136 \times 10^{+00}$	$6.656 \times 10^{+01}$
	1 – 2	$1.090 \times 10^{-01}$	$1.191 \times 10^{+00}$	$2.991 \times 10^{-01}$	$1.211 \times 10^{+01}$
	2 – 2.5	$2.896 \times 10^{-02}$	$2.446 \times 10^{-01}$	$5.335 \times 10^{-03}$	$2.887 \times 10^{+00}$
MAX. $\Delta\Phi\%$	0 – 1	417.57	533.67	-100.16	383.21
	1 – 2	28.78	30.55	-12.11	20.16
	2 – 2.5	-7.71	-6.28	0.37	-4.86
MIN. $\Delta\Phi\%$	0 – 1	99.87	99.85	-845.28	99.81
	1 – 2	19.77	18.01	-54.88	15.37
	2 – 2.5	-5.25	-3.70	0.98	-3.66

**Table B.8:** Effect of refining the epicardial surface on the epicardial surface potentials using a moving dipole source with bilinear Lagrange interpolation. All regions, except the torso surface, are maintained at the refinement level set by the reference model.

**Effect of Refining the Epicardial Surface on Torso Surface Potentials  
using a Dipole Source with Bilinear Lagrange Interpolation**

MEASURE	Refinement Level	Peak P	Peak R	Peak T	QRS Integral
REL. RMS	0 – 1	$6.539 \times 10^{-02}$	$1.125 \times 10^{-01}$	$1.018 \times 10^{-01}$	$1.147 \times 10^{-01}$
	1 – 2	$1.203 \times 10^{-02}$	$1.967 \times 10^{-02}$	$1.522 \times 10^{-02}$	$1.873 \times 10^{-02}$
	2 – 2.5	$2.365 \times 10^{-03}$	$3.914 \times 10^{-03}$	$3.980 \times 10^{-03}$	$3.701 \times 10^{-03}$
SI	0 – 1	0.997	0.994	0.996	0.994
	1 – 2	1.000	1.000	1.000	1.000
	2 – 2.5	1.000	1.000	1.000	1.000
MAX. $ \Delta\Phi $	0 – 1	$1.019 \times 10^{-02}$	$4.195 \times 10^{-01}$	$9.065 \times 10^{-02}$	$6.452 \times 10^{+00}$
	1 – 2	$3.684 \times 10^{-03}$	$5.454 \times 10^{-02}$	$2.250 \times 10^{-02}$	$7.272 \times 10^{-01}$
	2 – 2.5	$9.561 \times 10^{-04}$	$1.287 \times 10^{-02}$	$6.614 \times 10^{-03}$	$1.720 \times 10^{-01}$
MIN. $ \Delta\Phi $	0 – 1	$1.870 \times 10^{-02}$	$6.520 \times 10^{-01}$	$3.655 \times 10^{-02}$	$8.774 \times 10^{+00}$
	1 – 2	$5.848 \times 10^{-03}$	$7.054 \times 10^{-02}$	$6.475 \times 10^{-03}$	$9.252 \times 10^{-01}$
	2 – 2.5	$9.455 \times 10^{-04}$	$1.664 \times 10^{-02}$	$1.019 \times 10^{-03}$	$2.169 \times 10^{-01}$
MAX. $\Delta\Phi\%$	0 – 1	-11.72	-40.29	11.64	-37.15
	1 – 2	-4.06	-4.98	-2.81	-4.02
	2 – 2.5	1.05	1.17	0.83	0.95
MIN. $\Delta\Phi\%$	0 – 1	4.08	12.47	8.92	13.59
	1 – 2	1.26	1.33	1.56	1.41
	2 – 2.5	-0.20	-0.31	-0.24	-0.33

**Table B.9:** Effect of refining the epicardial surface on the torso surface potentials using a moving dipole source with bilinear Lagrange interpolation. All regions, except the torso surface, are maintained at the refinement level set by the reference model.

### **B.3 Forward Simulation with an Activation Source**

The convergence results for forward simulations with the dipole source are displayed in Tables (B.10)–(B.19). These results are analysed in detail in Section 5.6.3.

The reference converged torso model was composed of the epicardial, left and right endocardial, the left and right lungs and the torso surfaces with each surface refined once in each direction.

The epicardial potentials and torso surface potentials for each simulations were compared with those from the reference simulation. To compare solutions between different refinement levels, the epicardial potentials were compared at 37 common locations and the torso surface potentials at 254 common locations. These locations corresponded to the nodal positions at the lowest level of refinement.

The signals were compared using the error metrics defined in Section 3.2.3. Key events in the cardiac cycle were used as temporal markers for comparisons. They were Peak Q at 12 ms, Peak R at 31 ms, Peak S at 43 ms and QRS interval of 10–45 ms. These times were determined by solving the forward problem and examining the resultant signals on the dominant chest leads.



**Effect of Refining the Epicardial Surface on Epicardial Surface Potentials  
Using an Activation Source**

MEASURE	REFINEMENT LEVEL	PEAK Q	PEAK R	PEAK S	QRS INTEGRAL
REL. RMS	0 – 1	$2.933 \times 10^{-02}$	$1.081 \times 10^{-01}$	$1.055 \times 10^{-01}$	$4.374 \times 10^{-02}$
	1 – 2	$1.041 \times 10^{-02}$	$4.095 \times 10^{-02}$	$4.702 \times 10^{-02}$	$2.498 \times 10^{-02}$
SI	0 – 1	1.000	0.994	0.995	0.999
	1 – 2	1.000	0.999	0.999	1.000
MAX. $ \Delta\Phi $	0 – 1	$4.627 \times 10^{-03}$	$6.834 \times 10^{-03}$	$2.495 \times 10^{-03}$	$2.355 \times 10^{-02}$
	1 – 2	$1.091 \times 10^{-03}$	$1.702 \times 10^{-03}$	$6.292 \times 10^{-04}$	$5.607 \times 10^{-03}$
MIN. $ \Delta\Phi $	0 – 1	$3.357 \times 10^{-03}$	$1.843 \times 10^{-03}$	$1.488 \times 10^{-03}$	$2.690 \times 10^{-02}$
	1 – 2	$8.230 \times 10^{-05}$	$3.028 \times 10^{-03}$	$1.572 \times 10^{-03}$	$2.338 \times 10^{-02}$
MAX. $\Delta\Phi\%$	0 – 1	-3.780	-7.140	-2.170	1.350
	1 – 2	-0.890	1.780	-0.550	-0.320
MIN. $\Delta\Phi\%$	0 – 1	3.340	1.360	6.760	1.200
	1 – 2	0.080	2.230	-7.150	1.040

**Table B.10:** Effect of refining the epicardial surface on the torso surface potentials using an activation source. All regions, except the epicardial surface, were maintained at refinement level specified by the reference model (left and right ventricular chambers, both lungs and torso surfaces at level 1). The different comparison metrics used are listed in the first column. The second column outlines the different levels of refinement used for each surface, while the remaining columns show the comparisons at different time instances.

**Effect of Refining the Epicardial Surface on Torso Surface Potentials  
Using an Activation Source**

MEASURE	REFINEMENT LEVEL	PEAK Q	PEAK R	PEAK S	QRS INTEGRAL
REL. RMS	0 – 1	$7.029 \times 10^{-02}$	$3.065 \times 10^{-01}$	$2.456 \times 10^{-01}$	$5.011 \times 10^{-02}$
	1 – 2	$1.456 \times 10^{-02}$	$5.926 \times 10^{-02}$	$1.469 \times 10^{-01}$	$3.678 \times 10^{-02}$
SI	0 – 1	0.998	0.946	0.981	0.999
	1 – 2	1.000	0.998	0.993	1.000
MAX. $ \Delta\Phi $	0 – 1	$6.340 \times 10^{-03}$	$5.491 \times 10^{-04}$	$1.484 \times 10^{-02}$	$8.905 \times 10^{-02}$
	1 – 2	$7.701 \times 10^{-04}$	$1.618 \times 10^{-03}$	$2.557 \times 10^{-03}$	$8.671 \times 10^{-03}$
MIN. $ \Delta\Phi $	0 – 1	$2.023 \times 10^{-03}$	$2.175 \times 10^{-02}$	$3.233 \times 10^{-04}$	$2.835 \times 10^{-03}$
	1 – 2	$6.245 \times 10^{-04}$	$9.605 \times 10^{-03}$	$2.808 \times 10^{-04}$	$2.160 \times 10^{-02}$
MAX. $\Delta\Phi\%$	0 – 1	-13.170	1.460	-24.700	-11.510
	1 – 2	1.600	4.300	4.260	1.120
MIN. $\Delta\Phi\%$	0 – 1	2.740	44.410	-3.170	-0.350
	1 – 2	-0.850	-19.610	2.750	2.660

**Table B.11:** Effect of refining the torso surface on the torso surface potentials using an activation source. All regions, except the torso surface, were maintained at refinement level specified by the reference model.

**Effect of Refining the Left Ventricular Chamber on Epicardial Surface Potentials  
Using an Activation Source**

MEASURE	REFINEMENT LEVEL	PEAK Q	PEAK R	PEAK S	QRS INTEGRAL
REL. RMS	0 – 1	$3.210 \times 10^{-02}$	$6.778 \times 10^{-02}$	$8.201 \times 10^{-02}$	$2.517 \times 10^{-02}$
	1 – 2	$9.624 \times 10^{-03}$	$1.728 \times 10^{-02}$	$1.707 \times 10^{-02}$	$1.150 \times 10^{-02}$
SI	0 – 1	1.000	0.998	0.998	1.000
	1 – 2	1.000	1.000	1.000	1.000
MAX. $ \Delta\Phi $	0 – 1	$2.655 \times 10^{-04}$	$1.982 \times 10^{-03}$	$2.424 \times 10^{-03}$	$7.119 \times 10^{-03}$
	1 – 2	$8.881 \times 10^{-04}$	$2.261 \times 10^{-04}$	$6.160 \times 10^{-04}$	$1.035 \times 10^{-02}$
MIN. $ \Delta\Phi $	0 – 1	$3.479 \times 10^{-03}$	$3.438 \times 10^{-03}$	$1.222 \times 10^{-03}$	$6.018 \times 10^{-03}$
	1 – 2	$5.276 \times 10^{-04}$	$5.384 \times 10^{-05}$	$3.132 \times 10^{-05}$	$8.333 \times 10^{-04}$
MAX. $\Delta\Phi\%$	0 – 1	-0.220	2.070	2.110	0.410
	1 – 2	-0.730	-0.240	0.540	-0.590
MIN. $\Delta\Phi\%$	0 – 1	-3.460	2.540	-5.560	0.270
	1 – 2	-0.520	0.040	-0.140	0.040

**Table B.12:** Effect of refining the left ventricular surface on the epicardial surface potentials using an activation source. All regions, except the left ventricular surface, were maintained at refinement level specified by the reference model.

**Effect of Refining the Left Ventricular Chamber on Torso Surface Potentials  
Using an Activation Source**

MEASURE	REFINEMENT LEVEL	PEAK Q	PEAK R	PEAK S	QRS INTEGRAL
REL. RMS	0 – 1	$2.161 \times 10^{-02}$	$7.205 \times 10^{-02}$	$9.760 \times 10^{-02}$	$1.683 \times 10^{-02}$
	1 – 2	$6.300 \times 10^{-03}$	$9.582 \times 10^{-03}$	$1.931 \times 10^{-02}$	$1.027 \times 10^{-02}$
SI	0 – 1	1.000	0.999	0.997	1.000
	1 – 2	1.000	1.000	1.000	1.000
MAX. $ \Delta\Phi $	0 – 1	$2.581 \times 10^{-04}$	$6.946 \times 10^{-04}$	$1.772 \times 10^{-05}$	$1.976 \times 10^{-02}$
	1 – 2	$4.895 \times 10^{-04}$	$7.905 \times 10^{-05}$	$2.925 \times 10^{-04}$	$2.398 \times 10^{-03}$
MIN. $ \Delta\Phi $	0 – 1	$7.256 \times 10^{-04}$	$3.689 \times 10^{-03}$	$2.435 \times 10^{-03}$	$1.005 \times 10^{-02}$
	1 – 2	$1.036 \times 10^{-04}$	$3.016 \times 10^{-04}$	$6.626 \times 10^{-04}$	$1.321 \times 10^{-03}$
MAX. $\Delta\Phi\%$	0 – 1	-0.540	1.850	-0.030	2.550
	1 – 2	-1.020	-0.210	0.490	-0.310
MIN. $\Delta\Phi\%$	0 – 1	0.980	7.530	-23.890	-1.240
	1 – 2	-0.140	0.620	-6.500	0.160

**Table B.13:** Effect of refining the left ventricular surface on the torso surface potentials using an activation source. All regions, except the left ventricular surface, were maintained at refinement level specified by the reference model.

**Effect of Refining the Right Ventricular Chamber on Epicardial Surface Potentials  
Using an Activation Source**

MEASURE	REFINEMENT LEVEL	PEAK P	PEAK R	PEAK T	QRS INTEGRAL
REL. RMS	0 – 1	$1.022 \times 10^{-01}$	$5.925 \times 10^{-02}$	$2.721 \times 10^{-02}$	$7.256 \times 10^{-02}$
	1 – 2	$1.929 \times 10^{-02}$	$3.932 \times 10^{-02}$	$1.284 \times 10^{-02}$	$2.236 \times 10^{-02}$
SI	0 – 1	0.995	0.998	1.000	0.997
	1 – 2	1.000	0.999	1.000	1.000
MAX. $ \Delta\Phi $	0 – 1	$4.120 \times 10^{-03}$	$3.531 \times 10^{-03}$	$5.570 \times 10^{-04}$	$5.595 \times 10^{-02}$
	1 – 2	$5.487 \times 10^{-04}$	$7.078 \times 10^{-03}$	$4.018 \times 10^{-05}$	$8.005 \times 10^{-03}$
MIN. $ \Delta\Phi $	0 – 1	$8.101 \times 10^{-04}$	$2.647 \times 10^{-03}$	$5.024 \times 10^{-05}$	$5.169 \times 10^{-02}$
	1 – 2	$4.108 \times 10^{-04}$	$2.791 \times 10^{-04}$	$1.910 \times 10^{-04}$	$1.645 \times 10^{-02}$
MAX. $\Delta\Phi\%$	0 – 1	3.370	3.690	0.480	3.200
	1 – 2	-0.450	-7.390	-0.030	0.460
MIN. $\Delta\Phi\%$	0 – 1	0.810	-1.950	-0.230	2.300
	1 – 2	-0.410	0.210	-0.870	-0.730

**Table B.14:** Effect of refining the right ventricular surface on the epicardial surface potentials using an activation source. All regions, except the right ventricular surface, were maintained at refinement level specified by the reference model.

**Effect of Refining the Right Ventricular Chamber on Torso Surface Potentials  
Using an Activation Source**

MEASURE	REFINEMENT LEVEL	PEAK P	PEAK R	PEAK T	QRS INTEGRAL
REL. RMS	0 – 1	$3.883 \times 10^{-02}$	$3.025 \times 10^{-02}$	$2.523 \times 10^{-02}$	$4.613 \times 10^{-02}$
	1 – 2	$9.546 \times 10^{-03}$	$3.651 \times 10^{-02}$	$9.022 \times 10^{-03}$	$8.034 \times 10^{-03}$
SI	0 – 1	0.999	1.000	1.000	0.999
	1 – 2	1.000	0.999	1.000	1.000
MAX. $ \Delta\Phi $	0 – 1	$2.763 \times 10^{-04}$	$1.203 \times 10^{-03}$	$2.531 \times 10^{-04}$	$2.046 \times 10^{-02}$
	1 – 2	$1.778 \times 10^{-04}$	$1.799 \times 10^{-03}$	$2.823 \times 10^{-05}$	$7.352 \times 10^{-03}$
MIN. $ \Delta\Phi $	0 – 1	$2.203 \times 10^{-03}$	$9.565 \times 10^{-04}$	$1.125 \times 10^{-03}$	$2.691 \times 10^{-02}$
	1 – 2	$6.764 \times 10^{-05}$	$1.997 \times 10^{-03}$	$8.021 \times 10^{-05}$	$8.680 \times 10^{-03}$
MAX. $\Delta\Phi\%$	0 – 1	0.570	-3.200	0.420	2.640
	1 – 2	0.370	-4.780	-0.050	0.950
MIN. $\Delta\Phi\%$	0 – 1	2.980	-1.950	-11.040	-3.310
	1 – 2	-0.090	-4.080	0.790	-1.070

**Table B.15:** Effect of refining the right ventricular surface on the torso surface potentials using an activation source. All regions, except the right ventricular surface, were maintained at refinement level specified by the reference model.

**Effect of Refining the Lung Surfaces on Epicardial Surface Potentials  
Using an Activation Source**

MEASURE	REFINEMENT LEVEL	PEAK Q	PEAK R	PEAK S	QRS INTEGRAL
REL. RMS	0 – 1	$3.817 \times 10^{-02}$	$4.821 \times 10^{-02}$	$7.418 \times 10^{-02}$	$4.271 \times 10^{-02}$
	1 – 2	$9.819 \times 10^{-03}$	$1.120 \times 10^{-02}$	$2.128 \times 10^{-02}$	$1.646 \times 10^{-02}$
SI	0 – 1	1.000	1.000	0.999	0.999
	1 – 2	1.000	1.000	1.000	1.000
MAX. $ \Delta\Phi $	0 – 1	$1.105 \times 10^{-02}$	$3.531 \times 10^{-04}$	$1.257 \times 10^{-02}$	$9.341 \times 10^{-02}$
	1 – 2	$2.237 \times 10^{-03}$	$1.102 \times 10^{-04}$	$2.821 \times 10^{-03}$	$4.083 \times 10^{-02}$
MIN. $ \Delta\Phi $	0 – 1	$1.781 \times 10^{-04}$	$9.501 \times 10^{-03}$	$2.669 \times 10^{-04}$	$1.552 \times 10^{-02}$
	1 – 2	$6.822 \times 10^{-05}$	$2.192 \times 10^{-03}$	$1.509 \times 10^{-05}$	$1.072 \times 10^{-03}$
MAX. $\Delta\Phi\%$	0 – 1	-9.030	0.370	-10.930	-5.340
	1 – 2	1.830	0.120	2.450	2.330
MIN. $\Delta\Phi\%$	0 – 1	0.180	7.010	1.210	0.690
	1 – 2	-0.070	-1.620	0.070	-0.050

**Table B.16:** Effect of refining the lung surfaces on the epicardial surface potentials using an activation source. All regions, except the lung surfaces, were maintained at refinement level specified by the reference model.

**Effect of Refining the Lung Surfaces on Torso Surface Potentials  
Using an Activation Source**

MEASURE	REFINEMENT LEVEL	PEAK Q	PEAK R	PEAK S	QRS INTEGRAL
REL. RMS	0 – 1	$1.158 \times 10^{-02}$	$3.435 \times 10^{-02}$	$1.426 \times 10^{-02}$	$1.860 \times 10^{-02}$
	1 – 2	$1.568 \times 10^{-03}$	$3.707 \times 10^{-03}$	$6.697 \times 10^{-03}$	$2.745 \times 10^{-03}$
SI	0 – 1	1.000	1.000	1.000	1.000
	1 – 2	1.000	1.000	1.000	1.000
MAX. $ \Delta\Phi $	0 – 1	$2.083 \times 10^{-04}$	$1.498 \times 10^{-03}$	$5.325 \times 10^{-04}$	$4.741 \times 10^{-03}$
	1 – 2	$5.203 \times 10^{-05}$	$1.878 \times 10^{-04}$	$1.218 \times 10^{-04}$	$1.800 \times 10^{-03}$
MIN. $ \Delta\Phi $	0 – 1	$2.910 \times 10^{-04}$	$1.366 \times 10^{-03}$	$9.416 \times 10^{-05}$	$9.583 \times 10^{-03}$
	1 – 2	$9.835 \times 10^{-07}$	$1.451 \times 10^{-04}$	$7.940 \times 10^{-05}$	$2.971 \times 10^{-04}$
MAX. $\Delta\Phi\%$	0 – 1	0.430	3.980	-0.890	0.610
	1 – 2	-0.110	-0.500	0.200	0.230
MIN. $\Delta\Phi\%$	0 – 1	-0.390	2.790	0.920	1.180
	1 – 2	0.000	-0.300	0.780	0.040

**Table B.17:** Effect of refining the lung surfaces on the torso surface potentials using an activation source. All regions, except the lung surfaces, were maintained at refinement level specified by the reference model.

**Effect of Refining the Torso Surface on Epicardial Surface Potentials  
Using an Activation Source**

MEASURE	REFINEMENT LEVEL	PEAK Q	PEAK R	PEAK S	QRS INTEGRAL
REL. RMS	0 – 1	$1.651 \times 10^{-02}$	$1.898 \times 10^{-02}$	$3.327 \times 10^{-02}$	$2.804 \times 10^{-02}$
	1 – 2	$3.592 \times 10^{-03}$	$9.129 \times 10^{-03}$	$7.274 \times 10^{-03}$	$5.332 \times 10^{-03}$
SI	0 – 1	1.000	1.000	1.000	1.000
	1 – 2	1.000	1.000	1.000	1.000
MAX. $ \Delta\Phi $	0 – 1	$6.268 \times 10^{-04}$	$6.946 \times 10^{-04}$	$1.548 \times 10^{-03}$	$2.118 \times 10^{-02}$
	1 – 2	$3.407 \times 10^{-04}$	$1.727 \times 10^{-04}$	$4.951 \times 10^{-04}$	$4.501 \times 10^{-03}$
MIN. $ \Delta\Phi $	0 – 1	$8.276 \times 10^{-04}$	$4.805 \times 10^{-04}$	$9.144 \times 10^{-05}$	$1.414 \times 10^{-02}$
	1 – 2	$1.060 \times 10^{-04}$	$2.158 \times 10^{-04}$	$7.657 \times 10^{-06}$	$4.103 \times 10^{-03}$
MAX. $\Delta\Phi\%$	0 – 1	-0.510	-0.730	-1.350	-1.210
	1 – 2	0.280	-0.180	0.430	0.260
MIN. $\Delta\Phi\%$	0 – 1	0.820	-0.350	-0.420	0.630
	1 – 2	-0.110	-0.160	-0.030	-0.180

**Table B.18:** Effect of refining the torso surface on the epicardial surface potentials using an activation source. All regions, except the torso surface, were maintained at refinement level specified by the reference model.

**Effect of Refining the Torso Surface on Torso Surface Potentials  
Using an Activation Source**

MEASURE	REFINEMENT LEVEL	PEAK Q	PEAK R	PEAK S	QRS INTEGRAL
REL. RMS	0 – 1	$1.686 \times 10^{-02}$	$3.412 \times 10^{-02}$	$4.229 \times 10^{-02}$	$2.918 \times 10^{-02}$
	1 – 2	$3.309 \times 10^{-03}$	$9.713 \times 10^{-03}$	$8.361 \times 10^{-03}$	$4.965 \times 10^{-03}$
SI	0 – 1	1.000	0.999	0.999	1.000
	1 – 2	1.000	1.000	1.000	1.000
MAX. $ \Delta\Phi $	0 – 1	$6.110 \times 10^{-04}$	$7.038 \times 10^{-04}$	$1.614 \times 10^{-03}$	$2.784 \times 10^{-02}$
	1 – 2	$2.973 \times 10^{-04}$	$4.538 \times 10^{-04}$	$4.743 \times 10^{-04}$	$6.201 \times 10^{-03}$
MIN. $ \Delta\Phi $	0 – 1	$9.267 \times 10^{-04}$	$9.402 \times 10^{-04}$	$3.216 \times 10^{-04}$	$3.724 \times 10^{-02}$
	1 – 2	$2.981 \times 10^{-04}$	$7.091 \times 10^{-04}$	$1.533 \times 10^{-04}$	$5.754 \times 10^{-03}$
MAX. $\Delta\Phi\%$	0 – 1	-1.270	-1.870	-2.690	-3.600
	1 – 2	0.620	-1.210	0.790	0.800
MIN. $\Delta\Phi\%$	0 – 1	1.260	1.920	3.150	4.580
	1 – 2	-0.400	-1.450	-1.500	-0.710

**Table B.19:** Effect of refining the torso surface on the torso surface potentials using an activation source. All regions, except the torso surface, were maintained at refinement level specified by the reference model.



# **C** *Inverse Simulation Results*

Presented in this appendix are the results from the simulation study examining the effects of experimental and modelling errors on the activation and potential based inverse algorithms.

The errors are divided into three classes: data errors, material property errors and geometrical errors. The results for each simulation are displayed in tabular form in Sections (C.1)–(C.4) using the RMS error metric defined in Equation (3.7) and the similarity index error metric defined in Equation (3.9). The shaded columns correspond to the simulation which corresponds to control conditions (except for the electrical noise simulations, where this corresponds to a minimal noise level of  $1 \mu\text{V}$  RMS noise) and should theoretically have the most accurate results. These results are analysed and presented graphically in Chapter 7.

## C.1 Effect of Signal Errors

### Gaussian Electrical Noise – RMS

APPROACH	TECHNIQUE	1	5	10	50	100
ACTIVATION	REG-0	4.3	4.6	5.1	6.4	8.0
	REG-5	4.1	4.7	5.4	6.2	8.0
	REG-50	4.4	4.6	5.4	6.4	7.9
	REG-500	4.2	4.9	5.4	6.5	9.0
TSVD GREENSITE	OPTIMAL	4.1	3.2	5.5	6.2	8.5
TSVD STANDARD	OPTIMAL	3.7	3.8	4.0	5.8	7.1
TIKHONOV GREENSITE	CRESO	4.7	4.5	5.0	6.4	8.5
	L-CURVE	2.9	4.8	5.3	8.3	8.8
	OPTIMAL	3.0	4.5	4.6	5.9	8.3
	ZCROSS	2.5	5.0	5.4	8.4	8.2
TIKHONOV STANDARD	CRESO	3.2	3.5	4.3	8.0	7.9
	L-CURVE	3.1	3.6	4.8	6.6	7.2
	OPTIMAL	3.2	3.9	4.3	5.9	7.0
	ZCROSS	3.2	4.5	4.9	7.2	8.5

**Table C.1:** Effect of Gaussian electrical noise on inverse simulations using the RMS error metric defined in Section 3.2.3.

### Gaussian Electrical Noise – Similarity Index

APPROACH	TECHNIQUE	1	5	10	50	100
ACTIVATION	REG-0	0.94	0.94	0.92	0.87	0.79
	REG-5	0.95	0.93	0.91	0.88	0.78
	REG-50	0.94	0.94	0.91	0.87	0.79
	REG-500	0.96	0.93	0.92	0.87	0.71
TSVD GREENSITE	OPTIMAL	0.95	0.97	0.92	0.89	0.80
TSVD STANDARD	OPTIMAL	0.96	0.96	0.95	0.90	0.85
TIKHONOV GREENSITE	CRESO	0.94	0.94	0.93	0.88	0.80
	L-CURVE	0.98	0.93	0.92	0.81	0.78
	OPTIMAL	0.97	0.94	0.94	0.91	0.81
	ZCROSS	0.98	0.93	0.92	0.80	0.80
TIKHONOV STANDARD	CRESO	0.97	0.97	0.95	0.81	0.81
	L-CURVE	0.97	0.96	0.93	0.87	0.85
	OPTIMAL	0.97	0.96	0.95	0.90	0.85
	ZCROSS	0.97	0.94	0.93	0.84	0.77

**Table C.2:** Effect of Gaussian electrical noise on inverse simulations using the similarity index error metric defined in Section 3.2.3.



**Uncorrelated Electrode Displacement – RMS**

APPROACH	TECHNIQUE	0	5	10	15
ACTIVATION	REG-0	5.1	5.4	6.6	7.6
	REG-5	5.4	5.6	6.7	7.7
	REG-50	5.4	5.5	6.8	7.2
	REG-500	5.4	5.5	5.9	6.2
TSVD GREENSITE	OPTIMAL	5.5	6.7	8.9	9.7
TSVD STANDARD	OPTIMAL	4.0	7.3	9.6	9.5
TIKHONOV GREENSITE	CRESO	5.0	6.9	9.6	10.2
	L-CURVE	5.3	7.8	10.9	10.7
	OPTIMAL	4.6	6.9	8.2	9.3
	ZCROSS	5.4	9.7	12.3	12.0
TIKHONOV STANDARD	CRESO	4.3	6.7	7.9	9.3
	L-CURVE	4.8	7.5	8.1	8.9
	OPTIMAL	4.3	6.8	8.1	8.6
	ZCROSS	4.9	7.4	8.1	10.5

**Table C.3:** Effect of Gaussian electrode displacement on inverse simulations using the RMS error metric defined in Section 3.2.3.

**Uncorrelated Electrode Displacement – Similarity Index**

APPROACH	TECHNIQUE	0	5	10	15
ACTIVATION	REG-0	0.92	0.91	0.86	0.81
	REG-5	0.91	0.91	0.86	0.81
	REG-50	0.91	0.91	0.85	0.83
	REG-500	0.92	0.91	0.90	0.88
TSVD GREENSITE	OPTIMAL	0.92	0.89	0.77	0.76
TSVD STANDARD	OPTIMAL	0.95	0.85	0.72	0.75
TIKHONOV GREENSITE	CRESO	0.93	0.87	0.79	0.77
	L-CURVE	0.92	0.84	0.70	0.69
	OPTIMAL	0.94	0.88	0.84	0.80
	ZCROSS	0.92	0.77	0.73	0.73
TIKHONOV STANDARD	CRESO	0.95	0.89	0.83	0.78
	L-CURVE	0.93	0.85	0.83	0.80
	OPTIMAL	0.95	0.88	0.83	0.81
	ZCROSS	0.93	0.85	0.82	0.72

**Table C.4:** Effect of Gaussian electrode displacement on inverse simulations using the similarity index error metric defined in Section 3.2.3.

### Correlated Electrode Displacement – RMS

APPROACH	TECHNIQUE	-10	-5	0	5	10
ACTIVATION	REG-0	6.3	5.4	5.1	5.7	7.0
	REG-5	6.3	5.6	5.4	5.7	7.0
	REG-50	6.4	5.9	5.4	5.8	7.1
	REG-500	6.8	5.8	5.4	6.0	7.1
TSVD GREENSITE	OPTIMAL	7.8	5.7	5.5	6.4	8.5
TSVD STANDARD	OPTIMAL	9.1	6.3	4.0	5.6	8.6
TIKHONOV GREENSITE	CRESO	13.3	6.1	5.0	8.7	11.6
	L-CURVE	10.1	6.5	5.3	7.9	11.0
	OPTIMAL	8.0	5.5	4.6	6.9	9.4
	ZCROSS	14.3	7.7	5.4	8.9	9.6
TIKHONOV STANDARD	CRESO	22.4	6.1	4.3	7.4	10.0
	L-CURVE	10.0	6.5	4.8	7.5	9.6
	OPTIMAL	8.1	5.1	4.3	6.2	8.8
	ZCROSS	9.3	6.2	4.9	7.3	9.6

**Table C.5:** Effect of correlated electrode displacement on inverse simulations using the RMS error metric defined in Section 3.2.3.

### Correlated Electrode Displacement – Similarity Index

APPROACH	TECHNIQUE	-10	-5	0	5	10
ACTIVATION	REG-0	0.87	0.91	0.92	0.90	0.85
	REG-5	0.87	0.90	0.91	0.90	0.84
	REG-50	0.87	0.89	0.91	0.90	0.84
	REG-500	0.85	0.90	0.92	0.90	0.85
TSVD GREENSITE	OPTIMAL	0.85	0.91	0.92	0.90	0.80
TSVD STANDARD	OPTIMAL	0.79	0.89	0.95	0.91	0.80
TIKHONOV GREENSITE	CRESO	0.48	0.89	0.93	0.81	0.68
	L-CURVE	0.76	0.88	0.92	0.84	0.66
	OPTIMAL	0.85	0.92	0.94	0.87	0.75
	ZCROSS	0.40	0.83	0.92	0.79	0.74
TIKHONOV STANDARD	CRESO	0.12	0.90	0.95	0.85	0.75
	L-CURVE	0.76	0.88	0.93	0.85	0.75
	OPTIMAL	0.84	0.93	0.95	0.89	0.78
	ZCROSS	0.80	0.90	0.93	0.86	0.75

**Table C.6:** Effect of correlated electrode displacement on inverse simulations using the similarity index error metric defined in Section 3.2.3.

## C.2 Effect of Material Properties

### Transmembrane Jump – RMS

APPROACH	TECHNIQUE	80	90	100	110	120
ACTIVATION	REG-0	5.1	4.8	5.1	5.0	5.1
	REG-5	5.0	5.1	5.4	5.5	5.5
	REG-50	5.1	5.3	5.4	5.4	5.6
	REG-500	5.1	5.5	5.4	5.7	5.9

**Table C.7:** Effect of transmembrane jump on inverse simulations using the RMS error metric defined in defined in Section 3.2.3.

### Transmembrane Jump – Similarity Index

APPROACH	TECHNIQUE	80	90	100	110	120
ACTIVATION	REG-0	0.92	0.93	0.92	0.92	0.93
	REG-5	0.92	0.92	0.91	0.91	0.91
	REG-50	0.92	0.92	0.91	0.92	0.91
	REG-500	0.92	0.92	0.92	0.92	0.91

**Table C.8:** Effect of transmembrane jump on inverse simulations using the similarity index error metric defined in Section 3.2.3.

### Width of Activation Upstroke – RMS

APPROACH	TECHNIQUE	1	2	4	5	6	8
ACTIVATION	REG-0	5.5	5.1	5.1	5.1	4.9	5.1
	REG-5	5.4	5.1	5.0	5.4	5.3	5.1
	REG-50	5.9	5.2	5.3	5.4	5.4	5.4
	REG-500	5.6	5.4	5.4	5.4	5.5	5.6

**Table C.9:** Effect of width of the activation upstroke on inverse simulations using the RMS error metric defined in defined in Section 3.2.3.

### Width of Activation Upstroke – Similarity Index

APPROACH	TECHNIQUE	1	2	4	5	6	8
ACTIVATION	REG-0	0.92	0.92	0.92	0.92	0.93	0.92
	REG-5	0.92	0.93	0.93	0.91	0.91	0.91
	REG-50	0.90	0.92	0.92	0.91	0.91	0.91
	REG-500	0.92	0.92	0.92	0.92	0.91	0.91

**Table C.10:** Effect of width of the activation upstroke on inverse simulations using the similarity index error metric defined in Section 3.2.3.

### Lung Conductivities – RMS

APPROACH	TECHNIQUE	0.01	0.03	0.05	0.10	0.15	0.22
ACTIVATION	REG-0	5.2	5.4	5.1	4.9	4.9	4.8
	REG-5	5.5	5.4	5.4	4.9	4.8	4.9
	REG-50	5.7	5.3	5.4	5.3	5.1	5.1
	REG-500	5.6	5.6	5.4	5.5	5.4	5.2
TSVD GREENSITE	OPTIMAL	6.4	5.0	5.5	5.0	5.3	4.6
TSVD STANDARD	OPTIMAL	7.0	4.5	4.0	4.0	4.5	4.7
TIKHONOV GREENSITE	CRESO	15.7	6.1	5.0	5.4	5.3	6.1
	L-CURVE	6.8	5.5	5.3	5.4	6.1	6.3
	OPTIMAL	5.3	4.4	4.6	4.6	4.8	5.0
	ZCROSS	8.2	5.6	5.4	5.8	6.1	6.8
TIKHONOV STANDARD	CRESO	10.2	5.1	4.3	4.9	4.6	5.3
	L-CURVE	5.4	4.5	4.8	4.8	4.9	5.0
	OPTIMAL	6.0	4.9	4.3	4.3	4.4	4.7
	ZCROSS	5.5	4.9	4.9	5.0	5.2	5.2

**Table C.11:** Effect of lung conductivities on inverse simulations using the RMS error metric defined in Section 3.2.3.

### Lung Conductivities – Similarity Index

APPROACH	TECHNIQUE	0.01	0.03	0.05	0.10	0.15	0.22
ACTIVATION	REG-0	0.92	0.91	0.92	0.93	0.92	0.93
	REG-5	0.91	0.91	0.91	0.93	0.93	0.92
	REG-50	0.91	0.92	0.91	0.91	0.92	0.92
	REG-500	0.91	0.91	0.92	0.92	0.91	0.92
TSVD GREENSITE	OPTIMAL	0.89	0.93	0.92	0.93	0.92	0.94
TSVD STANDARD	OPTIMAL	0.87	0.94	0.95	0.95	0.94	0.94
TIKHONOV GREENSITE	CRESO	0.40	0.89	0.93	0.92	0.92	0.90
	L-CURVE	0.87	0.91	0.92	0.92	0.90	0.90
	OPTIMAL	0.93	0.95	0.94	0.94	0.94	0.93
	ZCROSS	0.81	0.91	0.92	0.91	0.90	0.88
TIKHONOV STANDARD	CRESO	0.73	0.92	0.95	0.93	0.94	0.92
	L-CURVE	0.91	0.94	0.93	0.93	0.93	0.93
	OPTIMAL	0.90	0.93	0.95	0.95	0.95	0.94
	ZCROSS	0.91	0.93	0.93	0.93	0.92	0.92

**Table C.12:** Effect of lung conductivities on inverse simulations using the similarity index error metric defined in Section 3.2.3.

### C.3 Effect of Geometric Errors

**Heart Translation in the Lateral Directions – RMS**

APPROACH	TECHNIQUE	-30	-20	-10	0	10	20
ACTIVATION	REG-0	10.8	6.8	5.3	4.6	6.8	9.0
	REG-5	10.7	6.7	5.5	4.6	6.9	9.1
	REG-50	10.8	7.0	5.4	4.9	6.5	9.0
	REG-500	10.8	6.8	5.5	5.2	6.5	9.0
TSVD GREENSITE	OPTIMAL	14.7	11.8	7.5	4.5	10.2	11.3
TSVD STANDARD	OPTIMAL	13.0	9.2	5.9	3.9	8.9	11.0
TIKHONOV GREENSITE	CRESO	17.4	18.6	6.6	5.6	13.8	21.2
	L-CURVE	14.2	16.4	6.8	5.0	13.8	17.4
	OPTIMAL	10.8	9.3	6.1	4.8	9.0	11.4
	ZCROSS	15.9	13.9	6.5	5.0	14.2	22.8
TIKHONOV STANDARD	CRESO	11.8	14.0	15.6	3.6	11.4	26.7
	L-CURVE	12.2	11.3	6.1	5.2	7.6	18.6
	OPTIMAL	10.8	9.6	5.5	4.4	8.9	10.2
	ZCROSS	11.1	10.9	6.2	5.3	8.7	12.9

**Table C.13:** Effect of heart translation in the lateral directions on inverse simulations using RMS error metric defined in Section 3.2.3.

**Heart Translation in the Lateral Directions – Similarity Index**

APPROACH	TECHNIQUE	-30	-20	-10	0	10	20
ACTIVATION	REG-0	0.57	0.85	0.91	0.94	0.86	0.72
	REG-5	0.58	0.85	0.90	0.94	0.85	0.72
	REG-50	0.58	0.84	0.91	0.93	0.88	0.72
	REG-500	0.58	0.85	0.91	0.93	0.88	0.74
TSVD GREENSITE	OPTIMAL	0.45	0.71	0.84	0.94	0.68	0.69
TSVD STANDARD	OPTIMAL	0.46	0.76	0.90	0.96	0.76	0.72
TIKHONOV GREENSITE	CRESO	0.36	-0.18	0.87	0.91	0.24	0.06
	L-CURVE	0.70	0.35	0.87	0.93	0.57	0.34
	OPTIMAL	0.71	0.81	0.90	0.93	0.77	0.65
	ZCROSS	0.65	0.57	0.88	0.93	0.53	-0.05
TIKHONOV STANDARD	CRESO	0.47	0.32	0.49	0.96	0.58	0.18
	L-CURVE	0.49	0.64	0.90	0.92	0.83	0.35
	OPTIMAL	0.67	0.77	0.91	0.95	0.78	0.72
	ZCROSS	0.69	0.69	0.90	0.92	0.78	0.54

**Table C.14:** Effect of heart translation in the lateral directions on inverse simulations using the similarity index error metric defined in Section 3.2.3.

**Heart Translation in the Posterior-Anterior Directions – RMS**

APPROACH	TECHNIQUE	-15	-10	-5	0	10	20	30
ACTIVATION	REG-0	6.7	5.7	4.6	4.6	7.6	10.3	11.7
	REG-5	6.8	5.4	4.6	4.6	7.8	10.0	12.5
	REG-50	6.7	5.8	5.0	4.9	7.6	10.2	11.8
	REG-500	6.3	6.0	5.2	5.2	7.1	9.9	11.0
TSVD GREENSITE	OPTIMAL	9.0	7.4	5.0	4.5	8.0	11.5	12.5
TSVD STANDARD	OPTIMAL	8.4	7.1	5.4	3.9	9.1	11.1	18.1
TIKHONOV GREENSITE	CRESO	13.8	9.1	7.8	5.6	20.3	15.0	16.3
	L-CURVE	11.3	9.0	5.9	5.0	8.8	12.8	15.3
	OPTIMAL	9.0	7.4	6.0	4.8	6.7	7.8	9.8
	ZCROSS	11.7	8.3	6.1	5.0	10.2	12.1	16.8
TIKHONOV STANDARD	CRESO	12.1	8.8	6.9	3.6	14.4	16.8	20.2
	L-CURVE	9.5	8.3	5.3	5.2	12.9	15.1	20.4
	OPTIMAL	8.3	7.6	5.7	4.4	7.4	9.2	11.9
	ZCROSS	9.7	8.5	6.0	5.3	8.3	11.1	13.0

**Table C.15:** Effect of heart translation in the posterior-anterior directions on inverse simulations using the RMS error metric defined in Section 3.2.3.

**Heart Translation in the Posterior-Anterior directions – Similarity Index**

APPROACH	TECHNIQUE	-15	-10	-5	0	10	20	30
ACTIVATION	REG-0	0.87	0.90	0.93	0.94	0.83	0.69	0.53
	REG-5	0.86	0.91	0.93	0.94	0.82	0.69	0.49
	REG-50	0.87	0.89	0.92	0.93	0.84	0.69	0.55
	REG-500	0.88	0.88	0.92	0.93	0.88	0.75	0.64
TSVD GREENSITE	OPTIMAL	0.85	0.88	0.93	0.94	0.81	0.69	0.58
TSVD STANDARD	OPTIMAL	0.80	0.87	0.92	0.96	0.78	0.76	0.46
TIKHONOV GREENSITE	CRESO	0.51	0.83	0.85	0.91	0.21	0.51	0.32
	L-CURVE	0.75	0.85	0.91	0.93	0.79	0.54	0.37
	OPTIMAL	0.84	0.88	0.91	0.93	0.87	0.84	0.74
	ZCROSS	0.78	0.86	0.90	0.93	0.73	0.61	0.33
TIKHONOV STANDARD	CRESO	0.50	0.81	0.88	0.96	0.45	0.52	0.21
	L-CURVE	0.79	0.86	0.93	0.92	0.63	0.50	0.30
	OPTIMAL	0.83	0.88	0.91	0.95	0.84	0.79	0.68
	ZCROSS	0.78	0.85	0.91	0.92	0.83	0.72	0.61

**Table C.16:** Effect of heart translation in the posterior-anterior directions on inverse simulations using the similarity index error metric defined in Section 3.2.3.

**Heart Translation in the Superior-Inferior Directions – RMS**

APPROACH	TECHNIQUE	-30	-20	-10	0	10	20	30
ACTIVATION	REG-0	10.4	8.4	5.5	4.6	5.7	7.6	9.8
	REG-5	10.5	8.2	5.4	4.6	5.9	7.7	9.7
	REG-50	10.4	8.1	5.8	4.9	5.8	7.9	9.9
	REG-500	10.1	8.2	5.9	5.2	6.3	8.2	9.8
TSVD GREENSITE	OPTIMAL	13.4	10.9	7.6	4.5	6.5	9.9	11.8
TSVD STANDARD	OPTIMAL	12.2	9.4	7.3	3.9	9.3	12.4	11.4
TIKHONOV GREENSITE	CRESO	16.6	15.2	8.0	5.6	10.7	16.6	16.1
	L-CURVE	18.1	12.2	6.5	5.0	7.3	15.1	19.7
	OPTIMAL	12.1	9.7	6.9	4.8	6.2	8.6	9.3
	ZCROSS	14.1	11.7	6.2	5.0	6.9	15.1	14.7
TIKHONOV STANDARD	CRESO	13.1	12.1	9.8	3.6	9.7	13.6	15.3
	L-CURVE	14.3	9.3	6.3	5.2	6.6	13.1	17.4
	OPTIMAL	10.8	9.1	6.3	4.4	6.9	8.7	8.8
	ZCROSS	12.2	9.0	6.4	5.3	6.3	10.9	14.5

**Table C.17:** Effect of heart translation in the superior-inferior directions on inverse simulations using the RMS error metric defined in Section 3.2.3.

**Heart Translation in the Superior-Inferior Directions – Similarity Index**

APPROACH	TECHNIQUE	-30	-20	-10	0	10	20	30
ACTIVATION	REG-0	0.62	0.76	0.90	0.94	0.91	0.84	0.74
	REG-5	0.63	0.78	0.91	0.94	0.90	0.83	0.74
	REG-50	0.62	0.78	0.89	0.93	0.91	0.83	0.73
	REG-500	0.64	0.77	0.89	0.93	0.90	0.84	0.75
TSVD GREENSITE	OPTIMAL	0.48	0.65	0.83	0.94	0.88	0.77	0.63
TSVD STANDARD	OPTIMAL	0.53	0.73	0.85	0.96	0.74	0.53	0.61
TIKHONOV GREENSITE	CRESO	0.18	0.34	0.82	0.91	0.70	0.24	0.16
	L-CURVE	0.23	0.63	0.88	0.93	0.85	0.43	0.10
	OPTIMAL	0.57	0.72	0.86	0.93	0.89	0.80	0.77
	ZCROSS	0.26	0.64	0.88	0.93	0.86	0.32	0.16
TIKHONOV STANDARD	CRESO	0.32	0.48	0.74	0.96	0.72	0.32	0.23
	L-CURVE	0.23	0.71	0.88	0.92	0.88	0.53	0.15
	OPTIMAL	0.64	0.76	0.88	0.95	0.86	0.78	0.78
	ZCROSS	0.48	0.74	0.88	0.92	0.89	0.66	0.21

**Table C.18:** Effect of heart translation in the superior-inferior directions on inverse simulations using the similarity index error metric defined in Section 3.2.3.



**Heart Rotation in the Sagittal Plane – RMS**

APPROACH	TECHNIQUE	-45	-30	-15	0	15	30	45
ACTIVATION	REG-0	11.6	8.7	6.6	4.6	5.8	8.2	11.1
	REG-5	11.6	8.8	7.0	4.6	5.8	8.1	10.9
	REG-50	11.5	8.9	6.7	4.9	5.5	8.2	10.7
	REG-500	11.1	8.7	6.6	5.2	5.8	8.1	10.8
TSVD GREENSITE	OPTIMAL	12.1	10.2	6.4	4.5	7.9	14.3	12.1
TSVD STANDARD	OPTIMAL	12.0	9.8	5.9	3.9	8.4	11.5	13.1
TIKHONOV GREENSITE	CRESO	12.9	17.2	16.1	5.6	12.9	21.6	19.2
	L-CURVE	14.0	10.2	6.6	5.0	8.4	13.0	15.8
	OPTIMAL	13.7	10.7	6.0	4.8	9.1	14.4	15.5
	ZCROSS	12.9	10.2	7.0	5.0	8.7	12.8	15.3
TIKHONOV STANDARD	CRESO	13.1	11.6	5.3	3.6	8.4	17.1	18.1
	L-CURVE	12.6	9.6	5.9	5.2	8.3	11.8	15.2
	OPTIMAL	12.6	9.8	5.8	4.4	8.5	11.8	12.6
	ZCROSS	12.6	9.6	5.5	5.3	8.4	11.9	15.6

**Table C.19:** Effect of heart rotation in the sagittal plane on inverse simulations using the RMS error metric defined in Section 3.2.3.

**Heart Rotation in the Sagittal Plane – Similarity Index**

APPROACH	TECHNIQUE	-45	-30	-15	0	15	30	45
ACTIVATION	REG-0	0.51	0.73	0.86	0.94	0.90	0.78	0.59
	REG-5	0.51	0.73	0.84	0.94	0.90	0.78	0.60
	REG-50	0.51	0.72	0.85	0.93	0.91	0.78	0.60
	REG-500	0.53	0.73	0.86	0.93	0.90	0.78	0.58
TSVD GREENSITE	OPTIMAL	0.53	0.67	0.88	0.94	0.82	0.50	0.62
TSVD STANDARD	OPTIMAL	0.61	0.69	0.89	0.96	0.79	0.62	0.43
TIKHONOV GREENSITE	CRESO	0.34	0.25	0.46	0.91	0.40	0.18	-0.01
	L-CURVE	0.44	0.70	0.88	0.93	0.81	0.58	0.43
	OPTIMAL	0.48	0.67	0.89	0.93	0.77	0.47	0.38
	ZCROSS	0.52	0.70	0.87	0.93	0.80	0.60	0.47
TIKHONOV STANDARD	CRESO	0.43	0.59	0.92	0.96	0.81	0.23	0.08
	L-CURVE	0.54	0.72	0.90	0.92	0.81	0.64	0.45
	OPTIMAL	0.53	0.70	0.90	0.95	0.78	0.59	0.51
	ZCROSS	0.53	0.72	0.91	0.92	0.81	0.64	0.42

**Table C.20:** Effect of heart rotation in the sagittal plane on inverse simulations using the similarity index error metric defined in Section 3.2.3.

**Heart Rotation in the Coronal Plane – RMS**

APPROACH	TECHNIQUE	-15	0	15	30	45
ACTIVATION	REG-0	6.1	4.6	6.4	8.7	10.0
	REG-5	6.1	4.6	6.5	8.7	10.0
	REG-50	6.2	4.9	6.6	8.6	10.1
	REG-500	5.7	5.2	6.7	8.5	9.9
TSVD GREENSITE	OPTIMAL	7.7	4.5	6.7	11.8	12.4
TSVD STANDARD	OPTIMAL	5.9	3.9	6.1	9.0	13.4
TIKHONOV GREENSITE	CRESO	9.3	5.6	18.2	9.4	20.4
	L-CURVE	7.7	5.0	6.7	9.6	10.8
	OPTIMAL	7.4	4.8	7.4	11.3	13.5
	ZCROSS	8.0	5.0	8.0	9.5	11.2
TIKHONOV STANDARD	CRESO	8.0	3.6	13.4	9.1	16.1
	L-CURVE	8.1	5.2	6.8	8.9	11.3
	OPTIMAL	7.2	4.4	6.8	9.8	11.2
	ZCROSS	7.8	5.3	6.8	9.0	11.6

**Table C.21:** Effect of heart rotation in the coronal plane on inverse simulations using the RMS error metric defined in Section 3.2.3.

**Heart Rotation in the Coronal Plane – Similarity Index**

APPROACH	TECHNIQUE	-15	0	15	30	45
ACTIVATION	REG-0	0.89	0.94	0.87	0.74	0.66
	REG-5	0.89	0.94	0.87	0.75	0.67
	REG-50	0.88	0.93	0.86	0.76	0.66
	REG-500	0.90	0.93	0.86	0.76	0.67
TSVD GREENSITE	OPTIMAL	0.83	0.94	0.89	0.61	0.58
TSVD STANDARD	OPTIMAL	0.90	0.96	0.90	0.79	0.54
TIKHONOV GREENSITE	CRESO	0.77	0.91	0.13	0.75	0.11
	L-CURVE	0.84	0.93	0.88	0.73	0.65
	OPTIMAL	0.85	0.93	0.86	0.66	0.54
	ZCROSS	0.82	0.93	0.84	0.73	0.65
TIKHONOV STANDARD	CRESO	0.82	0.96	0.31	0.76	0.16
	L-CURVE	0.81	0.92	0.88	0.77	0.64
	OPTIMAL	0.85	0.95	0.87	0.73	0.68
	ZCROSS	0.83	0.92	0.88	0.76	0.62

**Table C.22:** Effect of heart rotation in the coronal plane on inverse simulations using the similarity index error metric defined in Section 3.2.3.

**Heart Size – RMS**

APPROACH	TECHNIQUE	0.65	0.81	1.00	1.21	1.43
ACTIVATION	REG-0	7.3	5.2	4.6	5.3	6.3
	REG-5	7.4	5.2	4.6	5.4	6.4
	REG-50	7.6	5.5	4.9	5.7	6.5
	REG-500	7.2	5.3	5.2	6.1	7.1
TSVD GREENSITE	OPTIMAL	12.1	6.8	4.5	6.9	9.8
TSVD STANDARD	OPTIMAL	16.2	7.2	3.9	6.2	8.7
TIKHONOV GREENSITE	CRESO	14.1	13.2	5.6	8.2	10.2
	L-CURVE	10.9	5.2	5.0	6.3	8.6
	OPTIMAL	8.2	6.9	4.8	6.6	8.3
	ZCROSS	8.4	5.0	5.0	6.8	8.5
TIKHONOV STANDARD	CRESO	12.8	8.7	3.6	6.9	10.4
	L-CURVE	5.5	5.0	5.2	6.0	8.5
	OPTIMAL	8.3	5.7	4.4	7.5	8.6
	ZCROSS	6.1	5.3	5.3	5.9	8.2

**Table C.23:** Effect of Gaussian electrical noise on inverse simulations using the RMS error metric defined in Section 3.2.3.

**Heart Size – Similarity Index**

APPROACH	TECHNIQUE	0.65	0.81	1.00	1.21	1.43
ACTIVATION	REG-0	0.83	0.92	0.94	0.92	0.88
	REG-5	0.82	0.92	0.94	0.92	0.88
	REG-50	0.81	0.91	0.93	0.91	0.88
	REG-500	0.82	0.91	0.93	0.91	0.87
TSVD GREENSITE	OPTIMAL	0.62	0.87	0.94	0.86	0.72
TSVD STANDARD	OPTIMAL	0.32	0.84	0.96	0.89	0.78
TIKHONOV GREENSITE	CRESO	0.47	0.58	0.91	0.80	0.68
	L-CURVE	0.68	0.92	0.93	0.88	0.78
	OPTIMAL	0.81	0.86	0.93	0.87	0.79
	ZCROSS	0.81	0.93	0.93	0.86	0.78
TIKHONOV STANDARD	CRESO	0.49	0.79	0.96	0.86	0.59
	L-CURVE	0.91	0.93	0.92	0.89	0.78
	OPTIMAL	0.80	0.91	0.95	0.84	0.78
	ZCROSS	0.89	0.92	0.92	0.89	0.79

**Table C.24:** Effect of heart size on inverse simulations using the similarity index error metric defined in Section 3.2.3.

**Torso Size – RMS**

APPROACH	TECHNIQUE	0.69	0.81	1.00	1.32	1.72
ACTIVATION	REG-0	7.9	6.3	4.6	8.1	11.0
	REG-5	8.2	6.0	4.6	8.1	10.8
	REG-50	7.9	6.1	4.9	8.0	10.9
	REG-500	7.8	6.2	5.2	7.8	10.4
TSVD GREENSITE	OPTIMAL	9.4	8.7	4.5	12.8	11.8
TSVD STANDARD	OPTIMAL	10.2	9.4	3.9	10.2	11.4
TIKHONOV GREENSITE	CRESO	14.1	9.2	5.6	15.7	16.1
	L-CURVE	12.6	8.5	5.0	12.5	13.5
	OPTIMAL	9.5	7.7	4.8	7.5	10.9
	ZCROSS	13.0	8.5	5.0	10.1	12.8
TIKHONOV STANDARD	CRESO	12.4	7.6	3.6	15.7	19.4
	L-CURVE	12.4	7.4	5.2	11.0	15.3
	OPTIMAL	9.2	7.6	4.4	8.2	11.6
	ZCROSS	11.6	8.4	5.3	9.6	15.0

**Table C.25:** Effect of torso size on inverse simulations using the RMS error metric defined in Section 3.2.3.

**Torso Size – Similarity Index**

APPROACH	TECHNIQUE	0.69	0.81	1.00	1.32	1.72
ACTIVATION	REG-0	0.82	0.88	0.94	0.80	0.62
	REG-5	0.80	0.89	0.94	0.81	0.63
	REG-50	0.82	0.89	0.93	0.81	0.61
	REG-500	0.84	0.91	0.93	0.85	0.68
TSVD GREENSITE	OPTIMAL	0.75	0.78	0.94	0.66	0.61
TSVD STANDARD	OPTIMAL	0.71	0.75	0.96	0.74	0.65
TIKHONOV GREENSITE	CRESO	0.49	0.76	0.91	0.48	0.50
	L-CURVE	0.56	0.79	0.93	0.64	0.50
	OPTIMAL	0.73	0.81	0.93	0.84	0.67
	ZCROSS	0.53	0.78	0.93	0.74	0.59
TIKHONOV STANDARD	CRESO	0.58	0.82	0.96	0.42	0.49
	L-CURVE	0.58	0.84	0.92	0.76	0.60
	OPTIMAL	0.74	0.83	0.95	0.81	0.67
	ZCROSS	0.62	0.79	0.92	0.80	0.62

**Table C.26:** Effect of torso size on inverse simulations using the similarity index error metric defined in Section 3.2.3.

## C.4 Typical Experimental Error

### Typical Simulation with Double Point Source – RMS

APPROACH	TECHNIQUE	CONTROL	TYPICAL
ACTIVATION	REG-0	4.3	9.2
	REG-5	4.1	9.1
	REG-50	4.4	8.9
	REG-500	4.2	8.2
TSVD GREENSITE	OPTIMAL	7.1	10.7
TSVD STANDARD	OPTIMAL	6.4	10.2
TIKHONOV GREENSITE	CRESO	6.0	11.8
	L-CURVE	8.5	11.4
	OPTIMAL	5.4	10.9
	ZCROSS	7.9	11.3
TIKHONOV STANDARD	CRESO	7.0	11.6
	L-CURVE	6.6	10.6
	OPTIMAL	6.0	11.4
	ZCROSS	7.8	11.4

**Table C.27:** Effect of typical experimental errors with double point source using the RMS error metric defined in Section 3.2.3.

### Typical Simulation with Double Point Source – SI

APPROACH	TECHNIQUE	CONTROL	TYPICAL
ACTIVATION	REG-0	0.94	0.73
	REG-5	0.95	0.73
	REG-50	0.94	0.73
	REG-500	0.96	0.78
TSVD GREENSITE	OPTIMAL	0.86	0.72
TSVD STANDARD	OPTIMAL	0.88	0.74
TIKHONOV GREENSITE	CRESO	0.90	0.62
	L-CURVE	0.79	0.68
	OPTIMAL	0.92	0.70
	ZCROSS	0.82	0.69
TIKHONOV STANDARD	CRESO	0.85	0.66
	L-CURVE	0.87	0.72
	OPTIMAL	0.89	0.65
	ZCROSS	0.82	0.66

**Table C.28:** Effect of typical experimental errors with double point source using the similarity index error metric defined in Section 3.2.3.

**Typical Simulation with Eikonal Source – RMS**

APPROACH	TECHNIQUE	CONTROL	TYPICAL
ACTIVATION	REG-0	10.6	10.9
	REG-5	10.8	11.0
	REG-50	11.0	11.7
	REG-500	10.4	10.8
TSVD GREENSITE	OPTIMAL	8.4	10.4
TSVD STANDARD	OPTIMAL	7.8	15.5
TIKHONOV GREENSITE	CRESO	8.2	14.0
	L-CURVE	9.2	15.8
	OPTIMAL	7.3	13.9
	ZCROSS	9.3	16.7
TIKHONOV STANDARD	CRESO	4.9	14.8
	L-CURVE	7.6	14.3
	OPTIMAL	7.1	14.3
	ZCROSS	7.6	14.7

**Table C.29:** Effect of typical experimental errors with eikonal source using the RMS error metric defined in Section 3.2.3.

**Typical Simulation with Eikonal Source – SI**

APPROACH	TECHNIQUE	CONTROL	TYPICAL
ACTIVATION	REG-0	0.45	0.36
	REG-5	0.44	0.40
	REG-50	0.40	0.34
	REG-500	0.48	0.39
TSVD GREENSITE	OPTIMAL	0.45	0.47
TSVD STANDARD	OPTIMAL	0.54	0.04
TIKHONOV GREENSITE	CRESO	0.54	0.30
	L-CURVE	0.48	0.23
	OPTIMAL	0.60	0.29
	ZCROSS	0.48	0.26
TIKHONOV STANDARD	CRESO	0.80	0.18
	L-CURVE	0.52	0.26
	OPTIMAL	0.58	0.28
	ZCROSS	0.53	0.24

**Table C.30:** Effect of typical experimental errors with eikonal source using the similarity error metric defined in Section 3.2.3.

### Typical Simulation with Experimental Source - RMS

APPROACH	TECHNIQUE	CONTROL	TYPICAL
ACTIVATION	REG-0	2.5	3.9
	REG-5	2.6	3.9
	REG-50	2.7	4.0
	REG-500	2.3	3.7
TSVD GREENSITE	OPTIMAL	2.9	4.7
TSVD STANDARD	OPTIMAL	3.1	5.1
TIKHONOV GREENSITE	CRESO	3.2	4.3
	L-CURVE	2.8	4.4
	OPTIMAL	3.0	4.1
	ZCROSS	3.0	5.1
TIKHONOV STANDARD	CRESO	3.2	4.7
	L-CURVE	3.0	4.7
	OPTIMAL	3.2	5.2
	ZCROSS	3.4	4.7

**Table C.31:** Effect of typical experimental errors with experimentally derived source using the RMS metric defined in Section 3.2.3.

### Typical Simulation with Experimental Source – SI

APPROACH	TECHNIQUE	CONTROL	TYPICAL
ACTIVATION	REG-0	0.76	0.51
	REG-5	0.75	0.53
	REG-50	0.72	0.51
	REG-500	0.76	0.53
TSVD GREENSITE	OPTIMAL	0.78	0.41
TSVD STANDARD	OPTIMAL	0.74	0.32
TIKHONOV GREENSITE	CRESO	0.71	0.50
	L-CURVE	0.79	0.47
	OPTIMAL	0.76	0.56
	ZCROSS	0.76	0.34
TIKHONOV STANDARD	CRESO	0.74	0.37
	L-CURVE	0.70	0.39
	OPTIMAL	0.71	0.30
	ZCROSS	0.69	0.39

**Table C.32:** Effect of typical experimental errors with experimentally derived source using the similarity error metric defined in Section 3.2.3.



# *D* *CMISS Routines & Command Files*

All computations in this thesis were performed using the **CMISS** package. **CMISS** is a specialised finite element and boundary element program developed over the last 20 years in the Bioengineering Research Group at The University of Auckland. **CMISS** is capable of solving problems using a variety of numerical methods which can be used across multiple regions within the solution domain. It is especially suited to bioengineering problems. **CMISS** consists of two main components: a computational kernel written primarily in Fortran 77/90 (**CM**) and a graphical front end and user interface written in C/C++ (**CMGUI**). **CMGUI** incorporates a number of specialised tools for visualising and manipulating certain types of data. One of these tools is **UnEmap** which is designed for electrocardiographic signals. More information about **CMISS** can be obtained at <http://www.cmiss.org/>.

Some of the command files used in the course of this thesis are listed in Sections (D.3)–(D.8). They illustrate the different commands used to solve different problem types. The command files to fit signals to a finite element field, perform host mesh fitting on a generic mode and geometric surface fitting are further explained in Chapter 3. Section D.6 lists the command required for a forward problem simulation using a dipole source. This is used in the convergence analysis in Chapter 5. Section D.7 lists the commands used in an activation inverse problem where the analytic activation sequences has been read in. Section D.8 contains the commands used in Chapter 7. This comfile performs activation and potential inverses and applies typical experimental errors to the simulations.

## D.1 Computer Systems

The forward convergence results, presented in Chapter 5, were obtained using a Silicon Graphics Power Challenge (XL). This computer had  $16 \times 196$  MHz MIPS R10000 processors (Revision 2.6) with R10010 Floating Point Units (Revision 0.0). Each processor had a 32/32 kB data/instruction level-1 (primary) cache and a 2 MB level-2 (secondary) cache. There was a total of 8 GB of Physical RAM (8-way interleaved) and 8 GB virtual swap space. The operating system was IRIX 6.2 64 bit SMP-based Unix.

The results for the simulation study presented in Chapter 7 was performed on a Silicon Graphics Origin 2000. This computer had  $32 \times 250$  MHz MIPS R10000 processors (Revision 3.4) with R10010 Floating Point Units (Revision 0.0). Each processor had a 32/32 kB data/instruction level-1 (primary) cache and a 4 MB level-2 (secondary) cache. There was a total of 10 GB of Physical RAM (8-way interleaved) and 50 GB virtual swap space. The operating system was IRIX 6.5.10 64 bit SMP-based Unix.

More information can be obtained at <http://www.esc.auckland.ac.nz/HPC/>.

## D.2 Commonly Used Routines in CMISS

### D.2.1 General Routines

APNOIS	Noise is applied to temporally varying signals. Gaussian electrical noise can be applied to the potential values while geometric noise can be applied to the electrode locations.
COMPDAT	Data comparison using metrics defined in Section 3.2.3. Geometrical locations of the data are compared with the keyword geometry and field values associated with data points are compared with the keyword field.
COMPSIG	Signal comparison using metrics defined in Section 3.2.3. The comparisons can occur at a specific time, an interval start.time/end.time or an integral of the entire signal.
EVELEC	Evaluates a signal file from a nodally based solution history file. The electrodes can be evaluated at nodes or data.
EXNODE	Exports nodal position and values to CMGUI. The values maybe temporally varying potentials or activation times.
EXELEM	Exports element based information to CMGUI
EXSIGN	Exports CMISS format signal files to UnEmap format signal files. Exports individual and multiple signals to plain text data files and graphical traces to CMGUI
UPSIGN	Updates the geometric locations and element $\xi$ positions within a signal file

### D.2.2 Fitting Routines

DEDATA	Defines data position and any associated field values.
DEXI	Calculates the $\xi$ position of data points. The keyword <code>orthogonal</code> calculates orthogonal projections to the nearest surface. The keyword <code>closest</code> calculates the closest position of the data to an element. This may be a projection or a data point embedded within an element.
FIT	Fits geometric or field parameters to data points defined in DEDATA.
FITSIG	Fits a temporally varying potential field from electrodes specified in a signal file.

### D.2.3 Forward Problem Routines

APTRSF	Applies the transfer matrix to the heart/epicardial nodes to create epicardial/torso potentials.
ASSEMBLE2	Assembles the global unreduced matrices GK, GD for static linear BEM problems.
DEACTI	Computes an analytic activation field based on specified seed point locations.
EVTRSF	Evaluates a transfer matrix. The type of transfer matrix (transmembrane to torso surface/transmembrane to epicardial surface/epicardial surface to torso surface) is defined in IPTRSF.
IPANA9	Generates analytical transmembrane solutions for the spherical test examples in Section 5.5.2 given a dipole source and the appropriate coefficients.
IPACTV	Generates analytical activation fields based on the point activation sites as used for the double point heart activation source Section 6.4 and throughout Chapter 7.

### D.2.4 Inverse Problem Routines

EVINVE	Main routine for performing potential based inverses.
EVPHI	Generates the $\Phi(\mathbf{y}, t)$ array from a signal file
EVZCROSSING	Calculates the zero crossing estimate of the activation field given the $\Phi(\mathbf{y}, t)$ matrix
INTERQRANK	Computes the inter-equation truncation rank for Greensite's potential method.
RESFUN	Evaluates the residuals and Jacobian of the objective function being optimised.
SURFACELAPLACIAN	Calculates the surface Laplacian for regularising inverse activation problems.
TIKHONOV	Calculates the Tikhonov regularised solution.
TGSVD	Calculates the Truncated SVD regularised solution.

## D.3 Signal Fitting Comfile

Fits discrete temporally varying signals to a finite element mesh. The fitted signals are exported to CMGUI and UnEmap for visualisation.

---

```

#Example ea1 – Displaying p111 experimental results
#           Fits the signals, customising the model,
#           exports to cmgui and unemap
#

set fatal off                               # Force a crash with all errors
$FORMAT = "binary"                          # Set a fileformat

${INSIGN} = "p111"
${INSIGN}2 = "p111.update"

fem def para;r; full.pig                     # Array size parameters for problem
fem realloc
fem def coor 3,1                             # RC coordinates
fem def base;r; full.pig                    # Bicubic Herm surfaces with sectors
fem def node;r;torso_cust                   # P111 customised surface
fem def elem;r;torso_cust

fem export node;porky as porky               # Export the geometry to cmgui
fem export elem;porky as porky

#
# Adjusted raw p111 data to suit
# the new origin at the back
#
fem def data;r;p111
fem change data translate by 15,-110,0      # Position electrode to suit origin system
fem def data;w;p111.trans

fem def data;r;p111.trans                   # Define data
fem def xi;c closest                        # Calculate xi positions on reg 1
fem export data;p111 as elec error offset 10500 # Outputs the data positions & error vectors

#
#
# Create the surface electrodes & export to CMGUI
#
fem def data;c from_xi                      # Finds the global coords given xi
fem def data;w;p111_surf                   # Global coords of projections
fem export data;p111_surf as elec_surf 5000

#
#
# Update the input signal & export to UNEMAP
#
fem def data;r;p111_surf
fem up sig infile ${INSIGN} outfile ${INSIGN}2 $FORMAT
fem def export;r;unemap
fem export sig;${INSIGN}2 elec signal ${INSIGN}2

#
#
# Fit the signal
#
fem def field;r;torso_surface               # Bicubic Hermite field
fem def elem;r;torso_surface field         # Element fields
fem def fit;r;torso_surface signal class 2 #
fem fit sig class 2 $FORMAT tstart 0.10 tend 0.20 # Fit the signal between 0.1 and 0.2 s

```

```
#
#
# Export the fitted (nodally based) signals to UNEMAP
#
fem eva elec; fitted hist fitted fr node elec 13..213 $FORMAT us fit cl 2          # Evaluate nodally based signals
fem def export;r;unemap
fem export sig; fitted elec signal fitted

#
# Export reconstructed signals (from the input data pts)
# for a comparison
#
fem def data;r;p111_surf                                                         # Read in surface electrode positions
fem def xi;r;p111                                                                # Read in the xi coordinates
fem eva elec; fitted_data hist fitted fr data $FORMAT us fit cl 2              # Evaluate the signals

#
# Compare the input/recorded signals and the fitted signals
# evaluted at the electrodes
#
fem comp sign mast ${INSIGN}2 comp fitted_data $FORMAT time 0.15
fem comp sign mast ${INSIGN}2 comp fitted_data $FORMAT integral

fem eva elec;p111 hist fitted fr node elec 13..213 $FORMAT us fit cl 2          # Export the nodally based signals to UnEmap
fem def export;r;unemap
fem export sig;p111 elec signal p111

fem export node;pot hist fitted $FORMAT as potl us fit cl 2                     # Export temporally varying potential field to
fem export elem;pot field as potl using fit class 2                             # CMGUI

fem def export;r;trace                                                            # Export a trace to cmgui
fem li export
fem export sign;trace signal fitted elec

quit
```

---

## D.4 Host Mesh Customisation Comfile

Performs a non-linear customisation of a generic model to a specific subject using host mesh fitting.

---

```

# Example e42: Tri-Cubic Hermite Host Mesh Customisation
#
#
#
# Input files and parameters for comfile
#
$SLAVEFILES = "pig06" # Name of the input slave files
$CUSTFILES = "pig06_cust" # Name of the output customised slave files
$SLAVE = "1..6" # Regions to read the slave files into
$HOST = "7" # Region corresponding to the host mesh

#
# Logical controls for comfile [true|false]
#
$CALCXI = 1 # Calculate xi positions for the slave nodes
$FITTING = 1 # Fit the host mesh
$UPDATE = 1 # Update the slave mesh.
$OUTPUT = 1 # Write out customised ipnode/elem files.

# Array size parameters for problem
fem def para;r; fitting # Array size parameters for problem
fem def regi;r;seven # Seven regions (6 for slave, 1 for host)
fem def coor 3,1
fem def base;r; bicubic,tricubic # Bicubic Hermite basis functions (generic slave mesh)
# Tricubic Hermite basis functions (host mesh)

# Define the generic slave mesh
fem def node;r;$SLAVEFILES reg $SLAVE
fem def elem;r;$SLAVEFILES reg $SLAVE

# Export generic mesh to CMGUI
fem export node;pig_gen as pig_gen offset 10000 reg $SLAVE
fem export elem;pig_gen as pig_gen offset.elem 10000 reg $SLAVE

#
# Defines the host mesh and calculates the xi
# positions of the slave mesh nodes within the host mesh.
#
if ( $CALCXI==1 )
{
fem def node;r;host reg $HOST # Define host mesh (single element)
fem def elem;r;host reg $HOST
fem up node deriv 1 reg $HOST # Update the derivatives of host mesh
fem up node deriv 2 reg $HOST
fem up node deriv 3 reg $HOST
fem ref xi 3 reg $HOST # Refine the host mesh (now has 2 elements)

fem export node;host as host offset 1000 reg $HOST # Export host mesh to CMGUI
fem export elem;host as host offset.elem 1000 reg $HOST

# Calculate the xi positions for landmarks points
# within the elements define in region $HOST
fem def data;r;gen_landmark9 reg $HOST
fem def xi;c contain reg $HOST
fem export data;gen_landmark as gen_landmark error offset 16000 reg $HOST
fem def xi;w;gen_landmark reg $HOST

# Calculate the xi positions of each node
# point of region $SLAVE within the elements
# defined in region $HOST
fem def xi;c nodes contain of $SLAVE in $HOST
fem def xi;w;generic nodes contain of $SLAVE in $HOST
} #CALCXI

#
# Minimises the error between landmark points by adjusting the
# host mesh.
#
if ( $FITTING==1 )

```



```

{
fem def data;r;p111_Jandmark9 reg $HOST                               # Define the measured landmark positions
fem def xi;r;gen_Jandmark reg $HOST
fem export data;p111_Jandmark as p111_Jandmark error offset 17500 reg $HOST

fem def field;r;host_cub_ref      reg $HOST                          # Tricubic Hermite fields with 2 elements
fem def elem;r;host_ref field    reg $HOST
fem def fit;r;host_tricub_ref geom reg $HOST

fem list data error reg $HOST                                        # Output starting error.
fem fit reg $HOST
fem update nodes reg $HOST
fem list data error reg $HOST                                        # Output final error.

fem def node;w;host_cust reg $HOST                                   # Save the customised host mesh geometry
fem def elem;w;host_cust reg $HOST

fem export nodes;host_cust as host_cust offset 2000 reg $HOST        # Export the customised host mesh to CMGUI
fem export elements;host_cust as host_cust offset_elem 2000 reg $HOST
fem export data;data_cust as data_cust error offset 18000 reg $HOST
} #FITTING

#
# Update the slave mesh according to the deformed host mesh.
#
if ( $UPDATE==1 )
{
fem def node;r;host_cust reg $HOST
fem def elem;r;host_cust reg $HOST
fem def node;r;$SLAVEFILES reg $SLAVE
fem def elem;r;$SLAVEFILES reg $SLAVE
fem def xi;r;generic nodes of $SLAVE in $HOST

fem up mesh posit of 1 in $HOST                                     # Moves the nodes of region 1 & 6 (effectively all nodes)
fem up mesh posit of 6 in $HOST                                     # according to the xi positions in $HOST

fem export node;pig_cust as pig_cust offset 20000 reg $SLAVE        # Export the customised slave meshes
fem export elem;pig_cust as pig_cust offset_elem 20000 reg $SLAVE
fem export elem;skin as skin reg 1 offset_elem 20000 elem 1281..2336
fem export elem;lungs as lungs reg 2..3 offset_elem 20000
fem export elem;lvendo as lvendo reg 4 offset_elem 20000
fem export elem;rvendo as rvendo reg 5 offset_elem 20000
fem export elem;heart as heart reg 6 offset_elem 20000

fem def data;r;electrode reg 1                                     # Export the torso surface electrode positions
fem def xi;c close reg 1                                          # measured by the FARO arm
fem list data error reg 1                                         # & their orthogonal projections
fem exp data;cust_error as cust_error error offset 24000 reg 1    # onto the customised mesh
} #UPDATE

if ( $OUTPUT==1 )                                                # Save the slave mesh for later use
{
fem def node;w;$CUSTFILES reg $SLAVE
fem def elem;w;$CUSTFILES reg $SLAVE
} #OUTPUT

quit

```

---

## D.5 Geometric Fitting Comfile

Geometric fitting by performing iterative linear fits. The orthogonal  $\xi$  projections and normalised scale factors are updated after each fit.

---

```

# Example e43: Finite Element Geometric Fitting To Epicardial Data
#
#
#

$FITNAME = "epi" # Base name for the fit#
$OUTPUT = "epi_ref0c" # Name of the initial input mesh
$FITNAME = "epi" # Name of the fitted output mesh

fem def para;r; fitting_lin # Array size parameters for problem
fem def coor 3,1 # Rectangular Cartesian coordinates
fem def base;r; bicubic_fit # Sets up three basis functions
# - 1 standard bicubic Hermite element
# - 2 simplex element collapsed at x2=0
# - 3 simplex element collapsed at x2=1

fem def node;r;$MODEL # Reads in an initial mesh and calculates
fem def elem;r;$MODEL # linear approximations for the derivatives
fem up node deriv 1 linear # in the xi=1 & 2 directions
fem up node deriv 2 linear

fem export node;${FITNAME}_init as ${FITNAME}_init offset 40000
fem export elem;${FITNAME}_init as ${FITNAME}_init offset_elem 40000

#
# Calculate the initial xi projections
# - alternatively the command fem def xi;c orthog can be used
# it is slower but may produce better results in some cases
#
fem def data;r;$FITNAME
fem def xi;c close
fem li data err # Calculates the initial xi projections
fem export data;${FITNAME}_data as ${FITNAME}_data error # & the keyword ERROR exports the projection vectors to CMGUI

#
# Setup the interpolation for the fitting problem -
# alternatively it may be easier use the commands
# "fem up field from geometry" to setup these fields automatically
#
fem def field;r;epi
fem def elem;r;epi field

#
# Defines the fitting problem by setting smoothing parameters
# and setting some fixed nodes.
#
fem def fit;r;epi2 geometry

#
# First fit
#
fem fit
fem update node fit # Updates the nodal arrays then recalculates normalised scale factors
fem update scale_factor normalise
fem def xi;c close old # The OLD option on 'def xi;c' means that the
fem li data err # last projections are used as initial estimates for
# the non-linear projection calculation.

#
# Second fit
#

```

```
fem fit
fem update node fit
fem update scale_factor normalise
fem def xi;c close old
fem li data err

#
# Third fit
#
fem fit
fem update node fit
fem update scale_factor normalise
fem def xi;c close old
fem li data err

#
# Export the fitted geometry
#
fem export data;${FITNAME}_data as ${FITNAME}_data error
fem export node;${FITNAME} as ${FITNAME} offset 30000
fem export elem ${FITNAME} as ${FITNAME} offset_elem 30000

quit
```

---

## D.6 Forward Problem With Dipole Source Comfile

Calculates the body surface potentials given a constant current dipole heart source by solving the forward problem of electrocardiology. A coupled generalised Laplace's equation is solved in the four regions modelled. These include the epicardial, left and right lung and the skin surfaces.

---

```

set fatal off

$CMVER      ="sp1"
$BATCHVER   ="07"
$EXCMGUI    =1
$BILINEAR   =1

$INPUT      = "/xlv1/eng_sci/cheng/porky/data/lungheart_torso$BATCHVER"
$OUTPUT     ="tmp"

#
# Forward simulation for lungheart torso
#
fem def para;r;big_dense$BATCHVER
fem def reg;r;four
fem def coor 3,1

fem def node;r;$INPUT reg all
if ($BILINEAR==0)
{
  fem def base;r;bicubic
  fem def elem;r;$INPUT reg all
} else
{
  fem def base;r; bicubic.bilinear
  fem def elem;r;{$INPUT}.jin reg all
}

#
# Group nodes for solve, initial conditions
# and electrode comparisons
#
if ($MODEL eq "01") # Model 01
{
  fem group node 804 as FIXEDNODE
  fem group node 765,1018 as SURFENDS
  fem group node 766..1017,1019..1798 as SURFNORM
  $COMPNODES ="1..37,765..1018"
} elseif ($MODEL eq "05") # Model 05
{
  fem group node 1274 as FIXEDNODE
  fem group node 1235,1488 as SURFENDS
  fem group node 1236..1487,1489..5412 as SURFNORM
  $COMPNODES ="1..37,1235..1488"
} elseif ($MODEL eq "07") # Model 07
{
  fem group node 1274 as FIXEDNODE
  fem group node 1235,1488 as SURFENDS
  fem group node 1236..1487,1489..2268 as SURFNORM
  $COMPNODES ="1..37,1235..1488"
} elseif ($MODEL eq "08") # Model 08
{
  fem group node 1896 as FIXEDNODE
  fem group node 1855,2108 as SURFENDS
  fem group node 1856..2107,2109..2888 as SURFNORM
  $COMPNODES ="1..37,1855..2108"
} elseif ($MODEL eq "09") # Model 09
{
  fem group node 3162 as FIXEDNODE
  fem group node 3123,3376 as SURFENDS
  fem group node 3124..3375,3377..4156 as SURFNORM

```

```

$COMPNODES ="1..37,3123..3376"
} elseif ($MODEL eq "11") # Model 11
{
  fem group node 810 as FIXEDNODE
  fem group node 771,1024 as SURFENDS
  fem group node 772..1023,1025..1804 as SURFNORM
  $COMPNODES ="1..37,771..1024"
} elseif ($MODEL eq "12") # Model 12
{
  fem group node 689 as FIXEDNODE
  fem group node 650,903 as SURFENDS
  fem group node 651..902,904..1683 as SURFNORM
  $COMPNODES ="1..37,650..903"
} elseif ($MODEL eq "13") # Model 13
{
  fem group node 1274 as FIXEDNODE
  fem group node 1235,1488 as SURFENDS
  fem group node 1236..1487 as SURFNORM
  $COMPNODES ="1..37,1235..1488"
}

if ($BILINEAR==0)
{
  # using bicubic fields
  fem def equ;r;forward_reg4 reg all
  fem def mat;r;forward_reg4 reg all
  fem def ini ;r;forward_reg4 reg all
  fem def sour;r;pig_scale reg 4
  fem def coup;r;forward
  fem def solv;r;forward_reg4 coup reg all
} else
{
  # using bilinear fields
  fem def equ;r;forward_reg4_lin reg all
  fem def mat;r;forward_reg4 reg all
  fem def ini ;r;forward_reg4_lin reg all
  fem def sour;r;pig_scale reg 4
  fem def coup;r;forward
  fem def solv;r;forward_reg4_lin coup reg all
}

# Solve the problem
fem solv coup
fem eval elec;$OUTPUT hist $OUTPUT from node elec $COMPNODES bin reg all
fem def export;r;291
fem export sign;$OUTPUT elec sign $OUTPUT

#
# Exporting to CMGUI
#
if ($EXCMGUI==1)
{
  fem exp node;pig as pig reg all
  fem exp elem;skin as skin reg 1
  fem exp elem;lungs as lungs reg 2,3
  fem exp elem;heart as heart reg 4

  $TMPDIR="/tmp/cheng/dipole"
  fem ex node;"$TMPDIR/$OUTPUT" history $OUTPUT binary as soln
  fem ex elem;"$TMPDIR/$OUTPUT" field as soln
}

fem def para;w;/tmp/tmp minimal
quit

```

## D.7 Activation Inverse Problem Comfile

Performs an activation inverse solution from torso surface signals which have been generated from a known activation sequence. The activation sequence has been derived from the eikonal cardiac source described in Section 4.6.3. The zero-crossing estimates and optimised activation times and torso surface signals are compared to the known activation times and torso surface signals as a measure of validity of the solution.

```

# -----#
# Generic Analytic Activation Inverse
# -----#

set fatal off                                # Force a crash with all errors

$DESCRIPTION    = "noise 10 varying lapl"    # Description for run
$SVARY          = "b100_500"                # Regularisation and transmembrane jump variables

$BASEDIR        = "/xlv1/eng_sci/cheng/porky/data_model/" # Base directory for comfile
$SOUT           = ". /output6/"             # Output directory for run specific files
$OUTTRSF        = ". /common/"             # Output directory for generated transfer matrices
$COMMON         = ". /common/"             # Output directory for common files

$EMAIL          = 1                          # Setup email notifications when job completes
$SUBJECT        = "refined eikonal"          # Description for email
$EMAILFROM      = "Leo"
$EMAILADDR      = "l.cheng@auckland.ac.nz"

#
# Signal dependents
#
$CUTOFF         = 0.00106                    # Cutoff for phi SVD
$TSTART        = 1                          # remember to change ipopti
$TEND          = 100                         # and the comp sign
$TRSFMETH      = "method 3 win 5"           # Transfer method
$ACTIV_TYPE     = "eikonal_05"

$COMP1         = "integral"                  # Comparisons for torso signals & activation times
$COMP2         = "start 0.03 end 0.09"

#
# Logical controls [true|false]
#
$ANALYSE       = 1                          # Analyse the results
$RM_BINSIG     = 1
$TRANS2TORSO   = 0                          # Generate the appropriate transfer matrices
$TRANS2EPI     = 0
$EPI2TORSO     = 0
$ZEROCROSS     = 1                          # Generate zcrossing estimate
$OPTIM         = 1                          # Optimise activation times
$ANALYTIC      = 1                          # Generate an analytic solution
$EXPORT        = 1                          # Export results and model to CMGUI
$FORMAT        = "binary"                   # Use binary file formats [binary|ascii]

#
# Mesh dependents
#
$MODEL         = "${BASEDIR}pig05"          # Model to use
$TORSO         = 1                          # Assign region numbers
$LUNGS         = "2,3"
$LVENDO        = 4
$RVENDO        = 5
$HEART         = 6

```

```

$TORSONODES      = "765..1798"
$TORSOELEMENTS  = "801..1856"
$HEARTNODES     = "1..37,440..466,467..504"
$EPINODES       = "1..37"

system "mkdir -p "$OUT
system "echo ${DESCRIPTION} > ${OUT}START.txt"

#
# Start commands
#
fem def para;r; transfer_n_r6_big
fem def coor 3,1
fem def reg;r; six
fem def base;r; bicubic_bilinear
fem def node;r;$MODEL reg all
fem def elem;r;$MODEL_in reg all

# Array size parameters for problem
# Rectangular Cartesian coordinates
# Six region problem (epi, 2 endos, 2 lungs, skin)
# Bicubic bases for geometry, Bilinear bases for dependant variables
# Node and element files to define geometry

if ( $EXPORT==1 )
{
  fem export node;${COMMON}pig as pig reg all
  fem export elem;${COMMON}skin as skin reg $TORSO
  fem export elem;${COMMON}heart as heart reg $HEART
  fem export elem;${COMMON}lungs as lungs reg $LUNGS
  fem export elem;${COMMON}rvendo as rvendo reg $RVENDO
  fem export elem;${COMMON}lvendo as lvendo reg $LVENDO
} #EXPORT

# Export geometry of model

fem group node 804 as FIXEDNODE
fem group node 765,1798 as SURFENDS
fem group node 766..1797 as SURFNORM

# Group the skin surfaces for boundary conditions

#
# -----#
# Setup equations
# -----#
#
fem def eq;r;poisson_n_r6 reg all
fem def mat;r;mate_n_r6 reg all
fem def init ;r;noflux_n_r6 reg all
fem def coup;r;laplace
fem def solv;r;nosalu_n_r6 coup reg all
fem def inve;r;lapl_SVARY
fem li inver

# Laplace's eqn for region 1..5, Poisson equation for region 6
# Passive conductivities for regions 1..5 Bidomain conductivities for region 6
# No flux BCs with reference node

# Setup of inverse parameters (transmembrane jump for 100mV)

if ( $TRANS2TORSO==1 )
{
  #
  # Double Layer Transfer Matrix (trans - mem to body)
  #
  fem def solv;r;nosalu_n_r6 coup reg all
  fem def tran;r;trans2torso
  fem eva tran svd
  fem write matrix;${OUTTRSF}trans2torso matric T_BH $FORMAT
} # TRANS2TORSO

if ( $TRANS2EPI==1 )
{
  #
  # Double Layer Transfer Matrix (trans - mem to epi)
  #
  fem def solv;r;nosalu_n_r6 coup reg all
  fem def trans;r;trans2epi
  fem eva tran svd

  fem write matrix;${OUTTRSF}trans2epi matric T_BH $FORMAT
}

if ( $EPI2TORSO==1 )

```

```

{
#
# Single Layer Transfer Matrix (epi to torso)
#
fem def solv;r;nosalu_nr6 coup reg all
fem def tran;r;epi2torso
fem eva tran

fem write matrix;${OUTTRSF}epi2torso matric T_BH $FORMAT
}

if ( $ANALYTIC==1 )
{
#
# Setup analytic activation profile
#
fem def init;r;noflux_nr6 reg all
fem def ini;r;$ACTIV_TYPE reg $HEART # Read in an activation profile in the HEART region
fem up sol depen from_ind 1 to_ind 7 from_clas 1 to_clas 1 reg $HEART # Copy the activation sequence to the analytic index (7)
fem exp nod;${OUT}input as input field us solv reg $HEART # Export the analytic/input activation profile
fem exp ele;${OUT}input as input field us solv reg $HEART

#
# Create an input torso signal (trans2torso)
#
fem def trans;r;trans2torso
fem read matrix;${OUTTRSF}trans2torso $FORMAT
fem def init;r;noflux_nr6 reg all
fem def ini;r;$ACTIV_TYPE reg $HEART
fem app trans activ tstart $TSTART tend $TEND outf ${OUT}tmp $FORMAT $TRSFMETHOD # Create analytic torso surface signals
fem eva elec;${OUT}input_torso his ${OUT}tmp fr nod elect $TORSONODES $FORMAT reg $TORSO
fem def expo;r;unemap_254
fem exp sign;${OUT}input_torso elect signal ${OUT}input_torso # Export the torso surface signals
fem eva elec;${OUT}input_activ hist ${OUT}tmp tend 0.001 from node $FORMAT reg $HEART # & Store the activation times in a signal

#
# Create some noisy signals
#
fem def noise;r;noise_10micro # Apply gaussian electrical noise to the analytic signals
fem apply noise sign ${OUT}input_torso $FORMAT outfil ${OUT}input_torso_noise
fem def expo;r;unemap_254
fem exp signal;${OUT}input_torso_noise elect signal ${OUT}input_torso_noise

#
# Create epicardial signals (trans2epi)
#
fem def trans;r;trans2epi
fem read matrix;${OUTTRSF}trans2epi $FORMAT
fem def init;r;noflux_nr6 reg all
fem def ini;r;$ACTIV_TYPE reg $HEART

fem app trans activ tstart $TSTART tend $TEND outf ${OUT}tmp $FORMAT $TRSFMETHOD
fem eva elec;${OUT}input_epi his ${OUT}tmp fr nod elect $EPINODES $FORMAT reg $TORSO
fem def expo;r;unemap_37
fem exp sign;${OUT}input_epi elect signal ${OUT}input_epi

#
# Create torso signals (epi2torso)
#
fem def trans;r;epi2torso
fem read matrix;${OUTTRSF}epi2torso $FORMAT
fem def init;r;noflux_nr6 reg all
fem def ini;r;$ACTIV_TYPE reg $HEART

fem app trans hist infile ${OUT}tmp outf ${OUT}tmp2 $FORMAT
fem eva elec;${OUT}epi2torso his ${OUT}tmp2 fr nod elect $TORSONODES $FORMAT reg $TORSO
fem def expo;r;unemap_254
fem exp sign;${OUT}epi2torso elect signal ${OUT}epi2torso
} #analytic

if ( $ZEROCROSS==1 )
{

```



```

#
# Phi Processing
#
fem def trans;r;trans2torso
fem def ini;r;$ACTIV_TYPE reg $HEART
fem read matrix;${OUTTRSF}trans2torso $FORMAT

fem eva phi signal ${OUT}input_torso_noise $FORMAT # Evaluate the PHI matrix from
fem eva phi svd # Evaluate the SVD of the PHI matrix
fem eva phi svd_cutoff $CUTOFF data ${OUT}phi

#
# Zeroxing Calculation
#
fem
fem eva zeroxing # Calculate the zero crossing estimation
fem up init from zcrossing

fem def export;r;zeroxing # Export the zcrossing jumps and signals
fem exp sign;${OUT}zeroxing_zero_crossing
fem def export;r;zeroxing_ranges
fem exp sign;${OUT}zeroxing_ranges_zero_crossing

fem exp node;${OUT}zcross as zcross field using solv reg $HEART # Export the zcrossing activation profile
fem exp elem;${OUT}zcross as zcross field using solv reg $HEART

#
# Create torso signals and zcross activation sequence
#
fem app tran activ tstart $TSTART tend $TEND outf ${OUT}tmp $FORMAT $TRSMETHOD
fem eva elec;${OUT}zcross his ${OUT}tmp from node elec $TORSONODES $FORMAT reg $TORSO
fem def expo;r;unemap_254
fem exp sign;${OUT}zcross elect signal ${OUT}zcross
fem eva elec;${OUT}zcross_activ hist ${OUT}tmp tend 0.001 from node $FORMAT reg $HEART
} # ZEROCROSS

if ( $OPTIM==1 )
{
fem def optim;r;inverse region $HEART # Optimises the torso surface signals by
fem app tran activ tstart $TSTART tend $TEND outf ${OUT}tmp $FORMAT $TRSMETHOD # adjusting the activation times
fem eva resid wrt pot list 1 tstart $TSTART tend $TEND
fem li optim summ

optimise

fem app tran activ tstart $TSTART tend $TEND outf ${OUT}tmp $FORMAT $TRSMETHOD #
fem eva resid wrt pot list 1 tstart $TSTART tend $TEND
fem li optim summ

fem ex node;${OUT}optim as optim field us solv reg $HEART # Export the optimised activation profile
fem ex elem;${OUT}optim as optim field us solv reg $HEART

#
# Create torso signals and optimised activation sequence
#
fem app tran activ tstart $TSTART tend $TEND outf ${OUT}tmp $FORMAT $TRSMETHOD
fem eva elec;${OUT}optim his ${OUT}tmp from node elec $TORSONODES $FORMAT reg $TORSO
fem def expo;r;unemap_254
fem exp sign;${OUT}optim elect signal ${OUT}optim

fem eva elec;${OUT}optim_activ hist ${OUT}tmp tend 0.001 from node $FORMAT reg $HEART
}

if ( $ANALYSE==1 )
{
fem comp sign mast ${OUT}input_torso_noise comp ${OUT}zcross bin $COMP1 # Compare the analytic & zcrossing torso surface signals
fem comp sign mast ${OUT}input_torso_noise comp ${OUT}zcross bin $COMP2

```

```

fem comp sign mast ${OUT}input_torso_noise comp ${OUT}optim bin $COMP1      # Compare the analytic & optimised torso surface signals
fem comp sign mast ${OUT}input_torso_noise comp ${OUT}optim bin $COMP2

fem comp sign mast ${OUT}input_activ comp ${OUT}zcross_activ bin           # Compare the analytic & zcrossing estimate activation times
fem comp sign mast ${OUT}input_activ comp ${OUT}optim_activ bin           # Compare the analytic & optimised activation times

fem check sol reg 6
}

#
# End of Computations
#

if ( $EMAIL == 1)
{
  system "echo \"Subject:$SUBJECT \nContent:text \n$DESCRIPTION\" | /usr/lib/sendmail -F $EMAILFROM $EMAILADDR"
} # EMAIL

system "echo ${DESCRIPTION} > ${OUT}END.txt"                                # Records the finishing time
system "rm ${OUT}tmp.binhis"                                                # Remove temporary files
system "rm ${OUT}tmp2.binhis"

if ($RM_BINSIG==1)
{
  #
  # Tidies up the output directories – removes unneeded binsig files
  #
  system "rm ${OUT}epi2torso.binsig"
  system "rm ${OUT}input_epi.binsig"
  system "rm ${OUT}input_torso.binsig"
  system "rm ${OUT}input_torso_noise.binsig"
  system "rm ${OUT}input_activ.binsig"
  system "rm ${OUT}zcross.binsig"
  system "rm ${OUT}optim.binsig"
} # RM_BINSIG

=$OUT
=$DESCRIPTION

quit

```

---



## D.8 Activation and Potential Simulation Comfile

Commands used in the simulation studies in Chapter 7. Activation and potential inverse approaches are used to reconstruct the activation sequence at the heart level from known heart sources and torso surface potentials.

```

#-----#
# Double Point Activation & Potential Simulation
#-----#

set fatal off                                # Force a crash with all errors
itp set echo on
{

EMAIL            = 1                          # Setup email information on simulation completion
EMAILFROM        = "Leo"
EMAILADDR        = "l.cheng@auckland.ac.nz"

$SUBJECT          = "typical errors -- double points"      # Brief description of simulation
$DESCRIPTION      = "noise 50 lapl 0.0"

$ACTIVATION       = 0
$POTENTIAL        = 0

# RUNA/RUNB are the varying parameters and are also
# the names of the output directories
#
# RUNA
# the varying parameter
# [0..1] where 0 is the control
#
# RUNB
# RUNB varies [0..3] corresponding to laplacian value 0,5,50,500
# for POTENTIAL approach this should always be [0]
#

$RUNA             = 0
$RUNB             = 5
@INDEXA           = (0,1)
@INDEXB           = (0,5,50,500,5000)
$VARY             = $INDEXA[$RUNA]

if ($ACTIVATION==1)
{
  $OUT             = "output_activation/output$RUNA$RUNB"    # Output directory for activation sims
  $INVER           = "b1${VARY}0.$INDEXB[$RUNB]"
  $CUTOFF          = 0.028
} else
{
  $OUT             = "output_potential/output$RUNA"          # Output directory for potential sims
  $INVER           = "null"
  $CUTOFF          = 13
}

#
# Directory locations
#
$BASEDIR          = "/xlv1/eng_sci/cheng/porky/data_model"    # Base directory of sims
$COMMON           = ".common"                                # Output location for common files
$OUTTRSF          = $OUT                                     # Output location for transfer matrices

#
# Signal dependents
#

```

```

$TSTART                = 1      #remember to change ipoti
$TEND                  = 100     # and the comp sign
$STRSMETH               = "method 3 win 5"
$ACTIV_TYPE            = "right.epi.double"

$COMP1                  = "integral"          # Comparisons for torso signals & activation times
$COMP2                  = "start 0.03 end 0.06"

#
# Logical Controls [true|false]
#
$ANALYSE                = 1
$RM_BINSIG              = 1
$TRANS2TORSO           = 0                # Create correct transfer matrices
$TRANS2EPI              = 0
$EPI2TORSO             = 0
$TRANS2TORSO_WRONG     = 0                # Create incorrect transfer matrices
$TRANS2EPI_WRONG       = 0
$EPI2TORSO_WRONG       = 0
$ANALYTIC              = 1                # Create the analytic signals
$EXPORT                 = 1                # Export results to CMGUI
$FORMAT                 = "binary"        # File formats

$ZEROCROSS             = 1                # Controls for activation approach
$OPTIM                  = 1
$TIKHONOV              = 1                # Controls for the potential approach
$TSVD                   = 1

#
# Mesh dependents
#
$MODEL                  = "${BASEDIR}fullheart01" # Model number to use
$TORSO                  = 1                # Assign region numbers
$LVENDO                 = 2
$RVENDO                 = 3
$HEART                  = 4

$TORSONODES            = "153..1186"      # Group torso nodes & elements
$TORSOELEMENTS         = "1..1216"

if ( $ACTIVATION==1 )
{
  $HEARTNODES = "1..152,1187..1456"      # Assign epicardial and endocardial nodes for activation map
} else
{
  $HEARTNODES = "1..152"                  # Assign epicardial nodes for activation map
} #activation
$EPINODES = "1..152"                      # Assign the epicardial nodes

system "mkdir -p $OUT"
system "mkdir -p $COMMON"
system "echo ${DESCRIPTION} > ${OUT}START.txt"

#
# Start commands
#
fem def para;r; transfer_nr4_big          # Array size parameters for problem
fem def coor 3,1                          # Rectangular Cartesian coordinates
fem def regi;r;four                        # Four region problem (lungs not included)
fem def base;r; bicubic_bilinear          # Bicubic bases for geometry, Bilinear bases for dependant variables
fem def node;r;$MODEL reg all             # Node and element files to define geometry
fem def elem;r;${MODEL}_lin reg all

if ( $EXPORT==1 )                          # Export geometry of meshes
{
  fem export node;${COMMON} pig as pig reg all
  fem export elem;${COMMON} skin as skin reg $TORSO
}

```

```

fem export elem;${COMMON}heart as heart reg $HEART
fem export elem;${COMMON}rvendo as rvendo reg $RVENDO
fem export elem;${COMMON}lvendo as lvendo reg $LVENDO
} #export

fem group node 192      as FIXEDNODE
fem group node 154..1185 as SURFNORM
fem group node 153,1186 as SURFENDS

#
# Setup equations
#
fem def equ;r;poisson_nr4      reg all
fem def mat;r;mate_nr4        reg all
fem def init ;r;noflux_nr4     reg all
fem def coup;r;laplace
fem def solv;r;nosalu_nr4 coup reg all
fem def inve;r;lapl.$INVER
fem li inver

# Laplace's eqn for region 1..3, Poisson equation for region 4
# Passive conductivities for regions 1..3, Bidomain conductivities for region 4
# No flux & reference potential boundary conditions
# Setup of inverse parameters (transmembrane jump for 100mV)

#
# Calculate the correct transfer matrices
#
if ( $TRANS2TORSO==1 )
{
#
# Double Layer Transfer Matrix (trans-mem to body)
#
fem def solv;r;nosalu_nr4 coup reg all
fem def tran;r;trans2torso
fem eva tran svd
fem write matrix;${COMMON}trans2torso matric T_BH $FORMAT
} # trans2torso

if ( $TRANS2EPI==1 )
{
#
# Double Layer Transfer Matrix (trans-mem to epi)
#
fem def solv;r;nosalu_nr4 coup reg all
fem def trans;r;trans2epi
fem eva tran svd
fem write matrix;${COMMON}trans2epi matric T_BH $FORMAT
} # trans2epi

if ( $EPI2TORSO==1 )
{
#
# Single Layer Transfer Matrix (epi to torso)
#
fem def solv;r;nosalu_nr4 coup reg all
fem def tran;r;epi2torso
fem eva tran
fem write matrix;${COMMON}epi2torso matric T_BH $FORMAT
} # trans2torso

#
# Calculate the analytic activation sequence and toros surface signals
#
if ( $ANALYTIC==1 )
{
#
# Setup analytic activation using correct trsf matrix
#
fem def analytic;r;$ACTIV_TYPE activation region $HEART
fem list analytic activation region $HEART
fem def ini ;g activation region $HEART

fem exp nod;${OUT}input as input field us solv reg $HEART

```

```

fem exp ele;${OUT}input as input field us solv reg $HEART

#
# Create an input torso signal (trans2torso)
#
fem def trans;r;trans2torso
fem read matrix;${COMMON}trans2torso $FORMAT

fem def init ;r;noflux_nr4 reg all
fem def ini ;g activation region $HEART

cmiss("fem app trans activ tstart $TSTART tend $TEND outf ${OUT}tmp $FORMAT $TRSFMETH")
fem eva elec;${OUT}input_torso his ${OUT}tmp fr nod elect $TORSONODES $FORMAT reg $TORSO
fem def expo;r;unemap_254
fem exp sign;${OUT}input_torso elect signal ${OUT}input_torso
fem eval elec;${OUT}input_activ hist ${OUT}tmp tend 0.005 elec $HEARTNODES from node $FORMAT reg $HEART

if ($VARY==1)
{
#
# Add gaussian positional errors to electrode locations
#
fem def noise;r;noise_5mm
fem app noise sign ${OUT}input_torso $FORMAT outfil ${OUT}input_torso_noise
fem def data;w;${OUT}elec_error reg $TORSO
fem def xi ;c closest elem $TORSOELEMENTS reg $TORSO
fem export data;${OUT}elec_error as elec_error error offset 2000

#
# Create the surface electrodes
#
fem def data;c from_xi
fem def data;w;${OUT}projections
fem export data;${OUT}projections as projections offset 6000
fem eval elec;${OUT}input_torso_elec_noise his ${OUT}tmp fr data $FORMAT reg $TORSO

#
# Add gaussian electrical noise to signals
#
fem def noise;r;noise_50micro
fem apply noise sign ${OUT}input_torso_elec_noise $FORMAT outfil ${OUT}input_torso_noise
fem def export;r;unemap_254
fem exp signal;${OUT}input_torso_noise elect signal ${OUT}input_torso_noise
}
else {
#
# Add gaussian electrical noise to signals
#
fem def noise;r;noise_50micro
fem apply noise sign ${OUT}input_torso $FORMAT outfil ${OUT}input_torso_noise
fem def export;r;unemap_254
fem exp signal;${OUT}input_torso_noise elect signal ${OUT}input_torso_noise
}

#
# Create epicardial signals (trans2epi)
#
fem def trans;r;trans2epi
fem read matrix;${COMMON}trans2epi $FORMAT
fem def init ;r;noflux_nr4 reg all
fem def ini ;g activation region $HEART

cmiss("fem app trans activ tstart $TSTART tend $TEND outf ${OUT}tmp $FORMAT $TRSFMETH")
fem eva elec;${OUT}input_epi his ${OUT}tmp fr nod elect $EPINODES $FORMAT reg $TORSO

fem def expo;r;unemap_152
fem exp sign;${OUT}input_epi elect signal ${OUT}input_epi

#
# Create torso signals (epi2torso)
#
fem def trans;r;epi2torso

```

```

fem read matrix;${COMMON}epi2torso $FORMAT

fem def init ; r;noflux_nr4 reg all
fem def ini ; g activation region $HEART

fem app trans hist infile ${OUT}tmp outf ${OUT}tmp2 $FORMAT
fem eva elec;${OUT}epi2torso his ${OUT}tmp2 fr nod elect $TORSONODES $FORMAT reg $TORSO

fem def expo;r;unemap.254
fem exp sign;${OUT}epi2torso elect signal ${OUT}epi2torso

#
# Check we are getting consistent signals
# The rms should be 0.0 and the SI should be 1.0
#
# Epicardial approach should really use noisy signals created from
# epi2torso signal — however these should be theoretically be the same.
#
fem comp sign mast ${OUT}input.torso comp ${OUT}epi2torso bin $COMP1
fem comp sign mast ${OUT}input.torso comp ${OUT}epi2torso bin $COMP2
} #analytic

#
# Apply Typical Errors to Corrupt the Input & Create the "Wrong" Transfer Matrices
#

if ($VARY==1)
{
fem def inve; r;lapl,$INVER # Set the wrong transmembrane jump
fem li inver

fem change node scale by 1.1,1.05,1.05 reg $HEART # Scale the heart surface
fem li vol reg $HEART

$ABOUT = "4.302431,-132.240637,58.610737" # Centre of mass # Rotate the heart about THETA
$AXIS = "0,0,1" # THETA about z-axis
fem change node rotate by 10 about $ABOUT axis $AXIS reg $HEART

$ABOUT = "4.302431,-132.240637,58.610737" # Centre of mass # Rotate the heart about PHI
$AXIS = "0,1,0" # PHI about y-axis
fem change node rotate by 10 about $ABOUT axis $AXIS reg $HEART

fem change node trans by 5,8,-4 reg $HEART # Translate the heart

fem export node;${OUT}pig_vary as pig reg all # Export the new geometry to CMGUI
}

if ($TRANS2TORSO_WRONG==1)
{
#
# Double Layer Transfer Matrix (trans-mem to body)
#
fem def solv; r;nosalu_nr4 coup reg all
fem def tran; r;trans2torso
fem eva tran svd
fem write matrix;${OUTTRSFS}trans2torso matric T_BH $FORMAT
} # trans2torso

if ($TRANS2EPI_WRONG==1)
{
#
# Double Layer Transfer Matrix (trans-mem to epi)
#
fem def solv; r;nosalu_nr4 coup reg all
fem def tran; r;trans2epi
fem eva tran svd
fem write matrix;${OUTTRSFS}trans2epi matric T_BH $FORMAT
} # trans2epi

```



```

if ( $EPI2TORSO.WRONG==1 )
{
#
# Single Layer Transfer Matrix (epi to torso)
#
fem def solv;r;nosalu_nr4 coup reg all
fem def tran;r;epi2torso
fem eva tran
fem write matrix;${OUTTRSF}epi2torso matric T.BH $FORMAT
} # trans2torso

#
# Apply the Activation Inverse Approaches
#
if ( $ACTIVATION == 1 )
{
fem def trans;r;trans2torso
fem read matrix;${OUTTRSF}trans2torso $FORMAT
fem eval phi signal ${OUT}input_torso_noise $FORMAT # Assemble the PHI matrix from the signal
fem eval phi svd # Remove small singular values
fem eval phi svd_cutoff $CUTOFF data ${OUT}phi

if ( $ZEROCROSS==1 )
{
#
# Zeroxing Calculation
#
fem eval zeroxing # Evaluate the zero-crossing estimate
fem up init from_zcrossing

#
# Export the zcrossing jumps and ranges
#
fem def expo;r;zeroxing
fem exp sign;${OUT}zeroxing_zero_crossing
fem def expo;r;zeroxing_ranges
fem exp sign;${OUT}zeroxing_ranges_zero_crossing

#
# Export the zcross activation field
#
fem exp node;${OUT}zcross as zcross field using solv reg $HEART
fem exp elem;${OUT}zcross as zcross field using solv reg $HEART

#
# Create torso signals and zcross activation sequence
#
cmisss("fem app tran activ tstart $TSTART tend $TEND outf ${OUT}tmp $FORMAT $TRSFMETHOD")
fem eva elec;${OUT}zcross his ${OUT}tmp from node elec $TORSONODES $FORMAT reg $TORSO

fem def expo;r;unemap_254
fem exp sign;${OUT}zcross elect signal ${OUT}zcross
fem eval elec;${OUT}zcross_activ hist ${OUT}tmp tend 0.005 from node $FORMAT reg $HEART
} # ZEROCROSS

if ( $OPTIM==1 ) # Alter the activation sequence to minimise the
# difference between measured and calculated torso signals
{
fem def optim;r;inverse region $HEART

cmisss("fem app tran activ tstart $TSTART tend $TEND outf ${OUT}tmp $FORMAT $TRSFMETHOD")
fem eval resid wrt pot list 1 tstart $TSTART tend $TEND
fem li optim summ

optimise

cmisss("fem app tran activ tstart $TSTART tend $TEND outf ${OUT}tmp $FORMAT $TRSFMETHOD")
fem eval resid wrt pot list 1 tstart $TSTART tend $TEND
fem li optim summ
}

```

```

#
# Export the optimised activation
#
fem ex node;${OUT}optim as optim field us solv reg $HEART
fem ex elem;${OUT}optim as optim field us solv reg $HEART

#
# Create torso signals and optimised activation sequence
#
cmiss("fem app tran activ tstart $TSTART tend $TEND outf ${OUT}tmp $FORMAT $TRSFMETH")
fem eva elec;${OUT}optim his ${OUT}tmp from node elec $TORSONODES $FORMAT reg $TORSO
fem def expo;r;unemap_254
fem exp sign;${OUT}optim elect signal ${OUT}optim
fem eval elec;${OUT}optim_activ hist ${OUT}tmp tend 0.005 from node $FORMAT reg $HEART
} #optim

if ($ANALYSE==1)
{
#
# Compare analytic/input torso signals with the zerocrossing & optimised torso signals
#
fem comp sign mast ${OUT}input_torso_noise comp ${OUT}zcross bin $COMP1
fem comp sign mast ${OUT}input_torso_noise comp ${OUT}zcross bin $COMP2
fem comp sign mast ${OUT}input_torso_noise comp ${OUT}optim bin $COMP1
fem comp sign mast ${OUT}input_torso_noise comp ${OUT}optim bin $COMP2

#
# Compare analytic/input activation times with zerocrossing and optimised activation times
#
fem comp sign mast ${OUT}input_activ comp ${OUT}zcross_activ bin
fem comp sign mast ${OUT}input_activ comp ${OUT}optim_activ bin
fem check sol reg $HEART
}
} else
{
#
# Apply Epicardial Potential Inverse Approachs
#
fem def trans;r;epi2torso
fem read matrix;${OUT}TRSF }epi2torso $FORMAT

fem eval phi signal "${OUT}input_epi" PHILH_EXACT $FORMAT
fem eval phi signal "${OUT}input_torso_noise" $FORMAT
fem eval phi svd data ${OUT}phi
fem eval phi svd_cutoff $CUTOFF
fem def export;r;unemap_152

for $LOOP ( 1..2 )
{
#
# 2 Epicardial Inverse Approachs
#
$VALID = 0

if ( $LOOP==1 && $TIKHONOV==1 )
{
#
# GCV, L– curve, Quasi– opt Optimal, CRESO & Zero– crossing Tikhonov regularisation
#
$EPIAPPROACH = "tikhonov"

@x = (1,2,4..7)
$VALID = 1
} elseif ( $LOOP==2 && $TSVD==1 )
{
#
# GCV, L– curve, Quasi– opt & Optimal TSVD regularisation
#
$EPIAPPROACH = "tsvd"
@x = (1,2,4,5)
$VALID = 1
} #loop
}
}

```

```

if ( $VALID==1 )
{
for $COUP ( 1..2 )
{
foreach $METHOD ( @x )
{
fem def inve;r;${EPIAPPROACH}_-${COUP}_-${METHOD}
fem list inve

if ( $POTENTIAL==1 )
{
#
# Evaluate potential inverse
#
fem eval inve
fem eval elec;${OUT}${EPIAPPROACH}_-${COUP}_-${METHOD} from PHI.H bin
fem export sign;${OUT}${EPIAPPROACH}_-${COUP}_-${METHOD} elec sign "${OUT}${EPIAPPROACH}_-${COUP}_-${METHOD}"

if ( $ANALYSE==1 )
{
#
# Compare epicardial signals
#
fem comp sign mast "${OUT}input_epi" comp "${OUT}${EPIAPPROACH}_-${COUP}_-${METHOD}" basis both bin
} #analyse

if ( $RM_BINSIG==1 )
{
system "rm ${OUT}${EPIAPPROACH}_-${COUP}_-${METHOD}.binsig" # Files no longer required
} #RM_BINSIG
} else
{
#
# Activation times defined by maximum - dV/dt. The events
# must be saved to the original signal in UnEmap
#
if ( $ANALYSE==1 )
{
#
# Compare activation times
#
fem def import;r; epi_activ
fem import signal;${OUT}${EPIAPPROACH}_-${COUP}_-${METHOD} activation signal_output "${OUT}tmp"
fem comp sign mast "${OUT}input_activ" comp "${OUT}tmp" bin
system "rm ${OUT}tmp.binsig"
} #analyse
} #potential
} #method
} #coup
} #valid
} #loop
} #activation/potential approach

#
# End of Computations
#

if ( $EMAIL == 1 )
{
system "echo \"Subject:$SUBJECT \nContent:text \n$DESCRIPTION\" | /usr/lib/sendmail -F $EMAILFROM $EMAILADDR"
} # EMAIL

#
# Finish the comfile
#
system "echo ${DESCRIPTION} > ${OUT}END.txt"

if ( $ANALYTIC==1 )
{
system "rm ${OUT}tmp.binhis" # Remove temporary history files
}

```

```
system "rm ${OUT}tmp2.binhis"
}

if ( $RM.BINSIG==1)
{
#
# Tidies up the output directories – removes unneeded binsig files
#
if ( $ANALYTIC==1)
{
system "rm ${OUT}epi2torso.binsig"           # Remove files related to analytic approach
system "rm ${OUT}input_epi.binsig"
system "rm ${OUT}input_torso.binsig"
system "rm ${OUT}input_torso_noise.binsig"
system "rm ${OUT}input_activ.binsig"
}

if ( $ACTIVATION==1)
{
system "rm ${OUT}zcross.binsig"           # Remove files related to activation approach
system "rm ${OUT}optim.binsig"
}
} # RM.BINSIG

print "$OUT \n"
print "$DESCRIPTION \n"

} #itp set echo

quit
```

---

## References

- Akaike, H. (1974), 'A new look at the statistical model identification', *IEEE Trans. Automat. Contr.* **19**(6), 716–723.
- Ascension Technology Corporation (2000), 'Flock of Birds', Internet. <http://www.ascension-tech.com/products/flockofbirds/flockofbirds.htm>.
- Barr, R. C. & Spach, M. S. (1977), 'Sampling rates required for digital recording on intracellular and extracellular cardiac potentials', *Circulation* **55**, 40–48.
- Barr, R. C. & Spach, M. S. (1978), 'Inverse calculation of QRS-T epicardial potentials from body surface potential distributions for normal and ectopic beats in the intact dog', *Circ. Res.* **42**, 661–675.
- Beeler, G. W. & Reuter, H. (1977), 'Reconstruction of the action potential of ventricular myocardial fibres', *J. Physiol.* **268**, 177–210.
- Besterman, E. & Creese, R. (1979), 'Waller – Pioneer of electrocardiography', *Br. Heart J.* **42**, 61–54.
- BioSemi (2000), 'Activeone system', Internet. <http://www.biosemi.com>.
- Biosense Webster (2000), 'Carto', Internet. <http://www.cordiswebster.com>.
- Bradley, C. P. (1998), A three-dimensional torso model for electrocardiology, PhD thesis, The University of Auckland, New Zealand.
- Bradley, C. P., Pullan, A. J. & Hunter, P. J. (1997), 'Geometric modeling of the human torso using cubic Hermite elements', *Ann. Biomed. Eng.* **25**, 96–111.
- Bradley, C. P., Pullan, A. J. & Hunter, P. J. (2000), 'Effects of material properties and geometry on electrocardiographic forward simulations', *Ann. Biomed. Eng.* **28**(7), 721–741.

- Brody, D. A. (1956), 'A theoretical analysis of intracavity blood mass influence on the heart-lead relationship', *Circ. Res.* **4**, 731–738.
- Brooks, D. H., Ahmad, G. F., MacLeod, R. S. & Maratos, G. M. (1999), 'Inverse electrocardiography by simultaneous imposition of multiple constraints', *IEEE Trans. Biomed. Eng.* **46**(1), 3–18.
- Brooks, D. H. & MacLeod, R. S. (1997), 'Electrical imaging of the heart', *IEEE Signal Processing Magazine* **14**(1), 24–42.
- Budgett, D. M. (1995), Remote Sensing of the Epicardium, PhD thesis, Imperial College of Science, Technology and Medicine, University of London.
- Buist, M. L. & Pullan, A. J. (2001), From cell to body surface: A fully coupled approach, in 'Proceedings of 26th Annual Conference of the International Society for Computerized Electrocardiology', Hutchinson Island, FL.
- Cardiac Pathways Corporation (2000), 'Mercator High Density Array Catheter', Internet. [http://www.cardiac.com/products\\_catheters.html](http://www.cardiac.com/products_catheters.html).
- Cheng, L. K., Nash, M. N., Bradley, C. P., Pullan, A. J. & Paterson, D. J. (2000), Non-invasive electrical imaging of the heart: Animal studies, in 'Proceedings of the Physiological Society of New Zealand', Vol. 19, Physiological Society of New Zealand, Waiheke Island, New Zealand, p. 42.
- Clerc, L. (1976), 'Directional differences of impulse spread in trabecular muscle from mammalian heart', *J. Physiol.* **255**, 335–346.
- Colli Franzone, P., Guerri, L., Penacchio, M. & Taccardi, B. (1998), 'Spread of excitation in 3-D models of the anisotropic cardiac tissue. II effects of fiber architecture and ventricular geometry', *Math. Biosci.* pp. 131–171.
- Colli Franzone, P., Guerri, L., Taccardi, B. & Viganotti, C. (1985), 'Finite element approximation of regularised solutions of the inverse potential problem of electrocardiography and applications to experimental data', *Calcolo* **22**(1), 91–186.
- Cordier, F. & Magnenat-Thalmann, N. (2000), Comparison of two techniques for organ reconstruction using visible human data, in 'Modeling for Medical Applications, Siggraph 2000', New Orleans, LA.

- Crocombe, J. P. (1997), Customising computational models, Master's thesis, Department of Engineering Science, School of Engineering, The University of Auckland, New Zealand.
- Cuppen, J. & van Oosterom, A. (1984), 'Model studies with the inversely calculated isochrones of ventricular depolarization', *IEEE Trans. Biomed. Eng.* **31**, 652–659.
- Durrer, D., van Dam, R. T., Freud, G. E., Janse, M. J., Meijler, F. L. & Arzbaecher, R. C. (1970), 'Total excitation of the isolated human heart', *Circulation* **21**, 899–912.
- Einthoven, W. (1903), 'Die galvanometrische Registrierung des menschlichen Elektrokardiogramms, zugleich eine Beurtheilung der Anwendung des Capilar-Elektrometers in der Physiologie', *Pfluegers Arch.* **99**, 472–80.
- Faro Technologies Incorporated (2000), 'Faro Arm', Internet.  
<http://www.faro.com/products/faroarm.asp>.
- Fischer, G. (1999), Application of the Boundary Element Method and the Finite Element Method to the Magneto- and Electrocardiographic Forward and Inverse Problem, PhD thesis, Technical University Graz.
- Fischer, G., Tilg, B., Modre, R., Huiskamp, G. J. M., Fetzer, J., Rucker, W. & Wach, P. (2000), 'A bidomain model based BEM-FEM coupling formulation for anisotropic cardiac tissue', *Ann. Biomed. Eng.* **28**(10), 1229–1243.
- Fischer, G., Tilg, B., Wach, P., Modre, R., Leder, U. & Nowak, H. (1999), 'Application of high-order boundary elements to the electrocardiographic inverse problem', *Computer Methods and Programs in Biomedicine* **58**(1999), 119–131.
- Foster, K. R. & Schwan, H. P. (1989), 'Dielectric properties of tissue and biological materials: A critical review', *Crit. Rev. Biomed. Eng.* **17**(1), 25–104.
- Geddes, L. A. & Baker, L. E. (1967), 'The specific resistance of biological material - a compendium of data for the biomedical engineer and physiologist', *Med. & Biol. Engng.* **5**, 271–293.
- Geselowitz, D. B. (1985), 'Use of time integrals of the ECG to solve the inverse problem', *IEEE Trans. Biomed. Eng.* **32**(1), 73–75.
- Geselowitz, D. B. (1989), 'On the theory of the electrocardiogram', *Proceedings of the IEEE* **77**(6), 857–876.
- Goldberger, E. (1942), 'A simple, indifferent, electrocardiographic electrode of zero potential and a technique of obtaining augmented, unipolar, extremity leads', *Am. Heart J.* pp. 483–493.

- Golub, G. H., Heath, M. T. & Wahba, G. (1979), 'Generalized cross-validation as a method for choosing a good ridge parameter', *Technometrics* **21**, 215–223.
- Gornick, C. C., Adler, S. W., Pederson, B., Hauck, J., Budd, J. & Schweitzer, J. (1999), 'Validation of a new noncontact catheter system for electroanatomic mapping of left ventricular endocardium', *Circulation* **99**(6), 829–835.
- Green, L. S., Taccardi, B., Ershler, P. R. & Lux, R. L. (1991), 'Effects of conducting media on isopotential and isochrone distributions', *Circulation* **84**(6), 2513–2521.
- Greensite, F. (1992), 'A new method for regularization of the inverse problem of electrocardiography', *Math. Biosci.* **111**, 131–154.
- Greensite, F. (1995), 'Remote reconstruction of confined wavefront propagation', *Inverse Problems* **11**, 361–370.
- Greensite, F. & Huiskamp, G. (1998), 'An improved method for estimating epicardial potentials from the body surface', *IEEE Trans. Biomed. Eng.* **45**, 98–104.
- Gulrajani, R. M. (1998), 'The forward and inverse problems of electrocardiography', *IEEE Eng. in Med and Biol.* **17**(5), 84–101,122.
- Gulrajani, R. M., Roberge, F. A. & Savard, P. (1984), 'Moving dipole inverse ECG and EEG solutions', *IEEE Trans. Biomed. Eng.* **31**(12), 903–910.
- Hansen, P. C. (1992), 'Analysis of discrete ill-posed problems by means of the l-curve', *SIAM Review* **34**(4), 560–580.
- Hansen, P. C. (1998), *Rank-Deficient and Discrete Ill-Posed Problems: Numerical Aspects of Linear Inversion*, Society for Industrial and Applied Mathematics, Philadelphia.
- Hansen, P. C. & O'Leary, D. P. (1993), 'The use of the L-curve in the regularisation of discrete ill-posed problems', *SIAM J. Sci. Comput.* **14**(6), 1487–1503.
- Harris, G. M. (1996), Modelling the auditory brainstem response using an anatomically accurate model of the human head, Master's thesis, The University of Auckland, New Zealand.
- Hedley, W. J. (1998), Finite element modelling of the left ventricle using magnetic resonance image data, Master's thesis, Department of Engineering Science, The University of Auckland, New Zealand.



- Henriquez, C. S. (1993), 'Simulating the electrical behaviour of cardiac tissue using the bidomain model', *Crit. Rev. Biomed. Eng.* **21**, 1–77.
- Hoekema, R., Uijen, G. J. H., Stilli, D. & van Oosterom, A. (1998), 'Lead system transformation of body surface map data', *J. Electrocardiol.* **31**(2), 71–82.
- Holland, R. P. & Brooks, H. (1976), 'The QRS complex during myocardial ischemia: An experimental analysis in the porcine heart', *JCI* pp. 541–550.
- Holland, R. P. & Brooks, H. (1977), 'TQ-ST segment mapping: Critical review and analysis of current concepts', *Am. J. Cardiol.* pp. 10–129.
- Hren, R. & Stroink, G. (1995), 'Application of the surface harmonic expansions for modeling the human torso', *IEEE Trans. Biomed. Eng.* **42**(5), 521–524.
- Huiskamp, G. (1998), 'Simulation of depolarization in a membrane-equations-based model of the anisotropic ventricle', *IEEE Trans. Biomed. Eng.* **45**(7), 847–855.
- Huiskamp, G. & Greensite, F. (1997), 'A new method for myocardial activation imaging', *IEEE Trans. Biomed. Eng.* **44**, 433–446.
- Huiskamp, G. J. & van Oosterom, A. (1988), 'The depolarization sequence of the human heart surface computed from measured body surface potentials', *IEEE Trans. Biomed. Eng.* **35**(12), 1047–1059.
- Huiskamp, G. & van Oosterom, A. (1989), 'Tailored versus realistic geometry in the inverse problem of electrocardiography', *IEEE Trans. Biomed. Eng.* **36**(8), 827–835.
- Hunter, P. J., McNaughton, P. A. & Noble, D. (1975), 'Analytical models of propagation in excitable cells', *Prog. Biophys. Molec. Biol.* **30**(2/3), 99–144.
- Hyttinen, J., Puurtinen, H. G., Kauppinen, P., Nousiainen, J., Laarne, P. & Malmivuo, J. (2000), 'On the effects of model errors on forward and inverse ECG problems', *Intl. J. Bioelectromagnetism* **2**(2). Cardiomodel 2000.
- Johnson, C. R., MacLeod, R. S. & Ershler, P. R. (1992), 'A computer model for the study of electrical current flow in the human thorax', *Comput. Biol. Med.* **22**(5), 305–323.
- Johnston, P. R. & Gulrajani, R. M. (1997), 'A new method for regularization parameter determination in the inverse problem of electrocardiography', *IEEE Trans. Biomed. Eng.* **44**(1), 19–39.

- Johnston, P. R. & Gulrajani, R. M. (2000), 'Selecting the corner of the L-curve approach to Tikhonov regularisation', *IEEE Trans. Biomed. Eng.* **47**(2), 1293–1296.
- Johnston, P. R. & Kilpatrick, D. (1995), 'The inverse problem of electrocardiology: The performance of inversion techniques as a function of patient anatomy', *Math. Biosci.* **126**(2), 125–146.
- Katz, A. M. (1992), *Physiology of the Heart*, 2nd edn, Raven Press, Ltd., 1185 Avenue of the Americas, New York 10036.
- Keener, J. P. (1991), 'An eikonal-curvature equation for action potential propagation in myocardium', *JMB* **29**, 629–651.
- Klepfer, R. N., Johnson, C. R. & MacLeod, R. S. (1997), 'The effects of inhomogeneities and anisotropies on electrocardiographic fields: A 3-d finite-element study', *IEEE Trans. Biomed. Eng.* **44**(8), 706–719.
- Kossmann, C. E. & Johnston, F. D. (1935), 'The precordial electrocardiogram. I. the potential variations of the precordium and of the extremities in normal subjects', *Am. Heart J.* **10**. definition of the 6 chest leads.
- Langrill, D. M. & Roth, B. J. (2001), 'The effect of plunge electrodes during electrical stimulation of cardiac tissue', *IEEETBME* **48**(10), 1207–1211.
- Le Grice, I. J., Hunter, P. J. & Smaill, B. H. (1997), 'Laminar structure of the heart : A mathematical model', *Am. J. Physiol.* **272**(Heart Circ. Physiol. 41), H2466–H2476.
- Le Grice, I. J., Smaill, B. H., Chai, L. Z., Edgar, S. G., Gavin, J. B. & Hunter, P. J. (1995), 'Laminar structure of the heart: Ventricular myocyte arrangement and connective tissue architecture in the dog', *Am. J. Physiol.* **269**(38), H571–H582.
- Legget, M. E., Leotta, D. F., Bolson, E. L., McDonald, J. A., Martin, R. W., Li, X.-N., Otto, C. M. & Sheehan, F. H. (1998), 'System for quantitative three-dimensional echocardiography of the left ventricle based on a magnetic-field position and orientation sensing system', *IEEE Trans. Biomed. Eng.* **45**(4), 494–504.
- Lorensen, W. (1996), Marching through the visible human, in 'The Visible Human Project Conference', National Institutes of Health, Bethesda, MA.
- Lorensen, W. & Cline, H. (1987), 'Marching cubes: A high-resolution 3-d surface construction algorithm', *Computer Graphics* **21**(3), 163–169. SIGGRAPH '87 Proceedings.

- Luo, C. & Rudy, Y. (1994), 'A dynamic model of the cardiac ventricular action potential: I. Simulations of ionic currents and concentration changes', *Circ. Res.* **74**(6), 1071–1096.
- MacLeod, R. S. & Brooks, D. H. (1998), 'Recent progress in inverse problems in electrocardiology', *IEEE Engineering in Medicine and Biology Magazine* **17**(1), 73–83.
- MacLeod, R. S., Johnson, C. R. & Ershler, P. R. (1991), Construction of an inhomogeneous model of the human torso for use in computational electrocardiography, in 'Proceedings of the Annual International Conference of the IEEE', Engineering in Medicine and Biology Society, pp. 688–689.
- MacLeod, R. S., Taccardi, B. & Lux, R. L. (1995), Electrocardiographic mapping in a realistic torso tank preparation, in 'IEEE 17th Annual Conference', Vol. 1, Engineering in Medicine and Biology Society, pp. 245–246.
- Magenat-Thalmann, N. & Cordier, F. (2000), Construction of a human topological model, in 'Modeling for Medical Applications, Siggraph 2000', New Orleans, LA.
- Martin, R. O. & Pilkington, T. C. (1972), 'Unconstrained inverse electrocardiography: Epicardial potentials', *IEEE Trans. Biomed. Eng.* **19**(4), 276–285.
- Martin, R. O., Pilkington, T. C. & Morrow, M. (1975), 'Statistically constrained inverse electrocardiography', *IEEE Trans. Biomed. Eng.* **22**, 487–492.
- McFee, R. & Rush, S. (1968), 'Qualitative effects of thoracic resistivity variations on the interpretation of the electrocardiogram: The low resistance surface layer', *Am. Heart J.* **74**(1), 48–61.
- Messinger-Rapport, B. J. & Rudy, Y. (1986), 'The inverse problem in electrocardiography: A model study of the effects of geometry and conductivity parameters on the reconstruction of epicardial potentials', *IEEE Trans. Biomed. Eng.* **33**(7), 667–676.
- Messinger-Rapport, B. J. & Rudy, Y. (1988), 'Regularization of the inverse problem of electrocardiology: A model study', *Math. Biosci.* **89**, 79–118.
- Miller, III, W. T. & Geselowitz, D. B. (1978), 'Simulation studies of the electrocardiogram I. The normal heart', *Circ. Res.* **43**(2), 301–314.
- Modre, R. (2000), A Regularization Technique for Nonlinear Ill-Posed Problems Applied to Myocardial Activation Time Imaging, PhD thesis, Department of Biophysics, Institute of Biomedical Engineering, Technical University Graz, Austria.

- Moritz, W. E., Pearlman, A. S., McCabe, D. H., Medema, D. K., Ainsworth, M. E. & Boles, M. S. (1983), 'An ultrasonic technique for imaging the ventricle in three dimensions and calculating its volume', *IEEE Trans. Biomed. Eng.* **30**, 482–492.
- Narayana, N. (1972), *Basic Electromagnetics with Applications*, Prentice-Hall, Inc., New Jersey.
- Nash, M. P., Bradley, C. P., Cheng, L. K., Pullan, A. J. & Paterson, D. J. (2000a), 'Electrocardiographic inverse validation study: *In-vivo* mapping and analysis', *FASEB J.* **14**(4), A442.
- Nash, M. P., Bradley, C. P., Cheng, L. K., Pullan, A. J. & Paterson, D. J. (2000b), 'An experimental-computational framework for validating *In-vivo* ECG inverse methods', *Intl. J. Bioelectromagnetism* **2**(2).
- National Library of Medicine (1994), 'Visible human project', Internet.  
<http://www.nlm.nih.gov/research/visible/>.
- Netter, F. H. (1997), *Atlas of Human Anatomy*, 2nd edn, Navertis.
- Nielsen, P. M. F., Le Grice, I. J., Smaill, B. H. & Hunter, P. J. (1991), 'Mathematical model of geometry and fibrous structure of the heart', *Am. J. Physiol.* **260**(Heart Circ. Physiol. 29), H1365–H1378.
- Noble, D., Varghese, A., Kohl, P. & Noble, P. (1998), 'Improved guinea-pig ventricular model incorporating a diadic space,  $I_{Kr}$  and  $I_{Ks}$ , length- and tension-dependent processes', *Can. J. Cardiol.* **14**, 123–134.
- Okajima, M., Fujino, T., Kobayashi, T. & Yamada, K. (1968), 'Computer simulation of the propagation process in excitation of the ventricles', *Circ. Res.* **23**, 203–211.
- Oostendorp, T. F. & van Oosterom, A. (1989), 'Source parameter estimation in inhomogeneous volume conductors of arbitrary shape', *IEEE Trans. Biomed. Eng.* **36**(3), 382–391.
- Oster, H. & Rudy, Y. (1992), 'The use of temporal information in the regularization of the inverse problem of electrocardiography', *IEEE Trans. Biomed. Eng.* **39**, 65–75.
- Oster, H., Taccardi, B., Lux, R., Ershler, P. & Rudy, Y. (1997), 'Noninvasive electrocardiographic imaging. Reconstruction of epicardial potentials, electrograms, and isochrones and localization of single and multiple electrocardiac events', *Circulation* **96**, 1012–1024.
- Oster, H., Taccardi, B., Lux, R., Ershler, P. & Rudy, Y. (1998), 'Electrocardiographic imaging. Noninvasive characterization of intramural myocardial activation from inverse-reconstructed epicardial potentials and electrograms', *Circulation* **97**, 1496–1507.

- Petera, J. & Pittman, J. F. T. (1994), 'Isoparametric Hermite elements', *Int. J. Numer. Methods Eng.* **37**, 3489–3519.
- Plonsey, R. (1969), *Bioelectric Phenomena*, McGraw Hill, New York.
- Plonsey, R. & Barr, R. C. (1988), *Bioelectricity: A Quantitative Approach*, Plenum Press, 233 Spring Street, New York, NY 10013.
- Press, W. H., Teukolsky, S. A., Vetterling, W. T. & Flannery, B. P. (1992), *Numerical recipes in FORTRAN, the art of scientific computing*, 2nd edn, Cambridge University Press, Cambridge.
- Pullan, A. J. & Buist, M. L. (1998), The effect of external tissue impedance on extracellular potentials, in 'Electrocardiology '98. Proceedings of the XXV International Congress on Electrocardiology', World Scientific, Singapore, pp. 85–88.
- Ramanathan, C. & Rudy, Y. (2001a), 'Electrocardiographic imaging: I. Effect of torso inhomogeneities on body surface electrocardiographic potentials', *J. Cardiovasc. Electrophysiol.* **12**(2), 229–240.
- Ramanathan, C. & Rudy, Y. (2001b), 'Electrocardiographic imaging: II. Effects of torso inhomogeneities on noninvasive reconstruction of epicardial potentials, electrograms, and isochrones', *J. Cardiovasc. Electrophysiol.* **12**(2), 241–252.
- Roberts, D., Hersch, L. T. & Scher, A. M. (1979), 'Influence of cardiac fiber orientation on wavefront voltage, conduction velocity and tissue resistivity in the dog', *Circ. Res.* **44**, 701–712.
- Roberts, D. & Scher, A. M. (1982), 'Effect of tissue anisotropy on extracellular potential fields in canine myocardium *in situ*', *Circ. Res.* **50**, 342–351.
- Rosenthal, A., Restieaux, N. & Feig, S. (1971), 'Influence of acute variations in hemocrit on the QRS complex of the frank electrocardiogram', *Circulation* **XLIV**, 456–465.
- Roth, B. J. (1997), 'Electrical conductivity values used with the bidomain model of cardiac tissue', *IEEE Trans. Biomed. Eng.* **44**(4), 326–328.
- Rudy, Y. & Plonsey, R. (1979), 'The eccentric spheres model as the basis for a study of the role of geometry and inhomogeneities in electrocardiography', *IEEE Trans. Biomed. Eng.* **26**(7), 392–399.
- Rush, S. (1971), 'An inhomogeneous anisotropic model of the human torso for electrocardiographic studies', *Med. & Biol. Engng.* **9**, 201–211.

- Rush, S., Abildskov, J. A. & McFee, R. (1963), 'Resistivity of body tissues at low frequencies', *Circ. Res.* **12**, 40–50.
- Sachse, F. B., Frech, R., Werner, C. D. & Dössel, O. (1999), A model based approach to assignment of myocardial fibre orientation, in 'Proceedings of Computers in Cardiology', Hanover, Germany, pp. 145–148.
- Sachse, F. B., Werner, C. D., Mery-Waarden, K. & Dossel, O. (1998), Applications of the visible human male data set in electrocardiology: Calculation and visualization of body surface potential maps of a complete heart cycle, in 'The Second Visible Human Project Conference', National Institutes of Health, Bethesda, MA.
- Sands, G. B., Cheng, L. K. & Pullan, A. J. (2000), Non-invasive electrical imaging of the heart: Green Lane patient studies, in 'PSNZ 2000 Conference', Physiological Society of New Zealand, Waiheke Island, New Zealand.
- Sapidis, N. & Besl, P. (1995), 'Direct construction of polynomial surfaces from dense range images through region growing', *ACM: Transactions on Graphics* **14**(2), 171–200.
- Schilling, R. J., Peters, N. S. & Davies, D. W. (1998), 'Simultaneous endocardial mapping in the human left ventricle using a non-contact catheter: Comparison of contact and reconstructed electrograms during sinus rhythm', *Circulation* **98**(9), 887–898.
- Schmidt, R. (1986), 'Multiple emitter location and signal parameter estimation', *IEEE Trans. Antenn. Propagat.* **AP-34**(3), 276–280.
- Selker, H. P. (1989), 'Coronary care unit triage decision aids: How do we know when they work?', *Am. J. Med.* pp. 491–493.
- SippensGroenewegen, A., Spekhorst, H., van Hemel, N. M., Kingma, J. H., Hauer, R. N. W., de Bakker, J. M. T., Grimbergen, C. A., Janse, M. J. & Dunning, A. J. (1993), 'Localization of the site of origin of postinfarction ventricular tachycardia by endocardial pace mapping. Body surface mapping compared with the 12-lead electrocardiogram', *Circulation* **88**(5), 2290–2306.
- Skouibine, K., Trayanova, N. & Moore, P. (1999), 'Anode/cathode make and break phenomena during defibrillation: Does electroporation make a difference', *IEEE Trans. Biomed. Eng.* **46**, 769–777.

- Smeets, J., Ben-Haim, S., Rodriguez, L., Timmermans, C. & Wellens, H. (1998), 'New method for nonfluoroscopic endocardial mapping in humans. Accuracy assessment and first clinical results', *Circulation* **97**, 2426–2432.
- Spach, M. S. & Barr, R. C. (1975), 'Ventricular intramural and epicardial potential distributions during ventricular activation and repolarization in the intact dog', *Circ. Res.* pp. 243–257.
- Spach, M. S., Barr, R. C., Lanning, C. F. & Tucek, P. C. (1977), 'Origin of body surface QTS and the T wave potentials from epicardial potential distributions in the intact chimpanzee', *Circulation* **55**, 268–278.
- Stouboulis, T. & Haque, K. A. (1992), 'Recent experiences with error estimation and adaptivity, Part II: Error estimation for  $h$ -adaptive approximations on grids of triangles and quadrilaterals.', *Comp. Meth. in Appl. Mech and Eng.* pp. 359–430.
- Strickberger, A., Knight, B., Michaud, G., Pelosi, F. & Morady, F. (2000), 'Mapping and ablation of ventricular tachycardia guided by virtual electrograms using a non-contact, computerized mapping system', *J Am Coll Cardiol.* **35**(2), 414–421.
- Terzopoulos, D. (1986), 'Regularization of inverse visual problems involving discontinuities', *IEEE Trans. Pattern Anal. Machine Intell.* **PAMI-8**(4), 413–424.
- Throne, R. D. & Olson, L. G. (1995), 'The effects of errors in assumed conductivities and geometry on numerical solutions to the inverse problem of electrocardiography', *IEEE Trans. Biomed. Eng.* **42**(12), 1192–1200.
- Tikhonov, A. & Arsenin, V. (1977), *Solution of ill-posed problems*, John Wiley & Sons, Washington, D.C.
- Tilg, B. (1998), Noninvasive Functional Cardiac Electrical Source Imaging, PhD thesis, Department of Biophysics, Institute of Biomedical Engineering, Technical University Graz, Austria.
- Tilg, B., Wach, P., SippensGroenewegen, A., Fischer, G., Modre, R., Roithinger, F., Mlynash, M., Reddy, G., Roberts, T., Lesh, M. & Steiner, P. (1999), Closed-chest validation of source imaging from human ECG and MCG mapping data, *in* 'Proceedings of the First Joint Meeting of BMES & IEEE/EMBS', Atlanta, GA, p. 275.
- Tomlinson, K. A. (2000), Finite element solution of an eikonal equation for excitation wavefront propagation in ventricular myocardium, PhD thesis, The University of Auckland, New Zealand.



- Tomlinson, K. A., Pullan, A. J. & Hunter, P. J. (1999), Modeling myocardial excitation wavefront propagation in ventricles by finite element solution of an eikonal equation, *in* 'Proceedings of the First Joint Meeting of BMES & IEEE/EMBS', Atlanta, GA, p. 192.
- Tung, L. (1978), A Bidomain Model for Describing Ischemic Myocardial D-C Potentials, PhD thesis, M.I.T., Boston, MA.
- van Oosterom, A. & Huiskamp, G. J. (1989), 'The effect of torso inhomogeneities on body surface potentials quantified using "tailored" geometry', *J. Electrocardiol.* **22**(1), 53–72.
- Waller, A. D. (1887), 'A demonstration on man of electromotive changes accompanying the heart's beat', *J. Physiol.* **8**, 229–34.
- Waller, A. D. (1889), 'On the electromotive changes connected with the beat of the mammalian heart, and of the human heart in particular', *PTRSL* **180**, 169–194.
- Watanabe, Y. (1996), 'The state of body surface mapping in Japan', *J. Electrocardiol.* **28**(Supplement), 110–120.
- Wilson, F. N. & Bayley, R. H. (1950), 'The electric field of an eccentric dipole in a homogeneous spherical conducting medium', *Circulation* **1**, 84–92.
- Wilson, F. N., MacLeod, A. G. & Barker, P. S. (1933), *The Distribution of the Currents of Action and of Injury Displayed by Heart Muscle and Other Excitable Tissues*, University of Michigan Press, Ann Arbor.
- World Health Organisation (2000), 'World health report 2000', Internet.  
<http://www.who.int/whosis/>.
- Yamashita, Y. (1982), 'Theoretical studies on the inverse problem in electrocardiography and the uniqueness of the solution', *IEEE Trans. Biomed. Eng.* **29**(11), 719–725.
- Yamashita, Y. & Geselowitz, D. (1985), 'Source-field relationships for cardiac generators on the heart surface based on their transfer coefficients', *IEEE Trans. Biomed. Eng.* **32**(11), 964–970.
- Yamashita, Y. & Takahashi, T. (1984), 'Use of the finite element method to determine epicardial from body surface potentials under a realistic torso model', *IEEE Trans. Biomed. Eng.* **31**(9), 611–621.